U.PORTO
FEUP FACULDADE DE ENGENHARIA
UNIVERSIDADE DO PORTO

*Master's Thesis in Mechanical Engineering on*

# Impact of topography on rough contact by computational homogenization

Tiago Rui Silva Sabino

*Advisor:*
Prof. Francisco Manuel Andrade Pires, Ph.D.

*Co-advisors:*
António Manuel Couto Carneiro, M.Sc.
Rodrigo Pinto Carvalho, M.Sc.

Dissertation submitted to the Department of Mechanical Engineering of the Faculty of Engineering of the University of Porto in fulfillment of the requirements for the degree of Master in Mechanical Engineering

Porto, September 2021

CM2S

Computational Multi-Scale
Modeling of Solids and Structures

# Agradecimentos

Em primeiro lugar, gostaria de agradecer ao Prof. Francisco Andrade Pires, orientador desta dissertação, por todo o apoio dado e pela oportunidade de desenvolver o presente trabalho. O seu acompanhamento ao longo dos últimos anos foi essencial para o enriquecimento do meu percurso académico. Agradeço também pela oportunidade de integrar o seu grupo de investigação de qualidade exímia e que espelha todo o seu método e rigor.

Ao Eng. António Couto Carneiro, agradeço a paciência e disponibilidade imensuráveis dedicadas ao apoio da realização desta dissertação. As várias horas de acompanhamento à resolução dos obstáculos encontrados foram fundamentais para a execução deste trabalho. Ao Eng. Rodrigo Pinto Carvalho, gratifico todos os conselhos pertinentes, o sentido crítico e a constante partilha de conhecimento. A ambos agradeço a amizade, simpatia e por serem verdadeiros exemplos. Uma palavra de apreço é também dedicada a todos os membros do CM2S, por proporcionarem um ambiente de trabalho em cooperação ímpar.

Agradeço também aos Engs. Bruno Augusto, Pedro Campos e Luís Carvalho por todo o conhecimento transmitido e pela cooperação nos vários projetos em que estivemos envolvidos. A todos agradeço a disponibilidade e o companheirismo.

Um agradecimento é também feito a todos os amigos que me acompanharam ao longo do percurso académico e que tornaram esta experiência muito mais enriquecedora. Levo comigo recordações de muitos bons momentos. Uma palavra especial é dedicada ao Nuno e ao Francisco pela sua amizade.

Não posso deixar de agradecer a toda a minha família por todo o apoio. Em particular aos meus pais, Rui e Carmen, agradeço ajuda incondicional ao longo de toda a minha vida, todo o esforço e carinho.

À Ana Luísa, agradeço toda a companhia, paciência e compreensão ao longo dos últimos anos. A sua bondade e dedicação contribuíram diretamente para a execução deste trabalho e tornaram o meu percurso académico muito mais fácil.

A todos, o meu sincero obrigado,

Tiago Sabino

*Page intentionally left blank*

*First,*
*you have to finish.*

---

Michael Schumacher

*Page intentionally left blank*

# Abstract


## Impact of topography on rough contact by computational homogenization

**Keywords:** Rough contact; Non-Gaussian rough surfaces; Real contact area; Weibull Distribution; Contact homogenization.

In many engineering problems, it is common to consider smooth surfaces in contact, neglecting the effects of roughness on the micromechanical interactions. However, in the current engineering scenario, roughness has been verified to impact several physical phenomena such as friction, wear, adhesion, thermal and electric contact resistance, among others. In the past decades, theoretical and numerical approaches to rough contact have been made in the context of Gaussian surfaces, mainly due to the easier analytical treatment of the normal distribution of topography heights. Nonetheless, experimental results show that practical surfaces are often non-Gaussian with distinctive values of skewness and kurtosis.

In this work, the impact of non-Gaussian height distribution in the elastic, non-adhesive and frictionless contact between a self-affine topography and a rigid and flat plane is addressed using a finite element method framework, equipped with the dual mortar contact discretization. The non-Gaussian height distribution is modelled using the Weibull probability distribution in its two shapes, namely, the Weibull Maximum and Weibull Minimum, to assess both negatively and positively skewed surfaces, respectively. In the first stage, a numerical study on the statistics of non-Gaussian rough surfaces was performed recovering important quantities, namely the distribution of summits heights and its curvatures. The results were then compared with analytical solutions of the Gaussian case (Nayak's theory) and the effect of the height distribution and the spectral properties were extensively discussed.

In a second part, a finite element analysis of the non-Gaussian rough contact is explored, mainly in two-dimensional conditions due to computational limitations. An initial finite element study on the mesh convergence of the Representative Contact Element (RCE) was done, defining the ideal mesh size for further studies. Second, a larger study was performed to obtain insights about the contact area evolution of Weibull rough surfaces, also incorporating the analysis of the contact pressure distribution. The results were compared to numerical and theoretical Gaussian results highlighting the main differences. Several different topography's parameters were tested and the effects of each were discussed connecting, whenever possible, with statistical insights previously obtained. A final three-dimensional study supported some of the observations done in the previous study.

*Page intentionally left blank*

# Resumo

## Impacto da topografia no contacto rugoso através de homogeneização computacional

**Palavras-Chave:** Contacto rugoso; Superfícies rugosas não-Gaussianas; Área real de contacto; Distribuição de Weibull; Homogeneização computacional de contacto.

Em muitos problemas de engenharia é comum considerar-se superfícies lisas em contacto, desprezando os efeitos da rugosidade nas interações micromecânicas. Contudo, no panorama atual da engenharia, verifica-se que a rugosidade tem impacto em imensos fenômenos físicos, tais como a atrito, o desgaste, a adesão, a resistência térmica e elétrica no contacto, entre outros. Nas últimas décadas, abordagens teóricas e numéricas ao contacto rugoso têm sido desenvolvidas no contexto de superfícies Gaussianas, sobretudo motivado pelo fácil tratamento analítico da distribuição normal das alturas da topografia. No entanto, resultados experimentais têm vindo a mostrar que superfícies de interesse prático são frequentemente não-Gaussianas, possuindo valores distintos de assimetria e curtose.

Neste trabalho, o impacto da distribuição de alturas não-Gaussiana no contacto elástico, não-adesivo e sem atrito entre uma topografia auto-afim (*self-affine*) e um plano rígido é estudado através do método dos elementos finitos com a formulação dual mortar para a discretização do contacto. A distribuição de alturas é modelada através da distribuição de Weibull nas suas duas formas, nomeadamente, Weibull Máximo e Weibull Mínimo, para aproximar topografias com assimetrias negativas e positivas, respetivamente. Numa primeira abordagem, foi realizado um estudo numérico sobre as estatísticas de superfícies não-Gaussianas obtendo-se quantidades importantes tais como a distribuição das alturas dos picos e das suas curvaturas. Os resultados foram comparados com soluções analíticas para o caso Gaussiano (Teoria de Nayak) e foi discutido o impacto da distribuição de alturas e das propriedades espectrais.

Numa segunda parte, uma análise por elementos finitos do problema de contacto foi realizada, considerando, maioritariamente, casos bidimensionais devido a limitações computacionais. Um estudo inicial foi realizado com o intuito de verificar a convergência de malha de um Elemento de Contacto Representativo (ECR), tendo-se definido o tamanho de malha mais conveniente. Foi realizado um segundo estudo de maior dimensão com o intuito de observar o impacto e topografias modeladas com a distribuição de Weibull na evolução da área real de contacto, incorporando também a análise da distribuição das pressões de contacto. Os resultados obtidos foram comparados a soluções analíticas e numéricas do caso Gaussiano evidenciando as principais diferenças verificadas. Vários parâmetros de topografia foram testados e o seu impacto discutido, tendo-se incluído, sempre que possível, a ligação com os resultados estatísticos obtidos inicialmente. Para finalizar, um estudo tridimensional ajudou a suportar algumas das conclusões observadas.

*Page intentionally left blank*

# Contents

*Page intentionally left blank*

# List of Figures

**Chapter 3**
**Numerical study on the statistical geometry of rough surfaces**

**Chapter 4**
**Contact modelling with the dual mortar method**



**Chapter 5**
**Finite element analysis of non-Gaussian rough contact**

*Page intentionally left blank*

# List of Tables

# Nomenclature

### General abbreviations

| | |
|---|---|
| 2D | **Two D**imensional |
| 3D | **Three D**imensional |
| ACF | **A**uto**c**orrelation **F**unction |
| ACL | **A**uto**c**orrelation **L**ength |
| BEM | **B**oundary **E**lement **M**ethod |
| BGT | **B**ush-**G**ibson-**T**homas (model) |
| CM2S | Computational Multi-Scale Modelling of Solids ans Structures |
| CDF | **C**umulative **D**istribution **F**unction |
| DTFT | **D**iscrete-**T**ime **F**ourier **T**ransform |
| EDM | **E**letrical **D**ischarge **M**achining |
| FE | **F**inite **E**lement |
| FEM | **F**inite **E**lement **M**ethod |
| FFT | **F**ast **F**ourier **T**ransform |
| GW | **G**reenwood-**W**illiamson (model) |
| GW-McCool | **G**reenwood-**W**illiamson improved by **McCool** (model) |
| GW-SE | **G**reenwood-**W**illiamson **S**implified **E**lliptic (model) |
| HSM | **H**ertz-**S**ignorini-**M**oreau |
| IBVP | **I**nitial **V**alue **B**oundary **P**roblem |
| IFFT | **I**nverse **F**ast **F**ourier **T**ransform |
| KKT | **K**arush-**K**uhn-**T**ucker |
| `LINKS` | Large Strain Implicit Nonlinear Analysis of Solids Linking Structures |
| `LINKS-RC` | `LINKS` Module for Rough Contact Modelling |
| PDF | **P**robability **D**ensity **F**unction |
| PSD | **P**ower **S**pectral **D**ensity |
| PVW | **P**rinciple of **V**irtual **W**ork |
| RCE | **R**epresentative **C**ontact **E**lement |
| RMS | **R**oot **M**ean **S**quare |
| RSSE | **R**epresentative **S**elf-affine **S**urface **E**lement |
| RVE | **R**epresentative **V**olume **E**lement |

## General notation

| | |
|---|---|
| $a$, $A$ | Scalar |
| $\boldsymbol{a}$ | Vector |
| $\boldsymbol{A}$ | Second-order tensor |
| $\mathbf{A}$ | Matrix |
| $\mathscr{A}$ | Fourth-order tensor |
| $f(\bullet)$ | Continuous function |
| $f[\bullet]$ | Discrete function |

## Operators

| | |
|---|---|
| $\frac{\partial^n(\bullet)}{\partial a^n}$ | Partial derivative of order $n$ relative to $a$ |
| $\frac{\mathrm{d}^n(\bullet)}{\mathrm{d}a^n}$ | Total derivative of order $n$ relative to $a$ |
| det | Determinant of a second-order tensor |
| div$(\bullet)$ | Divergence of a tensor |
| erf$(\bullet)$ | Error function |
| $\gamma\bullet$ | Gamma function |
| $\mathcal{F}\{\bullet\}$ | Fourier transform |
| $\mathcal{F}^{-1}\{\bullet\}$ | Inverse Fourier transform |
| FFT$(\bullet)$ | Fast Fourier transform |
| $\boldsymbol{I}$ | Second-order identity tensor |
| i | Imaginary number ($\mathrm{i} = \sqrt{-1}$) |
| IFFT$(\bullet)$ | Inverse fast Fourier transform |
| max$\{\bullet,\bullet\}$ | Maximum operator |
| Pr$(\bullet)$ | Probability |
| $\delta(\bullet)$ | Dirac Delta function |
| $\delta_{ij}$ | Kronecker delta |
| $\nabla(\bullet)$ | Gradient operator |
| $\nabla^2(\bullet)$ | Laplacian operator |
| $\nabla_x(\bullet)$ | Spatial gradient operator |
| $\emptyset$ | Empty set |
| $\mathbf{0}$ | Zero tensor |
| $(\bullet)^*$ | Complex conjugate |
| $\|\bullet\|$ | Euclidean vector norm |
| $\overline{(\bullet)}$ | Spatial average |
| $\langle\bullet\rangle$ | Ensemble average |
| $\angle(\bullet)$ | Argument of complex number |
| $\|\bullet\|$ | Magnitude of complex number / Absolute value operator |
| $(\bullet)\cdot(\bullet)$ | Dot product |
| $(\bullet):(\bullet)$ | Tensor double contraction |
| $(\bullet)^{\mathrm{T}}$ | Transpose of a tensor |

| | |
|---|---|
| $(\bullet)^{-1}$ | Inverse of a tensor |
| $(\bullet)^{-\mathrm{T}}$ | Inverse of the transpose of a tensor |
| $(\dot{\bullet})$ | Total time derivative |
| $(\bullet) \otimes (\bullet)$ | Dyadic product |
| $(\bullet) \setminus (\bullet)$ | Set difference |
| $(\bullet) \times (\bullet)$ | Cartesian product |

### Subscripts

| | |
|---|---|
| $(\bullet)_{\mathrm{c}}$ | Contact |
| $(\bullet)_{\mathrm{ext}}$ | Exterior |
| $(\bullet)_{\mathrm{ext}}$ | External |
| $(\bullet)_{\mathrm{fit}}$ | Numerical fit |
| $(\bullet)_{\mathrm{fix}}$ | Fixed |
| $(\bullet)_{\mathrm{int}}$ | Internal |
| $(\bullet)_{\mathrm{max}}$ | Maximum value |
| $(\bullet)_{\mathrm{rms}}$ | Root mean square |
| $(\bullet)_x$ | Relative to the $x$ direction |
| $(\bullet)_y$ | Relative to the $y$ direction |
| $(\bullet)_+$ | Quantity in the positive periodic boundary |
| $(\bullet)_-$ | Quantity in the negative periodic boundary |

### Superscripts

| | |
|---|---|
| $(\bullet)^h$ | Discretized version of $(\bullet)$ with the FEM |
| $(\bullet)^{\mathrm{m}}$ | Mortar |
| $(\bullet)^{\mathrm{s}}$ | Non-mortar |
| $(\bullet)^{\eta}$ | Normal direction |
| $(\bullet)^{\tau}$ | Tangential direction |

### Domains and boundaries

| | |
|---|---|
| $\mathbb{Z}$ | Integer set |
| $\mathbb{R}$ | Real set |
| $\Omega_e$ | Finite element sub-domain |
| $\Omega_0$ | Domain of a body in the reference configuration |
| $\Omega_t$ | Domain of a body in the current configuration |
| $\partial\Omega_0$ | Boundary of a body in the reference configuration |
| $\partial\Omega_t$ | Boundary of a body in the current configuration |
| $\Gamma_\sigma$ | Neumann boundary in the reference configuration |
| $\Gamma_u$ | Dirichlet boundary in the reference configuration |
| $\gamma_\sigma$ | Neumann boundary in the current configuration |

| | |
|---|---|
| $\gamma_u$ | Dirichlet boundary in the current configuration |
| $\Gamma_\mathrm{c}$ | Potential contact boundary in the reference configuration |
| $\gamma_\mathrm{c}$ | Potential contact boundary in the current configuration |
| $\Gamma_\mathrm{a}$ | Active contact boundary in the reference configuration |
| $\partial\Omega_\mathsf{ext}$ | Exterior boundary |
| $\partial\Omega_\mathsf{fix}$ | Fixed boundary |
| $\partial\Omega_+$ | Positive periodic boundary |
| $\partial\Omega_-$ | Negative periodic boundary |

### Roughness Parameters

| | |
|---|---|
| $z_{\mathrm{rms},x}$ | Root mean square roughness/height of a continuous profile |
| $z_{\mathrm{rms},xy}$ | Root mean square roughness/height of a continuous surface |
| $z'_{\mathrm{rms},x}$ | Root mean square slope of a continuous profile |
| $z'_{\mathrm{rms},xy}$ | Root mean square slope of a continuous surface |
| $z''_{\mathrm{rms},x}$ | Root mean square curvature of a continuous profile |
| $z''_{\mathrm{rms},xy}$ | Root mean square mean curvature of a continuous surface |
| $R_q$ | Root mean square roughness of a discrete profile |
| $S_q$ | Root mean square roughness of a discrete surface |
| $R_{\Delta q}$ | Root mean square slope of a discrete profile |
| $S_{\Delta q}$ | Root mean square slope of a discrete surface |
| $R_{\Delta^2 q}$ | Root mean square curvature of a discrete profile |
| $S_{\Delta^2 q}$ | Root mean square curvature of a discrete surface |

### Roughness characterization and random processes

| | |
|---|---|
| $b$ | Frequency scale factor in the weak anisotropy power spectrum |
| $C_0$ | Scale factor of the PSD of a self-affine surface |
| $\hat{C}_0$ | Scale factor of the PSD of a discrete self-affine surface |
| $C'_0$ | Scale factor of the PSD of a self-affine profile |
| $\hat{C}'_0$ | Scale factor of the PSD of a discrete self-affine surface |
| $D_p$ | Profile fractal dimension |
| $D_s$ | Surface fractal dimension |
| $e$ | Error of form |
| $f_Z$ | Probability density function of topography heights |
| $F_Z$ | Cumulative distribution function of topography heights |
| $G$ | Profile fractal scale factor |
| $g$ | Surface fractal scale factor |
| $H$ | Hurst roughness exponent |
| $h$ | Topography height |
| $J$ | Profile-surface fractal scale factor in the strong anisotropy power spectrum |
| $k$ | Wavenumber/spatial frequency |

| | |
|---|---|
| $\boldsymbol{k}$ | Wavevector |
| $k_l$ | Low frequency cut-off |
| $k_r$ | Roll-off frequency |
| $k_s$ | High frequency cut-off |
| $\Omega_s$ | Sampling frequency |
| $L$ | Domain length |
| $l_s$ | Sampling wavelength, or sampling interval |
| $m_{\theta n}$ | Profile spectral moment of order $n$ |
| $m_n$ | Profile spectral moment of order $n$, from an isotropic rough surface |
| $m_{mn}$ | Surface spectral moment of order $mn$ |
| $R$ | Autocorrelation function |
| $\widetilde{R}$ | Discrete circular autocorrelation function |
| $\hat{R}$ | Discrete estimate of autocorrelation function |
| $w$ | Waviness profile |
| $z$ | Roughness profile |
| $\mathcal{Z}$ | Random variable associated with roughness height |
| $\alpha$ | Nayak's parameter or spectrum breadth |
| $\beta$ | Autocorrelation length |
| $\beta_2$ | Kurtosis of the heights distribution |
| $\gamma_1$ | Skewness of the heights distribution |
| $\gamma_2$ | Excess of kurtosis of the heights distribution |
| $\zeta$ | Ratio between the roll-off and short cut-off wavelength |
| $\lambda$ | Wavelength |
| $\lambda_l$ | Long wavelength cut-off |
| $\lambda_r$ | Roll-off wavelength |
| $\lambda_s$ | Short wavelength cut-off |
| $\lambda_l/\lambda_s$ | Wavelength ratio |
| $\xi$ | Ratio between the roll-off and large cut-off wavelength |
| $\mu_i$ | Central moment of order $i$ of the probability density function |
| $\mu_z$ | Mean height |
| $\sigma_z$ | Standard deviation of heights |
| $\tau$ | Position shift |
| $\Phi$ | Surface power spectral density |
| $\Phi_\theta$ | Profile power spectral density |
| $\hat{\Phi}$ | Discrete estimate of surface PSD |
| $\hat{\Phi}^\theta$ | Discrete estimate of profile PSD |
| $\phi$ | Phase |

### Statistics of random rough surfaces

| | |
|---|---|
| $z^*$ | Normalized height |
| $p_{\text{sum}}$ | Probability density of summits heights |

| | |
|---|---|
| $p'_{\text{sum}}$ | Joint probability density function for summits with normalized height $z^*$ and equivalent mean curvature $t_1$ |
| $P_{\text{sum}}$ | Probability distribution of summits *per* unit of area |
| $D_{\text{sum}}$ | Density of summits *per* unit of area |
| $q_{\text{sum}}$ | Cumulative density of summits |
| $\kappa_1, \kappa_2$ | Principal curvatures |
| $\kappa_m$ | Mean curvature |
| $\bar{\kappa}_m$ | Expected value of the mean curvature for summits of height $z^*$ |
| $t_1$ | Equivalent mean curvature |

### Weibull distribution

| | |
|---|---|
| $f_W$ | Probability density function of a Weibull distribution |
| $F_W$ | Cumulative distribution function of a Weibull distribution |
| $\mu_W$ | Mean of the PDF of a Weibull distribution |
| $\sigma_W$ | Variance of the PDF of a Weibull distribution |
| $\gamma_{1W}$ | Skewness of the PDF of a Weibull distribution |
| $\beta_{2W}$ | Kurtosis of the PDF of a Weibull distribution |
| $f_W^{Max.}$ | Probability density function of a Weibull Maximum distribution |
| $f_W^{Min.}$ | Probability density function of a Weibull Minimum distribution |

### Numerical generation of rough topography

| | |
|---|---|
| $L$ | Periodic length of the generated topography |
| $l_s$ | Sampling length |
| $M$, $N$ | Number of sampling points in $y$ and $x$ direction, respectively |
| $Z$ | DFT of the topography height |
| $z$ | Surface/profile height |
| $\eta$ | White noise signal |
| $\phi$ | Random phase |
| $\phi'$ | Random phase associated with $\eta'$ |
| $z_h^0$ | Initial random topography with correct PDF |
| $z_s^0$ | Initial random topography with correct PSD |
| $z_h^{i+1}$ | Random topography with correct PDF at the increment $i+1$ |
| $z_s^{i+1}$ | Random topography with correct PSD at the increment $i+1$ |
| $\epsilon_h$ | Error on the PDF of $z_s^{i+1}$ relative to $z_h^{i+1}$ by means of a discrete histogram count |
| $\epsilon_h^{tol}$ | Maximum tolerance on the $\epsilon_h$ |
| $n^b$ | Number of bins |
| $w_c$ | Width of the bin |
| $n_h^c$ | Normalized count of the topography $z_h^{i+1}$ |
| $n_s^c$ | Normalized count of the topography $z_s^{i+1}$ |

| | |
|---|---|
| $\epsilon_s$ | Error on the non-null PSD values of $z_h^{i+1}$ relative to $z_s^{i+1}$ |
| $\epsilon_s^{tol}$ | Maximum tolerance on the $\epsilon_s$ |
| $N_s$ | Number of frequencies with non-null PSD |
| $\epsilon_{s0}$ | Error on the null PSD values of $z_h^{i+1}$ relative to $z_s^{i+1}$ |
| $\epsilon_{so}^{tol}$ | Maximum tolerance on the $\epsilon_{so}$ |
| $N_{s0}$ | Number of frequencies with zero PSD |

### Micromechanical contact

| | |
|---|---|
| $A$ | Nominal contact area |
| $A_c$ | Real contact area |
| $E$ | Young modulus |
| $E^*$ | Effective Young modulus |
| $p$ | Contact pressure |
| $p_0$ | Nominal exterior pressure |
| $\nu$ | Poisson's ratio |

### Kinematics

| | |
|---|---|
| $A$ | Area of the current configuration |
| $A_0$ | Area of the reference configuration |
| $d$ | Number of spatial dimensions |
| $\boldsymbol{e}_1$, $\boldsymbol{e}_2$, $\boldsymbol{e}_3$ | Generic base vector of a Cartesian coordinate system |
| $\boldsymbol{F}$ | Deformation gradient |
| $J$ | Jacobian of the deformation gradient |
| $\boldsymbol{n}$ | Outward unit normal vector in the current configuration |
| $\boldsymbol{N}$ | Outward unit normal vector in the reference configuration |
| $t$ | Time |
| $\boldsymbol{u}$ | Displacement vector |
| $V$ | Volume of the current configuration |
| $V_0$ | Volume of the reference configuration |
| $\boldsymbol{X}$ | Position of a point in the reference configuration |
| $\boldsymbol{x}$ | Position of a point in the current configuration |
| $\varphi$ | Deformation map between the reference and current configurations |

### Strain, stress and constitutive laws

| | |
|---|---|
| $\boldsymbol{C}$ | Right Cauchy-Green strain tensor |
| $\mathscr{C}$ | Fourth-order constitutive tensor |
| $\boldsymbol{E}$ | Green-Lagrange strain tensor |
| $\boldsymbol{f}$ | Force in the current configuration |
| $\boldsymbol{P}$ | First Piola-Kirchoff stress tensor |

| | |
|---|---|
| $\boldsymbol{S}$ | Second Piola-Kirchoff stress tensor |
| $\boldsymbol{\sigma}$ | Cauchy stress tensor |
| $\Psi$ | Strain energy function |

### Governing equations

| | |
|---|---|
| $\boldsymbol{b}$ | Body forces in the current configuration |
| $H^1$ | Sobolev vector space |
| $\mathcal{M}$ | Solution space for the Lagrange multiplier vector |
| $m$ | Mass of a body |
| $T$ | Total simulation time |
| $t$ | Time |
| $\bar{\boldsymbol{t}}$ | Prescribed surface tractions in the current configuration |
| $\mathcal{U}$ | Solution space for the displacement field |
| $\bar{\boldsymbol{u}}$ | Prescribed displacements in the current configuration |
| $\mathcal{V}$ | Solution space for the virtual displacement field |
| $\boldsymbol{t}$ | Surface traction in the current configuration |
| $\delta\boldsymbol{u}$ | Virtual displacement field |
| $\delta\boldsymbol{\lambda}$ | Trial surface traction |
| $\delta\Pi$ | Virtual work |
| $\boldsymbol{\lambda}$ | Lagrange multiplier vector |
| $\lambda^{\eta}$ | Normal projection of the Lagrange multiplier vector |
| $\boldsymbol{\lambda}^{\tau}$ | Tangential component Lagrange multiplier vector |
| $\rho$ | Density in the current configuration |
| $\rho_0$ | Density in the reference configuration |

### Contact mechanics

| | |
|---|---|
| $g$ | Gap function |
| $\boldsymbol{g}$ | Gap vector |
| $\hat{\boldsymbol{x}}$ | Projected point |
| $p^{\eta}$ | Contact normal pressure |
| $\boldsymbol{v}^{\tau}$ | Tangential relative velocity |
| $\boldsymbol{t}_{\mathrm{c}}$ | Contact traction vector in the current configuration |
| $\boldsymbol{t}^{\tau}$ | Tangential contact traction in the current configuration |
| $\beta$ | Coulomb's friction law parameter |
| $\boldsymbol{\eta}$ | Outward unit normal vector to the non-mortar contact surface |
| $\mu$ | Coefficient of friction |
| $\psi$ | Coulomb's friction law slip function |

### Mortar finite element approximation and solution algorithm

| | |
|---|---|
| $C_j^{\eta}$ | Nonlinear complementarity function in the normal direction at the non-mortar node $j$ |
| $c^{\eta}$ | Complementarity parameter in the normal direction |
| $\mathbf{D}$ | First mortar coupling matrix |
| $\mathrm{D}_{jk}$ | Element from the first mortar coupling matrix |
| d | Nodal displacement |
| $\tilde{g}$ | Weighted gap |
| $\mathbf{M}$ | Second mortar coupling matrix |
| $\mathrm{M}_{jk}$ | Element from the second mortar coupling matrix |
| $N$ | Shape function for the displacements and geometry |
| $n^e$ | Number of finite elements |
| $n^{\mathrm{s}}$ | Number of non-mortar nodes |
| $n^{\mathrm{m}}$ | Number of mortar nodes |
| $n^{\lambda}$ | Number of non-mortar nodes carrying Lagrange multipliers |
| x | Nodal coordinates in the current configuration |
| z | Nodal Lagrange multiplier vector |
| $z$ | Component of the nodal Lagrange multiplier vector |
| $\boldsymbol{\xi}$ | Point in the element parameter space |
| $\Phi$ | Shape function for the Lagrange multiplier |

### Numerical model and multiscale approach

| | |
|---|---|
| $H_{\mathrm{sub}}$ | Height of the rough block |
| $H_{\mathrm{ref}}$ | Height of the refined mesh of the rough block |
| $\Delta x$ | Mesh spacing |

*Page intentionally left blank*

# Chapter 1

# Introduction

The purpose of this chapter is to provide an outline of the current dissertation as well as give some context to the work. In this work, the impact of non-Gaussianity on self-affine rough surfaces was studied, modelling the topography's height distribution with two different versions of the Weibull probability distribution. An initial numerical study was done on the surfaces statistics, where several statistical quantifiers of the summits were obtained. In a second part, the numerical modelling of non-Gaussian rough contact was done using the *Finite Element Method* (FEM), within a dual mortar contact formulation. The contact between a rough deformable block and a flat rigid surface was simulated considering elastic, non-adhesive and frictionless conditions. In both studies, the influence of the parameters that parametrize the topography was properly discussed.

## 1.1 Motivation

Contact constitutes one of the most fundamental and ubiquitous physical phenomena. Several applications of modern society rely on solutions that imply contact interactions, from the aerospace industry to nanotechnology applications. In this chapter, the motivation for this work is presented, highlighting the tribology context and importance, giving some historical context on the contact mechanics field and finally introducing the rough surfaces topic with the focus on non-Gaussian topographies.

### 1.1.1 Role of tribology

The engineering field typically devoted to the analysis of contact interfaces is commonly nominated *tribology*. This parlance was first introduced by Jost (1966) and is derived from the Greek word *tribos*, which means rubbing. In the current engineering scenario, tribology faces problems with great economic importance, e.g. reliability, maintenance and wear of technical equipment. Additionally, it also plays a crucial role in modern machinery applications when sliding or rolling surfaces are required, such as brakes, clutches and driving wheels. In the work from Tzanakis *et al.* (2012) it is reported that frictional losses can cost 1% of the gross national product in several nations. Also, in the automotive sector, it is reported that the power losses due to the tire-road interaction cost about 20-30% of the fuel consumption on a road vehicle (Nitsche, 2011). Recently, Holmberg and Erdemir (2017) have stated that around 23% of the worldwide energy consumption

comes from tribological contacts, of which 20% are addressed to overcome friction. The research in the tribology field can lead to higher efficiency and performance in many engineering applications as well as significant savings. Besides the heavy industry, tribology is also present in many other applications like bioengineering and nanotechnology.

### 1.1.2 Historical note

The interest in contact, friction and wear are not only major concerns of today's society, where the industrial needs demand several complex engineering solutions. In fact, reports on the awareness to contact and friction were found in ancient Egypt (circa 1880 BC) where it was found the use of lubricants on the transportation of large stone blocks (Bhushan, 1999). The first scientific approach to friction is accredited to the renaissance engineer–artist, Leonardo da Vinci (1452–1519), who have explored the sliding motion of a rectangular block on a flat surface. Later works, by Guillaume Amontons (1663-1705) and later by Charles-Augustin Coulomb (1736-1806) have cemented the fundamental laws of friction. To the Swiss mathematician, Leonhard Euler (1707-1783), is attributed the first analysis on the contact of rough surfaces, considering triangular asperities. One of the most paramount works within the contact mechanics field was made by Heinrich Hertz (1857-1894), who first introduced the theory of elasticity to frictionless contact in Hertz (1882). This work is often considered the keystone of the modern contact mechanics with several seminal analytical models built from its theory, e.g. the work of J. A. Greenwood, J. B. P. Williamson, *et al.* (1966) on elastic frictionless contact of random rough surfaces or K. L. Johnson *et al.* (1971) and Derjaguin *et al.* (1975) on the adhesive contact between compliant or hard spheres, respectively.

In the last century, within the context of contact mechanics and alongside the Hertz contact theory, several analytical models have been proposed. Despite providing important conclusions, these models are commonly limited to very simple conditions, like elastic frictionless contact, only considering small deformations. The lack of flexibility of the analytical models in pair with the astonishing fast developments in computer hardware has led the community to look forward to computational numerical methods. Tools like the finite element method have become the engineering workhorse when the purpose is to design or study complex engineering phenomena. Large deformations, multi-body interactions, non-linear material models are easily tackled by the currently available FEM frameworks. Within the friction modelling, the dual mortar methods applied to FEM are the current state of the art, enabling a more robust and trustworthy response of the simulations. The use of the numerical methods is also often supported by economic advantage, since empirical experiments are more expensive and, in a certain case, can even be impossible to perform.

### 1.1.3 Rough surfaces

The aforementioned ability of the FEM to untangle complex contact phenomena have potentiated the study of the micromechanical features, such as the contact between rough surfaces. In fact, the contact at the roughness levels has been proven to influence microscopical contact phenomena in several ways. One of the most notable aspects is the real contact area which tends to be smaller than the apparent area. Dieterich and Kilgore (1994) have performed several experiments highlighting this occurrence (cf. Figure 1.1).

The real contact area induced by roughness can have a significant impact on many physical phenomena. Many engineering systems with contact components like roller bearings, tire/road and wheel/rail, gears, electrical components or even micro and nanomechanical systems might be severely affected by such micromechanical behaviour, insofar as the macroscopic behaviour of these parts can be significantly affected by electro-thermo-chemico-mechanical relations at smaller scales. It has been extensively demonstrated that roughness plays a paramount role in friction (Ben-David *et al.*, 2010; Dieterich and Kilgore, 1994), contact electrical resistance (Yastrebov, Cailletaud, *et al.*, 2015), thermal contact resistance (Anciaux and Molinari, 2013), adhesion (Fuller and Tabor, 1975; Pastewka and Robbins, 2014), wear (Bowden and Tabor, 1951; Aghababaei *et al.*, 2016) and fluid motion in contact interfaces (Persson *et al.*, 2004). For all these phenomena, a precise determination of the real contact area for a given set of physical conditions is required in order to better design and explore the systems.

The modelling of rough contact has been an active field of research in the last decades, with several numerical and analytical models proposed in the literature. The first-class of analytical models commonly named *asperity-based models* settles on the definition of asperities, i.e., a summit on a rough surface. The first model formulated around this concept is attributed to J. A. Greenwood, J. B. P. Williamson, *et al.* (1966), and several other enhanced ramifications have emerged over the following years (Bush *et al.*, 1975; McCool, 1986; Thomas, 1998; J. Greenwood, 2006). These models base their principles on the summits height distribution results that have been by obtained by Nayak (1971), that extended the works of Longuet-Higgins and Deacon (1957a,b) A second class of models was initiated by Persson (2001a,b) and are based on the notion of contact pressure distribution with varying magnification. Nonetheless, all the currently available theories rely on some approximations and cannot produce precise results on the contact area evolution in more complex scenarios, thus opening that way for numerical analysis.

The above-presented models have one thing in common that is the assumption that random rough surfaces are defined by a Gaussian distribution. From the statistical results to the analytical contact models, all have assumed that the heights of a rough surface can be modelled by a simple normal distribution. Despite several attempts to justify this hypothesis by highlighting the apparent Gaussian behaviour of real surfaces, the main reason can be attributed to the easier analytical treatment of this distribution, for the most part. This fact has sustained the idea of Gaussian rough surfaces within the scientific community with several works being published on the matter.

Actual engineering surfaces are in fact non-Gaussian as they tend to deviate from the clear and symmetrical form of the Gaussian distribution. This type of topographies is commonly characterized by means of skewness and kurtosis, two statistical quantifiers that help to characterise the deviation from the Gaussian distribution. The majority of the machining processes results in surfaces with non-Gaussian height distributions (Thomas, 1998). In Figure 1.2 and example of a real machined surface, resultant from a boring process, is presented alongside the respective non-Gaussian height distribution. Also, in Figure 1.3 provides a visual representation of the skewness and kurtosis resulting from standard machining processes. It can be seen that while grinding, milling and honing tend to produced negatively skewed surfaces, turning and EDM results in height distri-

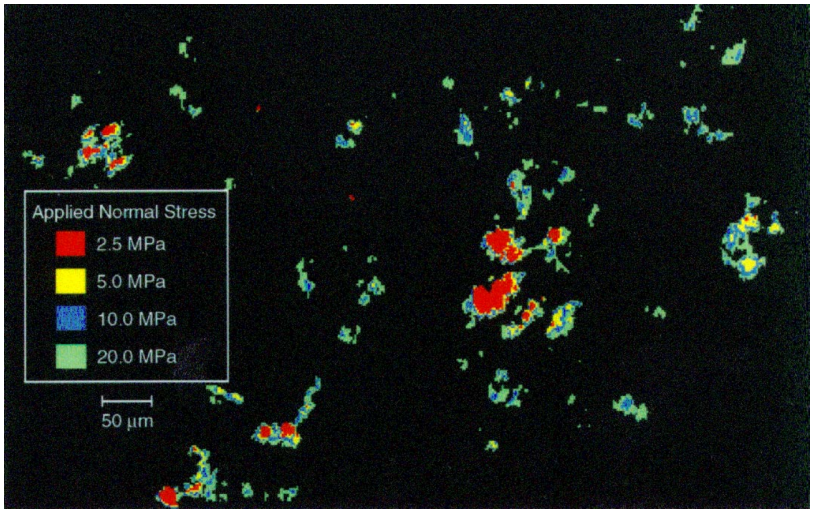


**Figure 1.1:** Photomicrograph by Dieterich and Kilgore (1994) showing the real contact area between a surface of acrylic plastic and other of soda-lime glass, at different loading states. With the load increase, the contact spots tend to expand as well as the number of contact spots.

bution with a positive value of skewness. Additionally, several studies can also be found highlighting the fact that Gaussian and non-Gaussian distribution may exhibit differences in different tribology problems such as interface stiffness, the evolution of the real contact area, adhesion, wear, plastic deformation and others (Pérez-Ràfols and Almqvist, 2019). From a computational standpoint, numerical studies on non-Gaussian surfaces have also been discouraged for two main reasons. First, the generation method of non-Gaussian rough surfaces, up to recently, was a cumbersome process with only some inefficient methods available. The second has to do with the characterization process of this type of topographies that is far more complex than in the Gaussian case. One can characterize the topography based on the skewness and kurtosis, resulting in an overwhelming range of possibilities, or by choosing a probability distribution to model the heights.

## 1.2 Objectives

The main goal of this work is to analyse the impact of non-Gaussian height distributions on the rough contact of self-affine surfaces. The problem under analysis is circumscribed to Signorini-type problems, i.e., the contact between a deformable rough block and a flat rigid surface, considering only elastic, non-adhesive and frictionless contact. To accomplish this an initial numerical routine is developed to obtain the topography statistics of random rough surfaces, taking advantage of already available random rough surface generation algorithms in the in-house numerical framework. With this tool at hand, statistical results on the geometry of non-Gaussian rough surfaces were obtained, giving a background for understanding the contact area results to be analysed later. In a second stage, simulations, using a FEM framework with dual mortar contact discretization, are performed in both 2D and 3D settings, placing focus on the 2D case for computational

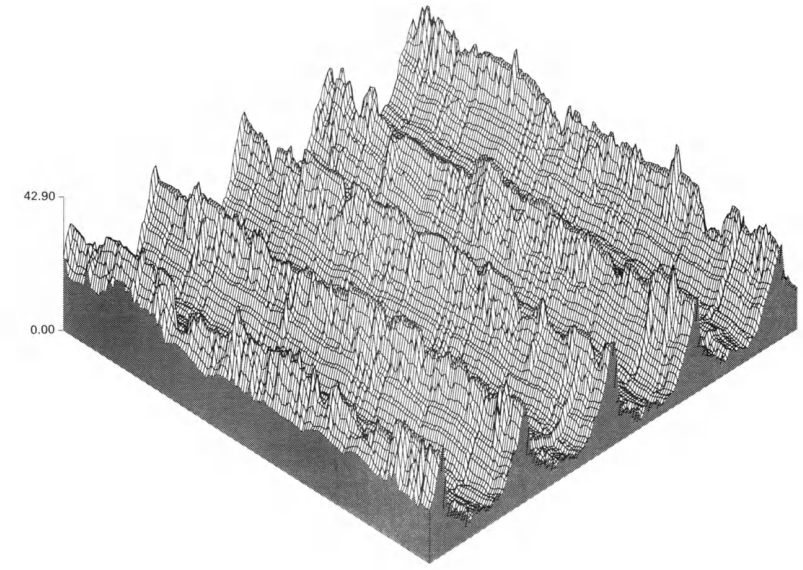


**(a)** Bored machined surface experimentally measured.

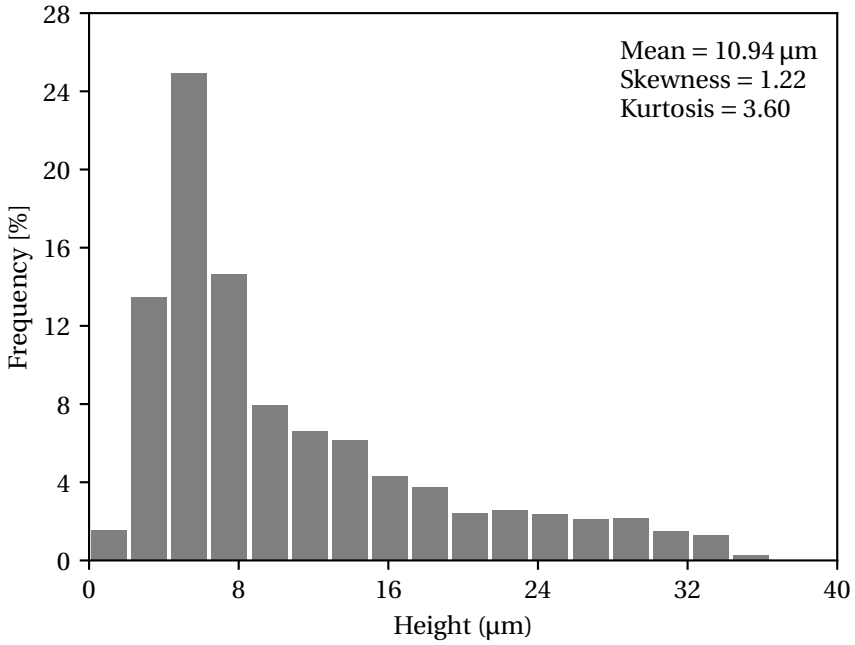


**(b)** Height distribution.

**Figure 1.2:** Example of a non-Gaussian surface obtained by a boring process—adapted from K. J. Stout *et al.* (1990).

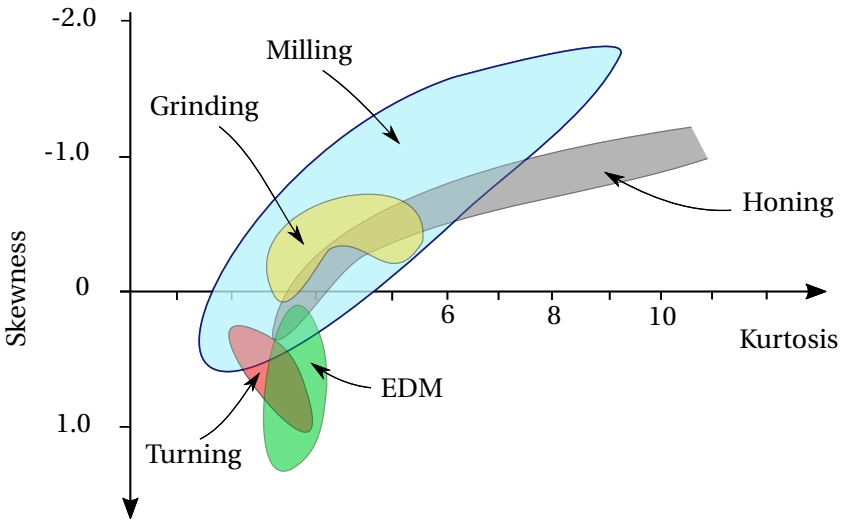


**Figure 1.3:** Experimental values of skewness and kurtosis for surfaces produced by typically machining processes. EDM stands for Electrical Discharge Machining. Results from Whitehouse (1994) adapted by Couto Carneiro (2019).

convenience. The results of real contact area evolution and contact pressure distribution are analysed to highlight the effect of the parameters that parametrize the rough surface on the micromechanical behaviour.

## 1.3 Outline

In sequence with the previous sections, where the motivation and objectives of this dissertation were introduced, a brief description of the chapters found in this document is presented in what follows.

**Chapter 2 - Rough surface characterization**

This chapter intends to give fundamental insights on the definition and characterization of multiscale roughness. The principal tools used to describe roughness are introduced from classical RMS parameters to the most important characterization method for the present work, the so-called Power Spectral Density (PSD), as well as the associated spectral moments. Also, the concepts of fractal surfaces and the definition of a self-affine rough surface are introduced, showing the typical mathematical treatment of this class of topographies. A more in-depth distinction between Gaussian and non-Gaussian surfaces is also done with the introduction of the moments of the height distribution.

**Chapter 3 - Numerical study on the statistical geometry of rough surfaces**

This chapter is fully dedicated to the study of the geometry statistics of random rough surfaces. As a starting point, the fundamental theory (Nayak's theory) on the statistics of random rough surfaces is introduced. The implemented numerical routine for the analysis of the statistics of rough surfaces is presented as well as the method for the generation of Gaussian topographies. The validation of the computational routine is done

by comparing the analytical solutions with the numerical results. In the second part, non-Gaussian topographies are addressed. The Weibull distribution is presented as well as the underlying mathematical formulation, being the parameters of the function adapted to values with engineering significance. A numerical study on the statistics of rough surfaces is presented, discussing the effect of the heigh distribution and the shape parameter. This chapter is closed with a final small study on the dependence of the spectral parameters.

**Chapter 4 - Contact Modelling with the Dual Mortar Method**

A presentation of the fundamental aspects of the FEM framework is provided, starting with a brief introduction to the continuum solid mechanics for solving contact with a dual mortar approach is done. Then the mortar-based finite element formulation is introduced in a weak form, only considering the frictionless contact. To conclude the chapter, the definition of the representative contact element is presented as well as the type of problem analysed in the current work. Further details are also given on the selected roughness model, material properties, boundary conditions, meshing process and methodologies for computing the real contact area.

**Chapter 5 - Finite Element analysis of non-Gaussian rough contact**

This entire chapter is dedicated to the simulation of the contact of non-Gaussian rough surfaces and the discussion of results. A first study is performed with the intent of exploring the effect of mesh discretization in the convergence of the contact area fraction. The convergence of the solution is analysed through different strategies for evaluating the real contact area and a viable mesh size parameter is selected. A second study, the larger and most relevant one, covers the evolution of the contact area with external pressure considering a wide range of different properties that define the non-Gaussian rough surface. The obtained results are then discussed extensively isolating the effect of each parameter and interpreting the results in the light of the statistical results obtained in Chapter 3. To end this chapter, a 3D application is examined with carefully selected due to computational limitations.

**Chapter 6 - Concluding remarks and future work**

The fundamental conclusions of this work and the relevant observations are summarized in this chapter. Future work suggestions within the topic of this dissertation are also presented.

**Appendix A - Numerical fit results in the numerical real contact area 2D FEM study**

This appendix presents the results from the numerical fitting process presented in Chapter 5.

*Page intentionally left blank*

# Chapter 2

# Rough surface characterization

In several fields of science and engineering, it is common to describe bodies in a way that eases the theoretical treatment of the underlying problem. For example, in the case of engineering surfaces, it is often considered smoothness, in order to allow for a geometry characterization based on analytical functions. In reality, however, it is virtually impossible to find surfaces that match their nominal shape as the manufacturing processes inevitably produce deviations relative to the desired shape. These deviations can be broken down in an abstract fashion, setting the foundation for the definition of roughness. In today's technological landscape, roughness plays an unquestionable role in several applications of engineering, especially, involving mechanical contact.

## 2.1 Roughness concepts

It is common to conceptualize surfaces as flat, despising the fact that roughness is naturally present. In nature, surfaces tend to be rough and roughness acts like a measure of the disorder, i.e., entropy. Under the light of the Second Law of Thermodynamics entropy can only be reduced with an external transfer of energy, and so is roughness. Thomas (1998) illustrates this idea by noting that surfaces tend to be smoother for higher machining times. Apart from roughness being a tangible concept, since a *rough surface* can be recognized by simply touching it with a finger, it is a scale-dependent property and distinguishes it from other intrinsic surfaces properties, such as colour. Similarly to hardness, roughness depends on the techniques and scale used in the observation, meaning that it is inherently more difficult to define (Thomas, 1998).

To better understand the concept of roughness, one can consider a real flat surface, produced by a machining process, with some nominal geometry and dimensions correctly defined (cf. Figure 2.1). This process will produce a surface that fits the designated requirements. However, deviations to the nominal shape are expected, which can be divided and their effects and origins individually inspected, in the light of the principle of superposition. First, one can consider that a flat surface with a slight slope is produced, due to a tool misalignment during the machining process, for example. This constitutes an error of form, as the surface does not match the nominal shape. Nevertheless, it does not compromise its smoothness, as it remains perfectly flat. Secondly, problems with

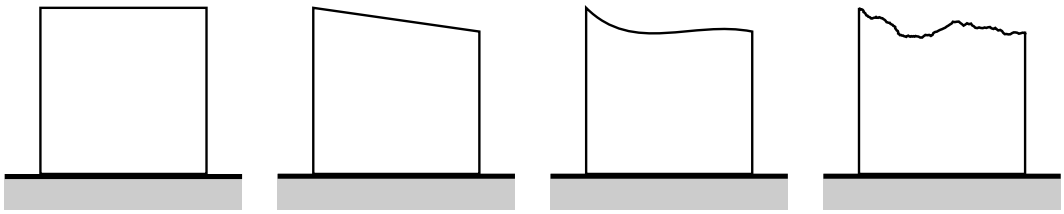


**Figure 2.1:** Different sources of error on real life surfaces. Adapted from Couto Carneiro (2019).

the machining tool, such as vibrations, may cause waviness, i.e., periodic defects on the surface, typically in a form of a random type wave (Whitehouse, 2004). Once more, the surface can still be considered smooth, as long as the wavelength is sufficiently large when compared with the surface size. Finally, one can see that for increasingly smaller values of wavelength the smoothness becomes compromised. In addition, the physical phenomena associated with the process of material removal generate random errors of high spatial frequency, which translates to short wavelengths defects. These constitute the source of what is nominated roughness: at this point, the surface is now deemed rough.

The presented example leads to a very simple description of a surface height $h(x, y)$, by simply superimposing the previously mentioned defects, i.e., the error of form $e(x, y)$, the waviness $w(x, y)$ and the roughness $z(x, y)$, viz.

$$h(x, y) = e(x, y) + w(x, y) + z(x, y) \, . \tag{2.1}$$

After this brief example, one can accept that the high-frequency variations are what becomes understandable as roughness. This hypothesis is in agreement with the already advanced concept of roughness as scale-dependent property. As an illustration of this scale dependency, Thomas and King (1977) explores the effects of progressively smaller wavelengths and amplitudes in physical systems, by creating an analogy with enlargements in a geographic map. In his work, he states that features as long as 10 m affect aircraft suspensions when landing in a rough airstrip. Similarly, for wavelengths around 1 m, effects are felt in road car and rail vehicles suspensions. The later case comprises amplitudes from 10 to 100 mm. For wavelengths below 10 cm, the surface features became responsible for the tyre-road interactions, such as skidding. For even shorter wavelengths, one can enter the domain of machined surfaces, where amplitudes of 0.1 to 1 mm can be responsible for drag increase due to hull friction. A step further into smaller wavelengths, from 1 mm down to 1 µm, roughness features may be associated with the origins of friction, wear, noise or even failure in bearings of different types. Finally, wavelengths below 1 µm down to 10 nm assume importance in some physical properties such as reflection and diffraction of electromagnetic radiation. The objective of this description is to point out the importance of the scale in surface analysis. Therefore, in an engineering context, one can state that the scale in which the surfaces are studied should be properly defined, as well as in the measurement process, where this variable plays a key role.

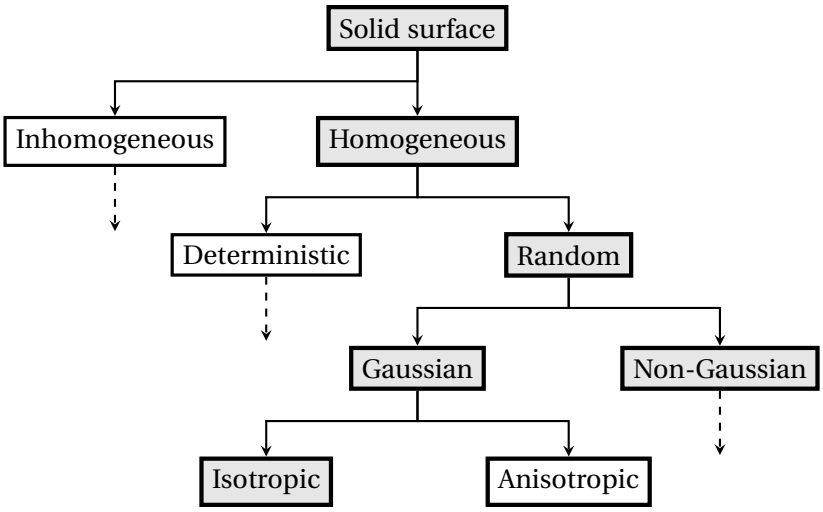


**Figure 2.2:** Classification of rough surfaces—adapted from Nayak (1971). The dashed lines indicate the paths where the sub-divisions may continue, and the coloured boxes the types of surfaces discussed in the current work. Adapted from Couto Carneiro (2019).

### 2.1.1 Classification of rough surfaces

The classification of surfaces is an important topic, as it allows to properly locate the research area within the context of the current work. Traditionally, the surface classification follows the typology shown in Figure 2.2 (Nayak (1971) and Bhushan (2013)). The first branch distinguishes the surfaces based on how the properties vary along the surface. A surface with a uniform distribution of geometrical features is classified as *homogeneous*, otherwise, it is considered *inhomogeneous*. Homogeneous surfaces may be *deterministic* or *random*, based on their stochastic nature. Roughness is obviously a random occurrence, despite some scenarios that may have predictable behaviour, such as on surfaces produced by turning. (Thomas, 1998). One can further divide the randomness of surface topography by looking at how the height distribution behaves. If one can use a normal distribution to describe the heights on a surface, it may be nominated *Gaussian*, otherwise, the surface is called *non-Gaussian*. The last sub-division refers to the directionality of rough properties. If roughness is independent of the orientation, the surface is called *isotropic*, alternatively, if one can clearly distinguish directions of different rough properties, a surface is called *anisotropic*.

The classification of rough surfaces is greatly associated with the process from which it originates. Surfaces that result from processes such as shot-peening, lapping or electropolishing, are subjected to a continuous process of random and discrete local events, producing a net effect that results in a Gaussian distribution of surface heights—a consequence of the Central Limit Theorem (Bhushan, 2013). In contrast, processes like turning and milling may lead to non-Gaussian and anisotropic surfaces. The latter category usually allow an easier visual identification, due to the presence of grooves along a preferential direction.

## 2.2 Roughness parameters

Historically, the characterization of surfaces has been sought with the so-called roughness parameters, which describe and characterize the surfaces by evaluating their geometrical features based on discrete data collected from experimentation. This approach is fundamental to roughness studies as it provides a straightforward method for comparing surfaces with different characteristics, for example, to compare the roughness state before and after loading tests.

The calculation of these parameters can be carried out seamlessly for both profiles and surfaces, as long as data is collected for the purpose. Commonly, the nomenclature used for profile parameters is $R_{(\cdot)}$, with a subscript depending on the specific parameter. Similarly, the surface parameters are described by the symbol $S_{(\cdot)}$. Both result in useful values for roughness analysis, nonetheless, the profile parameters, despite being cheaper and faster to execute, store inherently less information than surface parameters—this point will be clarified in the following paragraphs. This difference can be highlighted, with the following examples, and shown at in Figure 2.3, while introducing some common nomenclature and concepts. Consider a generic profile obtained by the intersection of a surface with an arbitrary plane parallel to $xOz$ or $yOz$. The profile's local maximum is defined as the points where

$$\frac{\partial z}{\partial x} = 0 \quad \text{or} \quad \frac{\partial z}{\partial y} = 0\,, \tag{2.2}$$

according to the plane considered, and is called a *peak*. For the surfaces case, the local maximum is termed *summit*, and must satisfy [1]

$$\|\nabla z\| = 0\,. \tag{2.3}$$

Attending at the definitions presented (Equation (2.2) and Equation (2.3)), and considering that profiles are simply intersections of the surface with a plane of measurement, one can see that peaks and summits may not occur at the same point, which ultimately may lead to erroneous conclusions—cf. Figure 2.3.

### 2.2.1 Root mean square parameters

Within the context of the current work, the most important parameters are the so-called *root mean square parameters*, typically abbreviated to *RMS*, from *root mean square*. These parameters gained relevance due to their applications in micromechanical contact models and the important relations with other parameters (K. L. Johnson, 1985).

**RMS heigh/roughness**

The *RMS height*, also called commonly called *RMS roughness*, is a measure of the surface height relatively to the mean plane. The continuous version of this parameter for a rough

[1] The operator $\|\cdot\|$ denotes the euclidean norm of vector and $\nabla(\cdot)$ the gradient of a function.

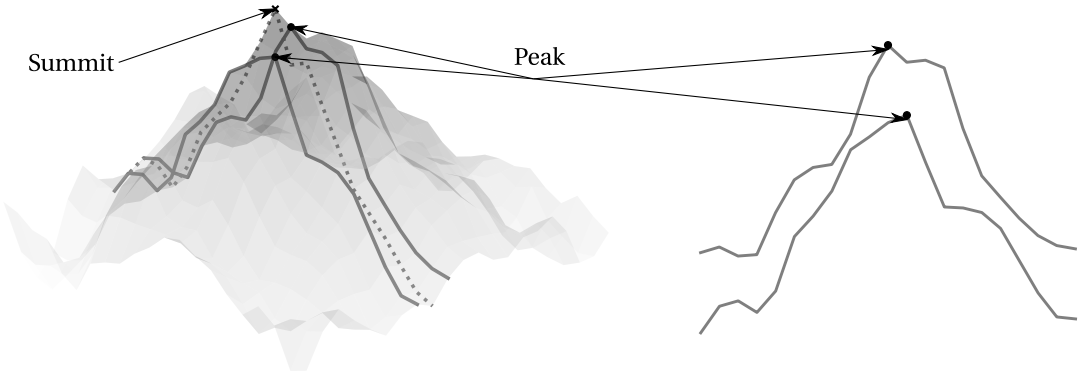


**Figure 2.3:** Distinction between peaks and summits. A profile peak may not coincide with a real surface summit.

profile $z(x)$ and a rough surface $z(x,y)$ writes

$$z_{\mathrm{rms},x} = \sqrt{\frac{1}{L}\int_0^L z^2(x)\ \mathrm{d}x} = \sqrt{\overline{z^2(x)}}\,; \tag{2.4a}$$

$$z_{\mathrm{rms},xy} = \sqrt{\frac{1}{L_x L_y}\int_0^{L_x}\int_0^{L_y} z^2(x,y)\ \mathrm{d}y\mathrm{d}x} = \sqrt{\overline{z^2(x,y)}}\,. \tag{2.4b}$$

where $\overline{(\bullet)}$ represents the spatial average operator. It is important to note that Equations 2.4 are very rare to apply, since in reality, one works with sampled surfaces and profiles, which leads to the discrete version of the parameter. Therefore, consider a profile $z(x)$, with $x \in [0, L]$, and with $N$ sampled points, uniformly spaced. In the same way, for a surface $z(x,y)$, with $(x,y) \in [0, L_x] \times [0, L_y]$, and with a grid of $N \times M$ equally spaced points. [2] [3] One writes the RMS height as

$$z_{\mathrm{rms},x} \approx R_q = \sqrt{\frac{1}{N}\sum_{n=0}^{N-1} z_n^2}\,; \tag{2.5a}$$

$$z_{\mathrm{rms},xy} \approx S_q = \sqrt{\frac{1}{MN}\sum_{m=0}^{M-1}\sum_{n=0}^{N-1} z_{m,n}^2}\,. \tag{2.5b}$$

By definition, the RMS height quantifies the global height variation, providing a numerical value that is sensible to surface height, especially the extreme values, namely valleys and summits. Nevertheless, these contribute indistinctly to the computation of the parameter, since it considers only the real squared values. However, the RMS height is by no means able to uniquely characterise a rough surface. To point out this aspect, two profiles with the same value of RMS height are shown in Figure 2.4. The profile of Figure 2.4a has larger slopes than the profile of Figure 2.4b, and the latter has a smoother aspect.

[2] The operator $[\bullet,\bullet] \times [\bullet,\bullet]$ represents the Cartesian product.

[3] $N$ and $M$ refer, respectively, to the $x$ and $y$ directions.

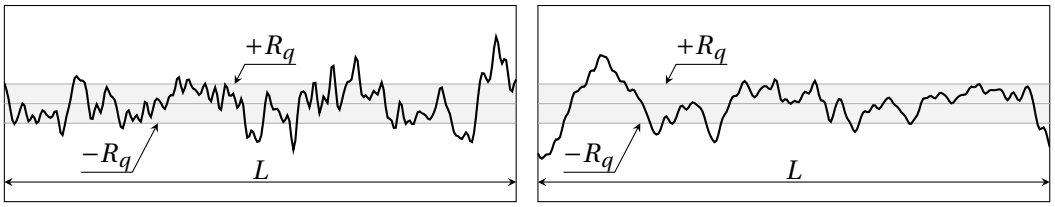


**(a)** Profile with large slopes. **(b)** Profile with small slopes.

**Figure 2.4:** Comparison between two profiles with the same value of RMS height $R_q$. Adapted from Couto Carneiro (2019).

Both share the same RMS height, however different overall characteristics can readily be identified, thus one can conclude that the RMS height is not sufficient to capture all the information of a rough surface.

**RMS slope**

The RMS height limitation to distinguish surfaces with considerable different surfaces characteristics, fosters the use of parameters associated with the slope. Similarly to the previous parameter, one writes the RMS slope of a continuous profile and a continuous surface as

$$z'_{\mathrm{rms},x} = \sqrt{\overline{\left(\frac{\mathrm{d}z(x)}{\mathrm{d}x}\right)^2}}\,; \tag{2.6a}$$

$$z'_{\mathrm{rms},xy} = \sqrt{\overline{\|\nabla z(x,y)\|^2}}\,. \tag{2.6b}$$

Once more, the discrete version must be employed to preform calculation on sampling data, either from experimental measurement or from numeric generation. Unlike RMS height, the RMS slope requires the numerical computation of derivatives. The ISO 25178 proposes the use of a first-order finite difference stencil, whereas, the ASME B46 recommends the use of a sixth-order stencil. However, both techniques may introduce either smoothing or artificially sharp corners, resulting in unwanted inaccuracies. An easier way to calculate this derivatives is based on a forward finite-difference scheme (Bhushan, 1999). Using this method, one writes the discrete version of RMS slope as follows

$$z'_{\mathrm{rms},x} \approx R_{\Delta q} = \sqrt{\frac{1}{(N-1)}\sum_{n=0}^{N-2}\left(\frac{z_{n+1}-z_n}{\Delta x}\right)^2}\,; \tag{2.7a}$$

$$z'_{\mathrm{rms},xy} \approx S_{\Delta q} = \sqrt{\frac{1}{(M-1)(N-1)}\sum_{m=0}^{M-2}\sum_{n=0}^{N-2}\left(\frac{z_{m,n+1}-z_{m,n}}{\Delta x}\right)^2+\left(\frac{z_{m+1,n}-z_{m,n}}{\Delta y}\right)^2}\,. \tag{2.7b}$$

**RMS curvature**

The RMS curvature follows similar concepts as the aforementioned parameters. Once again, there may exist surfaces with the same values of RMS slope, even though their

curvature features are considerably different. This parameter goes one step further into the derivation process, considering the second derivatives of the profile, and one writes the continuous version for profiles and surfaces as

$$z''_{\mathrm{rms},x} = \sqrt{\overline{\left(\frac{\mathrm{d}^2 z(x)}{\mathrm{d}x^2}\right)^2}}\,; \tag{2.8a}$$

$$z''_{\mathrm{rms},xy} = \frac{1}{2}\sqrt{\overline{\left[\nabla^2 z(x,y)\right]^2}}\,. \tag{2.8b}$$

For a better understanding on the concept of RMS curvature, one shall distinguish this value from the classic definition of curvature. For a profile $z(x)$, the geometric curvature definition comes

$$\kappa_R = \frac{z''(x)}{\left(1+[z'(x)]^2\right)^{\frac{3}{2}}}\,, \tag{2.9}$$

where $z'(x)$ and $z''(x)$, are the first and second derivatives in of the profile in order to $x$. On the other hand, for a surface $z(x,y)$, one writes [4]

$$\kappa_S = \frac{\left(\frac{\partial z}{\partial x}\right)\left(\frac{\partial^2 z}{\partial y^2}\right) - \left(\frac{\partial z}{\partial y}\right)\left(\frac{\partial^2 z}{\partial x^2}\right)}{\left[\left(\frac{\partial z}{\partial x}\right)^2 + \left(\frac{\partial z}{\partial y}\right)^2\right]^{\frac{3}{2}}}\,. \tag{2.10}$$

In this case, the second-order partial derivatives of the surface are necessary. From these equations (Equation (2.9) and Equation (2.10)), the difference between the continuous definition of the RMS curvature can be emphasized. It is interesting to note that, the profile's curvature $\kappa_R$ is only equal to the second derivative of the profile where the slope is equal to zero, i.e, $z'(x) = 0$, which coincides with profile peaks and valleys. This consideration supports the fact that in contact theories for rough surfaces the interest is frequently on the extreme values of the topography. As a result, the RMS curvature values are commonly used as an approximation for the mean curvature (McCool, 1986).

Similarly to the RMS slope, the discrete version of the RMS curvature implies the numerical computation of the derivative—second order in this case. In advance, one can realise that for a point on a smooth surface, the curvature varies according to the direction relative to which it is computed. At the same point, there are two orthogonal directions, termed *principal directions*, along which one finds the maximum and minimum curvatures. For the calculation of the RMS curvature, the average value of these curvatures, named *mean curvature*, is used. It can be proved that this mean value is equal for any two orthogonal directions considered in the same point (Sokolnikoff, 1964). Therefore, a well-suited formulation arises for the computation of the RMS curvature, along the $x$ and $y$ directions of the sampled surfaces. Using a centred finite difference scheme (Bhushan, 1999), one writes the discrete version of RMS curvature as

[4] For the sake of clarity, the arguments $x$ and $y$ were omitted from the Equation (2.10), writing $z$ instead of $z(x,y)$.

$$z''_{\mathrm{rms},x} \approx R_{\Delta^2 q} = \sqrt{\frac{1}{(N-1)} \sum_{n=0}^{N-3} \left( \frac{z_{n+1} - 2z_n + z_{n-1}}{\Delta x^2} \right)^2}\,; \tag{2.11a}$$

$$z''_{\mathrm{rms},xy} \approx S_{\Delta^2 q} = \left[ \frac{1}{(M-2)(N-2)} \sum_{m=0}^{M-3} \sum_{n=0}^{N-3} \frac{1}{4} \left( \frac{z_{m,n+1} - 2z_{m,n} + z_{m,n-1}}{\Delta x^2} + \right. \right. \tag{2.11b}$$

$$\left. \left. + \frac{z_{m+1,n} - 2z_{m,n} + z_{m-1,n}}{\Delta y^2} \right)^2 \right]^{\frac{1}{2}}.$$

### 2.2.2 Parameters limitations

To conclude, one must reinforce the fact that roughness is a general characteristic of surfaces, which implies a vast use of different techniques and methods for its evaluation, in many different scientific and engineering problems. This fact, extended by years of research, resulted in a large number of roughness parameters, with no significant scientific increment in the theoretical and practical understanding of roughness. The parameters exceeded hundreds and led to the satiric term *parameter rash*, originally introduced by Whitehouse (1982) in his work. A complete overview of all parameters does not exist, and it would be a potentially cumbersome task with a very small return on investment, since many of the parameters are just different ways of describing the same properties, in a way that some parameters are dependent on each other (Thomas, 1998). Naturally, over the years only, a few parameters have received acceptance within the scientific community (Mainsah *et al.*, 2001). The roughness parameters included in this description could have been a lot more. Even with the RMS parameters, the analysis could have gone further, into third and fourth derivatives, yet, problems with the numerical computation would probably arise, as well as lack of physical meaning within the surface roughness context.

One of the biggest limitations when working with parameters such as the ones presented before, is their scale dependency, and how the variations of sampling length, discretization methodology and measuring equipment and/or process, affect the results. Experimental results in the field have consistently supported these statements. Sayles and Thomas (1978) and Bhushan (1999) have shown that RMS height presents a very sensible behaviour to the low cut-off wavelength, frequently decreasing for shorter values of this dimension. P. I. Oden *et al.* (1992) observed in his work that for decreasingly smaller values of cut-off wavelength the RMS slope and curvature tend to increase. These results are clear evidence that these parameters are scale-depend, which invalidates a comprehensive characterisation of roughness purely based on scalar parameters.

## 2.3 Autocorrelation function

The drawbacks of the scale-dependent roughness parameters fostered the analysis based on the random nature of rough surfaces—although, as it will be seen later in the text, it revealed unfruitful in the search for scale-independency, This type of description is based on established stochastic analysis concepts, that follow a rigorous mathematical

description. Within the context of this work, a light version of this treatment suffices, and only fundamental concepts are presented. The reader is referred to Bendat and Piersol (2010) for a sound presentation on the characterization of a random process.

The surface height of a rough surface behaves as a *stochastic or random process*, and is considered a *random variable*, represented by $\mathcal{Z}$, with various realizations—$z^{(k)}(x)$, for profiles, and $z^{(k)}(x,y)$, for surfaces. All the possible surfaces that can be obtained are named the *ensemble*. For each realization there is a certain probability of the obtained surface being similar to a previous know reference. The *ensemble averages*, are a set of statistics, computed from $K$ realizations, that ease the random surface description. The ensemble mean value of $\mathcal{Z}$ is one of the ensemble averages and can be determined for a point $i$ of coordinates $(x_i, y_i)$, as

$$\mu_z(x_i) = \frac{1}{K}\sum_{k=0}^{K-1} z^{(k)}(x_i) = \langle z^{(k)}(x_i)\rangle\,, \tag{2.12a}$$

$$\mu_z(x_i, y_i) = \langle z^{(k)}(x_i, y_i)\rangle\,, \tag{2.12b}$$

where the operator $\langle\bullet\rangle$ denotes the ensemble average, that represents the mean height of the ensemble at a specific point $(x_i, y_i)$.

The *autocorrelation function* (ACF) comes as another important ensemble average and is defined by

$$R(x_i, x_i+\tau) = \langle z^{(k)}(x_i) z^{(k)}(x_i+\tau)\rangle\,; \tag{2.13a}$$

$$R(x_i, y_i, x_i+\tau_x, y_i+\tau_y) = \langle z^{(k)}(x_i, y_i) z^{(k)}(x_i+\tau_x, y_i+\tau_y)\rangle\,. \tag{2.13b}$$

for the profile and surfaces cases, respectively. One shall note the ACF of a surface is function of the point in which is calculated $(x_i, y_i)$ and the shift considered $(\tau_x, \tau_y)$. This quantity can be interpreted as the ensemble average of the product between a point and shifted version of it, given by a vector $(\tau_x, \tau_y)$. Ultimately, it can be associated with the probability of existing a point $(x_i, y_i)$ with $z_i^{(k)}$ and another point $(x_i+\tau_x, y_i+\tau_y)$ with $z_{i+\tau}^{(k)}$, in the same realization.

It is possible to simplify the presented ensemble averages attending to two different aspects. On the one hand, rough surfaces are frequently assumed as *stationary*, i.e., the ensemble averages became independent of $(x_i, y_i)$. Usually, the notion of the *weak-sense stationary* properties is considered, from which the position independence of the ensemble mean and ACF is assumed. On the other hand, rough surfaces are also considered *ergodic*, meaning that a single sample has sufficient information about every other samples. Ensemble averages can be rewritten in light of the stationary and ergodicity properties. The first condition removes the position dependency and leads to a constant value of the ensemble mean $\mu_z$ an to autocorrelation function (ACF) only dependent of the shift $(\tau_x, \tau_y)$. Moreover, the ergodicity property, states that the ensemble averages can be replaced by the sample averages. Taking this into account, Equations 2.12 are rewritten as

$$\mu_z = \overline{z(x)}\,, \tag{2.14a}$$

$$\mu_z = \overline{z(x,y)}\,. \tag{2.14b}$$

where the superscript $(k)$ was removed, as there is no need to refer to a particular realization any-more. For the ACF, one must note that unless the surface is infinite or periodic, the number of matching points decreases with the increase of the shift $(\tau_x, \tau_y)$. Therefore, considering a finite-length topography, by means of the ergodicity and the stationary properties, Equations 2.13 can be rewritten as

$$R(\tau) = \frac{1}{L-\tau} \int_0^{L-\tau} z(x)z(x+\tau)\ \mathrm{d}x\,, \tag{2.15a}$$

$$R(\tau_x, \tau_y) = \frac{1}{(L_x-\tau_x)(L_y-\tau_y)} \int_0^{L_x-\tau_x} \int_0^{L_y-\tau_y} z(x,y)z(x+\tau_x, y+\tau_y)\ \mathrm{d}y\mathrm{d}x\,. \tag{2.15b}$$

These equations reveal further insights about the meaning of the ACF. One can see the ACF as a measure of how similar a surface looks with a shifted copy of itself. Additionally, since this parameter is a function of the shift $\tau$ and not just a single value, it holds more information than pure roughness parameters, and has been a valuable tool for rough surface analysis. Starting at a null value of shift, $\tau = 0$, one can readily write the following relations

$$R(0) = (z_{\mathrm{rms},x})^2 = \overline{(z(x))^2} = \sigma_z^2\,, \tag{2.16a}$$

$$R(0,0) = (z_{\mathrm{rms},xy})^2 = \overline{\big(z(x,y)\big)^2} = \sigma_z^2\,, \tag{2.16b}$$

where the $\sigma_z$ is the standard deviation of topography heights. Equations 2.16 can be more easily understood by taking a closer look into Equations 2.4. The ACF has a maximum when no shift is applied since it corresponds to the integral of the product of the squared heights—integral of positive values. Therefore, the ACF starts on the squared value of the RMS heights and decreases from there on, since for increasing values of the shift, positive and negative values of height are multiplied, ultimately leading to the ACF decay. This decaying also stores information on the surface characteristics since, for a profile with high-frequency variations, the ACF has a faster decay than for a smoother surface, with more pronounced high-wavelength oscillations.

### 2.3.1 Exponentially decaying model

Whitehouse, Archard, *et al.* (1970) proposed a model that predicts an exponential decay of the ACF with the position shift, that is classically written as follows

$$R(\tau) = R_q^2\ \exp\left(-\frac{|\tau|}{\beta}\right)\,, \tag{2.17}$$

where $\beta$ is the autocorrelation length (ACL), and it can be defined as the value of shift that leads to a reduction of the ACF by a factor of $e^{-1}$, which is approximately 36.8% of the ACF value at the origin $(R_q^2)$ (Whitehouse, Archard, *et al.*, 1970; Panda *et al.*, 2016). The Figure 2.5 presents the evolution of the exponentially decaying ACF model for different values of $\tau$ and $\beta$. For the same length $L$ and RMS height, Figure 2.5 shows that the for higher values of $\beta$ the profile tends to be smoother, in the sense that high-frequency contributions have a smaller amplitude.

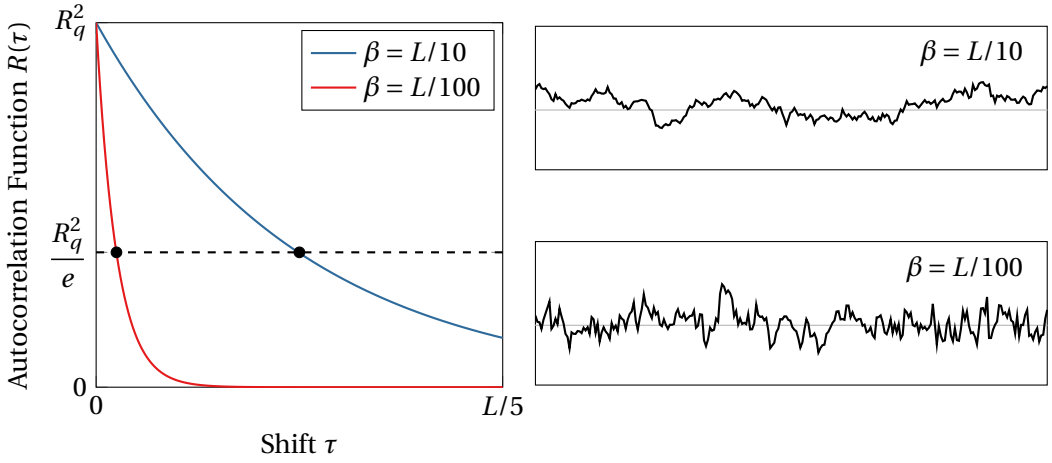


**Figure 2.5:** Effect of the shift $\tau$ and the ACL $\beta$ in the exponentially decaying ACF model and respective effects on rough profiles. Adapted from Couto Carneiro (2019).

One can extend the exponential decaying ACF model for surfaces, where two directions, $x$ and $y$, must be considered. To satisfy this condition, the autocorrelation lengths in both directions are introduced ($\beta_x$ and $\beta_y$), which leads to the ACF model

$$R(\tau_x, \tau_y) = S_q^2 \exp\left(-\sqrt{\left(\frac{\tau_x}{\beta_x}\right)^2 + \left(\frac{\tau_y}{\beta_y}\right)^2}\right). \tag{2.18}$$

In this fashion, the model allows the consideration of directional properties, that can be used to represent the anisotropic behaviour of the surfaces. For different values of ACL, one can obtain surfaces with notorious anisotropic properties. For instance, if $\beta_x$ is smaller than $\beta_y$, it means that along the $y$ direction one sees a smoother behaviour when compared with the orthogonal direction. For the particular case when $\beta_x = \beta_y$, the surface is isotropic.

This model has been discussed in the work of Nayak (1971), stating that the exponential model for the ACF does not allow the existence of slopes and curvatures, even though experimental results were obtained by Whitehouse, Archard, *et al.* (1970)—it should be, at least, fourth-order smooth at the origin. He justifies that based on the use of finite sampling interval, as it works as a filter for small-wavelength features, which change the ACF behaviour at the origin. Therefore, in the concluding remarks from Nayak's works, he states that the exponential ACF decaying may actually be verified, but not starting in the origin.

### 2.3.2 ACF limitations

The ACF is a big step towards the accurate description of topographies and all the respective random features. As remarked in previous sections, it is capable of giving information about the amplitudes and also the distribution of peaks and summits. However, some works point out limitations to this method. For example, Zhang *et al.* (2014) and Panda *et al.* (2016) verified experimentally that the ACL value varies with the sample size and

frequency. Thomas (1998) also stated that ACF depends on the cut-off length. Ultimately this leads to the conclusion that the ACF still fails in the full description of rough surfaces, as it presents some scale-dependency, as similarly observed for the RMS parameters.

**Remark 2.1 on the definition of autocorrelation function.**
*The autocorrelation function definition adopted in the current work is the one presented in Equation* (2.15)*. Within the bibliography dedicated to this topic, one may find differences in notation and designation. For example, in Thomas (1998) and Mainsah* et al. *(2001) an equivalent definition to the presented in the current work is termed "autocovariance function", while the designation "autocorrelation function" stands for the autocovariance normalized with the RMS height.*

## 2.4 Power spectral density

In the endeavour to find a scale-independent way of describing rough surfaces, one finally arrives at the *Power Spectral Density* (PSD)—arguably the most important characterization method for rough surfaces. This function has its origins in signal processing theory, which justifies its name. It measures the frequency content of a random signal, relating the frequency with the signal power (Panda *et al.*, 2016). The PSD can be defined in multiple ways, yet within the context of this work, and following the description already advanced, the definition of PSD is presented via the ACF—the reader is referred to Bendat and Piersol (2010) for a more detailed approach. The notation adopted for the PSD of a surface is $\Phi$ and, in a same fashion, $\Phi_\theta$ for a profile. From the Wiener-Khinchin theorem, one defines the PSD as the Fourier transform of the ACF as

$$\Phi_\theta(k) = \mathcal{F}\{R(\tau)\} = \int_{-\infty}^{+\infty} R(\tau) e^{-\mathrm{i}k\tau}\, \mathrm{d}\tau\,, \tag{2.19a}$$

$$\Phi(k_x, k_y) = \mathcal{F}\left\{R(\tau_x, \tau_y)\right\} = \iint_{-\infty}^{+\infty} R(\tau_x, \tau_y) e^{-\mathrm{i}(k_x\tau_x + k_y\tau_y)}\, \mathrm{d}\tau_x \mathrm{d}\tau_y\,. \tag{2.19b}$$

where $\mathcal{F}\{\bullet\}$ denotes the Fourier transform, and $\mathrm{i} = \sqrt{-1}$ stands for the imaginary number. One can rewrite the Equations 2.19 in terms of ACF, making use of the inverse Fourier transform, represented by the operator $\mathcal{F}^{-1}\{\bullet\}$,

$$R(\tau) = \mathcal{F}^{-1}\{\Phi_\theta(k)\} = \frac{1}{2\pi}\int_{-\infty}^{+\infty} \Phi_\theta(k) e^{\mathrm{i}k\tau} \mathrm{d}k\,, \tag{2.20a}$$

$$R(\tau_x, \tau_y) = \mathcal{F}^{-1}\left\{\Phi(k_x, k_y)\right\} = \frac{1}{4\pi^2}\iint_{-\infty}^{+\infty} \Phi(k_x, k_y) e^{\mathrm{i}(k_x\tau_x + k_y\tau_y)}\, \mathrm{d}k_x \mathrm{d}k_y\,. \tag{2.20b}$$

A more in-depth understanding of the Equations (2.19) and (2.20), requires a few comments on the notation and properties of such relations. For a one-dimensional case, the Fourier transform can be interpreted as the superposition of sinusoidal waves, characterized by a frequency/wave-number $k$, amplitude and phase. The same holds for the two-dimensional case, where two-dimensional waves are summed. In this scenario, each wave has a particular combination of amplitude, phase, frequency and propagation direction—in contrast with the one-dimensional case. The frequency and propagation direction are

given by a wave vector $\boldsymbol{k} = (k_x, k_y)$, where $k_x$ and $k_y$ are the frequencies directions $x$ and $y$, respectively. The PSD must verify the so-called *conjugate symmetry property*, that writes

$$\Phi_\theta(k) = \Phi_\theta(-k)^* \,, \tag{2.21a}$$

$$\Phi(\boldsymbol{k}) = \Phi(-\boldsymbol{k})^* \,. \tag{2.21b}$$

This condition can be understood by observing that Equation 2.20a represents the recovery of the real-valued ACF from the PSD. Since the transformation process involves the integration of complex-valued contributions of $e^{\mathrm{i}k\tau}$, it is necessary to include negative frequencies with equal amplitude, but with antisymmetric phases. Finally, it is worth to establish the relation between the surface and profile PSDs, as advanced in Equations (2.19). The relation has been derived in the work of Longuet-Higgins and Deacon (1957b), wiriting

$$\Phi_\theta(k) = \int_{-\infty}^{+\infty} \Phi(k_x, k_y)\ \mathrm{d}l \,, \tag{2.22}$$

with $l = \sqrt{k_x^2 + k_y^2 - k^2}$. This relation states the fact that two-dimensional waves have a one-dimensional projection along the profile defined by $\theta$. Their projection contribute to the profile PSD ($\Phi_\theta$), except if the $\theta$ is aligned with the direction of the wave vector $\boldsymbol{k}$.

**Remark 2.2 on the definition of Fourier transform.**
*In the current work, the definition for the one-dimensional Fourier transform adopted is*

$$F(k) = \mathcal{F}\left\{f(x)\right\} = \int_{-\infty}^{\infty} f(x) e^{-\mathrm{i}kx}\ \mathrm{d}x \,,$$

*and, accordingly, the inverse Fourier transform definition comes*

$$f(x) = \mathcal{F}^{-1}\left\{F(k)\right\} = \frac{1}{2\pi} \int_{-\infty}^{\infty} F(k) e^{\mathrm{i}kx}\ \mathrm{d}k \,.$$

*Consequently, all the results evolving Fourier transforms implie these relations, and one shall pay attention when comparing equations with other bibliographic sources.*

### 2.4.1 Relation with height spectrum

The relation between the topography eight and its PSD plays a pivotal role in the description of rough surfaces. The *autocorrelation theorem* for Fourier Transforms states that

$$\Phi(\boldsymbol{k}) = \lim_{\substack{L_x \to \infty \\ L_y \to \infty}} \frac{\left|\mathcal{F}\left\{z(x,y)\right\}\right|^2}{L_x L_y} \,, \tag{2.23}$$

and, for the profile case,

$$\Phi_\theta(k) = \lim_{L \to \infty} \frac{\left|\mathcal{F}\left\{z(x)\right\}\right|^2}{L} \,. \tag{2.24}$$

If an inverse Fourier Transform is directly applied in the surface height $z(x,y)$, one can write

$$z(x,y) = \frac{1}{4\pi^2} \iint_{-\infty}^{+\infty} Z(k_x, k_y) e^{\mathrm{i}(k_x x + k_y y)}\ \mathrm{d}k_x \mathrm{d}k_y \,. \tag{2.25}$$

where $Z(k_x, k_y)$, has to be determined. From the Equation (2.23), results

$$|Z(k_x, k_y)| = \sqrt{\Phi(k_x, k_y) L_x L_y}\,, \tag{2.26a}$$

$$\angle Z = \phi(k_x, k_y)\,, \tag{2.26b}$$

where, the Equation (2.26b) represents a random phase of a specific wave vector. With this, an expression for the surface height $z(x, y)$ as a function of the PSD emerges as [5]

$$z(x, y) = \frac{1}{4\pi^2} \iint_{-\infty}^{+\infty} \sqrt{\Phi(k_x, k_y) L_x L_y}\; e^{\mathrm{i}(k_x x + k_y y + \phi(k_x, k_y))}\; \mathrm{d}k_x \mathrm{d}k_y\,. \tag{2.27}$$

In a similar fashion, for a rough profile, it writes

$$z(x) = \frac{1}{2\pi} \int_{-\infty}^{+\infty} \sqrt{\Phi_\theta(k) L}\; e^{\mathrm{i}(kx + \phi(k))}\; \mathrm{d}k\,. \tag{2.28}$$

The previous equations establish a fundamental relation between the PSD of a rough surface and the Fourier transform of its heights. When the inverse Fourier transform was applied, it was possible to write $z(x, y)$ as a function of PSD. It is worth mentioning that the PSD gives information on the frequency content, discriminating the contribution of each frequency by its amplitude. The concept of the PSD and their relation with a rough profile is explored in the Figure 2.6. In this figure, the aforementioned symmetry of the PSD, relative to the origin, highlights the conjugate symmetry property. One verifies that the spectra in of Figure 2.6a and Figure 2.6 are represented by impulse functions $\delta(k)$, since it results from finite frequency contributions. In Figure 2.6e a continuum spectrum is presented together with a profile containing a continuous range of frequency content.

### 2.4.2 Spectral moments

The computation of the RMS parameters from the PSD holds another important step into the construction of a robust framework for rough surface analysis. It was previously seen that the RMS height can be computed from the ACF in the Equations (2.16). One can apply the same procedure to the PSD, and from the Equations (2.20), it comes

$$R(0) = (z_{\mathrm{rms},x})^2 = \frac{1}{2\pi} \int_{-\infty}^{+\infty} \Phi_\theta(k)\; \mathrm{d}k\,, \tag{2.29a}$$

$$R(0,0) = (z_{\mathrm{rms},xy})^2 = \frac{1}{4\pi^2} \int_{-\infty}^{+\infty} \int_{-\infty}^{+\infty} \Phi(k_x, k_y)\; \mathrm{d}k_x \mathrm{d}k_y\,. \tag{2.29b}$$

Similar relations can be obtained for the RMS slope and curvature by deriving the ACF in order to $\tau$, two and four times, respectively,

$$\left.\frac{\mathrm{d}^2 R(\tau)}{\mathrm{d}\tau^2}\right|_{\tau=0} = -\left(z'_{\mathrm{rms},x}\right)^2 = -\frac{1}{2\pi} \int_{-\infty}^{+\infty} k^2 \Phi_\theta(k)\; \mathrm{d}k\,; \tag{2.30}$$

$$\left.\frac{\mathrm{d}^4 R(\tau)}{\mathrm{d}\tau^4}\right|_{\tau=0} = \left(z''_{\mathrm{rms},x}\right)^2 = \frac{1}{2\pi} \int_{-\infty}^{+\infty} k^4 \Phi_\theta(k) \mathrm{d}k\,. \tag{2.31}$$

[5] The limit of the sample length to infity ($L_x \to \infty$ and $L_y \to \infty$) was dropped for the sake of clarity of the formulation presented, yet without compromising the general meaning of the expression.

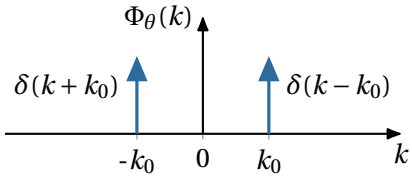


**(a)** PSD of a profile containing a single frequency

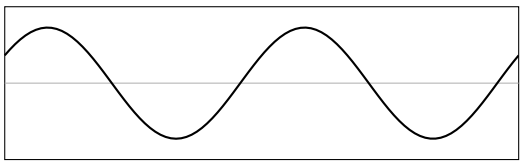

**(b)** Profile with single frequency contribution

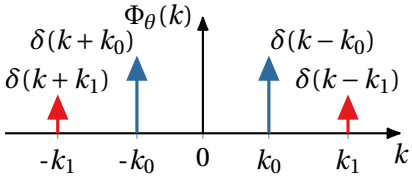


**(c)** PSD of a profile containing two frequencies

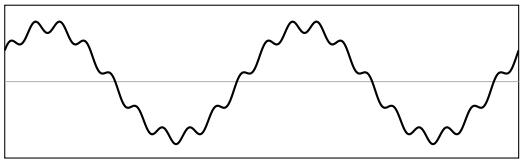

**(d)** Profile with two frequencies

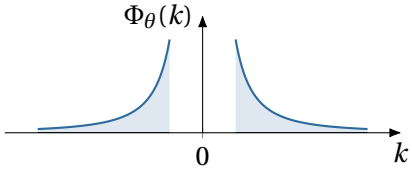


**(e)** PSD of a profile containing a wide range of frequencies

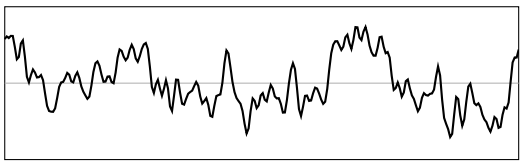

**(f)** Profile having a continuous range of frequencies

**Figure 2.6:** Interpretation of the PSD and associate rough topography for increasing frequency content. Adapted from Couto Carneiro (2019).

The aforementioned analysis motivates the definition of the spectral moments defined by

$$m_{\theta p} = \frac{1}{2\pi}\int_{-\infty}^{+\infty} k^p \Phi_\theta(k)\,\mathrm{d}k\,; \tag{2.32}$$

$$m_{pq} = \frac{1}{4\pi^2}\iint_{-\infty}^{+\infty} k_x^p k_y^q \Phi(k_x,k_y)\,\mathrm{d}k_x\mathrm{d}k_y\,, \tag{2.33}$$

for profiles and surfaces, respectively, with $p$ and $q$ being the order of the spectral moments. The notation used for $m_\theta$ follows the same sense of the PSD for a profile ($\Phi_\theta$). With this definition at hand, one can write the expressions that relate the spectral moments with the RMS parameters. A comparison between the Equation (2.32) and the Equations (2.29a), (2.30) and (2.31) show that with a proper choice of the moment order $p$, one can obtain an equivalence relation with the RMS height, slope and curvature of a rough profile as follows

$$z_{\mathrm{rms},x} = \sqrt{m_{\theta 0}}\,, \tag{2.34a}$$

$$z'_{\mathrm{rms},x} = \sqrt{m_{\theta 2}}\,, \tag{2.34b}$$

$$z''_{\mathrm{rms},x} = \sqrt{m_{\theta 4}}\,. \tag{2.34c}$$

Proceeding similarly, yet with a more time-consuming deduction, a similar set of equations is obtained for the surface case [6]

$$z_{\mathrm{rms},xy} = \sqrt{m_{00}}\,, \tag{2.35a}$$

$$z'_{\mathrm{rms},xy} = \sqrt{m_{20} + m_{02}}\,, \tag{2.35b}$$

$$z''_{\mathrm{rms},xy} = \sqrt{\frac{m_{40} + 2m_{22} + m_{04}}{4}}\,. \tag{2.35c}$$

The particular case of isotropic roughness allows the establishment of relations between the spectral moments for profiles and surfaces, since, the direction does not interfere anymore. Dropping the $\theta$ from the profiles moments, it is possible to prove that (Nayak, 1971)

$$m_{00} = m_0\,; \tag{2.36a}$$

$$m_{20} = m_{02} = m_2\,; \tag{2.36b}$$

$$m_{11} = m_{13} = m_{31} = 0\,; \tag{2.36c}$$

$$3m_{22} = m_{40} = m_{04} = m_4\,. \tag{2.36d}$$

The spectral moments lead to the definition of arguably on of the most important parameters for rough surface analysis, the so-called *Nayak's parameter* $\alpha$, defined as

$$\alpha = \frac{m_0 m_4}{m_2^2}\,. \tag{2.37}$$

This parameter, stated after the acknowledged work of Nayak (1971), plays a paramount role in rough contact mechanics and it measures the breadth of the surface spectrum.

## 2.5 Height distribution

Even though the PSD provides a comprehensive description of the spatial distribution of roughness, by means of spectral decomposition, it holds no information whatsoever about the statistical distribution of the surface heights. This statement can be understood from Equations (2.25) and (2.26): the PSD is only associated with the amplitude of the harmonics, but the phases dictate the actual distribution of heights. Therefore, to achieve a complete characterisation of the topography, the PSD must be complemented with the probability density of surface heights. In this analysis, one changes the attention from the height of a surface $z(x, y)$ (or a profile $z(x)$) to the heigh Probability Density Function (PDF), represented by $f_Z(z)$. This quantity is defined as the probability of having height values within an infinitesimal interval around a certain point z, viz.

$$f_Z(z)\mathrm{d}z = \Pr\left(\mathcal{Z} \in [z,\ z + \mathrm{d}z]\right)\,. \tag{2.38}$$

The height Cumulative Distribution Function (CDF), represented by $F_Z(z)$, indicates the probability of having a value equal or less than a value $z$,

$$F_Z(z) = \Pr\left(\mathcal{Z} \in [-\infty,\ z]\right) = \int_{-\infty}^{z} f_Z(t)\ \mathrm{d}t\,. \tag{2.39}$$

[6] A complete deduction of these relations is presented in the work of Couto Carneiro (2019).

### 2.5.1 PDF moments

It is common practice to characterise the PDF with its central moments, in particular, the moments of first, second, third and fourth orders. [7] The parameters that derive from the central moments provide a simple characterization of the shape of the PDF. The central moment of order $i$ can be expressed as

$$\mu_i = \int_{-\infty}^{+\infty} f_Z(z)\left(z-\mu_z\right)^i \, \mathrm{d}z, \quad \text{for } i = 2,...,\infty\,, \tag{2.40}$$

where $\mu_z$ is the value and it is the first-order non-central moment, calculated as

$$\mu_z = \int_{-\infty}^{+\infty} f_Z(z) z \, \mathrm{d}z\,. \tag{2.41}$$

The first order central moment is not included in the definition Equation (2.40). In turn, the second order central moment $\mu_2$ gives information on the variations of the distribution relative to its mean value $\mu_z$. Its value is equal to the variance of the distribution and writes as

$$\mu_2 = \int_{-\infty}^{+\infty} f_Z(z)\left(z-\mu_z\right)^2 \, \mathrm{d}z = \sigma_z^2\,, \tag{2.42}$$

where $\sigma_z$ is the standard deviation of the heights.[8] In this sequence, the description if one normalizes the third central moment with the cube of the standard deviation $\sigma_z^3$, a convenient parameter, termed *skewness*, arises, represented by the symbol $\gamma_1$ for a continuous variable, as reads

$$\gamma_1 = \frac{\mu_3}{\sigma_z^3} = \frac{1}{\sigma_z^3}\int_{-\infty}^{+\infty} f_Z(z)\left(z-\mu_z\right)^3 \, \mathrm{d}z\,. \tag{2.43}$$

Since the skewness constitutes a moment of odd order, it gives a sensitive measure of how the height distribution varies around the mean axis, i.e., it evaluates the symmetry of the PDF. For instance, for a (symmetric) Gaussian distribution it comes $\gamma_1 = 0$. The same idea may be applied to the fourth central moment, normalizing it is by the standard deviation to the fourth power, resulting in the *kurtosis* of the height distribution, represented by $\beta_2$ and writes

$$\beta_2 = \frac{\mu_4}{\sigma_z^4} = \frac{1}{\sigma_z^4}\int_{-\infty}^{+\infty} f_Z(z)\left(z-\mu_z\right)^4 \, \mathrm{d}z\,. \tag{2.44}$$

This parameter measures the overall presence of the outliers in the PDF. For a Gaussian distribution it verifies $\beta_2 = 3$. It is also common to evaluate the deviation of the kurtosis of a height distribution to the kurtosis of a normal distribution, termed the *excess of kurtosis*, and writes

$$\gamma_2 = \beta_2 - 3\,. \tag{2.45}$$

If $\gamma_2$ has a positive value one calls the height distribution *leptokurtic*, otherwise the distribution is coined *platykurtic*.

[7] Central moments are defined as the moments of PDF about the mean of the height distribution.

[8] The symbol used for the standard deviation of the height distribution $\sigma_z$ is the same used in Equation (2.16) for the standard deviation of the sample heights. Even though they are not exactly the same, if an ergodic case is considered, it constitutes a good approximation.

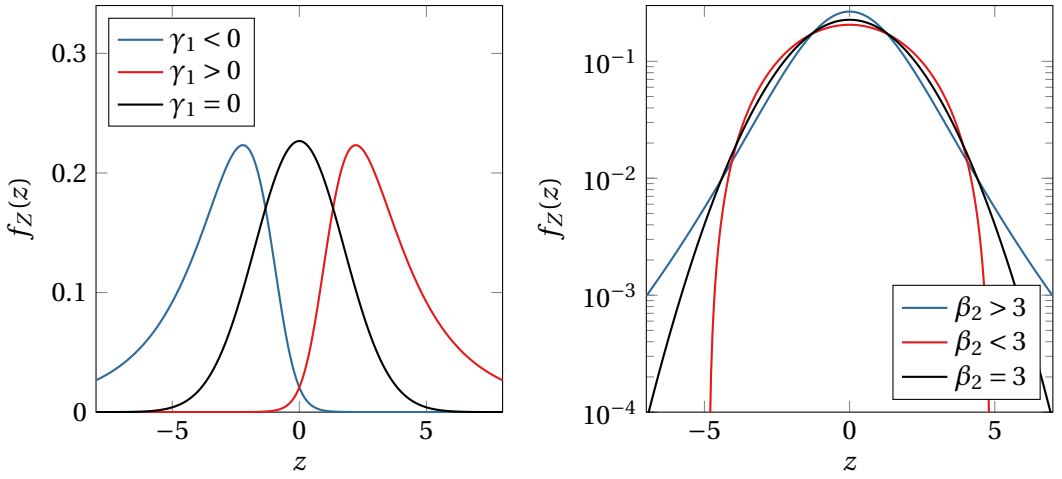


**(a)** Effect of skewness

**(b)** Effect of kurtosis

**Figure 2.7:** Effect of skewness and kurtosis on the shape of PDF. Adapted from Couto Carneiro (2019).

Both kurtosis and skewness admit discrete versions, for computation from artificially generated or measured profiles. The nomenclature adopted follows the one already introduced in the Section 2.2: one denominates the profile and surface skewness respectively $R_{sk}$ and $S_{sk}$, and the kurtosis $R_{ku}$ and $S_{ku}$.

The effect of these parameters on rough surface features can be assessed by looking at their geometrical interpretation. Skewness, as it is an odd power of the distance to the mean value, is sensible to the presence of summits and valleys, providing a biased measure of theirs presence and magnitude. Positive skewness indicates a predominance of summits over the valleys in the surface, and the converse applies for negative skewness. In analogy, as kurtosis is the fourth power of the heights, it holds substantially more information about extreme values that are larger than the average heights of the surface—independently of being summits or valleys. The effects of skewness and kurtosis on the PDF are presented on Figure 2.7. Skewness distorts the PDF of a surface to left or right, depending on the sign. For $\gamma_1 = 0$, the distribution is symmetric. In turn, the effect of the kurtosis in the PDF is more evident in the tails. For larger values of kurtosis, longer and higher tails are expected. To conclude, in Figure 2.8 four profiles, with different combinations of skewness and kurtosis are presented, in order to illustrate the previously exposed concepts.

### 2.5.2 Gaussian and non-Gaussian surfaces

The shape of the height distribution holds an important place in the rough surface characterization, as previously shown in Section 2.1.1. Historically, normal height distributions have frequently been favoured in research, due to the mathematical convenience the Gaussian distribution entails (Thomas, 1998). J. Williamson *et al.* (1969) claimed that surfaces that result from several random processes may exhibit a Gaussian distribution, as a result of the Central Limit Theorem. In fact, the analysis of Gaussian and isotropic sur-

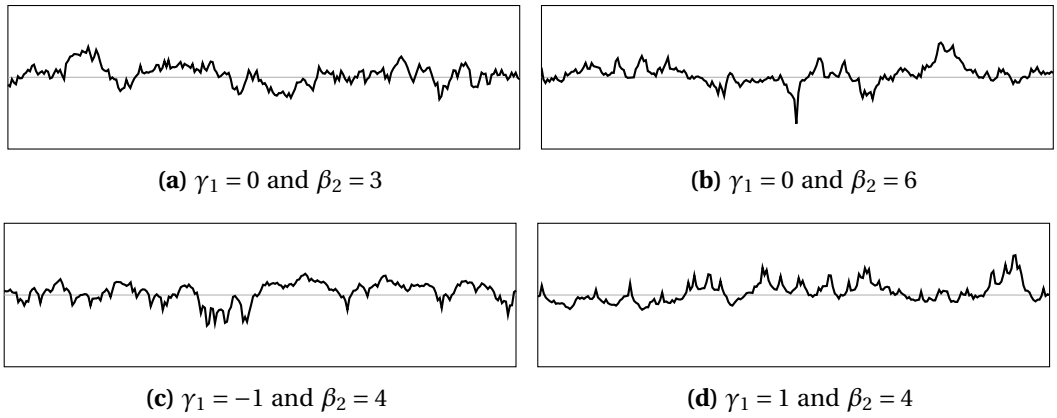

**(a)** $\gamma_1 = 0$ and $\beta_2 = 3$ **(b)** $\gamma_1 = 0$ and $\beta_2 = 6$

**(c)** $\gamma_1 = -1$ and $\beta_2 = 4$ **(d)** $\gamma_1 = 1$ and $\beta_2 = 4$

**Figure 2.8:** Effect of skewness and kurtosis on the topography of a rough profile. Adapted from Couto Carneiro (2019).

faces eases the characterization of roughness and provided a simple tool for investigation that, even though it may not be the most accurate in several scenarios, provides results that are in agreement with experimentation (Sayles and Thomas, 1979). One of the major problems when modelling surfaces as normally distributed is the loss of validity of this height distribution at the tails, i.e., the extreme values. This phenomenon may have a considerable impact on rough contact models as the surfaces summits are the first to contact, which may lead to dubious results (Bhushan, 1999; Thomas, 1998).

A significant number of engineering surfaces exhibit a non-Gaussian behaviour, and many machining surfaces resulting from different processes support this observation (K. Stout, 1980; Whitehouse, 1994). For example, grinding processes typically originate non-Gaussian height distributions, since the surface summits are removed leaving the surface with a higher prominence of valleys, i.e. with a negative skewness value. The characterization of surfaces with a non-Gaussian behaviour is commonly accomplished with skewness and kurtosis, as they provide a satisfactory approach to fully describe the PDF shape (Spedding *et al.*, 1980). Altogether, they constitute a simple tool for directly comparing height distribution with the Gaussian case, and are used not only in rough measurement but on contact models as well (Tomota *et al.*, 2019). Furthermore, some works have suggested that these two parameters affect wear and friction as well (Wang *et al.*, 2006; Sedlaček *et al.*, 2009; Kim *et al.*, 2006a). Typical values of the skewness go from $-2$ up to 2, and the kurtosis values commonly range between 2 and 10. Nonetheless, it should be remarked that values of skewness of $-6$ and kurtosis high as $-100$ have already been obtained by experimentation (Minet *et al.*, 2010).

## 2.6 Self-affine rough surfaces and profiles

Surfaces and profiles are composed of a superposition of many geometrical features at different scales. Their characterization is often strongly dependent on the scale, which makes models such as the ACF exponential model (Section 2.3.2) limited when one wants to achieve an accurate framework for surface description. One of the most accepted and

well-established roughness models in the literature that enables a seamless treatment of the concept of length-scale relies on the PSD characterisation. Sayles and Thomas (1978) observed that, for several and distinct types of surfaces, the PSD shows a direct relation with the measurement wavelength, in the sense that when the measurement wavelength changes, the PSD remains constant relative to the previous coarse measurement—is only extended. Experimentation allowed to postulate a power law for the power spectrum of a rough profile that writes as

$$\Phi_\theta(k) = Bk^{-c}\,, \tag{2.46}$$

where $B$ is named the *surface topothesy*, that despise from not having a properly defined physical meaning or interpretation has a unique role on the statistical definition of the features of a rough surface, since it is not dependent on the sampling length. The exponent $c$ is introduced to give a more general formulation to the Equation (2.46). It should be remarked that in the original works of Sayles and Thomas (1978) a power law with $c = 2$ has been observed.

### 2.6.1 Fractal theory concepts

The experimental validation of PSD of rough profiles as power-law has lead to the postulate that profiles are self-affine topographies. This type of curves follow the so-called *fractal theory* originated from the paramount works of Benoît Mandelbrot, in (Mandelbrot, 1967) and (Mandelbrot, 1982), that provided a way to deal and describe geometries in which the classic Euclidean geometry framework. Fractals curves are distinguished for being continuous and non-differentiable and for having an infinite perimeter (or surface area), yet a finite and circumscribed area (or volume) (Mandelbrot, 1982; Thomas, 1998). They also exhibit a *self-similar* or *self-affine* behaviour, which can be described as the property to look identical at different magnifications. For instance, it can be seen as the curves result from the superposition of the same pattern but at different scales. This curious behaviour is commonly found in a wide variety of examples, such as coastlines, tectonic faults, ocean's surfaces and in several engineering surfaces of interest (Yastrebov, Anciaux, *et al.*, 2015; Thomas, 1998).

One must distinguish the aforementioned self-similar and self-affine behaviours. To this end, Figure 2.9 shows an example of a self-similar fractal, that is characterized by a constant scaling in all magnifications. Therefore, for progressively higher magnifications the fractal shows exactly equal shapes (cf. Figure 2.9). On the other hand, self-affine fractals are a case of distorted self-similarity, where the scaling verified is not the same in all directions. In Figure 2.10, a self-affine rough profile with increasingly large magnifications is illustrated. First, it should be pinpointed that the fractal behaviour, in this case, must not be understood in a pure geometrical sense, but rather in a statistical sense. Second, the self-affine behaviour is shown as the observations at distinct levels of magnification look scaled in the vertical directions, relative to each other. This is the fundamental concept that fractal theory adds to the rough surface analysis. The concept of roughness within roughness preceded the establishment of fractal theory, as it was first introduced in the early works by Archard and Allibone (1957).

The fractal theory establishes the concept of *fractal dimension*, which provides a measure of how complex and detailed the fractal is at a specific scale. It differs from the

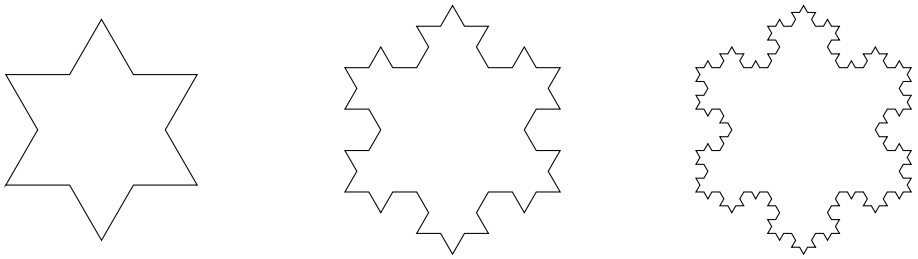

**Figure 2.9:** Example of a self-similar fractal curve—the Koch snowflake. Adapted from Couto Carneiro (2019).

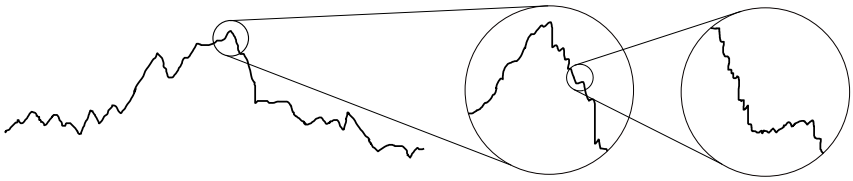

**Figure 2.10:** Example of self-affine rough profile. The fractal behaviour is seen at different levels of magnification. Adapted from Couto Carneiro (2019).

*topological dimension* as it admits different values for the same geometric entity. For instance, while all the examples of Figure 2.9 have the same topological dimension, the same does not apply to the fractal dimension. One represents the fractal dimension of a self-affine profile as $D_p \in [1,2]$. In turn, a self-affine surface has a fractal dimension, represented by $D_s \in [2,3]$. Not surprisingly, both dimensions are related for the case of isotropic roughness by

$$D_p = D_s - 1\,. \tag{2.47}$$

The fractal dimension leads to the definition one of the most commonly used parameters within the research of rough surfaces and profiles called the Hurst roughness exponent, or simply Hurst exponent, denoted by $H$. It is a different form to express the fractal dimension, and it is defined as

$$H = 2 - D_p \quad \text{for profiles}\,; \tag{2.48a}$$

$$H = 3 - D_s \quad \text{for surfaces}\,. \tag{2.48b}$$

The physical meaning of the fractal dimension and the Hurst exponent becomes clearer by inspecting the geometrical features of rough profiles and surfaces, for distinct values of $H$. In Figure 2.11, both profiles and surfaces are illustrated for two values of the Hurst exponent. For $H = 0.3$, both surface and profile, have a more space-filling geometry, which is obtained by the contribution of higher frequencies to the profile. The profile with the larger value the Hurst exponent ($H = 0.8$) has a smaller contribution of higher frequencies to the spectrum and so a smoother shape is obtained. Both topographies have exactly the same frequencies. However, the amplitude of the high frequencies for the lowest value of $H$ is amplified, leading to a more space-filling topography.

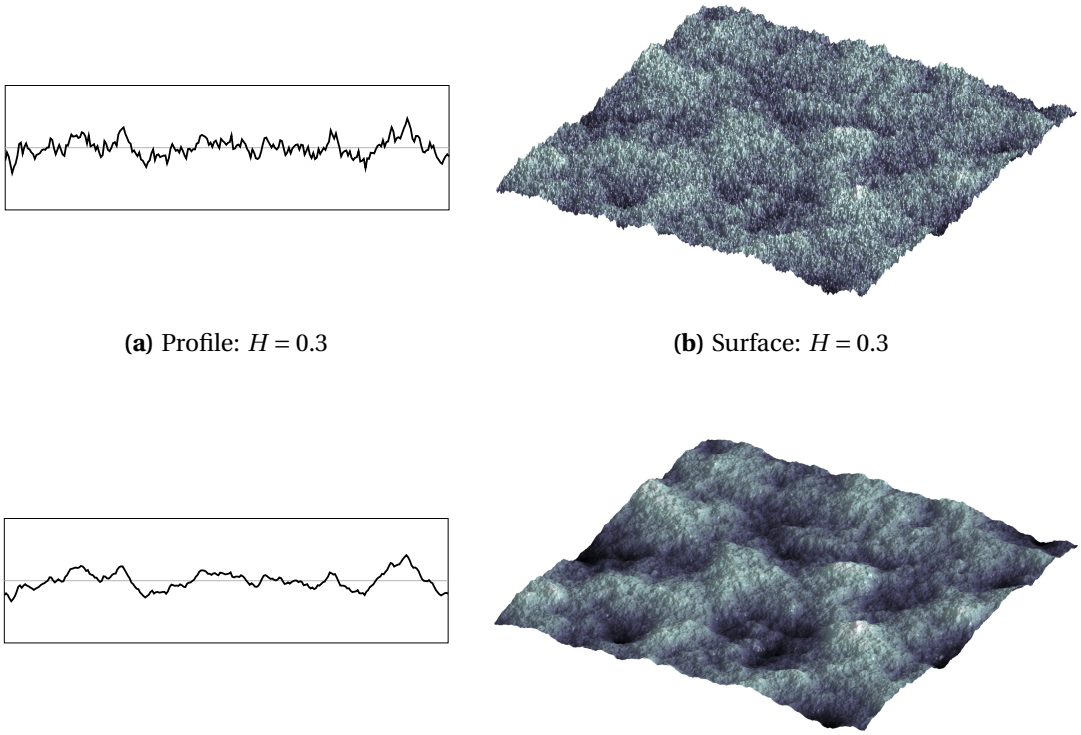

**(a)** Profile: $H = 0.3$ **(b)** Surface: $H = 0.3$

**(c)** Profile: $H = 0.8$ **(d)** Surface: $H = 0.8$

**Figure 2.11:** Hurst effect on rough profiles and surfaces. Adapted from Couto Carneiro (2019).

### 2.6.2 PSD of fractal surfaces and profiles

The fractal properties introduced in the previous section provide a valuable tool for assessing the descriptions of self-affine isotropic rough surfaces. By making use of the fractal dimensions and/or the Hurst exponent, one can write a variety of expressions for the PSD, following a power-law, as stated earlier. For profiles and surfaces, respectively, the PSD is commonly expressed as (Wu, 2000a; Russ, 1994; Yastrebov, Anciaux, *et al.*, 2015):

$$\Phi_\theta(k) = \frac{G^{2D_p-2}}{k^{5-2D_p}} = \frac{G^{2(1-H)}}{k^{1+2H}}\,, \tag{2.49a}$$

$$\Phi(k_x,k_y) = \frac{g^{2D_p-2}}{\left(k_x^2+k_y^2\right)^{3-D_p}} = \frac{g^{2D_s-4}}{\left(k_x^2+k_y^2\right)^{4-D_s}} = \frac{g^{2(1-H)}}{\|\boldsymbol{k}\|^{2(H+1)}}\,. \tag{2.49b}$$

The constants $G$ and $g$ are the profile and surface, fractal scale constants, respectively, which are a measure of the absolute scale of roughness.

Equations (2.49) imply that the fractal behaviour of surfaces extends all over the frequency domain. However, real engineering surfaces cannot be fractal at all scales. For instance, for very small scales, the fractal behaviour tends to cease, as the atomic scale comes into play. Identically, rough surfaces are only fractal up to some large scale, typ-

ically in the order of magnitude of the surface length. In practice, rough surfaces frequently exhibit a power spectrum with two distinctive zones: one where the fractal behaviour dominates and another where it ceases and the PSD shows an approximately constant value, as shown on Figure 2.12. The fractal zone is encompassed between a *high-frequency cut-off* $k_s$ and the *roll-off frequency* $k_r$. The frequency $k_r$ marks the transition to the constant PSD, called the *plateau*, that extends until the *low-frequency cut-off* $k_l$. For frequencies higher than $k_s$ and smaller than $k_l$ the PSD is zero, meaning that no contributions of frequencies outside the range $[k_l,\ k_s]$ exist in the rough topography. This type of behaviour has been experimentally observed and characterized (Persson *et al.*, 2004; Vallet *et al.*, 2009). For example, it can be seen in machined surfaces, since the majority of the high frequencies of the surfaces are kept while the lower are removed by the manufacturing process. The formulation, conventionally adapted for this type of surfaces comes as

$$\Phi_\theta(k) = \begin{cases} C_0' & , \quad k_l \le k < k_r \\ C_0' \left(\dfrac{k_r}{k}\right)^{1+2H} & , \quad k_r \le k \le k_s \\ 0 & , \quad \text{elsewhere}\,. \end{cases} \tag{2.50}$$

$$\Phi(k_x, k_y) = \begin{cases} C_0 & , \quad k_l \le \|\boldsymbol{k}\| < k_r \\ C_0 \left(\dfrac{k_r}{\|\boldsymbol{k}\|}\right)^{2(H+1)} & , \quad k_r \le \|\boldsymbol{k}\| \le k_s \\ 0 & , \quad \text{elsewhere}\,; \end{cases} \tag{2.51}$$

where $C_0$ and $C_0'$, are scale constants. These expressions highlight the dependency of the previously introduced Hurst exponent $H$ on the fractal scale. One sees that in a log-log scale, the slope of the curve is dictated by $H$, and for larger values of $H$ the decay is faster (cf. Figure 2.12).

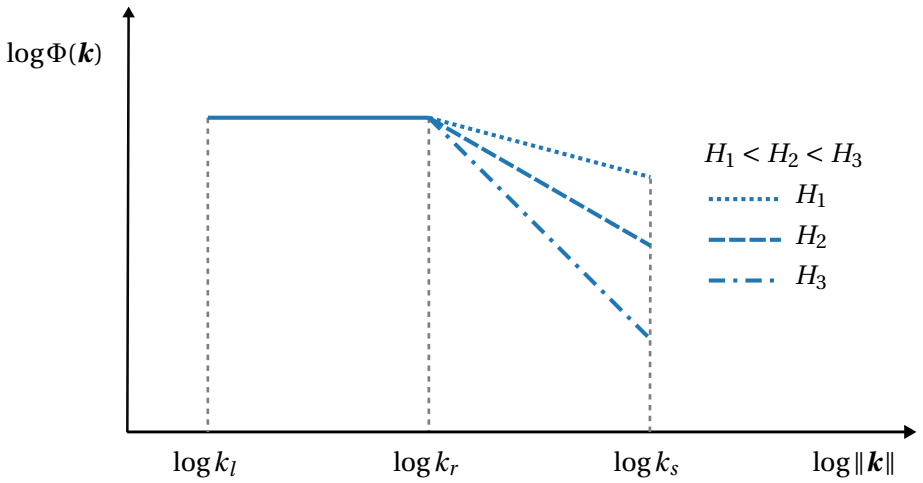


**Figure 2.12:** Typical PSD shape of an isotropic rough surface. The fractal part, i.e., between $k_r$ and $k_s$ is represented for various value of the Hurst exponent $H$, that characterize the slope of the PSD. The higher the Hurst exponent the decay of the PSD is faster.

*Page intentionally left blank*

# Chapter 3

# Numerical study on the statistical geometry of rough surfaces

Virtually all engineering surfaces are random to some extent, thereby tools for properly describing roughness are necessary for a comprehensive understanding of this ubiquitous phenomenon. The random nature of rough surfaces has already been carefully addressed in Section 2.1.1, together with an overview of characterisation techniques, walking towards a scale-independent portrayal of roughness. Complementing the introduced models, the statistical description of the geometry rough surfaces constitutes an important part of the understanding of their physical behaviour and is widely used for studying their contact mechanics (wear, friction and adhesion). As detailed in the previous chapter, the surface height distribution provides general information on the shape of the surface features. For example, by computing the skewness and kurtosis, the non-Gaussianity of the surface can be determined, giving a general sense of the distribution and presence of summits and valleys. The summits of the topography are one of the most important features of roughness since contact will always start at these locations. Exemplarily, the summit height distribution has been used in many contact models for rough surfaces, as the summits constitute the first contact spots. Thus, more than inspecting the global height distribution, more in-depth statistical information can be obtained by looking exclusively at the distribution of summit heights and respective curvatures. These statistical parameters play a key role in the contact mechanics, especially, in the real contact area.

While the statistical description of the geometry of Gaussian rough surfaces is already well-established since the seminal work by Nayak (1971), non-Gaussian rough surfaces may exhibit very different mechanical responses (Pérez-Ràfols and Almqvist, 2021). This calls for a better understanding of non-Gaussian topographies, by means of a proper statistical characterization and comparison. The central goal of the present chapter is to extend the statistical description by Nayak into the realm of non-Gaussian topographies, to provide novel and useful insights for contact models of non-Gaussian topographies. The statistical description will be centred on the distribution of summit heights and curvatures, extracted from discrete random topographies with controlled properties. First, the study will focus on the Gaussian topographies, for the sake of validation, and then transition to the non-Gaussian scenario, where the Weibull distribution will be used for parametrising the height distribution. The statistics of rough surfaces can be directly

measured in real surfaces using a stylus or optical devices. Nonetheless, such practice is very time-consuming and does not allow a flexible characterization. An alternative employed in this work, that comes with several convenient advantages, is the numerical generation of rough surfaces. With this approach, one can obtain specific topographies with predefined statistics and spectral properties, which can then feed parametric studies through the adjustment of the required properties. Moreover, this procedure also a faster collection of large amounts of data, when compared with real surface measurements. Roughness generation strategies are widely known, and different approaches can be found in the literature for both Gaussian and Non-Gaussian topographies. Within this work, discrete random Gaussian topographies will be generated with the algorithm proposed in (Wu, 2000b), while the recent method proposed in (Pérez-Ràfols and Almqvist, 2019) will be used for the non-Gaussian case.

## 3.1 Gaussian topography

Before diving into the study of non-Gaussian topographies, the particular and well-known case of Gaussian surfaces is analysed and used as a validation for the succeeding statistical study. The key aspects of the statistical geometry of Gaussian topographies are first outlined, together with the numerical technique employed for the generation of the random topographies. Last, a numerical framework for studying the geometry statistics is built and validated against the Gaussian benchmark.

### 3.1.1 Nayak's theory

Following the works of Longuet-Higgins and Deacon (1957a,b) on the description of the ocean moving surfaces, the paramount work of Nayak (1971) assumed a surface to be stationary, random and with a Gaussian distribution of heights. With these considerations, and basing the analysis around the PSD and the spectral moments, the geometry statistics of both profiles and surfaces are obtained, depending uniquely on the previously introduced Nayak's parameter $\alpha$ (Equation (2.37)). Within the context of this work, only the results referring to surfaces are presented. For a complete description of Nayak's theory, the interested reader is referred to (Nayak, 1971) and (Rigazzi, 2014).

Typically, non-dimensional variables are used in the derivation of the statistics of rough surfaces. One writes the normalized height $z^*$ as the ratio between the height and the square root of the zeroth-order spectral moment $m_0$. From the Equations (2.16a), (2.35a) and (2.36a) it comes

$$z^* = \frac{z}{\sqrt{m_0}} = \frac{z}{\sigma_z}\,, \tag{3.1}$$

where it can be interpreted as the normalisation of the heights by the respective standard deviation. Bearing that in mind, the probability density of summits heights $p_{\text{sum}}(z^*)$ is defined as

$$p_{\text{sum}}\left(z^*\right) = \frac{P_{\text{sum}}(z^*)}{D_{\text{sum}}}\,, \tag{3.2}$$

where $D_{\text{sum}}$ is the density of summits *per* unit of area and $P_{\text{sum}}(z^*)$ is the probability distribution of summits *per* unit of area, which must be interpreted as a probability measure of observing a summit with the given height, among all possible points—summits and

non-summits. The density of summits is obtained by integrating the probability distribution of summits $P_{\text{sum}}(z^*)$ all over the domain, i.e.,

$$D_{\text{sum}} = \int_{-\infty}^{\infty} P_{\text{sum}}\left(z^*\right) \mathrm{d}z^* \,. \tag{3.3}$$

Considering the static and isotropic conditions of a Gaussian rough surface, Nayak (1971) arrives to an analytical expression of $p_{\text{sum}}(z^*)$ as

$$p_{\text{sum}}\left(z^*\right) = \frac{\sqrt{3}}{2\pi}\left(\Pi_1 + \Pi_2 + \Pi_3\right) \,, \tag{3.4}$$

where $\Pi_1$, $\Pi_2$ and $\Pi_3$ are auxiliary variables, introduced for the sake of clarity, defined as

$$\Pi_1 = \exp\left(-C_1 z^{*2}\right)\left[\frac{3(2\alpha-3)}{\alpha^2}\right]^{\frac{1}{2}} z^* \,, \tag{3.5a}$$

$$\Pi_2 = \frac{3\sqrt{2\pi}}{2\alpha}\exp\left(-\frac{1}{2}z^{*2}\right)\left[1-\operatorname{erf}\left(\beta\right)\right]\left(z^{*2}-1\right) \,, \tag{3.5b}$$

$$\Pi_3 = \sqrt{2\pi}\left[\frac{\alpha}{3(\alpha-1)}\right]^{\frac{1}{2}} \exp\left[\frac{\alpha z^{*2}}{2(\alpha-1)}\right]\left[1+\operatorname{erf}\left(\gamma\right)\right] \,, \tag{3.5c}$$

and $\operatorname{erf}(\bullet)$ denotes the error function

$$\operatorname{erf}(x) = \frac{2}{\sqrt{2\pi}}\int_0^x e^{-a^2}\mathrm{d}a \,. \tag{3.6}$$

A few auxiliary parameters were introduced in the analysis, alongside the already mentioned Nayak's parameter $\alpha$. All the parameters are dependent on $\alpha$ and write [1]

$$C_1 = \frac{\alpha}{2\alpha-3} \,, \tag{3.7a}$$

$$C_2 = C_1\left(\frac{12}{\alpha}\right)^{\frac{1}{2}} \,, \tag{3.7b}$$

$$\beta = \left[\frac{3}{2(2\alpha-3)}\right]^{\frac{1}{2}} z^* \,, \tag{3.7c}$$

$$\gamma = \left[\frac{\alpha}{2(\alpha-1)(2\alpha-3)}\right]^{\frac{1}{2}} z^* \,. \tag{3.7d}$$

The probability density of summits height $p_{\text{sum}}(z^*)$ is presented on Figure 3.1 for different values of $\alpha$. Recall, that $\alpha$ is associated with the breadth of the PSD and for larger values of it the spectrum gets broader, suggesting the presence of higher frequencies with large amplitudes. It should be remarked that the results are limited by a lower value of $\alpha$, as it has been shown by Longuet-Higgins and Deacon (1957b) that $\alpha > 1.5$ for random

[1] Even though the parameter $C_2$ is not used is in the $p_{\text{sum}}\left(z^*\right)$, it will be introduced lately within the definition of joint probability density for summits heights and mean curvatures, $p'_{\text{sum}}\left(z^*, t_1\right)$. It may be advanced that the symbol $(\bullet)'$ is reserved for quantities associated with $p'_{\text{sum}}\left(z^*, t_1\right)$.

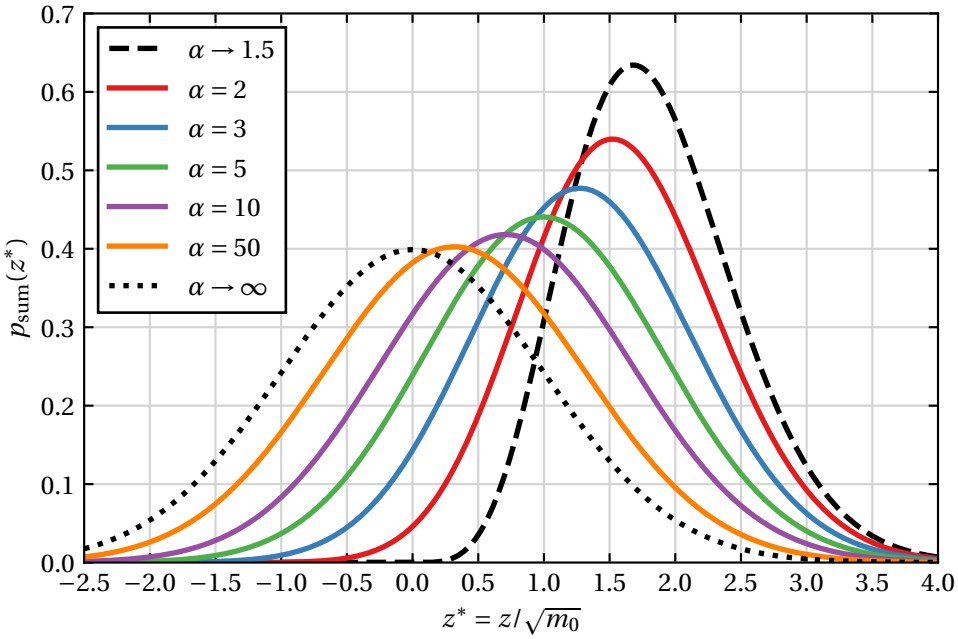


**Figure 3.1:** Probability density of summits heights $p_{\mathrm{sum}}(z^*)$ for different values of $\alpha$.

and isotropic surfaces. From these results, one can observe that for a Gaussian distribution of heights, the summits height distribution is non-Gaussian. This asymmetry was studied in the work by Yu and Polycarpou (2004b), where equations to quantify the skewness and the kurtosis of this distribution were derived and compared against numerically generated Gaussian surfaces. In fact, it can be seen that as the value of $\alpha$ decreases the probability of having higher summits increases, and $p_{\mathrm{sum}}(z^*)$ progressively deviates from the Gaussian. Otherwise, for larger values of $\alpha$, the distribution becomes more similar to a Gaussian case and, for a limit value, when $\alpha \to \infty$, it becomes perfectly Gaussian. This is a consequence of an infinitely broad spectrum, in which every point is a summit, ultimately leading to the case where the $p_{\mathrm{sum}}(z^*)$ matches the heigh distribution of the rough surface. From $p_{\mathrm{sum}}(z^*)$, the cumulative density of summits $q_{\mathrm{sum}}(z^*)$ can be obtained, by integration, as

$$q_{\mathrm{sum}}(z^*) = \int_{-\infty}^{z^*} p_{\mathrm{sum}}(z^*)\,\mathrm{d}z^*\,, \tag{3.8}$$

which can be interpreted as the probability of having a value less or equal than $z^*$. This quantity can be easily computed from Equation (3.4) and it is presented in Figure 3.2 for different values of $\alpha$. The results cement the conclusions previously seen for $p_{\mathrm{sum}}(z^*)$. For the same normalized height $z^*$, one sees that the higher the $\alpha$ value, the higher the cumulative density of summits becomes.

The theory by Nayak (1971) also encompasses the curvature values of the summits, condensed in a proper set of analytical expressions. The mean curvature of a point is introduced as the mean between the two principal curvatures $\kappa_1$ and $\kappa_2$. As has been said for the case of the discrete version of the RMS curvature (Section 2.2.1), the sum of

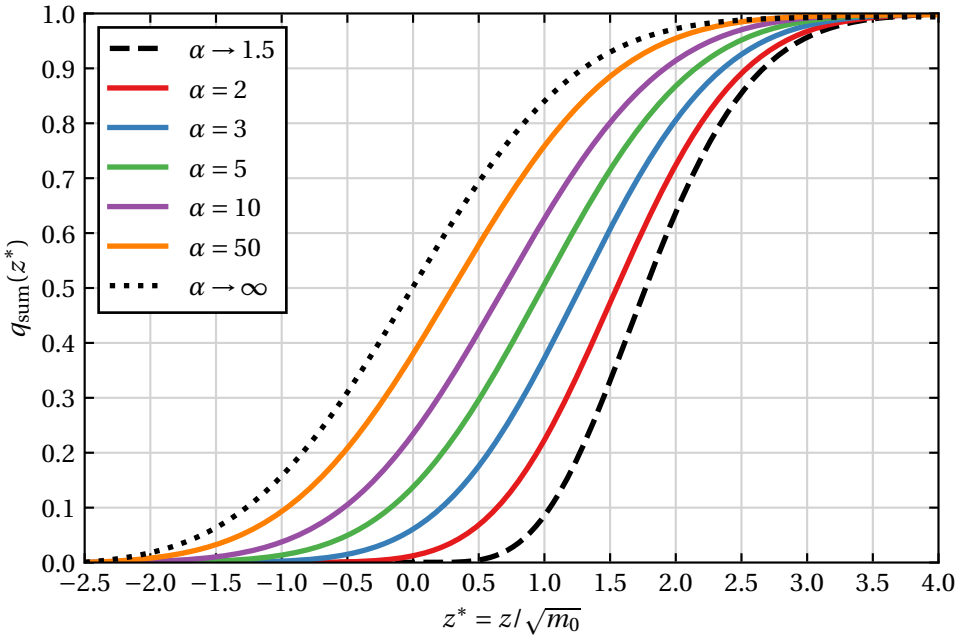


**Figure 3.2:** Cumulative density of summits heights $p_{\mathrm{sum}}(z^*)$ for different values of $\alpha$.

curvatures in any two orthogonal directions equals the sum of the principal directions, thus one can simply evaluate the curvature along the Cartesian directions, giving

$$\kappa_m = \frac{1}{2}(\kappa_1 + \kappa_2) = -\frac{1}{2}\left(\frac{\partial^2 z}{\partial x^2} + \frac{\partial^2 z}{\partial y^2}\right), \tag{3.9}$$

For the sake of non-dimensionalization, Nayak (1971) introduced the parameter $t_1$, treated as the equivalent mean curvature that is given by [2]

$$t_1 = \frac{1}{2}\left(\frac{3}{m_4}\right)^{\frac{1}{2}}\left(\frac{\partial^2 z}{\partial x^2} + \frac{\partial^2 z}{\partial y^2}\right) = -\left(\frac{3}{m_4}\right)^{\frac{1}{2}}\kappa_m\,, \tag{3.10}$$

and that has a negative domain, i.e., $t_1 < 0$, which means that higher mean curvatures $\kappa_m$ correspond to smaller equivalent mean curvatures $t_1$. The result of Nayak's approach holds a form of a joint probability density function for summits with normalized height $z^*$ and equivalent mean curvature $t_1$ *per* unit area, denoted by $p_{\mathrm{sum}}(z^*)$ and given by

$$p'_{\mathrm{sum}}(z^*, t_1) = \Pi'_1\Pi'_2\Pi'_3\,, \tag{3.11}$$

where $\Pi'_1$, $\Pi'_2$ and $\Pi'_3$ are, once again, auxiliary variables that ease the algebraic treatment,

[2] In Nayak's work the parameter $t_1$ is introduced alongside other two parameters $t_2$ and $t_3$, that are used in the analytical procedure but not for representation of a physical quantity. Within the context of this work, there is no need of introducing them. The same nomenclature for $t_1$ is adopted for convenience.

and come as

$$\Pi_1' = \frac{\sqrt{3C_1}}{2\pi} \exp\left(-C_1 z^{*2}\right), \tag{3.12a}$$

$$\Pi_2' = t_1^2 - 2 + 2\exp\left(-\frac{1}{2}t_1^2\right), \tag{3.12b}$$

$$\Pi_3' = \exp\left[-\frac{1}{2}\left(C_1 \alpha t_1^2 + C_2 \alpha t_1 z^*\right)\right]. \tag{3.12c}$$

This result is presented in Figure 3.3 for a value of $\alpha = 5$, and show a clear non-Gaussian behaviour for both normalized height $z^*$ and equivalent mean curvature $t_1$. A convenient quantity for the analysis of $p'_{\text{sum}}(z^*, t_1)$, also introduced by Nayak (1971), is the expected value of the mean curvature for summits of height $z^*$, represented by $\bar{\kappa}_m$, and written as

$$\bar{\kappa}_m\left(z^*\right) = \frac{\left(\frac{m_4}{3}\right)^{\frac{1}{2}} \int_{-\infty}^{0} t_1 p'_{\text{sum}}\left(z^*, t_1\right) \mathrm{d}t_1}{\int_{-\infty}^{0} p'_{\text{sum}}\left(z^*, t_1\right) \mathrm{d}t_1}. \tag{3.13}$$

Nayak (1971) obtains a complete analytical solution for the Equation (3.13), yet it is excluded from the current text due to his intricate analytical definition—and also to the fact that its numerical computation is straightforward. This quantity can be interpreted as the mean value of the mean curvatures for a given value of normalized height $z^*$. The dimensionless expected mean curvature $\bar{\kappa}_m/\sqrt{m_4}$ is presented in Figure 3.4 for different values of $\alpha$. From this figure, one sees that, with increasing height, the summits become sharper, i.e., possess higher mean curvature values. Also, the expected mean curvatures are larger for smaller values of $\alpha$, relative to the measure of the overall surface curvature. For progressively higher values of $\alpha$, the curvature progression with the height tends to reduce until the point where it becomes a constant value, i.e., for $\alpha \to \infty$. In this particular case, considering that an infinite spectral content is observed, the higher frequency corresponds to a wave with an infinitesimally short wavelength. For this harmonic contribution, the mean curvature, calculated with the second-order derivatives (cf. Equation (3.9)), would give an infinite curvature and so the expected mean curvature $\bar{\kappa}_m$ for any value of $z^*$. Additionally, one should note that the fourth-order spectral moment can be obtained from the Nayak's parameter through Equation (2.37), from where it is postulated that for an infinite $\alpha$, $m_4$ is also most likely infinite. Thus, the constant value of non-dimensional mean curvature $\bar{\kappa}_m/\sqrt{m_4}$ is justified, being given by $\bar{\kappa}_m/\sqrt{m_4} = 8/3\sqrt{\pi}$, in the sense that all summits look alike—infinitely sharp—independently of their height. Another way to look at these results is attending to the fact that $m_4$ provides a measure of the global curvature behaviour of a rough surface (cf. Equation 2.35c). This means that $\bar{\kappa}_m/\sqrt{m_4}$ measures, for each value of normalized height, the deviation relative to the average curvature of the surface, which explains why for $\alpha \to \infty$ a constant value of $\bar{\kappa}_m/\sqrt{m_4}$ is verified: the deviation of the summit curvature relative to the surface global curvature is identical at all heights. In lower limit of $\alpha = 1.5$, it comes that the relation between the average mean curvature and summit height is linear, $\bar{\kappa}_m/\sqrt{m_4} = \sqrt{2/3}z^*$, as can be seen in Figure 3.4. Again, this establishes that the higher the summit, the larger the mean curvature, on average.

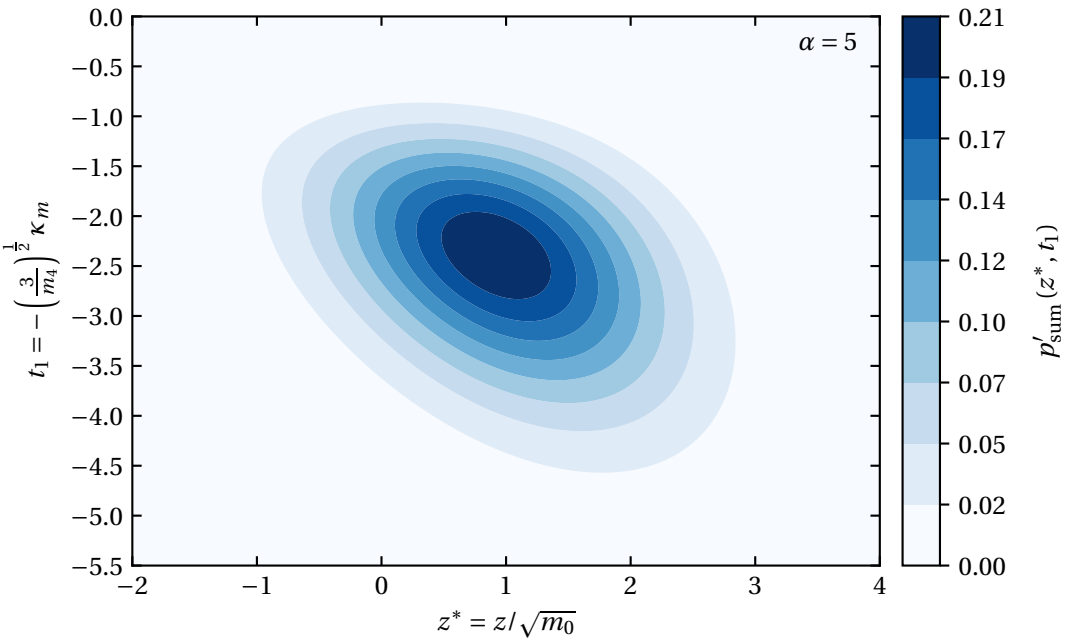


**Figure 3.3:** Joint probability distribution of normalized summits heights $z^*$ and equivalent mean curvature $t_1$ for a value of $\alpha = 5$.

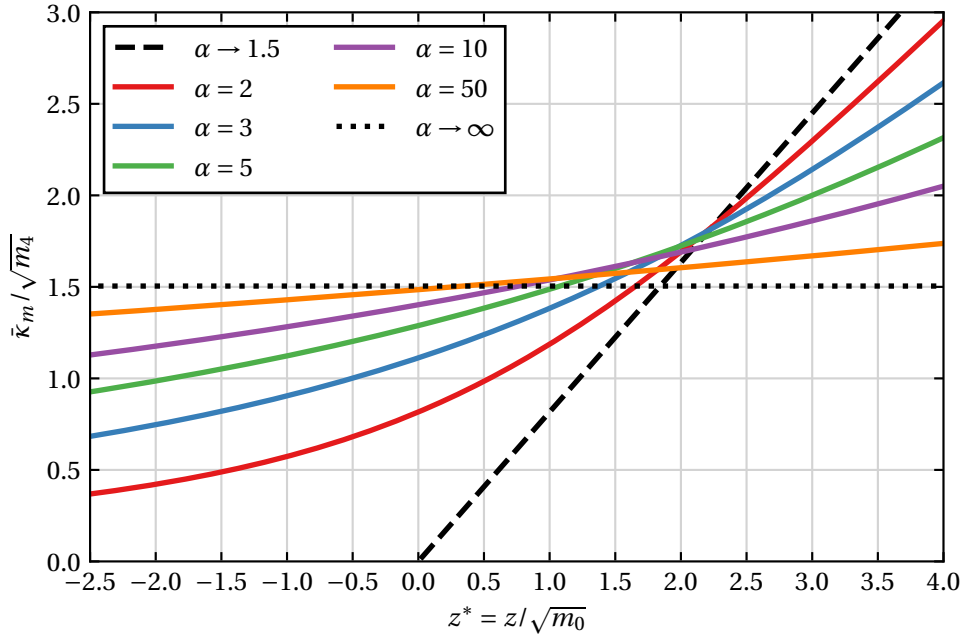


**Figure 3.4:** Dimensionless expected mean curvature curvature of summits heights $\bar{\kappa}_m$ for different values of $\alpha$.

### 3.1.2 Generation of Gaussian rough surfaces

For the numerical generation of Gaussian and non-Gaussian rough surfaces, the in-house code named `LINKS-RC` (Module for Rough Contact Modelling) was used (Figure 3.5). This code, written in `Python`, is developed by CM2S (Computational Multi-Scale Modelling of Solids and Structures) at the Faculty of Engineering of University of Porto, and constitutes a module of pre- and post-processing of `LINKS`, a `Fortran` finite element code for implicit small and large strain analysis, that will be introduced later in section Section 4.4.5. The framework for rough surface generation was initially developed in Couto Carneiro (2019).


**Figure 3.5:** `LINKS-RC` logo

The generation of random rough Gaussian topographies performed by `LINKS-RC` is based on the algorithm proposed by Wu (2000b). This method uses discrete Fourier transforms, in particular the Fast Fourier Transform (FFT) and the Inverse Fast Fourier Transform (IFFT), to generate an artificial rough surface from a prescribed power spectrum. It encompasses the generation of both profiles and surfaces with Gaussian height distributions, yet only the surface case will be covered. The flowchart of the algorithm for surface generation is presented in Figure 3.6. It should be mentioned that even though Figure 3.6 also shows the algorithm for a prescribed ACF, only the generation from a given PSD is relevant. The algorithm is based on the idea of a discrete random rough surface $z_{m,n}$ as a superposition of waves with certain values of frequency, amplitude and phase, viz.

$$z_{m,n} = \frac{1}{MN} \sum_{p=0}^{M-1} \sum_{q=0}^{N-1} \sqrt{MN\hat{\Phi}_{p,q}}\, e^{\mathrm{i}(2\pi(qm/M+pn/N)+\phi_{p,q})}, \quad \begin{cases} m = 0,1,...,M-1 \\ n = 0,1,...,N-1 \end{cases} . \tag{3.14}$$

In Equation (3.14), $M$ and $N$ represent the number of sampled points in the directions $y$ and $x$, respectively, that are uniformly distributed along the sample length in each direction. Equation (3.14) implies the use of $\hat{\Phi}_{p,q}$, which is the discrete estimate of the real power spectrum $\Phi(k_x, k_y)$ and $\phi_{p,q}$ is used for denote the random phases. If the real prescribed PSD has a limit on the frequency domain, i.e. has a frequency above which the spectrum is null (bandwidth limited), and considering that the Nyquist frequency is higher than the limit of PSD, the discrete PSD writes

$$\hat{\Phi}_{p,q} = \frac{1}{l_{s_x} l_{s_y}} \Phi\left(k_x = \frac{q}{N}\Omega_{s_x},\ k_y = \frac{p}{M}\Omega_{s_y}\right), \quad \begin{cases} p = -M/2+1,...,M/2 \\ q = 0,1,...,N/2 \end{cases} , \tag{3.15}$$

where $l_{s_x}$ and $l_{s_y}$ are the sampling wavelengths in each direction (point spacing), and $\Omega_{s_x} = 2\pi/l_{s_x}$ and $\Omega_{s_y} = 2\pi/l_{s_y}$ are respective sampling frequencies. The discrete power spectrum $\hat{\Phi}$ verifies a periodic behaviour in both directions, and due to the conjugate

symmetry property it shall hold

$$\hat{\Phi}_{p,q} = \hat{\Phi}_{M-p,N-q}, \quad \begin{cases} p = 0,...,M-1 \\ q = 0,...,N/2 \end{cases}, \tag{3.16}$$

meaning that only half of the frequency space needs to be defined as the input.

The next step is to obtain the random phases $\phi_{p,q}$, which will give the random nature to the rough surface, as the process from which the amplitudes were obtained was fully deterministic. The random phases should be generated by a random number generator, following a uniform distribution, and must obey the conjugate symmetry

$$\phi_{m,n} = -\phi_{M-m,N-n}, \quad \begin{cases} p = 0,...,M-1 \\ q = 0,...,N/2 \end{cases}. \tag{3.17}$$

The conjugate symmetry property and the periodicity of the discrete Fourier Transform also lead to the following relations

$$\phi_{0,0} = \phi_{0,N/2} = \phi_{M/2,0} = \phi_{M/2,N/2} = 0\,; \tag{3.18a}$$

$$\phi_{m,0} = -\phi_{M-m,0}, \quad m = 0,...,M/2\,; \tag{3.18b}$$

$$\phi_{0,n} = -\phi_{0,N-n}, \quad n = 0,...,N/2\,. \tag{3.18c}$$

Finally, after getting the amplitudes from the input PSD and having generated uniform random phases $\phi_{p,q}$, is possible to compute a discrete rough surface from Equation (3.14). By making use of IFFT, one obtains

$$z_{m,n} = \mathrm{IFFT}\left(\sqrt{MN\hat{\Phi}_{p,q}}\, e^{\mathrm{i}\phi_{p,q}}\right). \tag{3.19}$$

It should be pointed out that the Gaussian distribution of heights of the artificial discrete surface is obtained by the superposition of the height of each wave at every point. Since, the height is an independent random variable, from the central limit theorem, one should expect the Gaussian behaviour of the generated surface.

### 3.1.3 Summit detection and curvature evaluation

To perform the computation of the numerical statistics, some processing needs to be made on the generated data, namely the detection of summits and the collection of their height and curvature. When performing peak detection on profiles, the methodology is pretty straightforward, since a three-point scheme can detect a peak with good precision, unless the distance between sampled points is too large. For surfaces, some works propose a five-point stencil to perform the detection of summits (Whitehouse, Phillips, *et al.*, 1982, 1978). However, as stated by J. A. Greenwood and K. L. Johnson (1984), this method may not always detect a summit. To overcome this pitfall, a nine-point stencil is employed, as shown in Figure 3.7. If a point $z_{i,j}$ is larger than the 8 neighbouring points, it is classified as a summit. In Figure 3.8 an example of the summit detection is shown, giving a visual representation of the summit distribution on a Gaussian rough surface. Shedding some light over the previous discussion on the summit height distribution, one

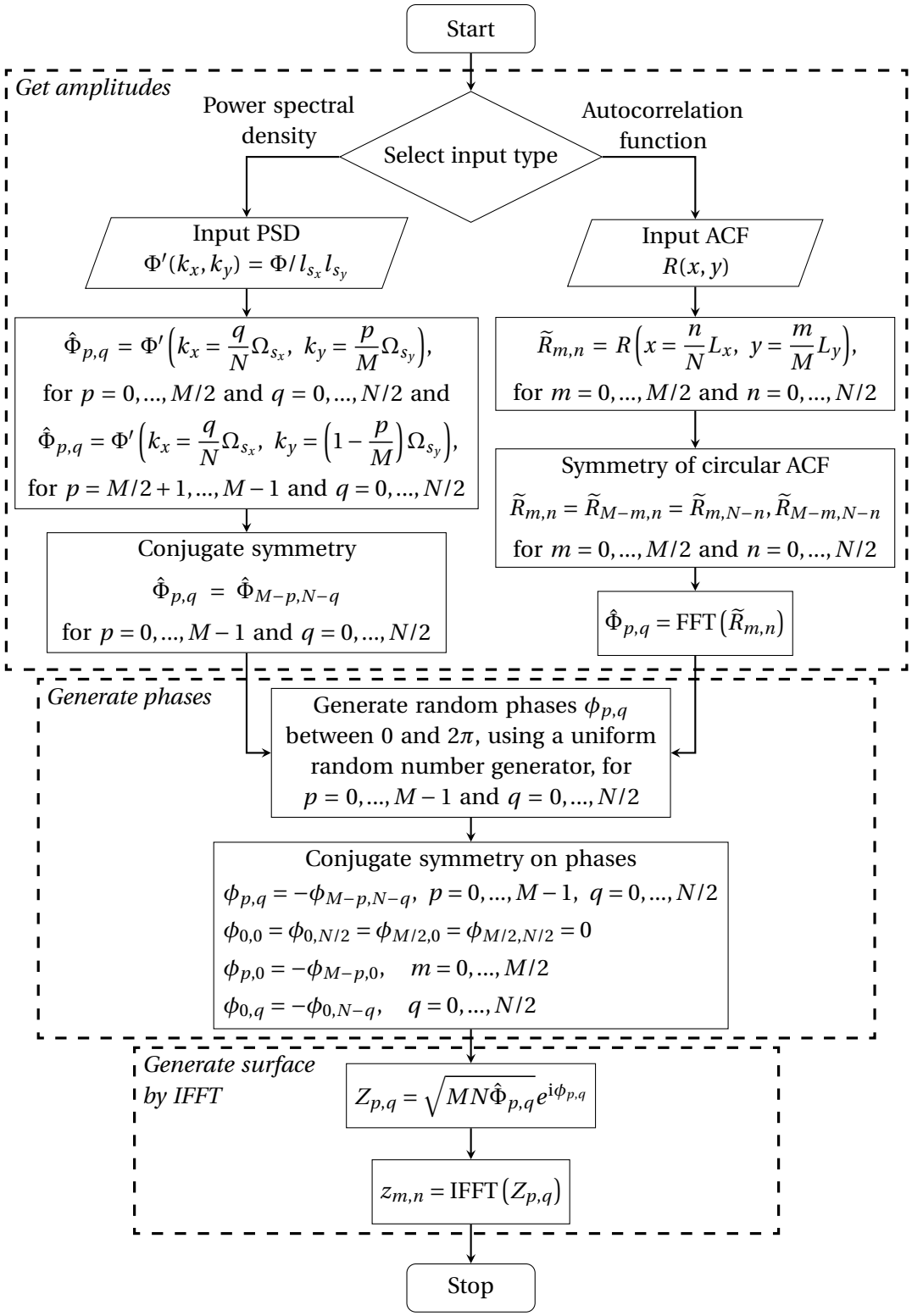


**Figure 3.6:** Flowchart of the Gaussian random rough surface generation algorithm. Adapted from Couto Carneiro (2019).

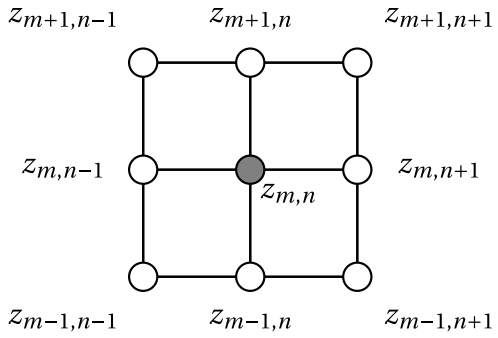


**Figure 3.7:** Nine-point stencil method used in the current work for summit detection. If a point $z_{i,j}$ is larger than the 8 neighbouring points, it it considered a summit.

sees that the majority of the summits has positive height (the mean height is zero), and it is a consequence of the low-frequency content of the generated topography. For higher frequency content surfaces it would be expected to have more summits at low levels of height.

With respect to the curvature evaluation, the mean curvature $\kappa_m$ is calculated using a central finite difference scheme along each direction, viz.

$$\frac{\partial^2 z}{\partial x^2} = \frac{z_{m,n+1} - 2z_{m,n} + z_{m,n-1}}{\Delta x^2}\,, \tag{3.20a}$$

$$\frac{\partial^2 z}{\partial y^2} = \frac{z_{m+1,n} - 2z_{m,n} + z_{m-1,n}}{\Delta y^2}\,. \tag{3.20b}$$

### 3.1.4 Numerical validation

As mentioned previously, the numerical study starts with the Gaussian case, as the statistical results have been extensively studied in Nayak's theory, introduced in Section 3.1.1. This way, one can compare directly the statistics obtained with the analytical model from Nayak (1971), allowing to infer on the global validity of the framework and to foresee problems in the non-Gaussian study. The numerical generation of random topographies was performed by prescribing the aforementioned fractal PSD, neglecting the non-fractal plateau, that is, $k_l = k_r$ —cf. Figure 2.12. Under these conditions, one rewrites the equation Equation (2.51) as

$$\Phi(k_x, k_y) = \begin{cases} C_0 \left( \dfrac{k_r}{\|\boldsymbol{k}\|} \right)^{2(H+1)} & , \quad k_l \le \|\boldsymbol{k}\| \le k_s \\ 0 & , \quad \text{elsewhere}\,. \end{cases} \tag{3.21}$$

At this point, the power spectrum of a rough surface is determined by the limit frequencies, i.e., $k_l$ and $k_s$, and the Hurst exponent—the scale factor is not considered here, since the representations are inherently non-dimensional. For simplicity, the Hurst exponent was fixed at a unique value, and by setting $k_l = 1$, one can look at the ratio $\lambda_l/\lambda_s$ as the controllable input parameter. The properties of the studied cases are presented in Table 3.1, where the Nayak's parameter for each case is also shown. This value is calculated

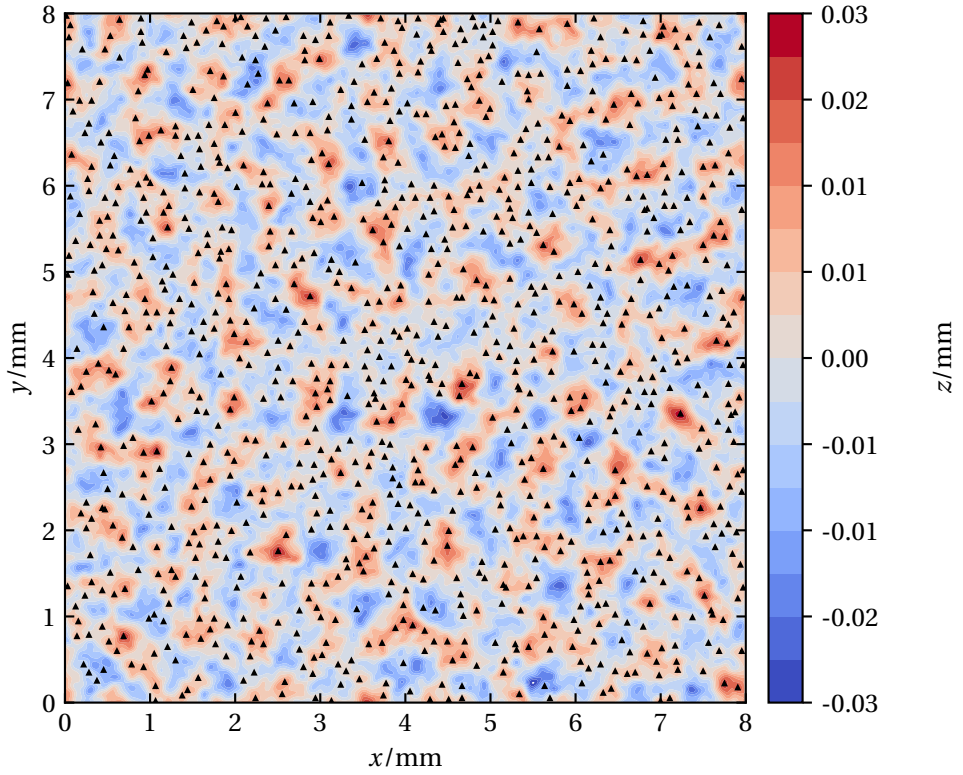


**Figure 3.8:** Detected summits, with the implemented routine, on a random Gaussian surface, with $H = 0.8$ and $\lambda_l/\lambda_s = 8$.

numerically with Equation (2.37) using the discrete spectral moments, computed from the discrete surfaces. Additionally, the topography size is also controlled by the parameter $L/\lambda_l$, where $L$ is the length of the topography with area $L \times L$. In turn, the discretization of the numerically generated surface is controlled by $\lambda_s/\Delta x$, where $\Delta x$ is the uniform spacing between points. If very high values of these parameters are used, the surface discretisation and representativeness is greatly improved, but the computational time of the generation process is significantly increased. This fact naturally has to be taken into account and convenient values should be considered. Following some works on the topic, such as Yastrebov, Anciaux, *et al.* (2012) and Couto Carneiro *et al.* (2020), the parameters $L/\lambda_l = 8$ and $\lambda_s/\Delta x = 8$ are a good compromise between computation time and accuracy, and have been employed in the current study. [3] To cope with the randomness effects inherent to the topography generation, several realizations have to be generated to obtain good representative results. For each case represented in Table 3.1, 1000 realizations were analysed, the summits were identified and processed, and the results of all realizations were assembled to evaluate the probability distributions.

Starting with the probability density of summit heights $p_{\text{sum}}(z^*)$, the obtained results are presented on Figure 3.9, for all the cases tested. In this figure, both numerical and

[3] Later on this work, in Section 4.4.1, the parameters required to, representatively, obtain a random rough surface will be better explored, within the definition of RCE (Representative Contact Element).

**Table 3.1:** Properties of the generated Gaussian surfaces studied for assessing the validity of the framework, for numerical statistics computation.

| $\lambda_l/\lambda_s$ | $H$ | $\alpha$ |
|---|---|---|
| 8 | 0.8 | 5.34 |
| 16 | 0.8 | 11.89 |
| 32 | 0.8 | 29.11 |
| 64 | 0.8 | 75.88 |
| 128 | 0.8 | 206.45 |

analytical results are shown, in a form of a histogram and a continuous curve (similarly to Figure 3.9), respectively. From the first graph, one sees that the numerical results match very closely the analytical solution. To highlight the discrete results, a zoomed version is presented, where one sees that the histogram recovers the theoretical results, in dashed lines, with a high degree of correlation. The joint probability density function of the normalized summit heights and the equivalent mean curvature $p'_{\text{sum}}(z^*, t_1)$ was also recovered, as shown in Figure 3.10. Both theoretical and numerical results are presented side by side to ease visual inspection of the accuracy of the numerical results, which accurately resembles the analytical predictions.

The results for the expected value of mean curvature for summits heights are shown in Figure 3.11 for the different tested cases. The results evidence interesting aspects that motivate further discussion. A good correlation between the numerical and the analytical results is seen, yet the smoother results are restricted to the fractions of $z^*$ where the probability density of summits height is higher. One sees that for $z^* < -0.5$ the numerical results of $\alpha = 5.34$ become less smooth than the other curves. This is a result of the small probability of $p_{\text{sum}}(z^*)$ for this range, as can be seen in Figure 3.9, which ultimately results in fewer curvature observations in this range. For smaller values of $z^*$, the same is seen for increasingly values of $\alpha$. To overcome this lack of representativeness more realizations could be used to completely recover the results, however, it also implies more computation time. Nevertheless, with the current number of realizations, the relative tendency of the results is perfectly captured.

For $z^* > 1$, a loss of smoothness due to small probability is also observed, additionally the numerical results tend to have increasing values of the expected mean curvature when compared with the theoretical counterpart. This difference is larger for the topographies with less spectral content. These deviations may have different justifications and may be a result of a superposition of several errors that have been inspected. First, the Nayak's parameter of each topography, calculated from the discrete PSD, is an approximation of the real $\alpha$ value, with the numerical value overestimating the analytical solution. This problem may be overcome by a finer discretization of the topographies, yet, once more, a compromise needs to be established to compute the results in useful time. It should be noted that this error alone is not sufficient to justify the distance between the numerical and the theoretical curves, as verified by the authors during the investigation. An alternative source of error in this computation may be associated with the error in

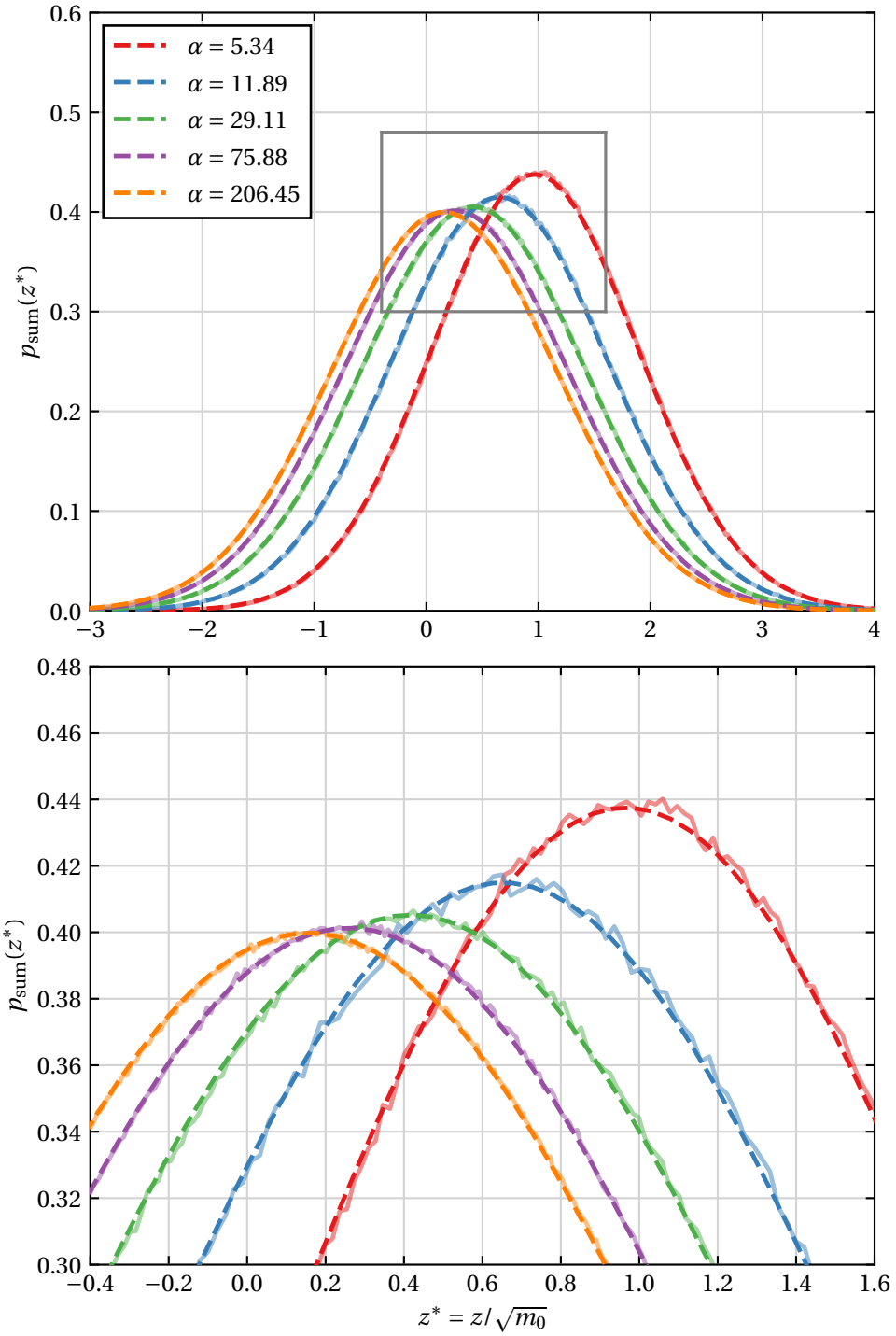


**Figure 3.9:** Probability density of summit heights $p_{\mathrm{sum}}(z^*)$ recovered from the numerical generated results for the different test cases. The numerical results are presented in a form of a histogram and compared with the analytical results (dashed lines) from Nayak's theory. A zoomed version of the first graph is shown to highlight the good correlation of the results.

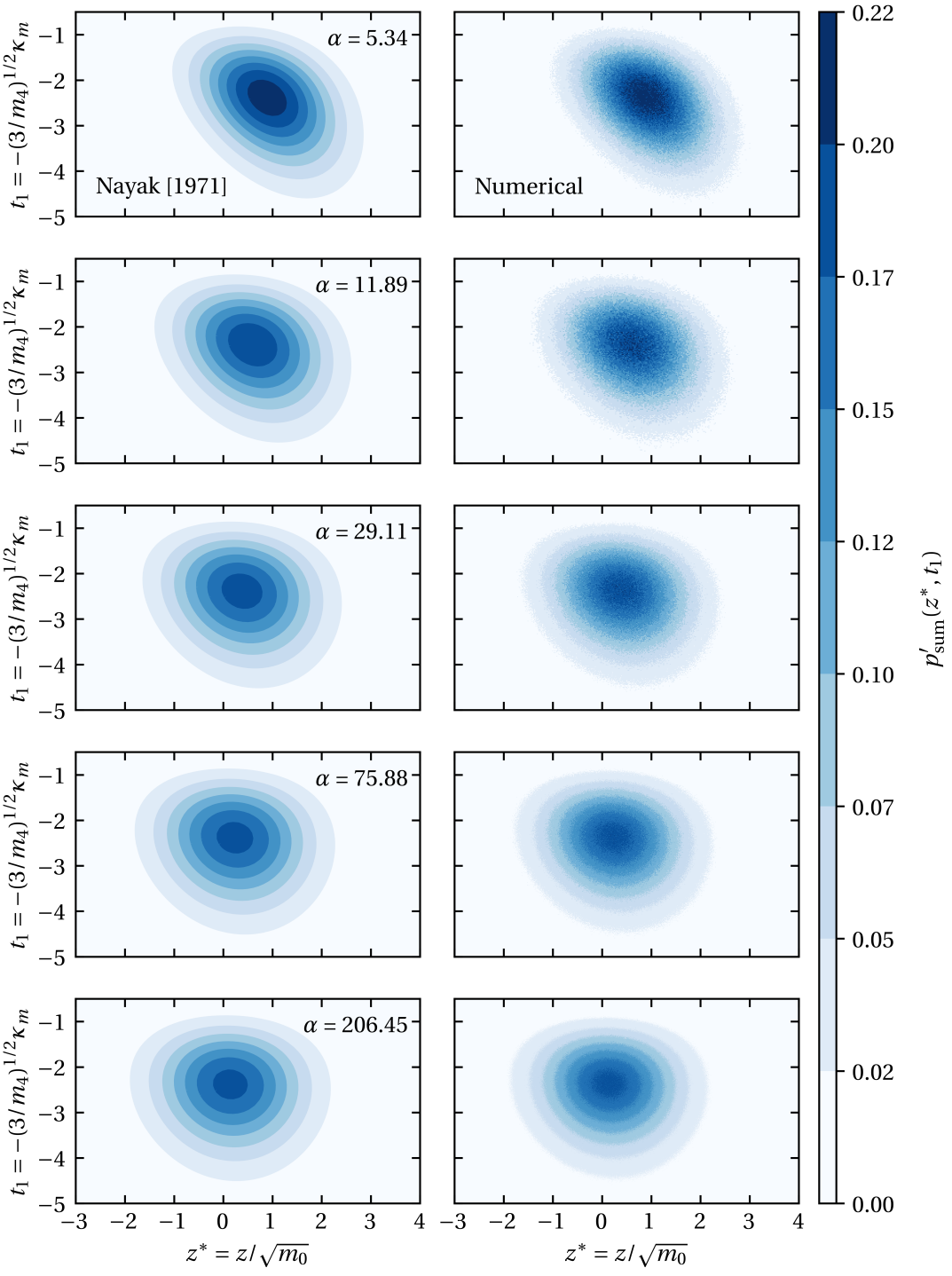


**Figure 3.10:** Joint probability density function of the normalized summit heights and the equivalent mean curvature $p'_{\mathrm{sum}}(z^*, t_1)$, recovered from the numerical generated results for the different test case. Both numerical (right) and theoretical (right) result are presented side by side to ease the comparison process.

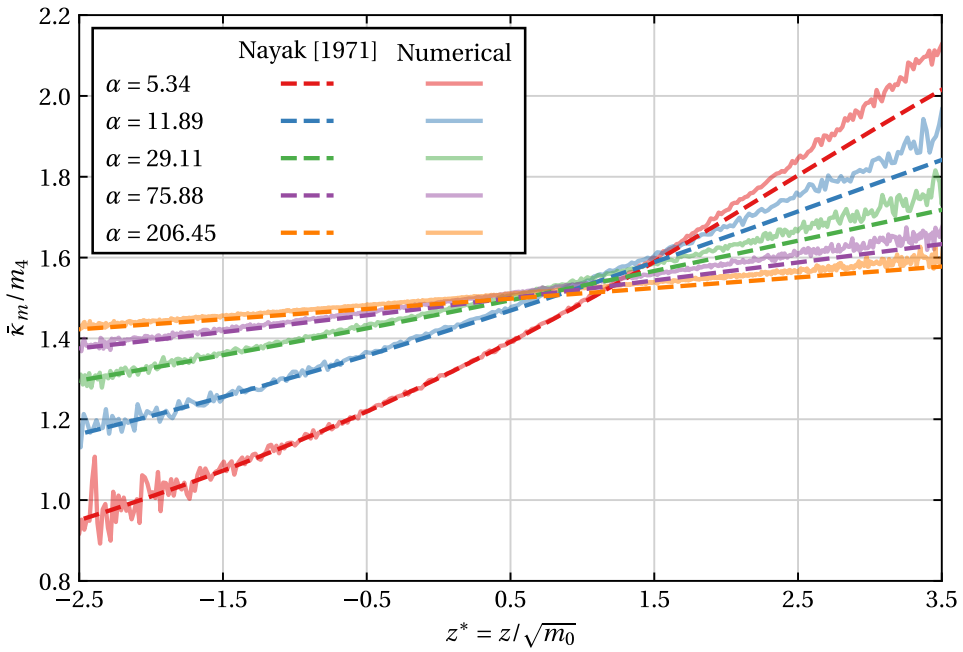


**Figure 3.11:** Dimensionless expected mean curvature of summits heights $\bar{\kappa}_m$ recovered from the numerical generated results, for the different test cases.

the numerical evaluation of derivatives. To investigate the impact of space discretization in the computation of the second-order derivatives, tests with a more discretized topography were performed. However, the results did not provide meaningful information, as the curves obtained were very similar. In fact, for finer discretization, the curvatures tend to be higher, meaning that a coarse discretization would approximate the numerical results to the analytical curves. The influence of the generated topography's size was also assessed with no relevant conclusions. One hypothesis also advanced was the height distribution of the generated topographies imposed tends to distort the expected Gaussian distribution in the tails. However, the authors verified that the Gaussian heigh distribution is recovered with great accuracy in the generated topographies, even in the tails. The lack of explanations for this problem led to the investigation on the effect of the number of realizations. It was observed that for an increasing number of realizations, the curve tends to get closer to the analytical results, however with a slow progression, which suggests that a significantly large number of realizations would be needed to completely fit the Gaussian result.

Following the conclusions from Nayak's theory, one sees that for small spectral content the theory predicts higher deviations between the summits expected mean curvature and the surfaces effective mean curvature (cf. Figure 3.11). This suggests that the summits are sharper than the global curvature of the topography. For higher spectral content, i.e. for higher values of $\alpha$, more summits arise at all height levels, including for lower values of $z^*$, therefore contributing to a more similar value between the expected mean curvature and the mean curvature of the topography. To better understand this concept, the Figure 3.12

is introduced. In this figure two Gaussian topographies used in the current study, with $\lambda_l/\lambda_s$ of 8 and 64, are shown in Figures 3.12a and 3.12c, respectively. One can readily see the difference in the spectral content of the surfaces, however, an easier method for evaluating the features of a rough surface is by simply looking into a profile extracted from the rough surface. This is seen in Figures 3.12b and 3.12, where the highlighted profile is presented. This constitutes the concept of a trace of a rough surface. By inspecting the profile with higher spectral content Figures 3.12d, it can be seen that summits are more likely to happen at lower heights, unlike what is seen in Figures 3.12b, for a small value of $\lambda_l/\lambda_s$.

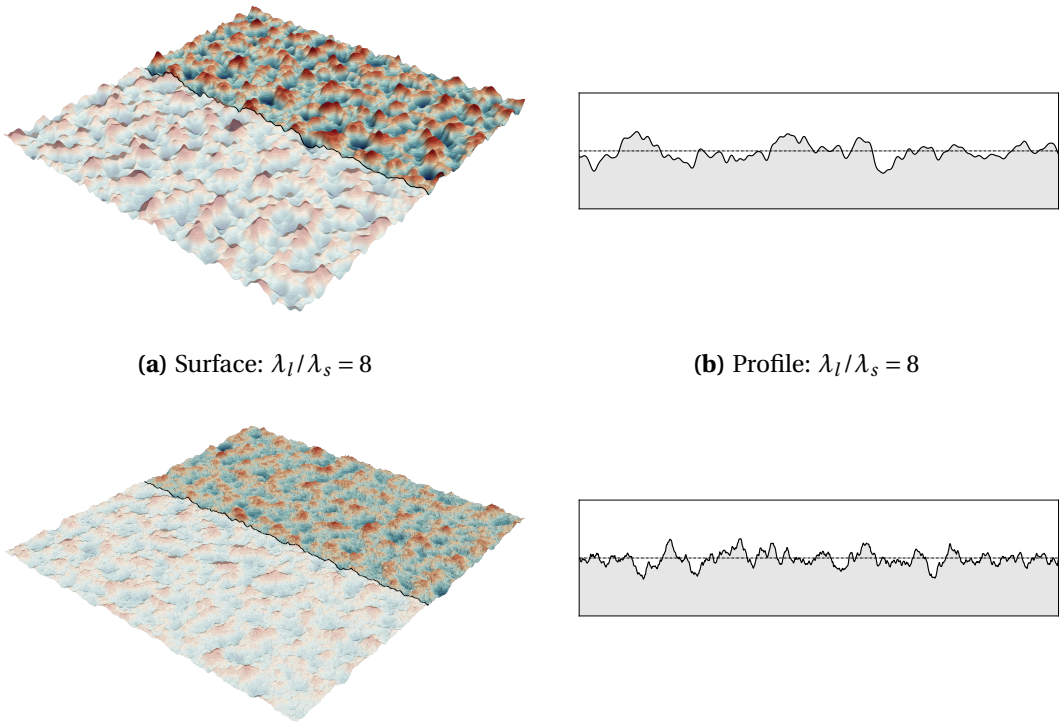

**(a)** Surface: $\lambda_l/\lambda_s = 8$ **(b)** Profile: $\lambda_l/\lambda_s = 8$

**(c)** Surface: $\lambda_l/\lambda_s = 64$ **(d)** Profile: $\lambda_l/\lambda_s = 64$

**Figure 3.12:** Effect of the spectral content on the topography of a rough topography. For each surface (Figures 3.12a and 3.12c the highlighted profile is represented, introducing the concept of the trace of a surface, which constitutes an easier way to assess the topography characteristics.

## 3.2 Non-Gaussian topography

The statistical study discussed previously is extended to the realm of non-Gaussian topographies in the following sections. The same outline will be adopted, with the exception that the summit identification will not be repeated here, as it remains valid from Section 3.1.3. Instead, a more detailed presentation of the non-Gaussian modelling approach based on the Weibull distribution will be introduced. Then, the algorithm em-

ployed for the generation of non-Gaussian topographies is outlined, followed by the numerical study.

### 3.2.1 Weibull distribution

The non-Gaussian behaviour of rough surfaces is commonly characterized by means of skewness and kurtosis. Both parameters provide a feasible tool and have been used in many in various scientific works on the field (G. Yang *et al.*, 2014; Manesh *et al.*, 2010; Kim *et al.*, 2006b). However, one of the drawbacks of modelling surfaces with only these two parameters is that the topography cannot be controlled by only one parameter and therefore difficulties arise when modelling and parametrizing topography's features. Additionally, a characterization based on skewness and kurtosis does not entail robust results for building a solid framework such as the one existing for the Gaussian surfaces. For Gaussian surfaces, the normal distribution can be used for modelling the height distribution of the topography, allowing to use of the well-established properties of such function to produce several analytical results, ranging from topography statistics (Longuet-Higgins and Deacon, 1957a,b; Nayak, 1971) to the micro-contact behaviour of rough surfaces (J. A. Greenwood, J. B. P. Williamson, *et al.*, 1966). Such approach, i.e., using a probability distribution to model the height distribution of non-Gaussian surfaces, has been an active research topic in the field, and several works have tried to settle the problem.

A remarkable first work on modelling non-Gaussian rough surfaces with a probability distribution function was made by Adler *et al.* (1981). In this work, a $\chi^2$ distribution function was used for modelling the non-Gaussianity of asperity heights. Two functions were proposed in order to achieve both positive and negative skewness values. For positive values of skewness a scaled version of the $\chi^2$ distribution, with two parameters, was proposed, whereas for negative skewness surfaces an inverted version of the $\chi^2$ distribution, with three parameters, was used. The mean number of maximum and minima values are derived in this work, as well as the conditional density of the curvature at the maxima and minima, for both profiles and surfaces.[4]

The Weibull distribution was introduced for modelling the height distribution by McCool (1992) due to its flexibility for approximating several practical cases, from closer to Gaussian up to more outlier-heavy cases, with significant values of skewness. The reproductive property under the addition of the Weibull distribution was assessed and McCool (1992) stated that, despite being non-reproductive, the sum of Weibull variables may be approximate by another Weibull distribution with the same mean and variance of the sum resultant distribution. This property is quite interesting, since it allows to approximate the reproducive property of the Gaussian surfaces with a non-Gaussian distribution, thenceforth constituting a more robust approach for dealing with real engineering problems.

McCool (2000) also extended the work of J. A. Greenwood, J. B. P. Williamson, *et al.* (1966) on rough contact modelling, by taking into account the asymmetry of the height distribution measured by the skewness of the Weibull distribution. A later work of Yu and Polycarpou (2001) used the Weibull distribution to model the distribution of heights

[4] For the surface case, the maxima expressions are not deducted nor presented, only the problem is mentioned.

which was introduced in the micro-contact elastoplastic model proposed by W. R. Chang *et al.* (1987)—an extension of J. A. Greenwood, J. B. P. Williamson, *et al.* (1966)—to obtain values of the contact load, the real area of contact and the number of contact asperities. A more recent work from the same authors extended the previous results to encompass the contact between two rough surfaces with Gaussian or non-Gaussian height distributions, with the latter case being modelled by a Weibull distribution function (Yu and Polycarpou, 2004a). L. Chang and Jeng (2013) also used the Weibull distribution to study the impact of negative skewness surfaces for both frictional and frictionless contacts. More recently Pérez-Ràfols and Almqvist (2019) validated their non-Gaussian topography generator with a Weibull distribution of heights. Taking advantage of the novel generation method, the same authors have studied the stiffness of rough surfaces with non-Gaussian height distributions using a Weibull distribution, as well. The typical linear relation obtained in the contact of Gaussian surfaces was not recovered and a power-law function was proposed instead. The effect of the Hurst exponent on the results was also mentioned, concluding that, unlike the Gaussian case, the Hurst exponent is not irrelevant anymore in the contact's stiffness, and it has an impact on the stiffness evolution.

In this work, only the most important aspects of this distribution will be covered and for a more complete description, the interested reader is referenced to N. L. Johnson *et al.* (1994) and Rinne (2008). Different parametrizations of this distribution can be defined. The most classical is the usually termed *two-parameter Weibull distribution* and the associated probability density function writes

$$f_W(z) = \frac{C}{A}\left(\frac{z}{A}\right)^{C-1} \exp\left[-\left(\frac{z}{A}\right)^{C}\right], \quad z > 0\,, \tag{3.22}$$

where $C > 0$ is the shape parameter and $A > 0$ is the scale parameter. A three-parameter version can be also considered by adding a parameter $B$, responsible for shifting the function horizontally, however for the sake of clarity only the two-parameter distribution will be considered in the following exposition. The CDF of the PDF given in Equation (3.22) is written as

$$F_W(z) = 1 - \exp\left[-\left(\frac{z}{A}\right)^{C}\right], \quad z > 0\,. \tag{3.23}$$

Looking into the moments of the distribution, one can write the mean of the PDF of the Weibull distribution as

$$\mu_W = A \cdot \Gamma\left(1 + \frac{1}{C}\right), \tag{3.24}$$

where $\Gamma(\bullet)$ is the Gamma function defined by

$$\Gamma(x) = \int_0^\infty a^{x-1} \exp(-a) \mathrm{d}a\,. \tag{3.25}$$

The variance can also be also be computed from the PDF parameters and comes

$$\sigma_W^2 = A^2 \Gamma\left(1 + \frac{2}{C}\right) - (\mu_W)^2\,. \tag{3.26}$$

Finally, the third-order moment normalized by the cube of the standard deviation, i.e., the skewness, comes

$$\gamma_{1W} = \frac{A^3\Gamma\left(1+\frac{3}{C}\right) - 3\mu_W\sigma_W^2 - \mu_W^2}{\sigma_W^3}\,, \tag{3.27}$$

and the kurtosis

$$\beta_{2W} = \frac{-A^4\Gamma\left(1+\frac{4}{C}\right) - 4\gamma_{1W}\mu_W\sigma_W^3 - 6\mu_W^2\sigma_W^2 - \mu_W^4}{\sigma_W^4}\,. \tag{3.28}$$

One should note that the Weibull distribution as written in Equation (3.22) assumes the shape of a exponential distribution if $C = 1$, and a Rayleigh distribution if $C = 2$ (N. L. Johnson *et al.*, 1994). One of the most interesting aspects of using the Weibull distribution to model the topography heights is that it allows controlling the shape of it adjusting only one parameter, the shape parameter $C$. In fact, neither the scale parameter $A$ nor the shift parameter $B$ are relevant when looking into the surface characteristics. This is a well-known property and has been used in several studies and commonly the scale parameter $A$ is fixed by setting a unitary value for the RMS height (Ciavarella and Afferrante, 2016; Pérez-Ràfols and Almqvist, 2019, 2021)—in other words, the scale can be applied *a posteriori*. In this work, since numerically generated topographies from a prescribed PSD are employed, the RMS height is automatically set, which implicitly defines the scaling parameter $A$, as well. Therefore, one can simply interpret Equation (3.22) by setting $A = 1$. Moreover, by definition, the topographies have zero mean, so the offset parameter $B$ is also tacitly defined from this condition.

Equation (3.22) only allows to model surfaces with positive values of skewness, while several works have pointed out that surfaces tend to be generally negatively skewed (McCool, 1992). This can be simply accommodated by imposing a negative argument $(-z)$ in Equation (3.22). This results in two different equations to model the height distribution, one with positive skewness and other with negative skewness. As it will be later mentioned in Section 3.2.3, where the generation of non-Gaussian surfaces is explained, the computational framework employed in this work makes use of the `SciPy` package to model the probability distributions. In this package, both negative and positive skewed versions of the Weibull distribution are available under the designation of *Weibull Minimum* and *Weibull Maximum* extreme value distributions, respectively. Henceforth, these distributions will be only called Weibull Minimum distribution (or just Weibull Min.) of the positively skewed and Weibull Maximum distribution (or just Weibull Max.) for the negatively skewed. The PDF of the Weibull Minimum distribution thus writes

$$f_W^{Min.}(z) = Cz^{C-1}\exp(-z)^C\,, \quad z > 0\,, \tag{3.29}$$

and for the Weibull Maximum comes

$$f_W^{Max.}(z) = C(-z)^{C-1}\exp\left(-(-z)^C\right), \quad z < 0\,. \tag{3.30}$$

In Figure 3.13 both distributions are plotted for several values of the shape parameter $C$. One sees that the distributions can change in form significantly, from an exponential to a near Gaussian distribution. The distributions are plotted as they were parametrized in Equations 3.29 and 3.30 with $A = 1$, therefore the zero mean is not observed in this figure.

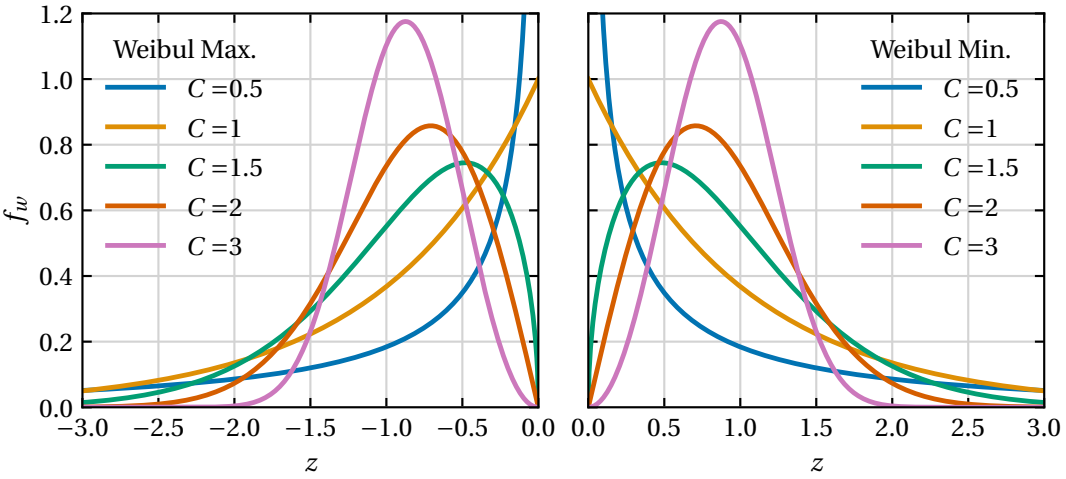


**Figure 3.13:** Behaviour of the Weibull Maximum (left) and Weibull Minimum (right) for several values of the shape parameter $C$. The distributions are shown as they are parametrized on Equations 3.29 and 3.30 with $A = 1$.

### 3.2.2 Selection of the shape parameter

The ability of the Weibull distribution to approximate real-life surfaces has already been demonstrated in several scientific works (McCool, 1992; Pérez-Ràfols and Almqvist, 2021). Yet, to perform a parametric study on the effect of the height distribution, one has to explore the influence of the unique independent parameter, $C$, and select appropriate values that resemble topographies found in practical scenarios. Still to this day, skewness and kurtosis are convenient approaches to condense the information on the shape of PDF and several works can be consulted to obtain reference values for these parameters (K. J. Stout *et al.*, 1990; Whitehouse and Whitehouse, 2011). Both skewness and kurtosis of the Weibull distribution can be directly computed from the equations Equation (3.27) and Equation (3.28), attending to the necessary modifications to accommodate the Weibull Maximum and Weibull Minimum variants.

To establish the connection between the more theoretically-flavoured Weibull distributions and the practice-oriented skewness and kurtosis, Figure 3.14 shows the evolution of the skewness and kurtosis of both Weibull Minimum and Weibull Maximum distributions for different values of the shape parameter $C$. Since there is only one independent parameter, the region of the skewness-kurtosis space that can be modelled is represented by a curve symmetric to the zero skewness axis, where each branch corresponds to the Weibull Min. and Max. variants. For each value of kurtosis, two symmetric values of skewness can be obtained, one for each variation of the PDF. The shape of the height distribution goes from a near to Gaussian case and extends to greater levels of kurtosis and skewness. The nearly Gaussian case can be modelled with the Weibull distribution for $C \approx 3.602$ where the skewness is 0 and the kurtosis is close to 3—the Weibull Maximum and Weibull Minimum intersect at this point. Moreover, $C = 3.602$ can also be considered the maximum value of the shape parameter, due to the asymptotic evolution of the skewness and kurtosis. In Figure 3.14 some experimental results of skewness and kurtosis of machined

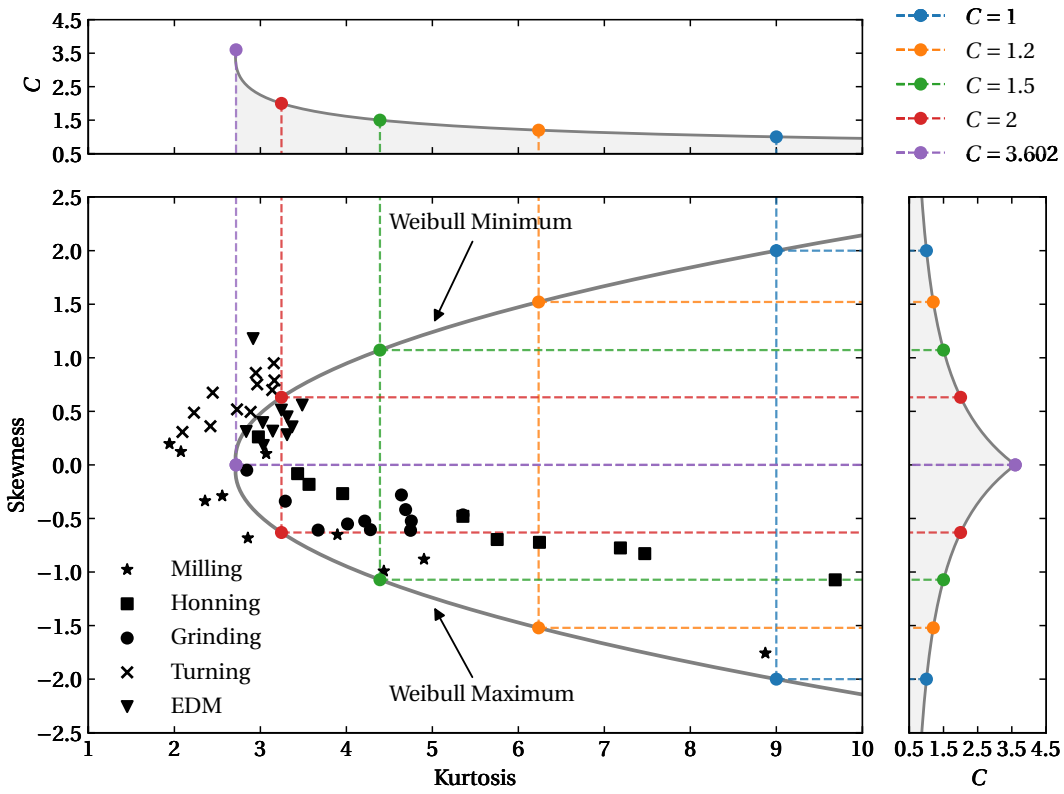


**Figure 3.14:** Evolution of skewness and kurtosis of the Weibull distribution (Weibull Maximum and Weibull Minimum) as a function of the shape parameter $C$. Experimental values of skewness and kurtosis of machining processes obtained and adapted from Whitehouse (1994) are also plotted to give a visual integration of the capability of the Weibull distribution to describe real shapes. The five values of the $C$ shape parameter used to perform the statistical studies are also highlighted.

surfaces are also plotted, according to the data provided in Whitehouse (1994). It can be seen that the Weibull distribution has a great potential for approximating and describing real-life surfaces, especially the Weibull Max. branch (negative skewness), which further motivates the selection of this PDF in the current work. To endorse this approach several ranges of skewness and kurtosis for different types of machining processes are also presented in table Table 3.2 (K. Stout, 1980), where it is seen that the majority of the cases of skewness and kurtosis can be recovered by topographies modelled with Weibull distribution.

To perform the numerical study and infer the impact of the height distribution on the topography statistics by adjusting the shape parameter $C$, specific values must be chosen. From the experimental results presented in Figure 3.14 and in Table 3.2, one sees that the Weibull Maximum shows more similarity to practical results since machined surfaces tend to be negatively skewed. To be able to represent a significantly wide range of skewness and kurtosis values with practical relevance, the shape parameter is chosen from

**Table 3.2:** Skewness and Kurtosis of the height distribution of surfaces resultant from several machining process. Adapted from K. Stout (1980).

| Process | Skewness | | Kurtosis | |
|---|---|---|---|---|
| | min. | max. | min. | max. |
| Turning | +0.2 | +1.0 | 2 | 4 |
| Milling | -1.6 | +0.2 | 2 | 10 |
| Grinding | -0.8 | +0.0 | 2 | 6 |
| Reaming | -1.0 | -0.5 | 3 | 8 |
| Honing | -1.0 | -0.5 | 3 | 10 |
| EDM | 0.0 | +1.2 | 2.5 | 4 |
| Sand blasting | 0.0 | +1.4 | 2.5 | 3 |

**Table 3.3:** Skewness and Kurtosis value for each value of $C$ selected to perform the numeric statistical study—for both Weibull Maximum and Minimum distributions.

| C | Weibull Max. | | Weibull Min. | |
|---|---|---|---|---|
| | Kurtosis | Skewness | Kurtosis | Skewness |
| 1 | 9 | -2.00 | 9.00 | 2.00 |
| 1.2 | 6.24 | -1.52 | 6.24 | 1.52 |
| 1.5 | 4.39 | -1.07 | 4.39 | 1.07 |
| 2 | 3.25 | -0.63 | 3.25 | 0.63 |
| 3.602 | 2.72 | 0.00 | 2.72 | 0.00 |

the list $C \in \{1,\ 1.2,\ 1.5,\ 2, 3.602\}$. The selected values are also illustrated in Figure 3.14, showing a good coverage of the experimental measurements. Even though the Weibull max. shows better correlation with experimental measurements, for each value of $C$, both versions of the distribution shall be considered, from here on. Additionally, in Table 3.3 for each study point, the computed values of skewness and kurtosis are presented as well. Finally, the resultant height distribution for each $C$ is presented in Figure 3.15, considering a zero mean set and a RMS height value of 1. This figure reinforces the idea of symmetry between distributions and also the tendency for lower values of $C$ being more distinct from the Gaussian case. Also, it can be reiterated that for $C = 3.602$ the approximate Weibull distributions are very close to the Gaussian case and, therefore, similar results are expected for both versions.

### 3.2.3 Generation of non-Gaussian rough surfaces

The generation of non-Gaussian surfaces performed by `LINKS-RC` is based on the method proposed by Pérez-Ràfols and Almqvist (2019). One of the most interesting features of this method, when compared to others, is that it allows the generation of surfaces with a prescribed PSD and height distribution, in an independent way. This characteristic gives great flexibility and extension to the non-Gaussian surfaces generator since one can separate the frequency content from the shape of the height PDF, allowing for a more suitable

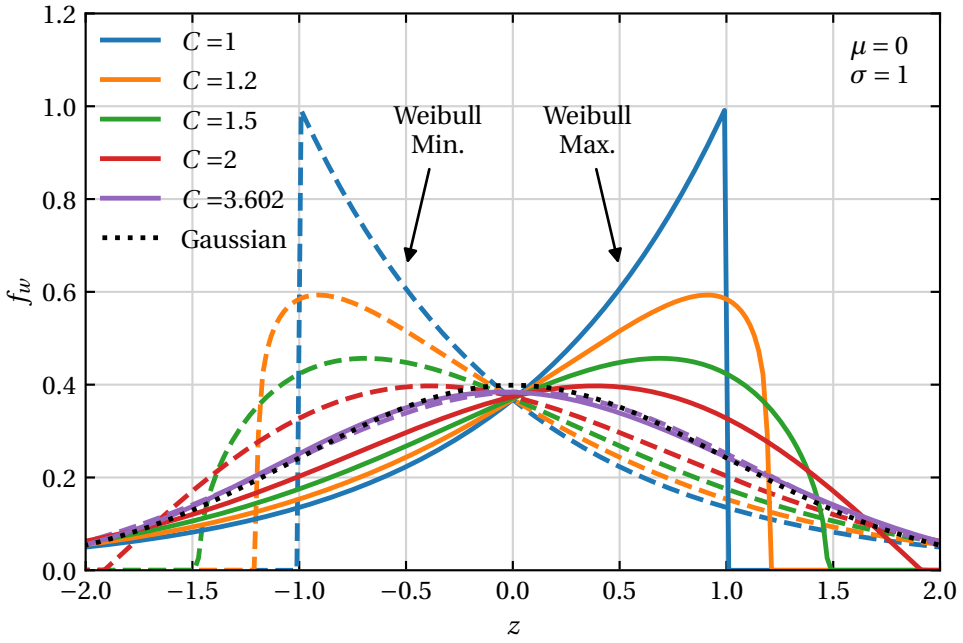


**Figure 3.15:** Height probability distribution of both Weibull Maximum and Minimum distributions for each C parameter value. A zero mean set and an RMS height value of 1 were considered for the computation of the distributions. The Weibull Minimum cases are represented by a dashed line whereas the solid line is used for the Weibull Maximum. The Gaussian case for the same values of mean and standard deviation is also represented (dotted line).

representation of real surfaces. The height distribution can be modelled using any type of statistical distribution, but the current work focuses on the Weibull distribution, which was implemented using the `SciPy` package. The flowchart that resumes the generation process is presented on Figure 3.16.

The first step of the algorithm is the generation of a Gaussian topography $z_s^0$ with the prescribed PSD. This step can be achieved using any of the well-known Gaussian surface generators available and described in the literature. For convenience, in the current work, the Gaussian surface, with a specific PSD, was generated using the previously described algorithm (Section 3.1.2), proposed by Wu (2000b). Secondly, a set of random numbers, following the target height distribution and with size $M \times N$ must be generated. The obtained set must be interpreted as random topography $z_h^0$ that has the correct height PDF but a wrong PSD. Apart from the prescribed height distribution, the topography $z_h^0$ should have zero mean, by definition, and has to be scaled to standard deviation given by the prescribed PSD of $z_s^0$. With the two initial topographies generated $z_s^0$ and $z_h^0$, the iteration process of the algorithm starts, from $i = 0$, until convergence is observed, measured by the computed errors for each iteration, as will be seen shortly. Each iteration $i+1$ starts by computing a new topography $z_s^{i+1}$, with the correct PSD, by correcting the

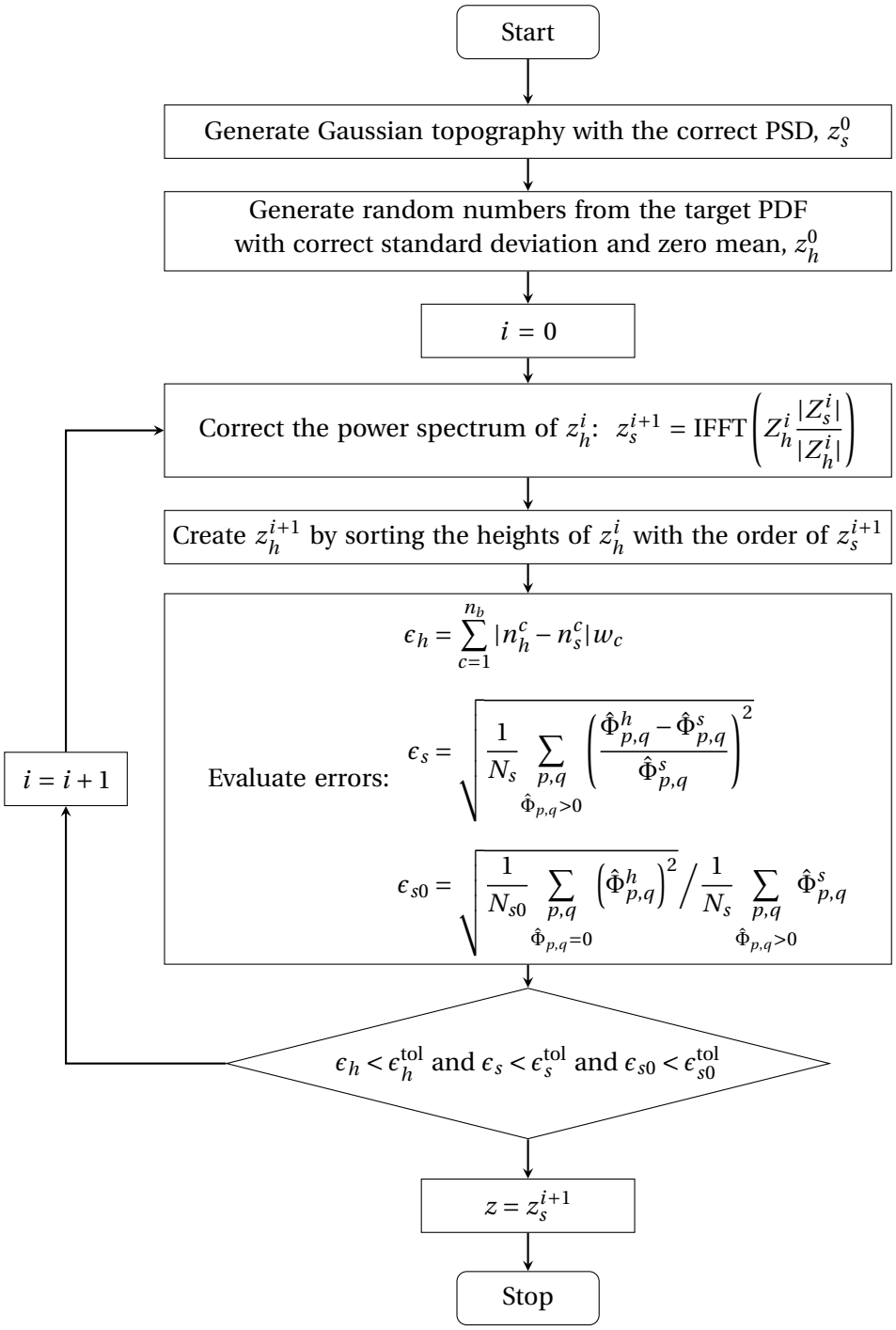


**Figure 3.16:** Flowchart of the non-Gaussian random rough surface generation algorithm.

power spectrum of $z_h^i$, i.e.

$$z_s^{i+1} = \text{IFFT}\left( Z_h^i \frac{|Z_s^i|}{|Z_h^i|} \right). \tag{3.31}$$

After the IFFT is computed the obtains a surface $z_s^{i+1}$ with a correct PSD, yet with a height distribution different from the prescribed. To overcome this, a new topography $z_h^{i+1}$ with the correct height PDF is computed by sorting the topography $z_h^i$, with respect to the order of $z_s^{i+1}$. The sorting process consists of the replacement of the $k^{\text{th}}$ largest value of $z_s^{i+1}$ by the $k^{\text{th}}$ largest value of $z_h^i$, in a process called *rank ordering*. This leads to a topography $z_h^{i+1}$ that has a correct distribution of heights but with an incorrect spectrum. For each iteration the obtained topographies $z_s^{i+1}$ and $z_h^{i+1}$ are evaluated at the light of three different type of errors that dictate if the iteration loop continues or stops. The first error evaluates the deviation of the height distribution by assessing the difference between the histogram of $z_s^{i+1}$ with the histogram of $z_h^{i+1}$, which has the correct height PDF. This error is computed by

$$\epsilon_h = \sum_{c=1}^{n^b} |n_h^c - n_s^c| w_c \tag{3.32}$$

where $n^b$ is the number of bins of the histogram and $w_c$ being the width of each bin, both computed through Scott's rule.[5] The parameters $n_h^c$ and $n_s^c$ are the normalized count of the topographies $z_h^{i+1}$ and $z_s^{i+1}$, respectively, for the bin $c$. The second error is used to evaluate the non-null PSD values of $z_h^{i+1}$ relative to the topography with the correct spectrum $z_s^{i+1}$. It writes

$$\epsilon_s = \sqrt{\frac{1}{N_s} \sum_{\substack{p,q \\ \hat{\Phi}_{p,q}>0}} \left( \frac{\hat{\Phi}_{p,q}^h - \hat{\Phi}_{p,q}^s}{\hat{\Phi}_{p,q}^s} \right)^2}, \tag{3.33}$$

where $N_s$ is the number of frequencies with a non-null PSD value. Finally, the third and last error evaluates the difference on the null PSD values of $z_h^{i+1}$ relative to $z_s^{i+1}$

$$\epsilon_{s0} = \sqrt{\frac{1}{N_{s0}} \sum_{\substack{p,q \\ \hat{\Phi}_{p,q}=0}} \left( \hat{\Phi}_{p,q}^h \right)^2} \Big/ \frac{1}{N_s} \sum_{\substack{p,q \\ \hat{\Phi}_{p,q}>0}} \hat{\Phi}_{p,q}^s, \tag{3.34}$$

where $N_{s0}$ is the number of frequencies with a null PSD value. After the computation of all three errors, the values obtained are compared with the tolerance values, i.e., the maximum value of each error allowed to finish the iteration process. Therefore, if $\epsilon_h < \epsilon_h^{\text{tol}}$, $\epsilon_s < \epsilon_s^{\text{tol}}$ and $\epsilon_{s0} < \epsilon_{s0}^{\text{tol}}$, the iteration cycle stops and advances to the final step, otherwise the loop continues for the next iteration. When the convergence is reached the final topographies $z_s^{i+1}$ and $z_h^{i+1}$ are very identical and the values of the prescribed parameters should be very similar to the correct ones. In the current work, the implementation adopted instructed to choose $z_s^{i+1}$, as it would satisfy the wanted power spectrum exactly.

[5] The Scott's rule computes the width of histogram as: $w_c = 3.49\sigma_z / \sqrt[3]{N_z}$, where $\sigma_z$ is the standard deviation of the height distribution and $N_z = M \times N$ the number of points of the discrete surface.

Overall the algorithm shows good convergence properties, yet, if very tight tolerances are taken, i.e., for values of $\epsilon_h^{\text{tol}}$, $\epsilon_s^{\text{tol}}$ or $\epsilon_{s0}^{\text{tol}}$ smaller than $10^{-3}$, the algorithm may need a large number iterations, due to the fact that the PSD usually covers a wide range of orders of magnitude. To increase the algorithm performance, whenever the convergence is detected and the iterative process is stuck in a value near to the tolerance, the implemented routine uses the already near value as the final one, which is equivalent to use a larger convergence tolerance.

Figure 3.17 shows two examples of surfaces generated with the exposed method. The surface height distribution is modelled using the Weibull distribution, in both maximum and minimum versions, allowing to obtain negatively and positively skewed surfaces, respectively. The topographies present very distinctive features, with the one from Figure 3.17a having a lot more predominance of summits in contrast with the surface from Figure 3.17b. The height distributions for both topographies are presented in Figure 3.18, where the numerical results are compared with the prescribed curve, and showcasing the accuracy of the method in obtaining the prescribed PDF. To conclude, Figure 3.19 shows exemplary non-Gaussian random topographies generated with the previous algorithm for each shape parameter $C$ selected in Section 3.2.2.

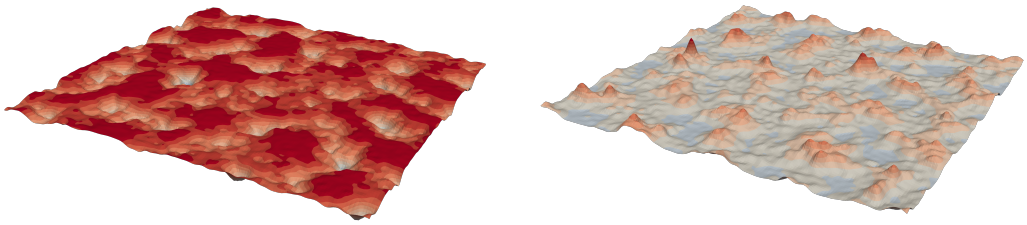

**(a)** Weibull Maximum: $C = 1.3$. **(b)** Weibull Minimum: $C = 1.3$.

**Figure 3.17:** Examples of non-Gaussian surfaces generated using the method proposed by Pérez-Ràfols and Almqvist (2019), and modelled with the Weibull distribution, with a shape parameter $C = 1.3$ and for both Maximum and Minimum cases—Figures 3.17a and 3.17b, respectively.

### 3.2.4 Numerical study

The numerical study on the statistics of non-Gaussian surface modelled with the Weibull distribution follows the same lines of the previous Gaussian study (Section 3.1.4). This time, the studied cases result from the combination of the four variables considered, i.e, the Weibull distribution type, the shape parameter $C$, the Hurst exponent $H$ and the wavelength ratio $\lambda_l/\lambda_s$. The shape parameter values have been defined previously in Section 3.2.2, where the following values were carefully selected $C \in \{1,\ 1.2,\ 1.5,\ 2, 3.602\}$. To assess the influence of the spectral content on the topography statistics, both the Hurst exponent and the ratio $\lambda_l/\lambda_s$ were also chosen as degrees of freedom of the study. In this case, large values of $\lambda_l/\lambda_s$ lead to much greater numerical generation times, relative to the Gaussian scenario, due to the inherently iterative character. For this reason, the bandwidths $\lambda_l/\lambda_s \in \{8,\ 16\}$ were selected. Regarding the Hurst exponent $H$, the values

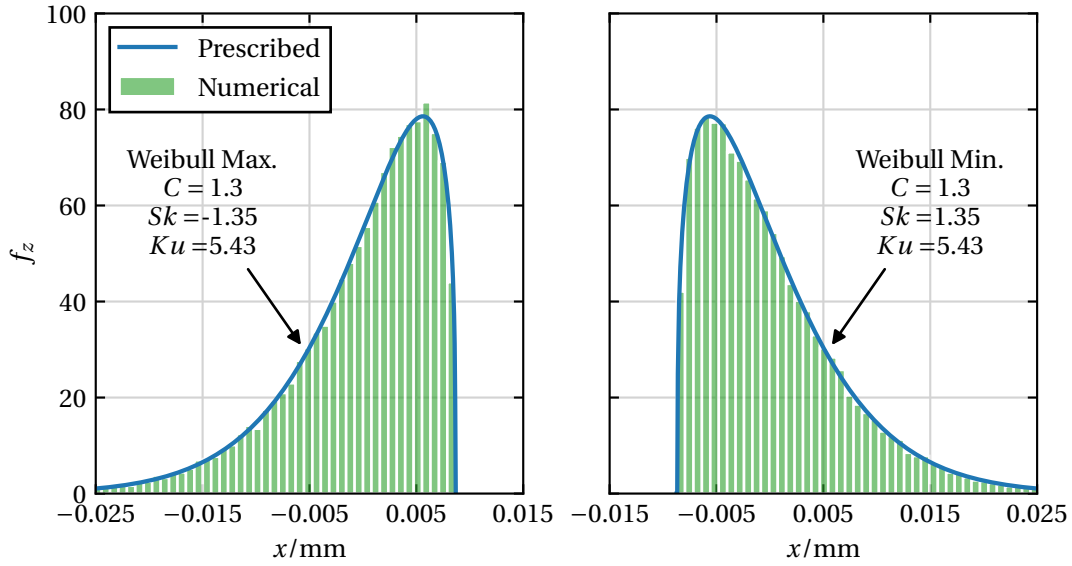


**Figure 3.18:** Comparison between the prescribed and the numerical heights distributions of the of two examples of non-Gaussian surfaces generated using the method proposed by Pérez-Ràfols and Almqvist (2019). Modelled using the Weibull distribution, with a shape parameter $C = 1.3$ and for both Maximum and Minimum cases—Figures 3.17a and 3.17b, respectively.

**Table 3.4:** Variables considered for the statistical study on non-Gaussian rough surfaces modelled with the Weibull distribution. The studied cases result from a combination of the exposed variables.

| Height Distribution | $C$ | $\lambda_l/\lambda_s$ | $H$ |
|---|---|---|---|
| Weibull Maximum | 1 | 8 | 0.2 |
| | 1.2 | | |
| | 1.5 | | |
| Weibull Minimum | 2 | 16 | 0.8 |
| | 3.602 | | |

$H \in \{0.2,\ 0.8\}$ were considered. Table 3.4 shows the cases outlined for the present study, constituting a total of 40 distinct combinations. For each particular study case, 1000 realizations with a self-affine behaviour restricted to the fractal part (cf. Equation (3.21)) were generated and evaluated. The length of the topography $L$ and sampling space $\Delta x$ were kept the same since no major problems arose from the Gaussian validation process (cf. Section 3.1.4), i.e., $L/\lambda_l = 8$ and $\lambda_s/\Delta x = 8$. The results obtained are discussed in the following sections, in terms of the probability measures of summit heights and mean curvatures. The analysis is divided considering the effect of the shape of the height distribution and the influence of the spectral content.

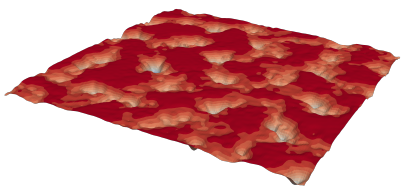

**(a)** Weibull Maximum: $C = 1$

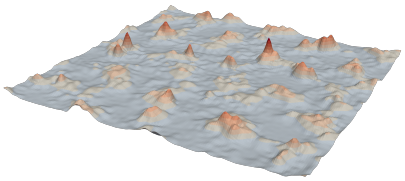

**(b)** Weibull Minimum: $C = 1$

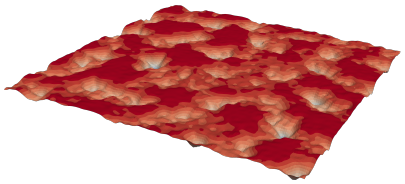

**(c)** Weibull Maximum: $C = 1.2$

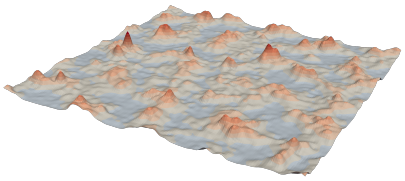

**(d)** Weibull Miniimum: $C = 1.2$

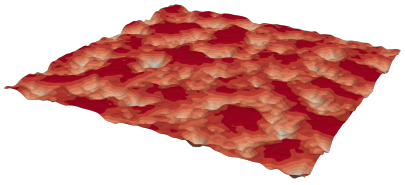

**(e)** Weibull Maximum: $C = 1.5$

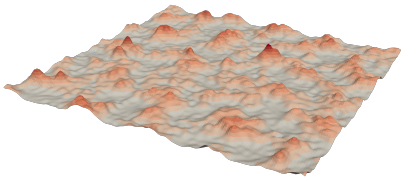

**(f)** Weibull Minimum: $C = 1.5$

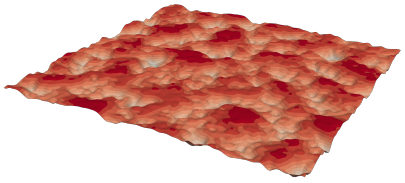

**(g)** Weibull Maximum: $C = 2$

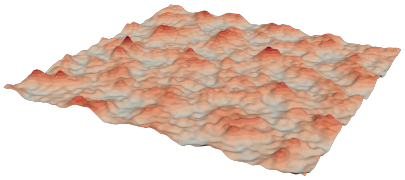

**(h)** Weibull Minimum: $C = 2$

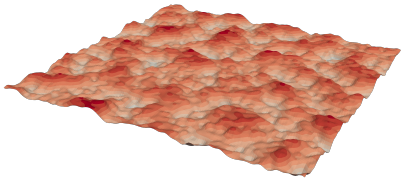

**(i)** Weibull Maximum: $C = 3.602$

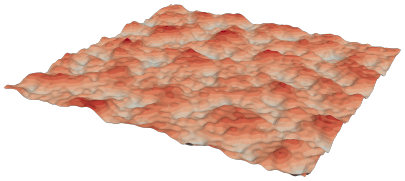

**(j)** Weibull Minimum: $C = 3.602$

**Figure 3.19:** Examples of non-Gaussian surfaces, modelled with the Weibull distribution, with the different shape parameter $C$ values, considered for the numerical study.

**Influence of the height distribution and the shape parameter**

The statistical results obtained may be analysed in the light of the type of height distribution considered and the shape of the height distribution, which for the Weibull distributions has an attractive simplicity, since one can simply see how the results are affected by the shape parameter $C$. Hence, by fixing a pair of the Hurst exponent $H$ and the wavelength ratio $\lambda_l/\lambda_s$, resulting in a distinctive value of the Nayak's parameter $\alpha$, one can see how $C$ influences the results for both Weibull Maximum and Minimum distributions.

**Probability density of summit heights** First off, the probability distribution of the normalized summit's height $p_{\text{sum}}(z^*)$ will be analysed and discussed. The results for the four combinations of $H$ and $\lambda_l/\lambda_s$ and presented from Figure 3.20 to Figure 3.23. In these figures, both Weibull Maximum and Minimum histograms are plotted individually, to privilege the visual inspection of the results. Also, the same vertical and horizontal scales are kept the same for all the results, in order to make the comparison between plots more convenient. Furthermore, profiles extracted from a realization with the characteristics in study are plotted below the histograms, facilitating the understanding of the results obtained, cf. Figure 3.12. For each case, the Nayak's solution of $p_{\text{sum}}(z^*)$ is computed from Equation (3.4) with the $\alpha$ value obtained numerically from the generation process—unique for each pair of $H$ and $\lambda_l/\lambda_s$. For the sake of graphical representation, the vertical axis represents the logarithm with based 10 of one plus the PDF of the normalized summit heights—$\log_{10}\left(p_{\text{sum}}(z^*)+1\right)$.[6] This option can be justified by looking at the plots referring to the Weibull Max. distribution, where extremely high peaks of probability are easily identified. The application of this change of variable heavily attenuates the values of the probability peaks and allows for a more easy comparison between all the plots.

One can start by analysing, for instance, the case where $H = 0.2$, depicted in Figures 3.20 and 3.21 since the general impact of the height distributions has been verified in this study to be uncorrelated with the spectral properties of the surface. The analysis is divided between each of the height distributions to better systematize the process of results discussion.

**Weibull Maximum** Starting with the Weibull Maximum results, one verifies that, like the height distribution, also the summits heights distribution has left-skewed histograms, which is a direct consequence of having heights concentrated near a positive height (cf. Figure 3.15). Additionally, these distributions also evidence huge differences in shape and magnitude compared with the Gaussian case—especially for lower values of $C$. In fact, while the Gaussian distribution tends to look like a slightly skewed normal distribution, the Weibull Maximum's histograms resemble an exponential distribution, with significant modal probability density. [7] Such trend on the distributions can be justified by the results from Nayak's theory (Section 3.1.1), where it was seen that, in a Gaussian surface, summits are more likely to happen at positive values of height (cf. Figure 3.1). The same effect is verified in non-Gaussian surfaces, with the addition that in topographies with a

[6] The vertical labels are written as $\log_{10} p_{\text{sum}}\left(z^*\right)+1$ for the sake of readability.

[7] One should recall that the relations between the differences between the histograms are moderately softened by the vertical logarithm operation.

significant concentration of positive heights, the effect translates into even higher concentrations of summits. A substantial degree of dependence on the shape parameter $C$ is also observed. For lower values of $C$, the distribution tends to have a progressively higher probability of having summits around the same height value. Yet, this maximum height, at which the mode is located, also tends to be increasingly smaller, causing a left-shifting in the histogram. This phenomenon can be better perceived if one looks after the height distribution of such topographies (cf. Figure 3.15). From what has been seen before, as a general statement, it can be postulated that the trend in the skewness of the topography height distribution and summit height distribution is identical. Nonetheless, the summit distribution is also sensitive to the heigh distribution's limits since there can be no summits above the maximum value of height. For instance, in Figure 3.15, it is seen that, for $C = 1$, the heigh distribution is limited at a maximum value of $z \approx 1$, whereas for $C = 1.5$, the probability of having heights at the value of $z = 1$ is lower yet, the distribution extends its upper bound up to $z \approx 1.5$. These features are directly conveyed to the summit heights distribution, Figure 3.21, where one sees that $C = 1$ has a higher concentration of summits around $z \approx 1$, while $C = 1.5$ possesses a more spread out summit heights distribution, with smaller mode values—in the latter case, the histogram is flattened and spreads to the right. This can be clarified by taking a look into the profiles of a representative topography presented in Figure 3.21. One sees that for $C = 1$, the heights have almost the same value—around zero since it is a zero-mean set—with some deep outlier valleys. Thus, it justifies why there is a large concentration of summits around high height values. With the increase of $C$, the profiles' heights become less concentrated around a single value, and the negative outliers become less deep. This evolves up to the point where an almost Gaussian topography is obtained, i.e., when $C = 3.602$. In this case, the PDF of the normalized summit heights is very near the Gaussian case and this is proven by the similarity to the theoretical curve plotted by a black dotted line.

**Weibull Minimum** In turn, the Weibull Minimum presents a right-skewed distribution, and this is in line with what was advanced previously, i.e., the summits heights distribution captures the shape of the height distribution of the topography (cf. Figure 3.15). Another aspect of interest is the fact that the order of magnitude of probability density does not differ much from the Gaussian case. [8] In this case, one gets less abrupt distributions, when compared with the Weibull Maximum distribution that acuminates into a large mode value. The reason for these results is once more justified by Nayak's theory. Since the summits tend to be more frequent at high values of height, in a distribution with predominant lower height values, a concentration of summits around a specific height is not trivially expected. Even so, summits with low height values are still dominant, as the height distribution imposes it.

As for the outliers values of the topography height distribution, it is verified that they add a superior contribution to $p_{\text{sum}}(z^*)$ when compared with the outlier values of the Weibull Maximum distribution. Fundamentally, this means that substantially high summits can be found in the topographies with more probability than in the Gaussian case.

[8] This fact is slightly hidden by different vertical scales adopted for each Weibull distribution yet, if a closer look is taken, one verifies that Weibull Minimum's distributions would fit in less than one-seventh of the vertical scale of the Weibull Maximum's cases.

The shape parameter $C$ has also a preponderant influence on the summit heights distribution. One sees that for $C = 1$ the distribution of the summit heights has an exponential-like shape, yet with a not so emphasised mode value and with the increase of $C$ the distributions approximate to the Gaussian case. A look into the profiles helps to realize these characteristics. For $C = 1$ one also verifies that several of a higher concentration of heights around zero, similarly to what was seen in Weibull Maximum distribution. Although, the outlier values are summits rather than valleys, counterbalancing the tendency of summits to only occur at lower heights—reasons why this type of topographies have more stable summits distributions around the same probability density values. Increasing the shape parameter and an expected approximation to the Gaussian topography occurs, with heights progressively more distributed in the height range, moving the summits from lower values up to higher ones. The $p_{\text{sum}}(z^*)$ becomes closer to the Gaussian distribution and, once again, a pretty close similarity is seen for $C = 3.602$.

The cases with $H = 0.8$ are presented in Figure 3.22 and Figure 3.23 and the results capture similar tendencies in terms of the influence of the height distribution. The Weibull Maximum's $p_{\text{sum}}(z^*)$ show a really close shape with slightly lower probability density around the mode. In turn, the Weibull Minimum case has some interesting results for lower $C$ values indicating an interesting influence of the spectral properties in the summit heights distribution. Both cases will be commented on later when assessing the influence of the spectral content.

**Joint probability density of summit heights and curvatures** Following the same lines of the numerical results of the Gaussian case, the joint probability distribution function of the normalized summit heights and the equivalent mean curvature $p'_{\text{sum}}(z^*, t_1)$ was also obtained for all the non-Gaussian studies. This quantity provides a feasible way to assess the effect of non-Gaussian height distributions in the summits curvatures, a feature that holds an important role in micromechanical contact phenomena of rough surfaces, such as in the real contact area evolution.

In Figure 3.24, the two-dimensional numerical histograms are presented for the particular case of $H = 0.2$ and $\lambda_l/\lambda_s = 8$—for the same value of normalized height value $z^*$, summits with with different curvature values $t_1$ can occur. Only one spectral scenario (a pair of $H$ and $\lambda_l/\lambda_s$) is considered, since here the focus is on the effect of height distribution and the shape parameter, and the conclusions drawn can be extended to the other cases. At first sight, one can immediately notice that the shapes of the joint distributions are very distinctive from the ones obtained for Gaussian topographies. The Weibull Maximum's histograms exhibit a less spread distribution, with a more restricted height domain that tends to expand with the increase of $C$. For increasing values of $C$, the joint PDF expands towards larger heights, until it becomes distributed with a similar shape to the Gaussian case—when $C = 3.602$.

In turn, the Weibull Minimum's histograms present more spread out distributions with higher levels of probability for lower values of heights, which is in tune with what was advanced in the $p_{\text{sum}}(z^*)$ results. These histograms also evidence that the higher the value of $z^*$ the smaller the equivalent mean curvature $t_1$, in an average sense. This translates to the fact that higher summit heights will tend to have higher summits curvatures. One

must remember that the domain of the equivalent mean curvature $t_1$ is negative which means that lower values of $t_1$ actually correlate to higher values of mean curvature $\kappa_m$.

**Expected mean curvature** The evaluation of the $p'_{\text{sum}}(z^*, t_1)$ is an important step, however, its analysis is not very simple and becomes more difficult to condense and compare the results, and are not as comprehensible as the expected mean curvature of summit heights $\bar{\kappa}_m$, which holds information on how curvatures evolve with the normalized height. One should note that the expected mean curvature condenses the information of $p'_{\text{sum}}(z^*, t_1)$ by averaging the curvatures for each value of $z^*$. Therefore, it can be seen as a "mean value" of the mean curvature for a certain value of $z^*$. It is not a complete description like $p'_{\text{sum}}(z^*, t_1)$ yet it provides a useful trend-line with important information of the topographic features. In Figure 3.25 and Figure 3.26 the expected mean curvatures normalized by the square root of the fourth-order moment are shown, for both Weibull Maximum and Minimum distributions. For each pair of $H$ and $\lambda_l/\lambda_s$ the different values of $C$ are plotted, fostering the inspection of the influence of this parameter. Additionally, the Gaussian result is also presented for the computed value of Nayak's parameter $\alpha$. The results were trimmed for the values with probabilistic significance, by visually inspecting $p'_{\text{sum}}(z^*, t_1)$.

**Weibull Maximum** Starting with the Weibull Maximum distribution values of expected mean curvature (Figure 3.25) one sees that a non-linear behaviour is captured, with a very distinctive evolution when comparing with the Gaussian result. While for Gaussian surfaces, increasingly values of height translate into higher values of curvature, the same does not apply for Weibull Maximum's curves. In fact, the opposite behaviour is verified with the curvatures decreasing with the increase of $z^*$. This means that in surfaces with negatively skewed height distributions the higher summits tend to have lower values of curvature. This can be justified in knowing that in these topographies the majority of the heights distribute over a *plateau* of positive heights where shallow summits and valleys occur, with a more emphasised behaviour for lower $C$ values. Thus, on this *plateau* there is not much space for pronounced summits to stand out as heights are limited to a maximum value, for a given prescribed RMS height. Consequently, summits with smaller curvatures emerge, a fact that is also accentuated for lower values of $C$. An interesting aspect of these curves is that they have a turning region ($z^* \in [0.0,\ 0.5]$) where changes in $C$ have the opposite impact in the evolution of the expected mean curvature, independently of the spectral content. The behaviour of these curves can be divided into two distinct areas, before and after the turning region, starting at the higher value of $z^*$ and going down to lower values. Before the turning region, i.e., for the surface's higher heights, a steep increase in curvature with decreasing height is verified for all values of $C$. In this region the increase of the shape parameter $C$ increases the value of the expected mean curvature $\bar{\kappa}_m/\sqrt{m_4}$. After the turning point, for lower heights, the curvature increase rate suffers a slowdown, which corresponds to the region of the outlier summits, with less representativeness, as can be seen by the noise in the curves in this region—recall that summits at low heights are less probable in the Weibull Maximum topographies. Here the shape parameter has the opposite effect, i.e., the mean curvature decreases with $C$, and it is verified that the maximum values of relative mean curvature are obtained for lower

values of the $C$. One can also verify that for larger values of $C$ the curves become flattered, which indicates that the summits are identical at all height levels in this region. In turn, for $C = 3.602$ as $z^*$ decreases, $\bar{\kappa}_m$ values also decrease, matching the theoretical results from Nayak (1971)—the deviations occur for large heights specially due to the inherent deviations between the Weibull distribution and the standard Gaussian distribution, even for $C = 3.602$. Last, it should be remarked that the previous observations apply to all levels of spectral content analysed.

**Weibull Minimum** The Weibull Minimum expected mean curvatures (Figure 3.26) differ significantly from the previous case. These curves present near to linear behaviour with a curvature growth trend that follows the Gaussian result. It is seen a progressive increase in curvature, that recover the Gaussian results of higher summits having higher expected mean curvature—however, with distinct growth rates. These curves also present an inversion region, where the curves of different $C$ values intersect each other and change their relative position. In this case, one should assess the results from lower to higher values of $z^*$, i.e., in from left to right in the graphs of Figure 3.26. Before the turning point (lower height values) one verifies that the larger the value of $C$ the closer is the expected mean curvature to the mean surface curvature for the same $z^*$—walking towards the Gaussian case. The reasons for this occurrence are explained in the same fashion as the Weibull Maximum case since one can consider that for surfaces with a right-skewed height distribution a *plateau* of lower height value is formed, where summits tend to have lower values of curvature. This effect is lost for higher values of $C$ since the heights become more spread out and so do the summits. From the turning point up to higher values of $z^*$ the curves keep growing yet the higher the $C$ the more similar is the $\bar{\kappa}_m$ value relative to the surface's mean curvature value, measured by $\sqrt{m_4}$. Being this region dominated by outlier values, the lower the $C$ the higher and sharper the outliers summits become, justifying in this way, their superior curvature values. One can look into the Weibull Minimum's profiles of Figures 3.20 to 3.23 to better comprehend this behaviour. For lower $C$ values the larger the height of the peak, the sharper it tends to be.

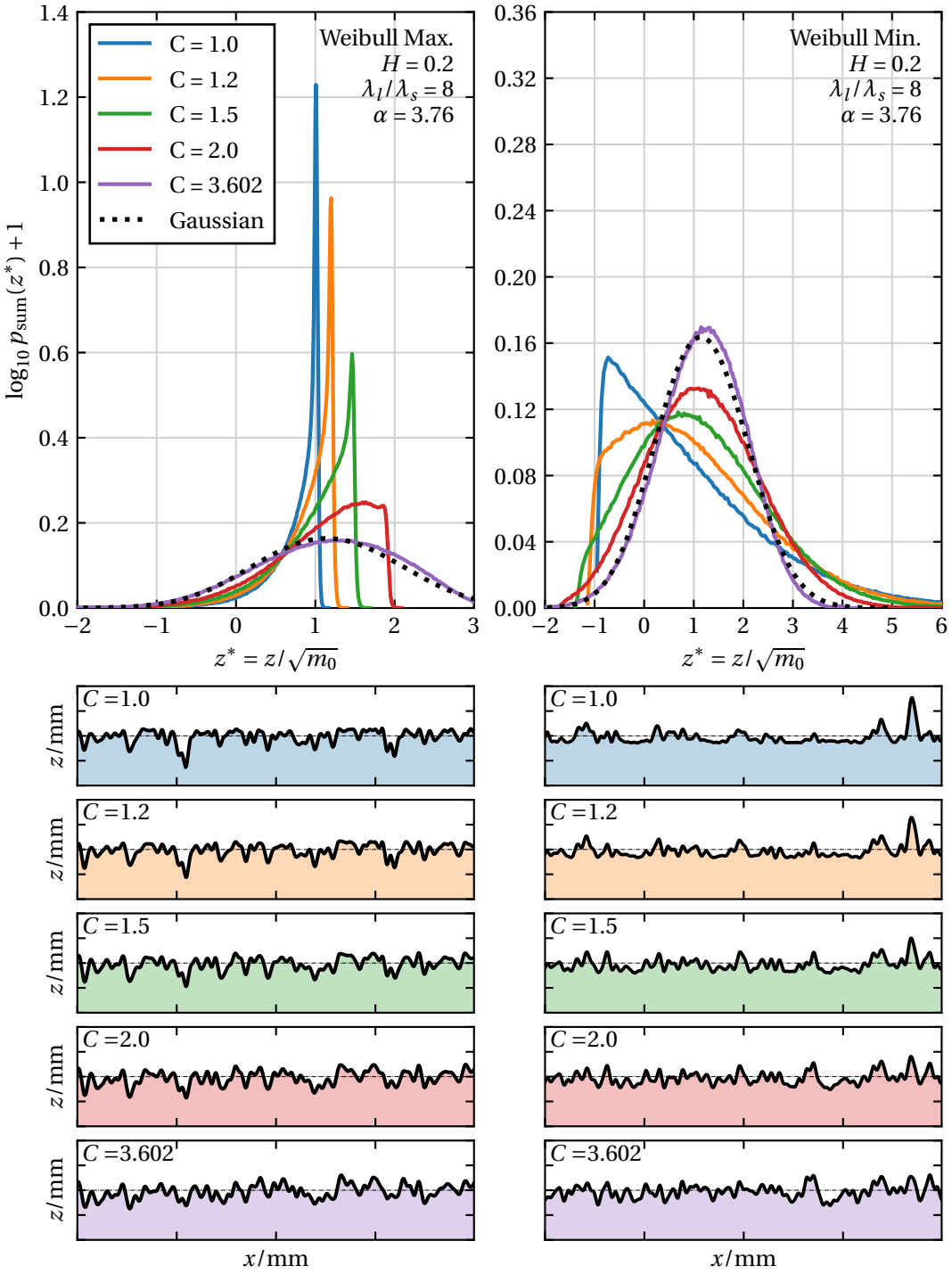


**Figure 3.20:** Influence of the shape parameter $C$ on the probability density of summit heights $p_{\text{sum}}(z^*)$ for both Weibull distributions with $H = 0.2$ and $\lambda_l/\lambda_s = 8$. For $C$ value a profile of the generated surface is presented giving a visual comprehension of the surfaces characteristics. The Gaussian results from the Nayak's Theory is presented by a dotted-black-line.

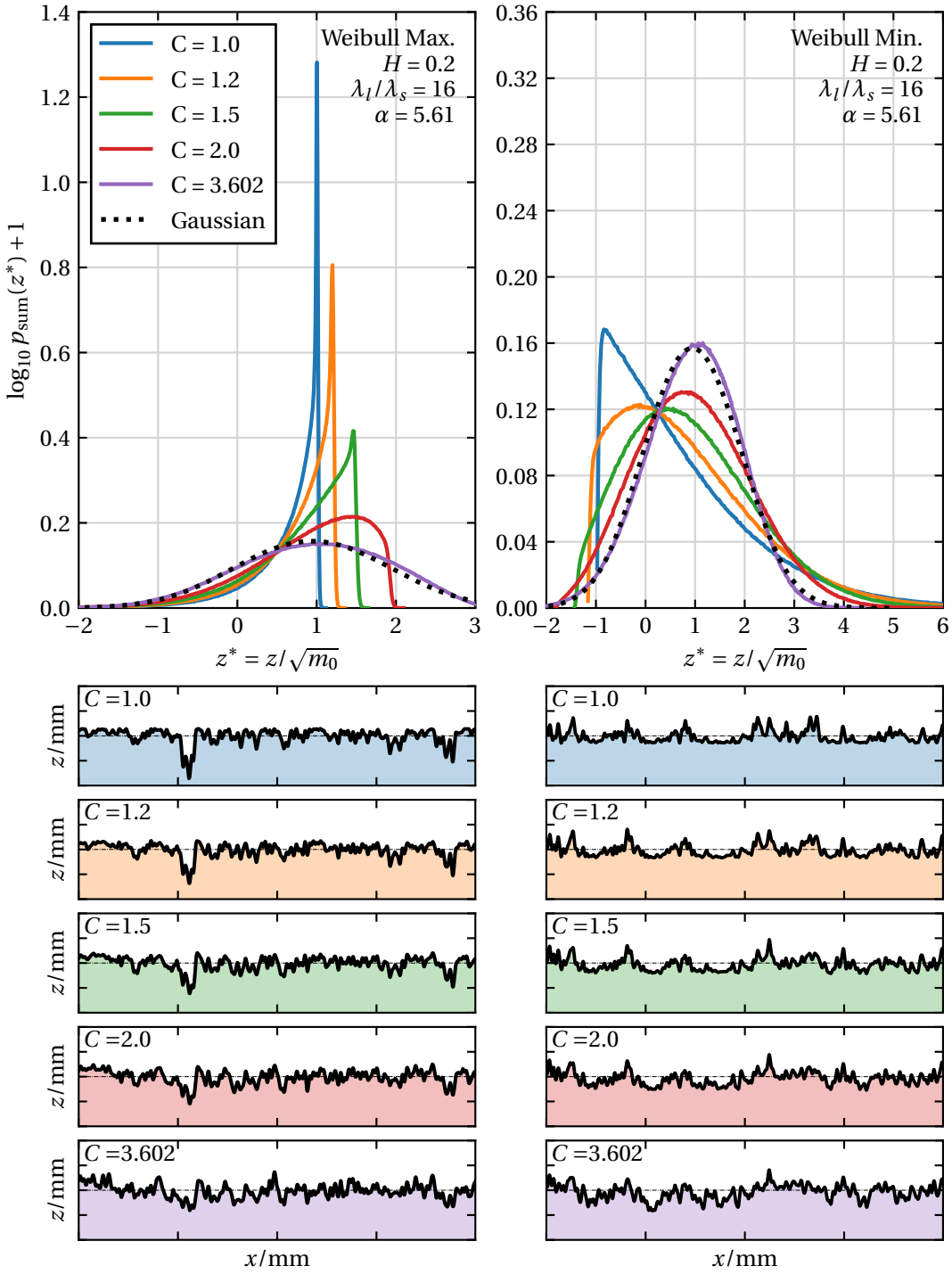


**Figure 3.21:** Influence of the shape parameter $C$ on the probability density of summit heights $p_{\text{sum}}(z^*)$ for both Weibull distributions with $H = 0.2$ and $\lambda_l/\lambda_s = 16$. For $C$ value a profile of the generated surface is presented giving a visual comprehension of the surfaces characteristics. The Gaussian results from the Nayak's Theory is presented by a dotted-black-line.

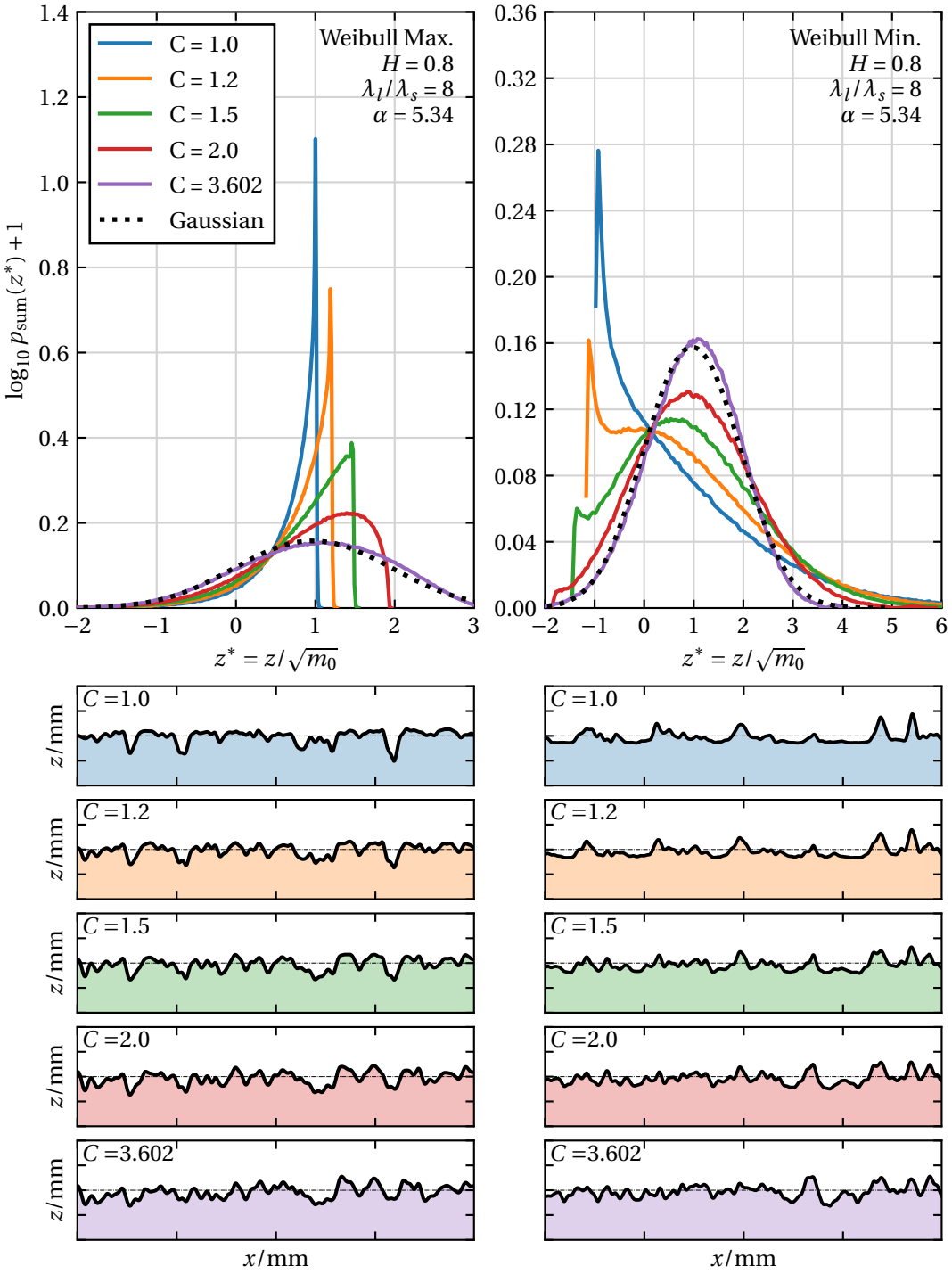


**Figure 3.22:** Influence of the shape parameter $C$ on the probability density of summit heights $p_{\text{sum}}(z^*)$ for both Weibull distributions with $H = 0.8$ and $\lambda_l/\lambda_s = 8$. For $C$ value a profile of the generated surface is presented giving a visual comprehension of the surfaces characteristics. The Gaussian results from the Nayak's Theory is presented by a dotted-black-line.

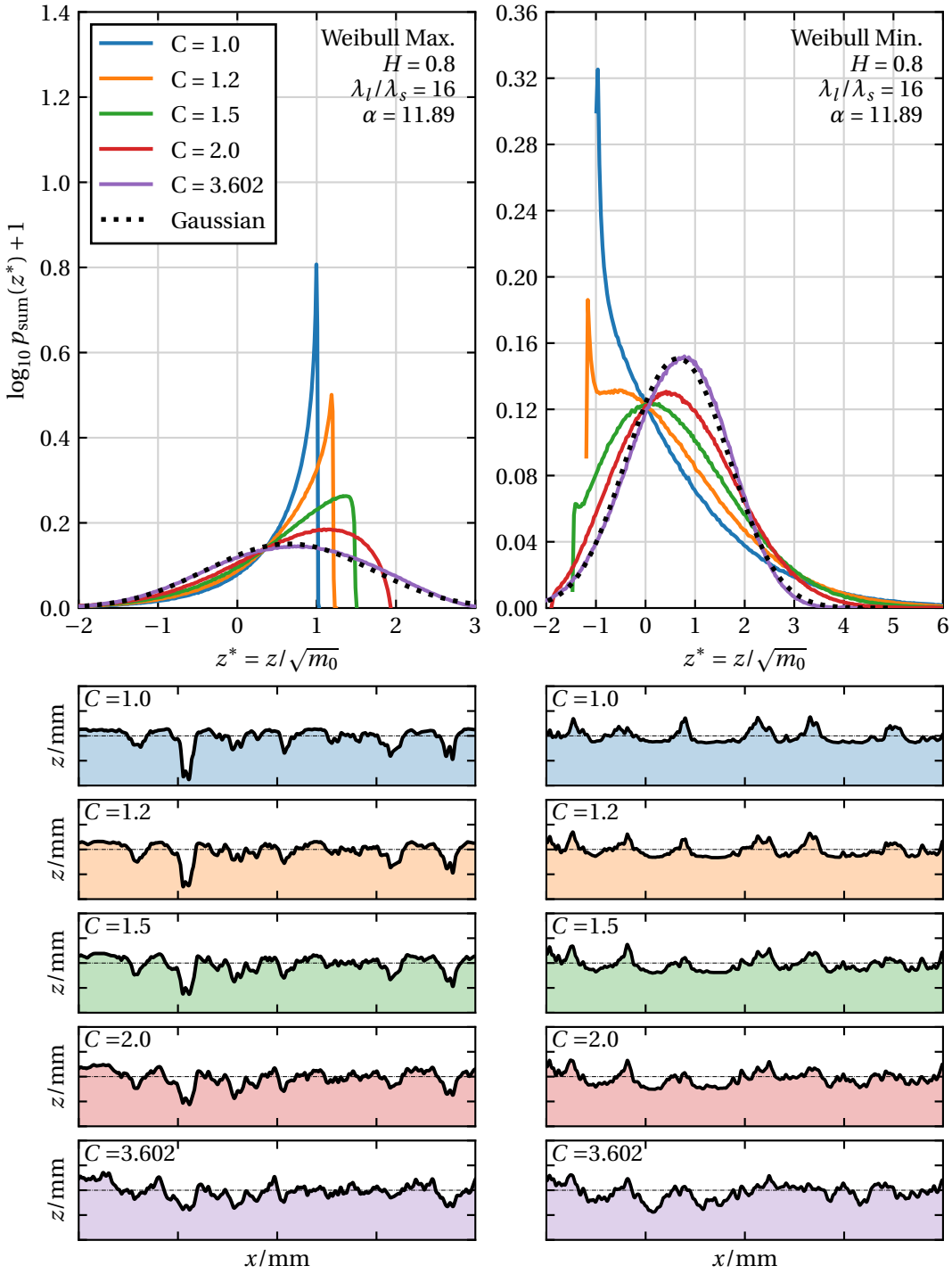


**Figure 3.23:** Influence of the shape parameter $C$ on the probability density of summit heights $p_{\text{sum}}(z^*)$ for both Weibull distributions with $H = 0.8$ and $\lambda_l/\lambda_s = 16$. For $C$ value a profile of the generated surface is presented giving a visual comprehension of the surfaces characteristics. The Gaussian results from the Nayak's Theory is presented by a dotted-black-line.

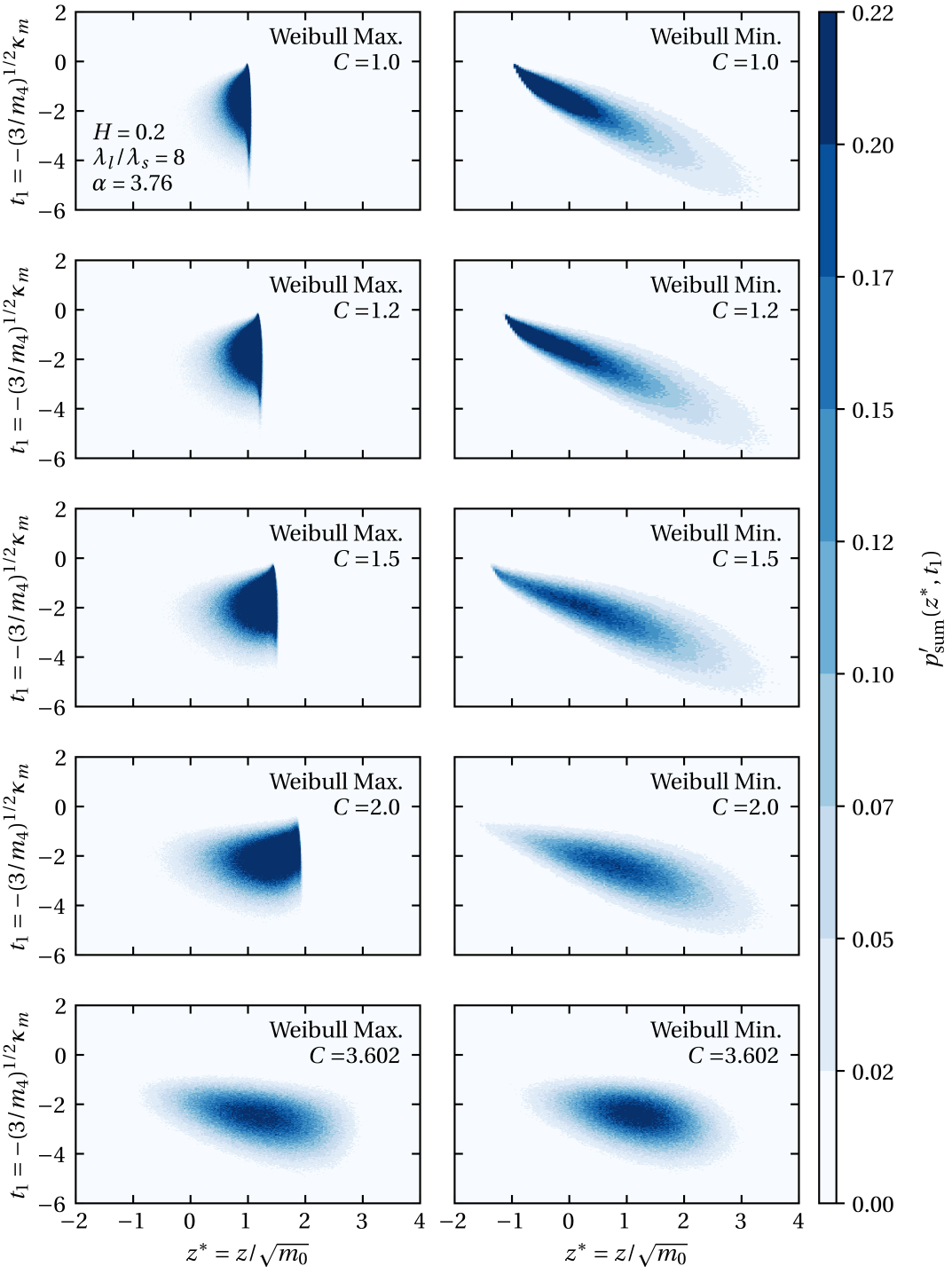


**Figure 3.24:** Influence of the shape parameter $C$ in the joint probability density function of the normalized summit heights and the equivalent mean curvature $p'_{\text{sum}}(z^*, t_1)$, recovered numerically obtained for a fixed valued $H = 0.2$ and $\lambda_l/\lambda_s = 8$

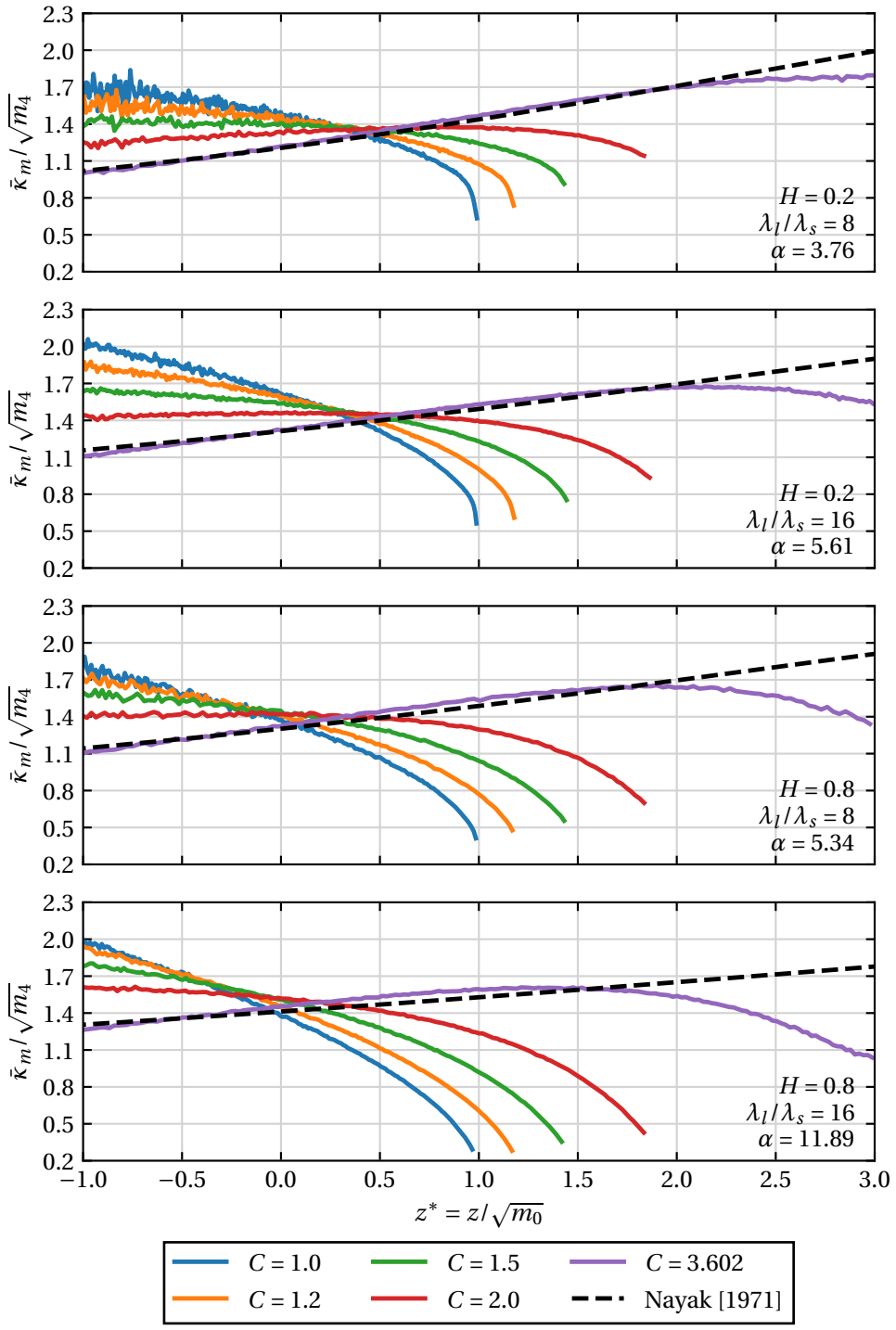


**Figure 3.25:** Influence of the shape parameter $C$ on the expected normalized mean curvature $\bar{\kappa}_m/\sqrt{m_4}$ of the Weibull maximum distribution, evaluated individually for each combination of $\lambda_l/\lambda_s$ with $H$.

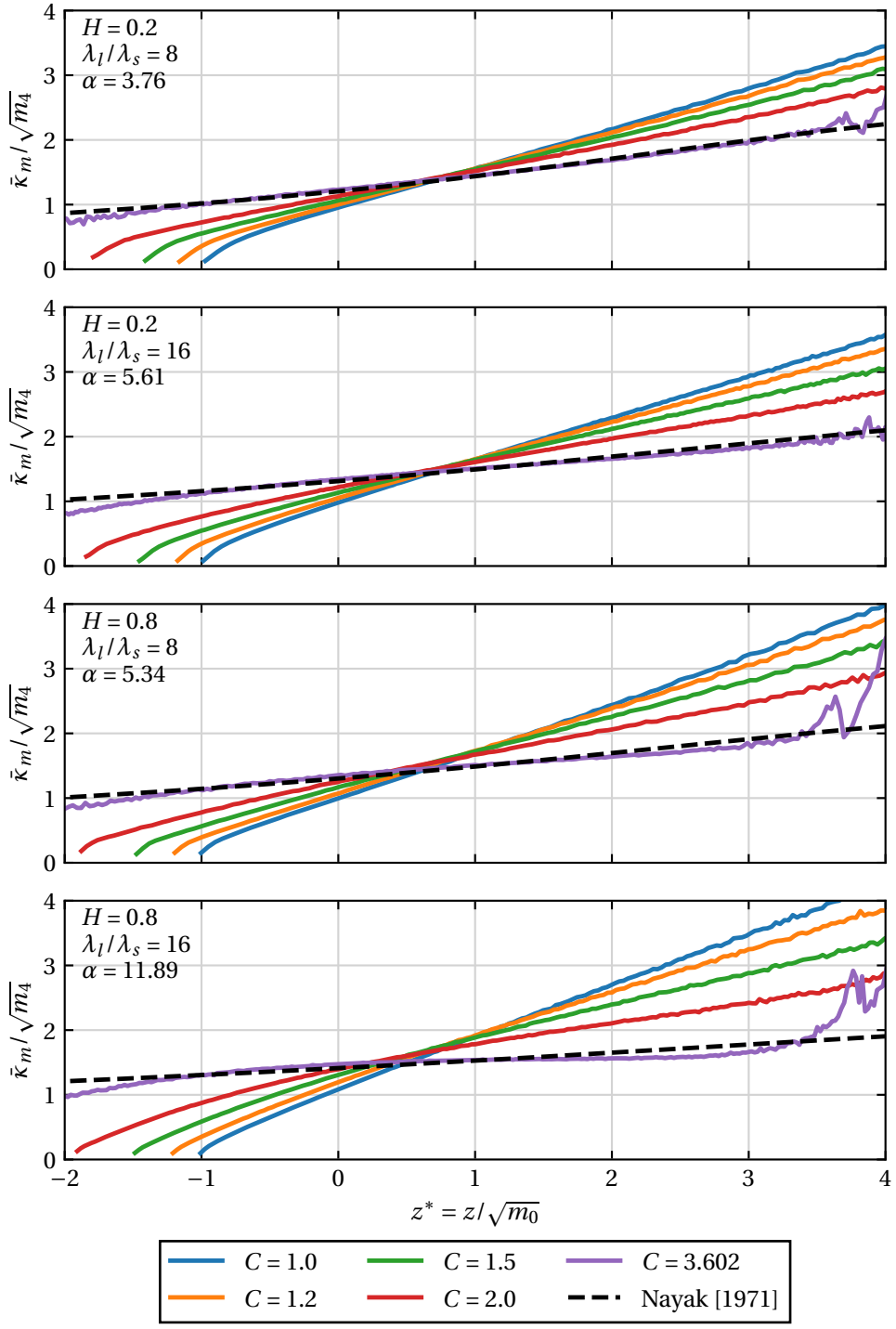


**Figure 3.26:** Influence of the shape parameter $C$ on the expected normalized mean curvature $\bar{\kappa}_m/\sqrt{m_4}$ of the Weibull minimum distribution, evaluated individually for each combination of $\lambda_l/\lambda_s$ with $H$.

**Influence of the spectral content**

Another relevant way to look at the results obtained is to study how the spectral content affects the geometry statistics in the non-Gaussian scenario. One can aggregate both the Hurst exponent $H$ and the wavelength ratio $\lambda_l/\lambda_s$ to characterize the surface spectral content—each pair of the previous variables corresponds to one value of Nayak's parameter. By fixing a value of $C$ for each Weibull distribution and varying the spectrum-related variables it is possible to visualise the results along a distinct dimension and drawn different conclusions.

**Probability density of summit heights** The one-dimensional histograms of the probability density of summits heights are present from Figure 3.27 to Figure 3.31, from the value of $C = 3.602$ down to $C = 1$. The results are presented in a descending order of $C$ as it eases the analysis. Unlike the previous section, the vertical scales are now adjusted to each particular $C$ value in order to favour a relative comparison between curves with different spectral properties.

**Weibull Maximum** The impact of the spectral content on the Weibull Maximum's histograms can be more easily perceived if one starts from the near to Gaussian case and goes into more left-skewed height distributions (lower values of $C$). By looking at the case of $C = 3.602$ (Figure 3.27), the classical behaviour predicted by Nayak (1971) is verified and one sees that as $\alpha$ increases, the mode shifts to the left and the peak probability density reduces—cf. Figure 3.1. In general, it can be said that the higher the value of the Nayak's parameter the closer to the surface's height distribution $p_{\text{sum}}(z^*)$ gets. The same behaviour is seen for other shape parameters as well, even though a wide range of $\alpha$ could not be explored, due to excessive computational cost. The $C = 2$ case (Figure 3.28) shows the same relation, with a more evidenced predominance of summits at the higher height levels—a consequence already discussed above. This effect is amplified by the decrease of the $C$ until it reaches the lower value of $C = 1$. Globally speaking, one verifies that Nayak's parameter $\alpha$ has a strong influence on $p_{\text{sum}}(z^*)$. On the one hand, it is verified that the histogram with $\alpha = 3.76$ is the one with higher mode value and also the most left-skewed, for any $C$ case—possibly with the exception of $C = 1$ where it comes in second yet with only a small difference. On the other hand, independently of the shape parameter, the histogram of $\alpha = 11.89$ is the one that shows the less left-skewed distribution with a small mode value. This case is also the one that presents more similarity with the height distribution, as presented in Figure 3.15. Contrary to the Gaussian case, where the topography statistics are only dependent on $\alpha$, here the Nayak's parameter appears to be insufficient to fully characterise the statistical geometry of the rough surfaces, especially for lower $C$ values. This can be seen, for example, in Figure 3.31, as the curves for two identical Nayak's parameter values ($\alpha = 5.61$ and $\alpha = 5.34$) are distinct.

**Weibull Minimum** For the Weibull Minimum summit heights distributions, similar results are captured yet with the opposite tendency, with more predominant values of probability for lower values of height, as was already observed in the previous section. Starting with $C = 3.602$ (Figure 3.27), the detected relations are also close to the Gaussian case with the distributions being placed according to Nayak's theory. With the increase

of the shape parameter and the distribution starts to get more right-skewed due to the presence of more summits at lower heights alongside higher outliers. Additionally, the Gaussian case tendency for having larger probability density in higher summits with the decrease of $\alpha$ is also verified. At the same time, the probability density of low-height summits increases with the increase of $\alpha$. For instance, if one looks at the case where $C = 1.5$ (Figure 3.29), it is possible to see that $\alpha = 3.76$ shows smaller probability of having lower summits heights, while $\alpha = 11.89$ showcases higher probability density for smaller heights. This is explained because the higher the $\alpha$ the more summits will occur at all heights—ultimately leading to the case where the summits heights distribution fits the height distribution of the topography. Since, summits are more likely to happen at higher heights, increasing the spectral content makes possible the occurrence of summits for lower height values thus pushing the summits height distribution to the left—the presence of summits with lower heights in the topography grows. In this case, a characterization solely based on Nayak's parameter may be insufficient, since dependence on the Hurst exponent can be observed. For example, when $C = 1.2$ and $C = 1$ (Figure 3.30 and 3.31), the histogram shapes can be distinguished by Hurst value, even when $\alpha$ is identical. While for $H = 0.2$ the distribution is smooth, for $H = 0.8$ it has a prominent maximum value of probability towards small heights. This indicates that higher values of $H$ lead to surfaces with a higher concentration of lower height summits, despite the Nayak parameter similar value.

**Expected mean curvature** In the previous section it was seen that, despite being an important result to have at hand, the joint probability distribution of normalized height and respective equivalent mean curvature $p'_{\text{sum}}(z^*, t_1)$ does not provide an easier method to assess the summits' curvature response. The expected mean curvature $\bar{\kappa}_m$, computed from $p'_{\text{sum}}(z^*, t_1)$, was used as a much more simple tool to analyse the curvature results. Therefore, in what follows, the $p'_{\text{sum}}(z^*, t_1)$ was omitted, for the sake of clarity, and the results based on $\bar{\kappa}_m/\sqrt{m_4}$ are presented instead. In Figure 3.32 and Figure 3.33 the normalized expected mean curvature curves are shown for the shape parameter cases up to $C = 2$.

**Weibull Maximum** Starting by the Weibull Maximum (Figure 3.32), one verifies that the non-linear behaviour previously advanced is seen yet, for larger $C$ values, the curves become flattered with a smaller tendency for curvature increasing for lower values of $z^*$. For higher heights one verifies that the $\alpha$ still play an important role, with higher $\bar{\kappa}_m/\sqrt{m_4}$ values being achieved by the $\alpha = 3.76$ curve. This means that topographies with lower $\alpha$ tend to have higher expected mean curvatures, relatively to the surfaces global curvature value, measured by $\sqrt{m_4}$. However, this relation is affect by the combination between the spectral properties as one verifies that the curve of $\alpha = 5.61$ has a greater $\bar{\kappa}_m/\sqrt{m_4}$ value than $\alpha = 5.34$, contradicting the exclusive $\alpha$ dependence hypothesis. This happens because of the different $H$ values, which might play a more influential role in this type of non-Gaussian topographies. It is seen, for higher height summits, the curves with the same value of $H$ tend to become closer, contradicting the ordering of the curves by $\alpha$ value. For lower heights, the relative position of the curves is inverted, i.e, the higher the $\alpha$ the higher the value of $\bar{\kappa}_m/\sqrt{m_4}$. Nonetheless, due to the lack of representation of

lower height summits in these types of topographies the relations between the curves become less explicit, especially for lower values of $C$.

**Weibull Minimum** One can then look into the Weibull Minimum results of expected mean curvature $\bar{\kappa}_m$. By grouping, the curves for the same $C$ values the linear behaviour is even more evidenced. For the lower values of height, proximity between all the different curves is obtained, suggesting a small dependency on the spectral content in this region. The opposite is verified as $z^*$ increases, where the spectral content becomes relevant with $H$ getting particular importance in the behaviour, as explained in the ongoing paragraph. One sees that surfaces with higher spectral content tend to have larger deviations to the global mean curvature of the rough surface—the summit curvature grows faster with summit height. Furthermore, the changes in the expected mean curvature with varying spectral content increase with the decrease of $C$. The reason underlying this behaviour has to do with the increase of the frequency content, which tends to produce more summits at all heights with large curvatures, relatively to the surface global curvature. The presented curve seems to not be only dependent on Nayak's parameter as it is seen in Gaussian topographies. In fact, both wavelength ratio $\lambda_l/\lambda_s$ and the Hurst exponent $H$ seem to interact with each other different, creating different results that do not always seem to be in tune with the $\alpha$ value. For instance, one verifies that for higher values of $z^*$, curves with the same $H$ tend to become closer and, for a given value of $\lambda_l/\lambda_s$, a notable variation in the curvatures is seen if the $H$ value is changed. To illustrate this phenomenon in Figure 3.34 the $C = 1.2$ case is explored in detail, plotting the results of the combination of wavelengths ratios $\lambda_l/\lambda_s$ of 8 and 16 with the Hurst exponents of 0.2, 0.5 and 0.8. [9] One sees that for a particular value of $\lambda_l/\lambda_s$ the Hurst exponent can increase or decrease the slope of the curves. Additionally, it is seen that apart from the maximum $\alpha = 11.89$ and the minimum $\alpha = 3.76$, the curves do not have a clearly defined order, with several curves intersecting each other. In fact, if one considers the regions of the curves with the same value of $\lambda_l/\lambda_s$, it is seen that both $\lambda_l/\lambda_s = 8$ and $\lambda_l/\lambda_s = 16$ areas also intersect, highlighting the more intertwined relation of the spectral variables. Finally, one should also note that, in Figure 3.33, an approximation of the curves with the increase of the $C$ value is also observed. Such behaviour occurs due to a larger similarity between the summits heights distribution (cf. Figure 3.28, for example), approximating the expected mean curvature at each $z^*$.

[9] The $H = 0.5$ was generated in particular for this example to add some more information.

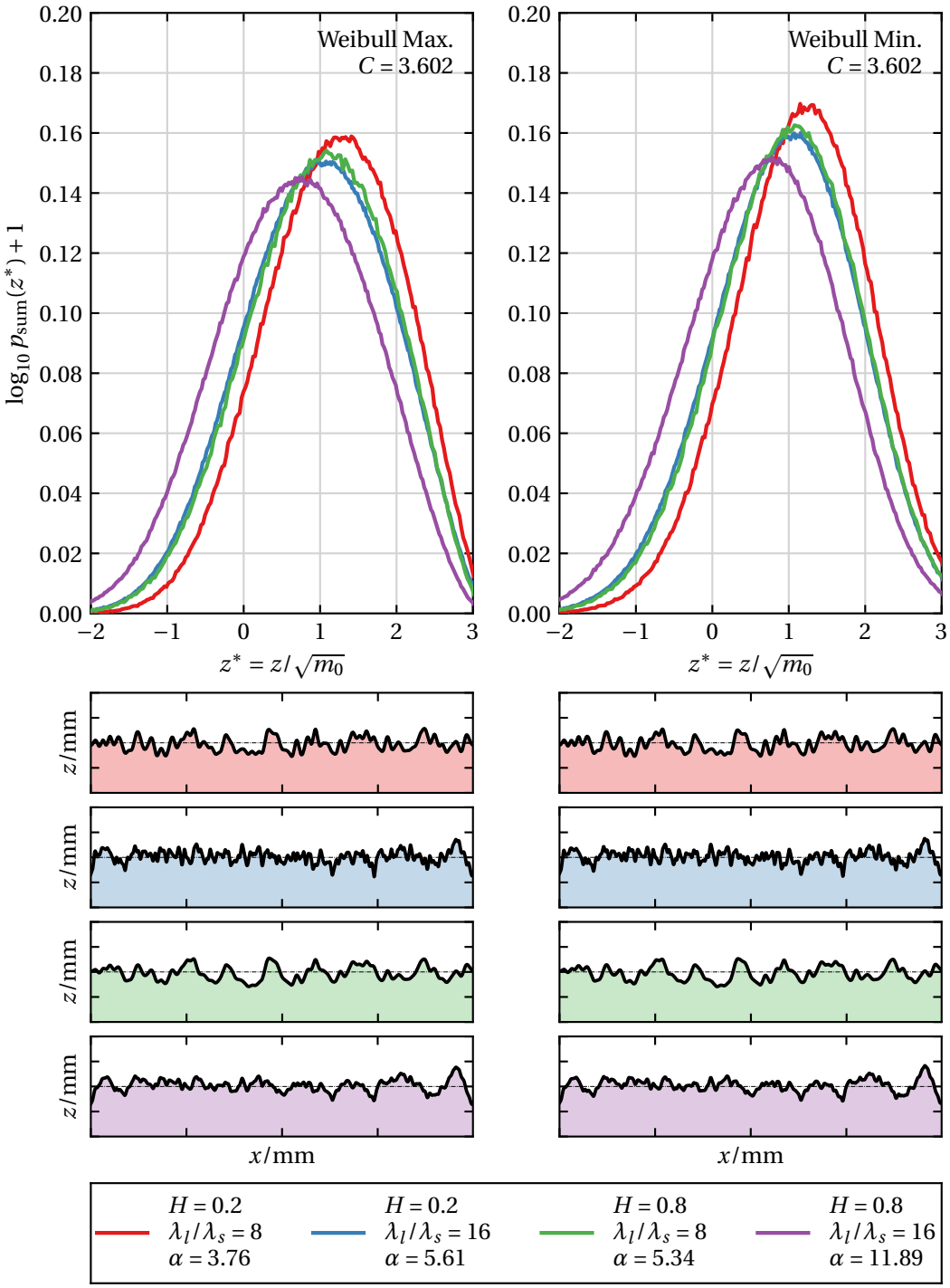


**Figure 3.27:** Influence of the spectral properties ($\lambda_l/\lambda_s$ and $H$) on the probability density of summit heights $p_{\mathrm{sum}}(z^*)$ for both Weibull distributions with a shape parameter of $C = 3.602$. For each pair of $\lambda_l/\lambda_s$ and $H$ a profile of the generated surface is presented giving a visual comprehension of the surfaces characteristics.

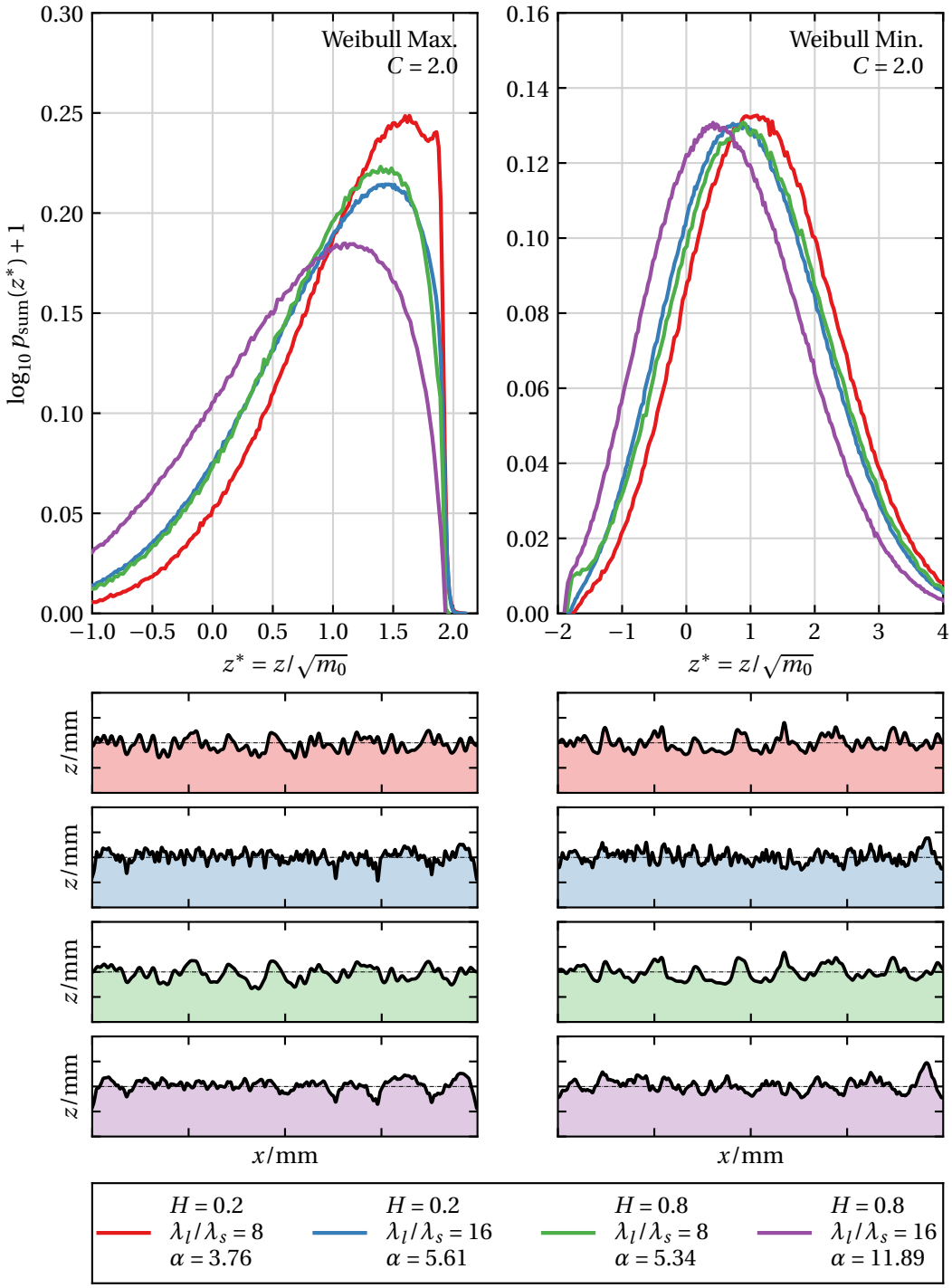


**Figure 3.28:** Influence of the spectral properties ($\lambda_l/\lambda_s$ and $H$) on the probability density of summit heights $p_{\text{sum}}(z^*)$ for both Weibull distributions with a shape parameter of $C = 2$. For each pair of $\lambda_l/\lambda_s$ and $H$ a profile of the generated surface is presented giving a visual comprehension of the surfaces characteristics.

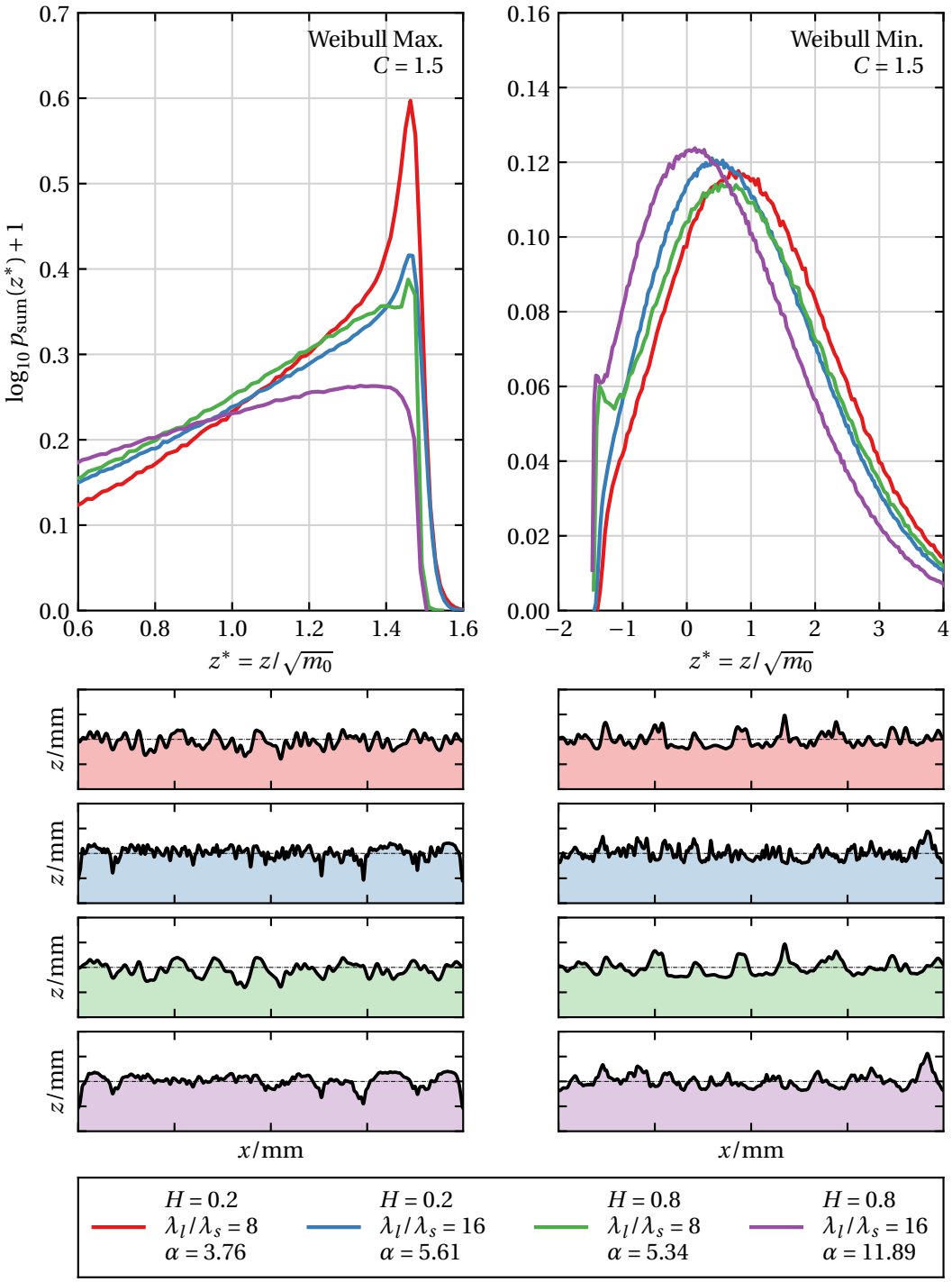


**Figure 3.29:** Influence of the spectral properties ($\lambda_l/\lambda_s$ and $H$) on the probability density of summit heights $p_{\mathrm{sum}}(z^*)$ for both Weibull distributions with a shape parameter of $C = 1.5$. For each pair of $\lambda_l/\lambda_s$ and $H$ a profile of the generated surface is presented giving a visual comprehension of the surfaces characteristics.

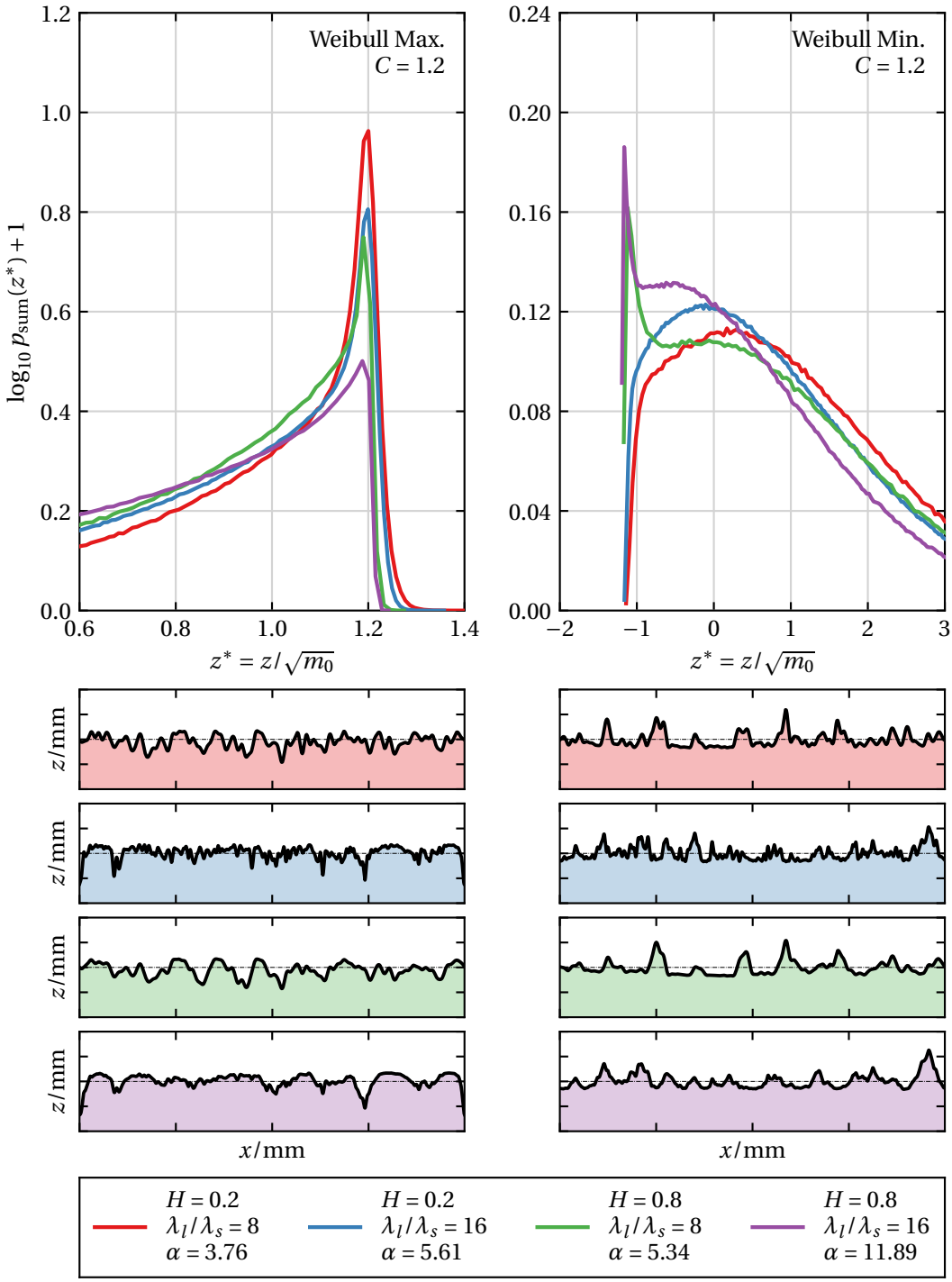


**Figure 3.30:** Influence of the spectral properties ($\lambda_l/\lambda_s$ and $H$) on the probability density of summit heights $p_{\mathrm{sum}}(z^*)$ for both Weibull distributions with a shape parameter of $C = 1.2$. For each pair of $\lambda_l/\lambda_s$ and $H$ a profile of the generated surface is presented giving a visual comprehension of the surfaces characteristics.

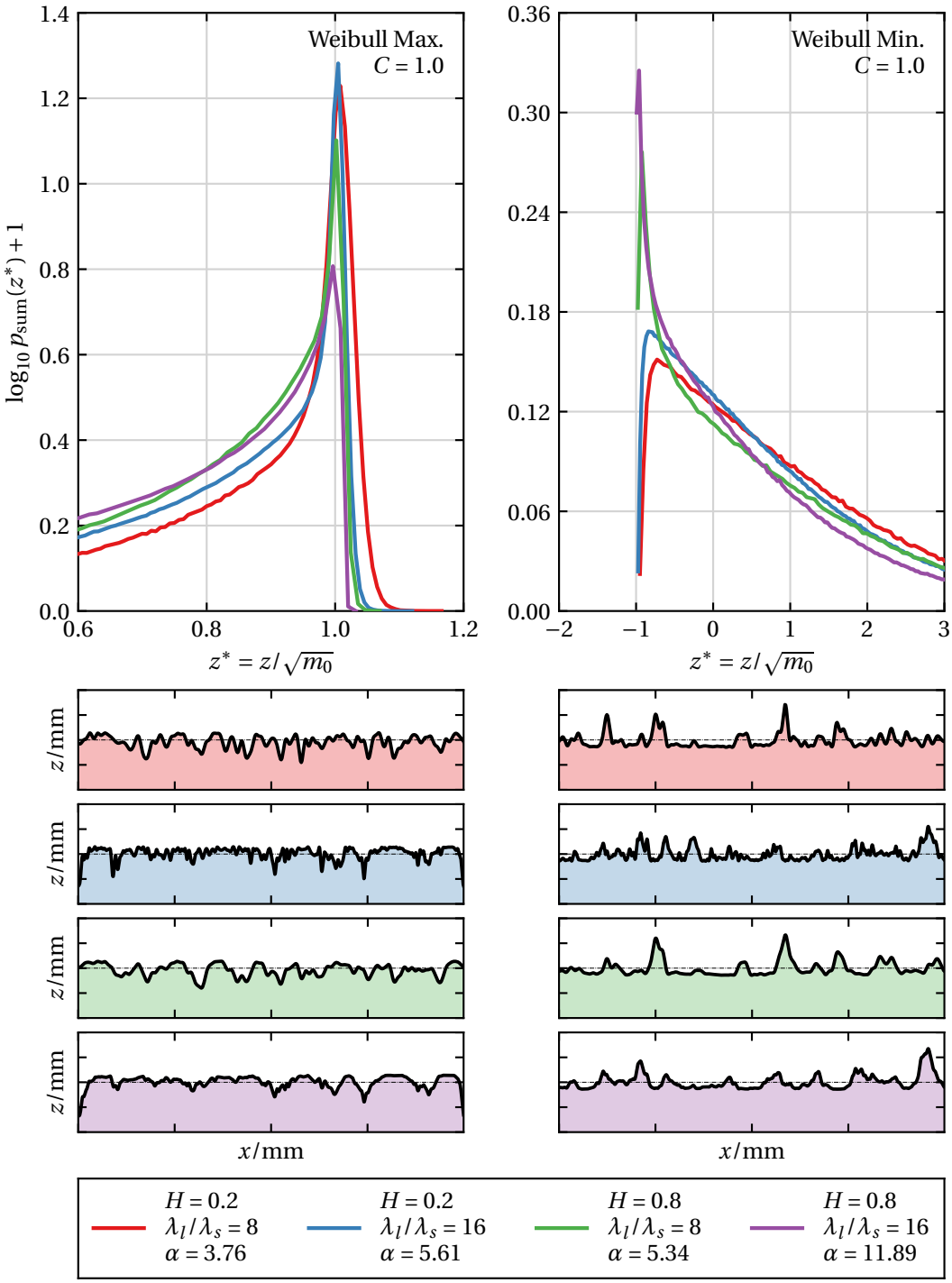


**Figure 3.31:** Influence of the spectral properties ($\lambda_l/\lambda_s$ and $H$) on the probability density of summit heights $p_{\mathrm{sum}}(z^*)$ for both Weibull distributions with a shape parameter of $C = 1$. For each pair of $\lambda_l/\lambda_s$ and $H$ a profile of the generated surface is presented giving a visual comprehension of the surfaces characteristics.

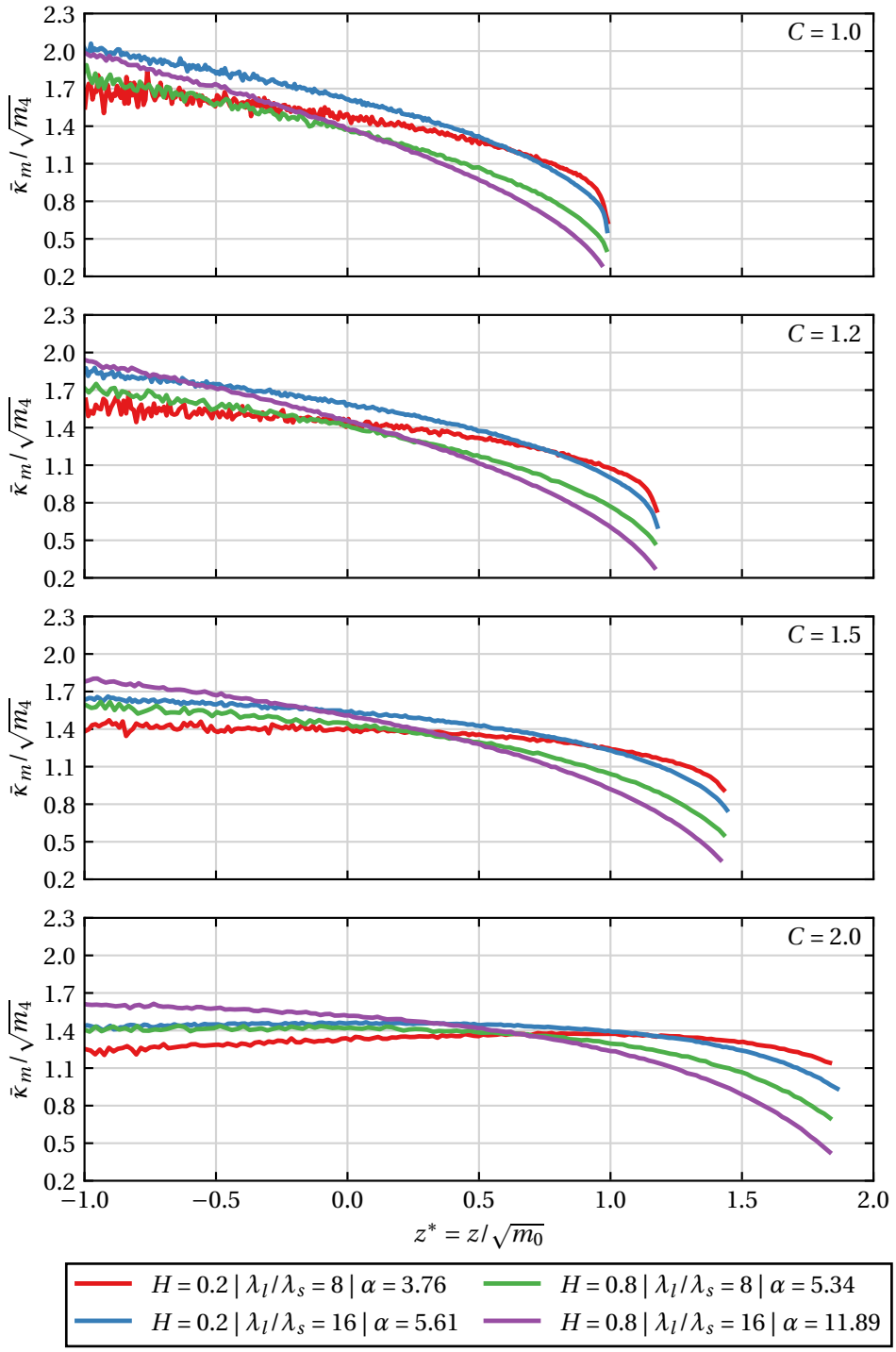


**Figure 3.32:** Influence of the spectral content on the expected normalized mean curvature $\bar{\kappa}_m/\sqrt{m_4}$ of the Weibull maximum distribution, evaluated individually for each case of the shape parameter $C$.

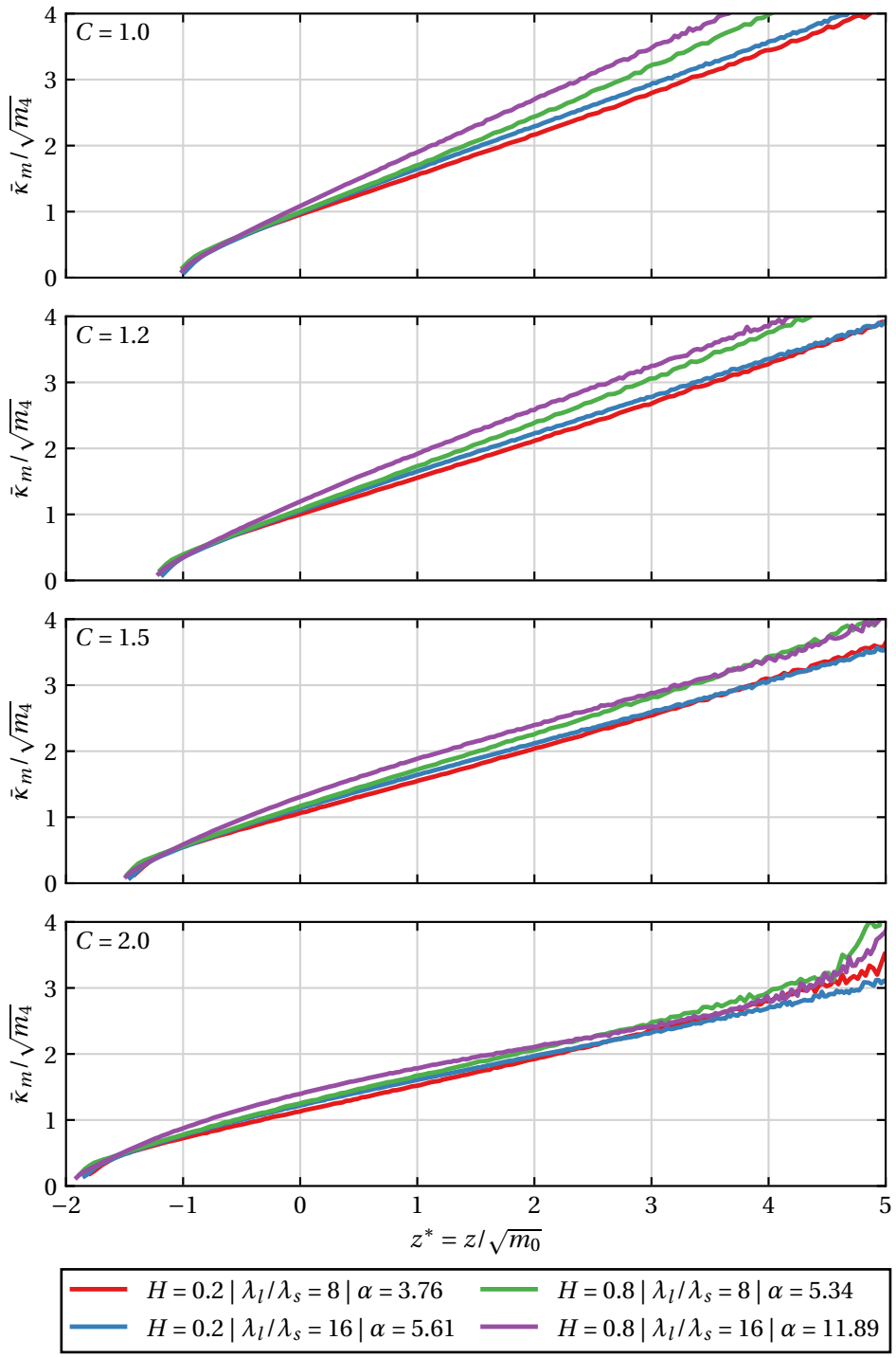


**Figure 3.33:** Influence of the spectral content on the expected normalized mean curvature $\bar{\kappa}_m/\sqrt{m_4}$ of the Weibull minimum distribution, evaluated individually for each case of the shape parameter $C$.

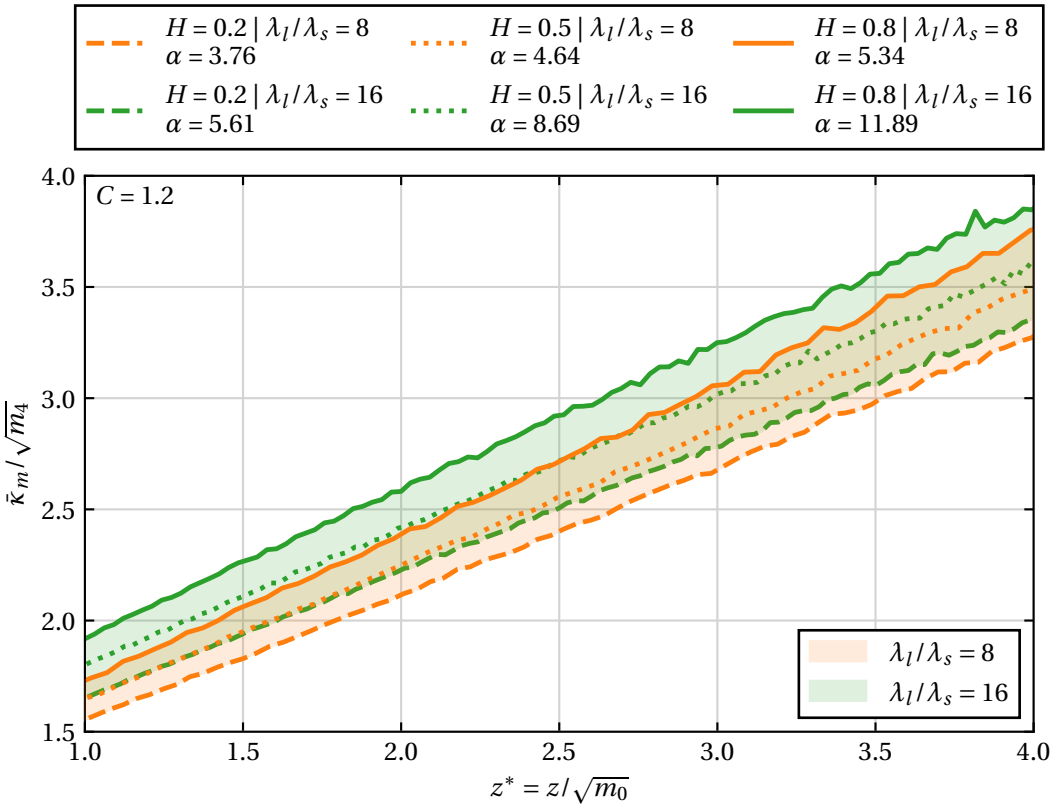


**Figure 3.34:** Influence of the Hurst exponent on the on the expected normalized mean curvature $\bar{\kappa}_m/\sqrt{m_4}$ of the Weibull minimum distribution, evaluated for $C = 1.2$. The results are plotted are a combination of the wavelengths ratios $\lambda_l/\lambda_s$ of 8 and 16 with the Hurst exponents of 0.2, 0.5 and 0.8.

**Density of summits**

An additional interesting quantity to analyse is the previously introduced density of summits $D_{\text{sum}}$ (cf. Equation (3.3)). This parameter gives the number of summits per unit of area and has an independent influence on physical phenomena involving rough contact. More summits may originate more contact clusters that might influence the way the real contact area evolves with the and external force. The computation of this quantity is trivial since it consists in storing the number of summits detected per surface and dividing by the sum of the areas of all the inspected topographies. The procedure was done for each of the 40 cases studied and the results are present in Figure 3.35. In this figure, the density of summits $D_{\text{sum}}$ is present as a function of the shape parameter for both Weibull distributions and all the spectral cases studied. One verifies that Weibull Maximum topographies tend to have more summits per area than the opposite case Weibull Maximum. This difference is augmented by lower values of the shape parameter, where the discrepancies between both Weibull distributions are higher. It can also be observed the number of summits tends to decrease with the increase of the shape parameter $C$. Furthermore, the spectral content seems to play have a meaningful impact on $D_{\text{sum}}$. With the increase of the wavelength ratio, $\lambda_l/\lambda_s$ an increase in the number of summits is verified, which is an expected result since with the addition of higher frequencies to the topography more summits are likely to happen. Similarly, the decrease of the Hurst exponent value is seen to increase the number o summits per unit of area. This can also be simply explained by the fact that lower values of $H$ means that a bigger preponderance is given to the higher frequencies on the PSD, which directly translates to a more fulfilled surface, where summits are more expected to happen (cf. Figure 2.11).

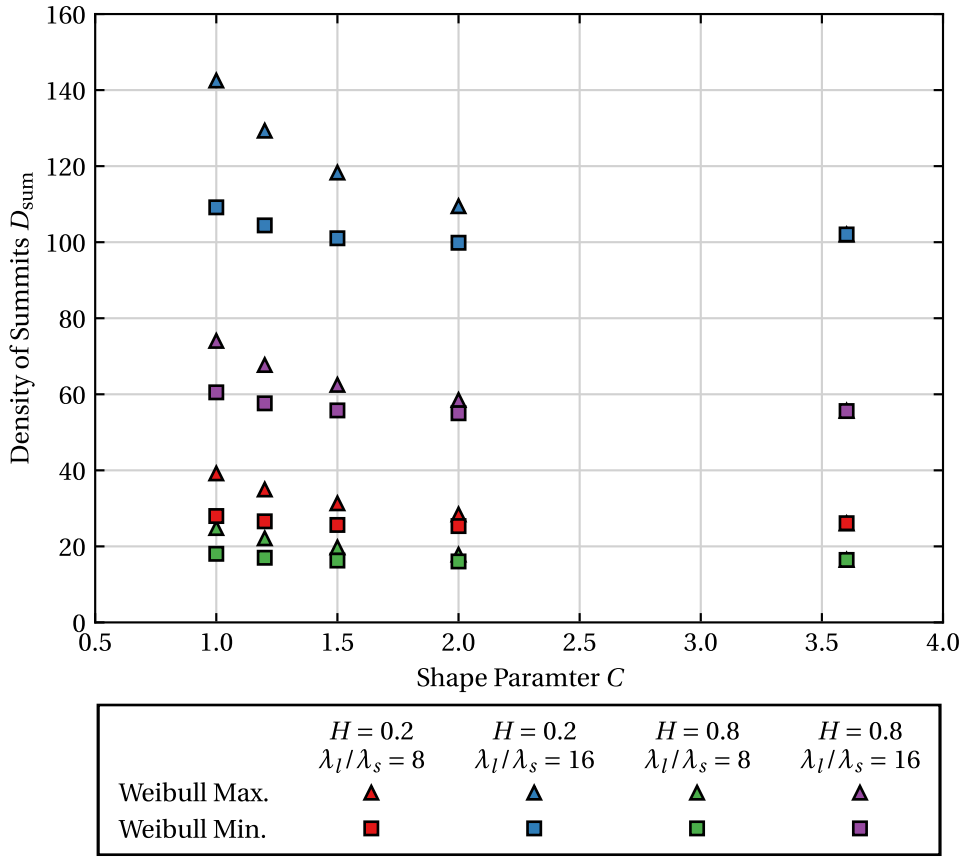


**Figure 3.35:** Density of summits per unit of area as a function of the shape parameter $C$ for both Weibull distributions in all the spectral scenarios.

### 3.2.5 On the Nayaks's parameter accuracy for characterizing the statistics of non-Gaussian rough surfaces

In the previous section, it was seen that the topography statistics are strongly affected by the spectral content. The approach pursued characterizing the spectral properties were the Hurst exponent $H$, the wavelength ratio $\lambda_l/\lambda_s$ and the ensuing Nayak's parameter $\alpha$. For Gaussian surfaces, the topography statistics are only dependent on $\alpha$, as it was obtained by Nayak (1971) and presented in Section 3.1.1. This result is very convenient yet as it allows the characterization based on only one parameter that aggregates all the information on the rough surface power spectrum. The previously discussed results showed some intriguing aspects that suggest the possibility of non-Gaussian statistics not being fully characterized by just one parameter—in addition to the PDF parameterisation, here by means of $C$. It was observed that for similar values of $\alpha$, the statistics obtained may be significantly different. This behaviour has raised the question if is the Nayak's parameter is sufficient for describing rough surfaces, or if the Hurst exponent and spectral bandwidth have independent effects on the topography statistics. Therefore, for testing the validity of the Nayak's parameter $\alpha$ as a unique parameter for characterizing the statistics of rough surfaces, a study on the impact of the Hurst exponent for a fixed value of $\alpha$ was carried out. The goal is to investigate how the Hurst exponent may affect the statistical geometry of non-Gaussian topographies that are characterized by the same value of $\alpha$.

One should start by relating the spectral properties that characterize a random rough surface, and therefore an analytical expression for the Nayak's parameter $\alpha$ may be recovered. The power spectral density of a self-affine rough surface, given by Equation (2.51), can be written in its discrete version as

$$\hat{\Phi}\left[\boldsymbol{k}=\left(\frac{q}{M}\Omega_{s_y},\, k=\frac{p}{N}\Omega_{s_x}\right)\right]=\begin{cases}\hat{C}_0 & , \quad k_l \le \|\boldsymbol{k}\| < k_s \\ \hat{C}_0\left(\dfrac{k_r}{\|k\|}\right)^{2(H+1)} & , \quad k_r \le \|k\| \le k_s \\ 0 & , \quad \text{elsewhere}\,, \end{cases} \tag{3.35}$$

being $\hat{C}_0$ the discrete surface scale constant. The discrete version of the PSD relates with the continuous one by

$$\hat{\Phi}[p,q]=\frac{1}{l_{s_x}l_{s_y}}\Phi\left(\frac{q}{N}\Omega_{s_x},\,\frac{p}{M}\Omega_{s_y}\right), \quad \begin{cases} p=0,1,...,M/2 \\ q=0,1,...,N/2 \end{cases} . \tag{3.36}$$

Using this result with the spectral moment definition (Equation (2.33)), the analytical

expressions for rough surfaces spectral moments and Nayak's parameter come

$$m_{00} = \frac{l_{s_x} l_{s_y} \hat{C}_0 k_r^2}{2\pi} \left( \frac{1-\xi^2}{2} + \frac{1-\zeta^{-2H}}{2H} \right); \tag{3.37a}$$

$$m_{20} = \frac{l_{s_x} l_{s_y} \hat{C}_0 k_r^4}{4\pi} \left( \frac{1-\xi^4}{4} + \frac{\zeta^{2-2H}-1}{2-2H} \right); \tag{3.37b}$$

$$m_{40} = \frac{3 l_{s_x} l_{s_y} \hat{C}_0 k_r^6}{16\pi} \left( \frac{1-\xi^6}{6} + \frac{\zeta^{4-2H}-1}{4-2H} \right); \tag{3.37c}$$

$$\alpha = \frac{3}{2} \left( 1-\xi^2 + \frac{1-\zeta^{-2H}}{H} \right) \left( \frac{1-\xi^6}{3} + \frac{\zeta^{4-2H}-1}{2-H} \right) \Big/ \left( \frac{1-\xi^4}{2} + \frac{\zeta^{2-2H}-1}{1-H} \right)^2 . \tag{3.37d}$$

One should note that when only the fractal part of the spectrum is considered, i.e, when $k_r = k_l$, one can rewrite the ratios as $\xi = 1$ and $\zeta = \lambda_l/\lambda_s$ and the analytical expressions for Nayak's parameter of profiles and surfaces can be simplified and the ratio $\xi$ is dropped from Equation (3.37d). Following the study of surfaces' statistics one can write the final relation between the $\alpha$, $H$ and $\lambda_l/\lambda_s$

$$\alpha = \frac{3}{2} \left( \frac{1-(\lambda_l/\lambda_s)^{-2H}}{H} \right) \left( \frac{(\lambda_l/\lambda_s)^{4-2H}-1}{2-H} \right) \Big/ \left( \frac{(\lambda_l/\lambda_s)^{2-2H}-1}{1-H} \right)^2 . \tag{3.38}$$

This expression can then be used to compute $\alpha$ as a function of $H$ and $\lambda_l/\lambda_s$. In Figure 3.36 this relation is plotted, showing that $\alpha$ increase with the increase of both $H$ and $\lambda_l/\lambda_s$. The evolution has an exponential-like character starting with a soft growth followed by a steep rise of $\alpha$ for higher values of both variables. From this representation, it can also be deduced that for each value of $\alpha$ there is an infinite number of combinations of $H$ and $\lambda_l/\lambda_s$ that result in a given $\alpha$.

In this study, the effect of the Hurst exponent $H$ for a given $\alpha$ on the statistics of the topography is examined. By numerically solving the Equation (3.38) in order to $\lambda_l/\lambda_s$, one can obtain the complementary value that for a given $H$ corresponds to the prescribed Nayak's parameter. With this procedure values of $H$ and $\alpha$ can be defined to perform a numerical study on the topography's statistics response. Here, three different values of each were chosen. The respective $\lambda_l/\lambda_s$ computed for each pair of $\alpha$ and $H$ are presented in Table 3.5. The rapid growth of $\lambda_l/\lambda_s$ for lower values of $H$ should not be overlooked, since surfaces with large bandwidth require more computational time. The same discretization, length and number of realizations were kept the same as in the former numerical studies. In the previous section, it was seen that the relative behaviour of the spectral properties is very similar for a certain value of the shape parameter $C$—cf. Figure 3.32 as an example. For this reason within this study, only one value of $C$ was studied for both Weibull Maximum and Minimum distribution. Since the concern is on the characterization of the spectral content of non-Gaussian surfaces the extreme value $C = 1$ was selected.

The captured results follow the same structure as the previous sections. Starting with the probability density of the summit heights $p_{\text{sum}}(z^*)$ the obtained results are presented in Figure 3.37 and Figure 3.38 for both Weibull Maximum and Minimum distributions, respectively. The Weibull Maximum histograms show some interesting differences that

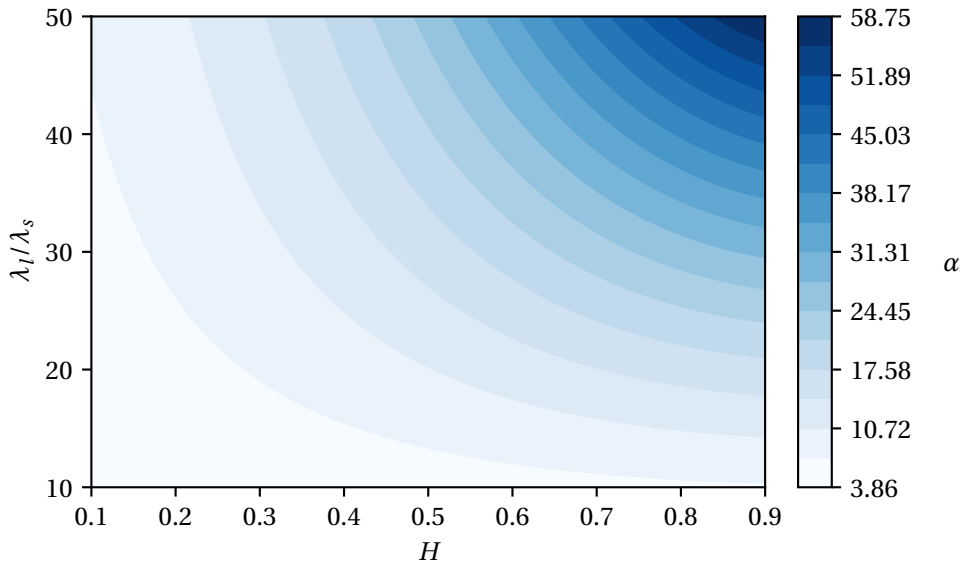


**Figure 3.36:** Influence of the Hurst exponent $H$ and the wavelength ratio $\lambda_l/\lambda_s$ on the Nayak's parameter $\alpha$, for self-affine rough surfaces with $k_r = k_l$.

**Table 3.5:** Studied values of Hurst exponent $H$ and the Nayak's parameter $\alpha$, and respective computed wavelength ratio $\lambda_l/\lambda_s$.

| $H$ \ $\alpha$ | 5 | 10 | 15 |
|---|---|---|---|
| 0.4 | 9.751 | 23.058 | 37.921 |
| 0.6 | 8.308 | 16.538 | 24.126 |
| 0.8 | 7.669 | 14.163 | 19.661 |

may indicate the influence of the Hurst exponent. For $\alpha = 5$, the lower the value of $H$ the higher is the probability of having higher heigh summits. This means that a power spectrum with a higher frequency contribution translates into a larger summits concentration for higher values of $z^*$. The Hurst influence is also observed in the decaying of $p_{\text{sum}}(z^*)$. When decaying for a higher value of $z^*$ the lower $H$ has a predominance, meaning that topographies with lower $H$ present even higher summits (with a value of height above the mode value). Otherwise, when decaying to lower values of height, the higher the Hurst the higher the probability of having summits in this region, i.e., lower $H$ values translate into a higher concentration of lower heigh summits. The discussed characteristics are seen for all the $\alpha$ values yet their magnitude seems to be lost with the increase of $\alpha$, becoming more and more similar. This might indicate that higher values of $\lambda_l/\lambda_s$ the effect of the Hurst exponent in $p_{\text{sum}}(z^*)$ might be irrelevant. On the other hand, the Weibull Minimum distribution shows that higher values of $H$ result in a higher concentration of lower height summits. One sees that for $\alpha = 5$ the histogram of $H = 0.8$ has the highest probability for the values around mode when comparing with the other Hurst cases. This effect is kept for all values of $\alpha$, even knowing that the concentration of lower

height summits tends to increase with $\alpha$, as it was previously seen. It can be interpreted as topographies with lower high-frequency contributions are more likely to have a higher concentration of lower heigh summits. The decaying process into higher heights verifies that the lower the $H$ the higher the concentration of summits.

The effect of Hurst on the curvatures of the topography was studied as well, comparing the normalized expected mean curvatures for the different cases. In Figure 3.39 and Figure 3.40 the curves of different Hurst exponents are present for the three $\alpha$ values in study, concerning Weibull Maximum and Minimum cases, respectively. The Weibull Maximum's curves (Figure 3.39) show a very similar relation among the different $\alpha$ values. In this case, for the same $\alpha$, smaller values of $H$ predict larger mean curvatures across all heights. In turn, the Weibull Minimum's curves (Figure 3.40) show very near results for values of small heights as expected from Figure 3.33. Progressively larger values of $H$ increase the curvature growth rate for the same $\alpha$. These results suggest that the spectral breadth $\alpha$ and Hurst roughness exponent $H$ have independent influences on the statistical geometry of the rough surfaces, especially in the evolution of curvatures at distinct heights.

To conclude, it might be said that, at a first sight, the results presented in Figures 3.37 and 3.38 may not present the clearest and most evident results. However one has to note that the current results have origin in a small auxiliary study where a high computational power was not allocated. For a more complete study of the effect of the spectral properties, a wider range of properties and hypotheses should have been studied. For example, the effect of the wavelength ratio should also be addressed by fixing a value of $\alpha$ and $\lambda_l/\lambda_s$ and computing the respective $H$ value. Moreover, to better highlight the effect of properties a higher number of realizations may have to be considered. Finally, it might be said that despite not highlighting some notable differences in the topography statistics, the effect of the spectral properties on physical phenomena evolving rough surfaces might be meaningful.

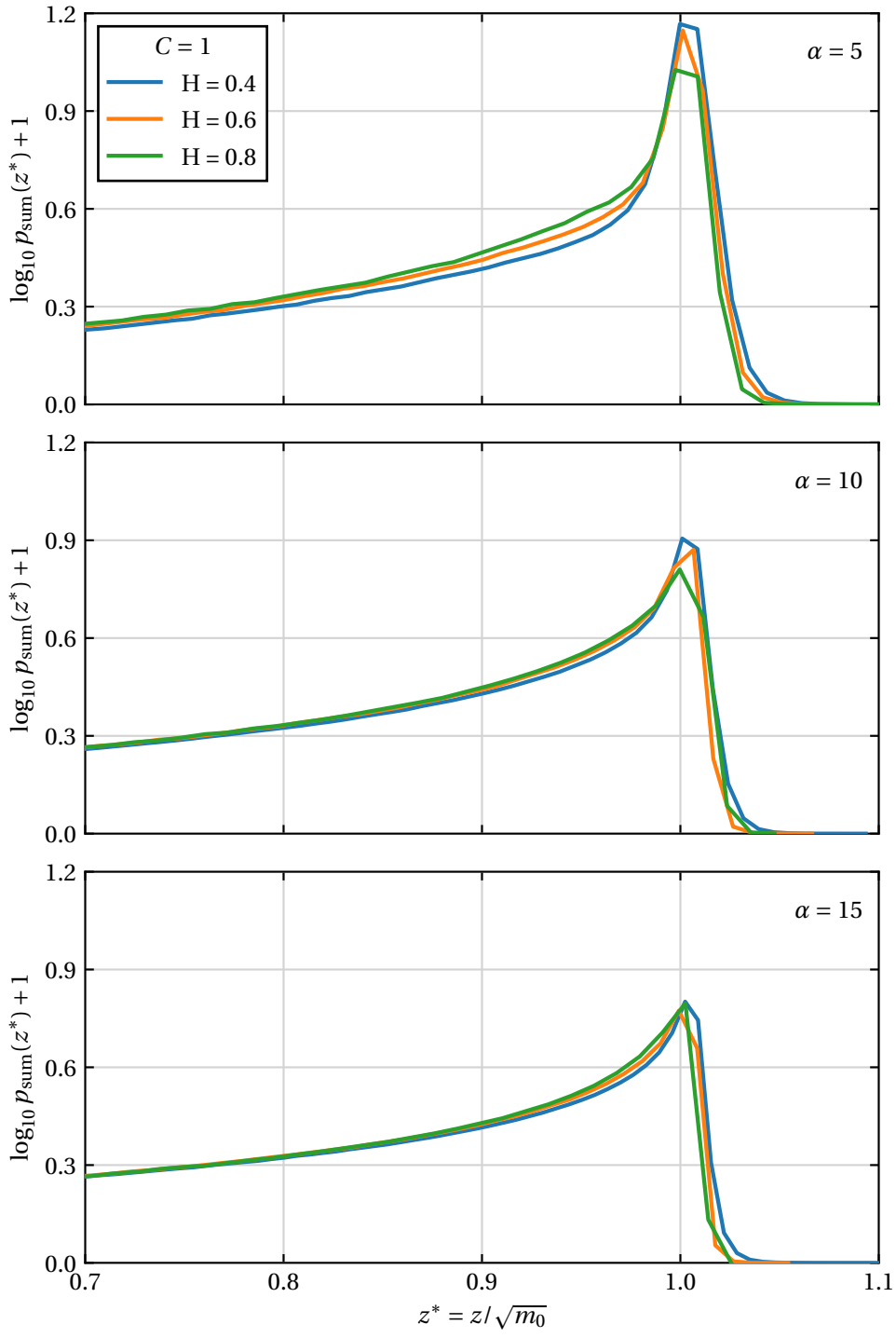


**Figure 3.37:** Influence of the Hurst exponent $H$ on the probability density of summit heights $p_{\mathrm{sum}}(z^*)$ for the Weibull Maximum distribution, with a shape parameter of $C = 1$, and plotted for 3 different values of $\alpha$. The value of $\lambda_l/\lambda_s$ was calculated so to match the prescribed values of $H$ and $\alpha$.

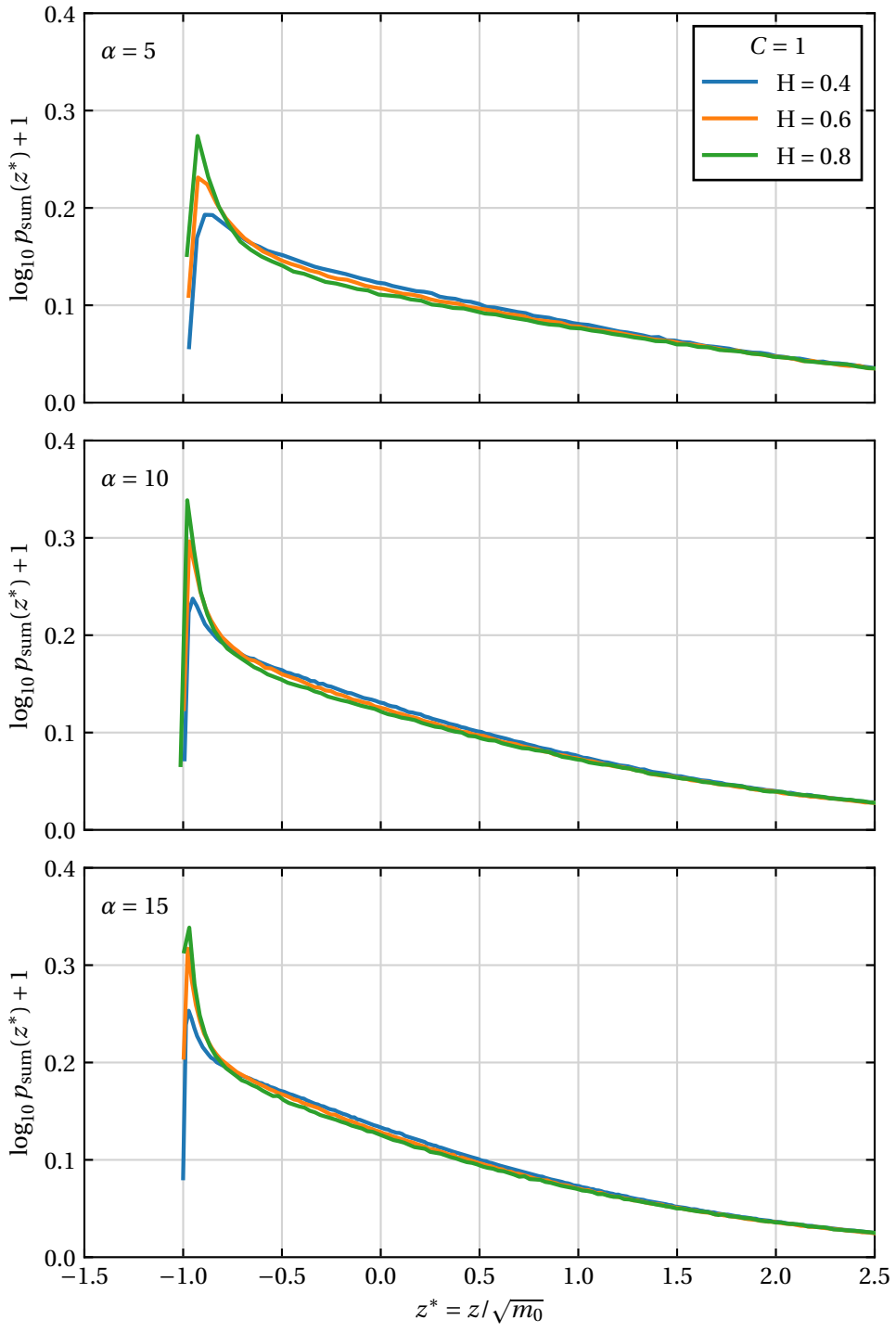


**Figure 3.38:** Influence of the Hurst exponent $H$ on the probability density of summit heights $p_{\mathrm{sum}}(z^*)$ for the Weibull Minimum distribution, with a shape parameter of $C = 1$, and plotted for 3 different values of $\alpha$. The value of $\lambda_l/\lambda_s$ was calculated so to match the prescribed values of $H$ and $\alpha$.

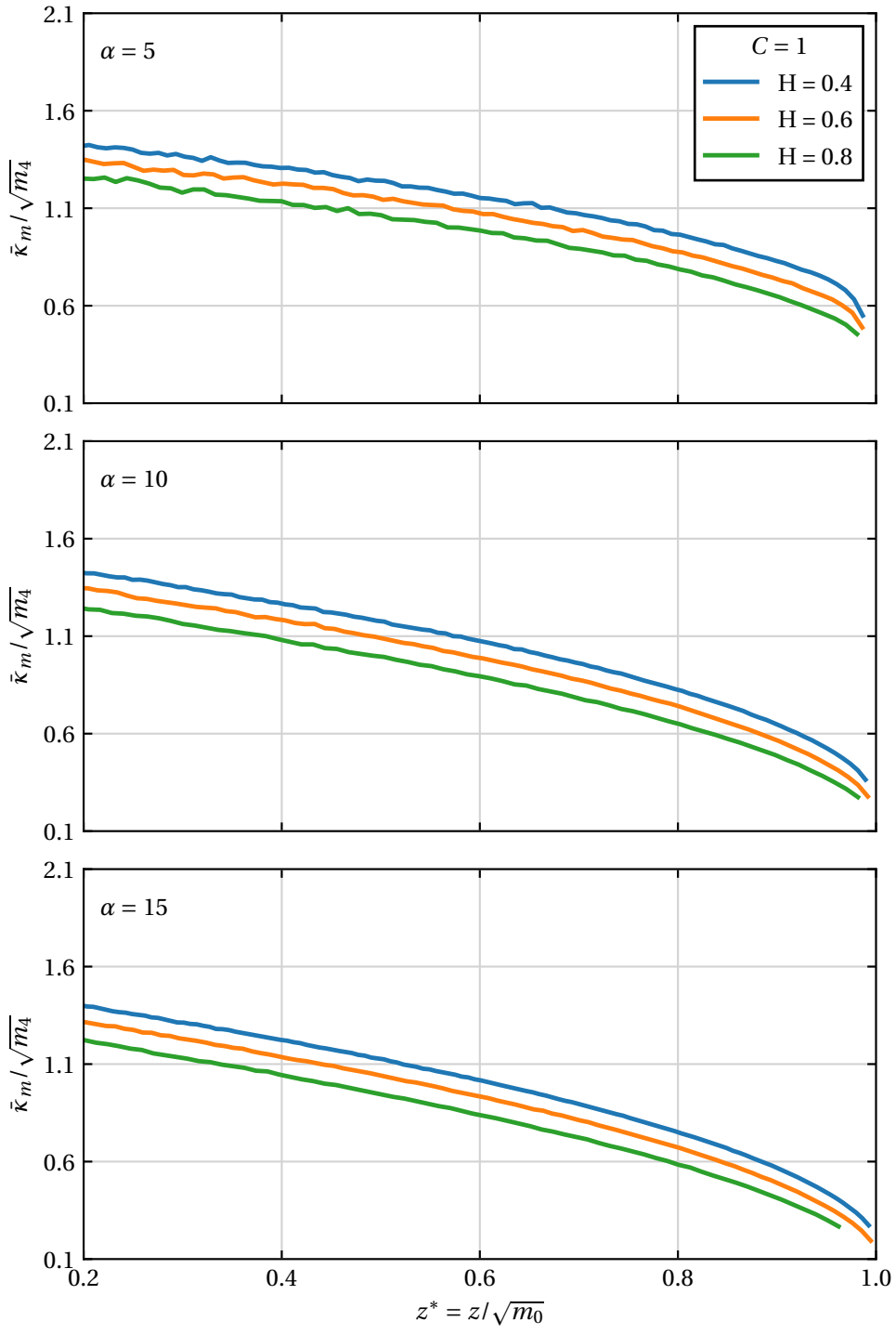


**Figure 3.39:** Influence of the Hurst exponent $H$ on the on the expected normalized mean curvature $\bar{\kappa}_m/\sqrt{m_4}$ of the Weibull Maximum distribution, with a shape parameter of $C = 1$, and plotted for 3 different values of $\alpha$. The value of $\lambda_l/\lambda_s$ was calculated so to match the prescribed values of $H$ and $\alpha$.

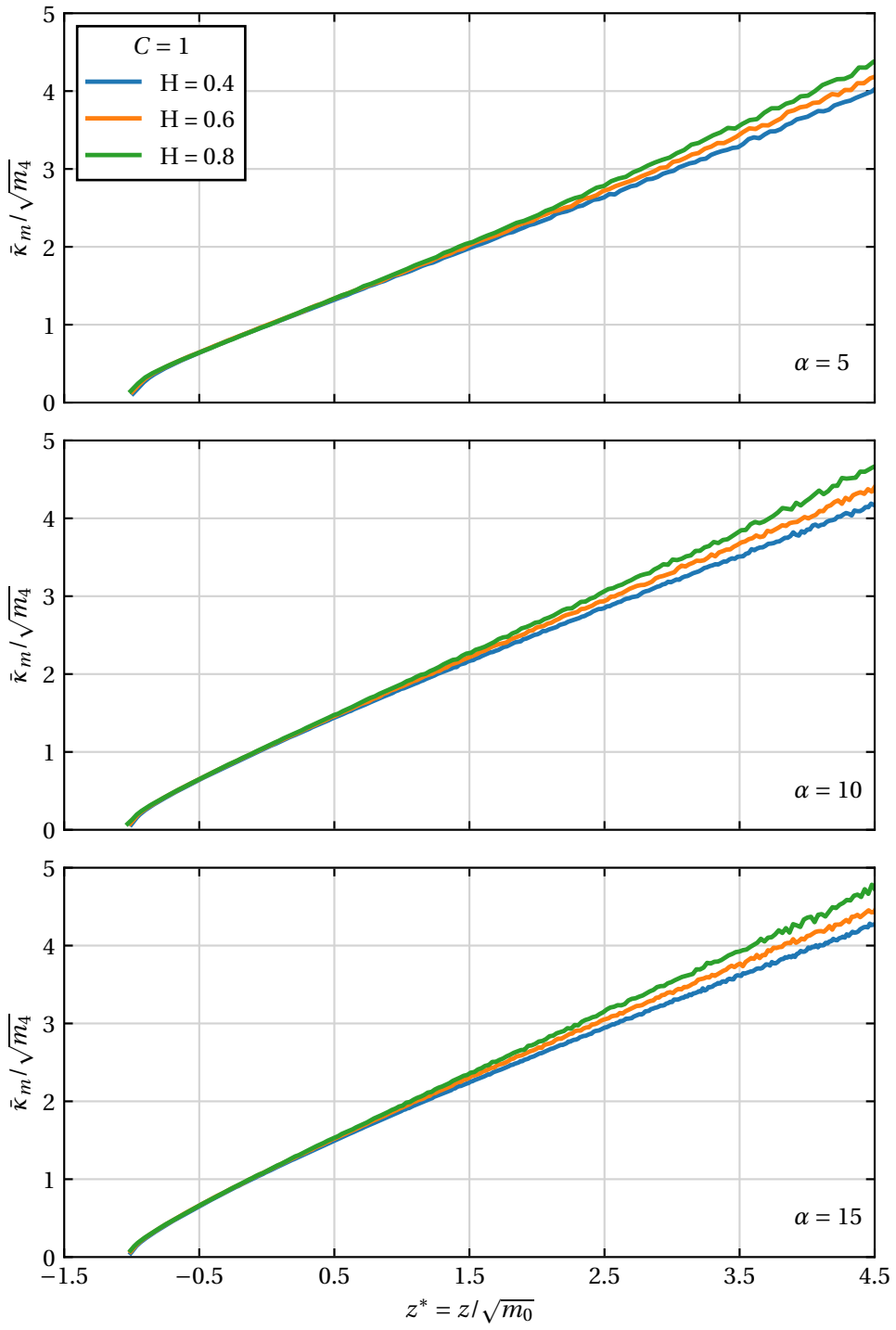


**Figure 3.40:** Influence of the Hurst exponent $H$ on the on the expected normalized mean curvature $\bar{\kappa}_m/\sqrt{m_4}$ of the Weibull Minimum distribution, with a shape parameter of $C = 1$, and plotted for 3 different values of $\alpha$. The value of $\lambda_l/\lambda_s$ was calculated so to match the prescribed values of $H$ and $\alpha$.

## 3.3 Closing comments

In this chapter, a study on the topography's geometry statistics was presented. A first approach was done by looking at the available analytical solutions for Gaussian topographies—Nayak's theory (Nayak, 1971). This solution has provided some useful insights on the characterization of rough surfaces that were later used for analysing the non-Gaussian results. A routine for numerically obtaining the statistics of random rough surfaces was developed and, taking advantage of Nayak's analytical solution, the framework was validated for the Gaussian case.

The approach to non-Gaussian topographies started with the introduction of the Weibull distribution, overviewing the principal research works on the topic and introducing the mathematical formulation of this function. It was verified that Weibull distribution can hold two different shapes from which one can model both negatively and positively skewed distributions. The values of the shape parameter $C$ were selected based on skewness and kurtosis values of practical engineering surfaces emphasizing the pertinence of Weibull distribution in the study of non-Gaussian topographies.

A numerical study on the surface statistics of non-Gaussian rough surfaces was done using the Weibull distribution. This study intended to recover the observed statistics for Gaussian surfaces and to analyse the impact of the new heigh distributions. Several parameters were tested within this study yet, the extension to higher values of the wavelength ratio $\lambda_l/\lambda_s$ was restricted due to computational limitations. With the increase of the PSD's bandwidth the topography discretization increases, thus meaning an increase in the time required to perform the summits detection as well as more available storage to store the discrete topography data. Additionally, the algorithm for the generation of rough surfaces (Pérez-Ràfols and Almqvist, 2019) iterates over a previous generated Gaussian surface to obtain the desired height distribution and PSD, requiring considerable more computational time. Nonetheless, the obtained results were sufficient to discuss and explore several characteristics of this type of topographies.

The shape of the distribution of the summit heights $p_{\text{sum}}(z^*)$ is seen to be dependent on the height distribution and on the tendency for summits to happen on higher heights. This leads to Weibull Maximum surfaces with significant concentrations of higher height summits, which contrasts with the Weibull Minimum that has a predominance of lower height summits but with a much smaller magnitude. Relatively to curvature results, while Weibull Maximum seems to have lower curvatures values for higher height summits, relatively to the Gaussian solution, the opposite is verified for Weibull Maximum. The shape parameter has a regulator effect and it can control how far the results are from the Gaussian case. The spectral properties were seen to also influence the summit heigh distribution with global trends being dependent on the Nayak's parameter. For instance, it was seen that Weibull Maximum follows the Gaussian trend of having a higher concentration of higher height summits for lower $\alpha$ values, while in Weibull Minimum topographies higher $\alpha$ translates into a higher concentration of lower height summits. Nevertheless, the results were not very clear and might have highlighted a certain dependence on the wavelength ratio and the Hurst exponent, rather than the Nayaks's parameter. To clarify this hypothesis, a small study on the dependence of the Nayak's parameter was done

with the focus on the effect of the Hurst exponent for the same $\alpha$. It was verified that very small differences may occur in the summit height distribution and on the curvature results. Weibull Minimum topographies are more affected having higher concentrations of lower height summits for higher Hurst values. An extension of this study should be made in order to obtain more sound conclusions.

# Chapter 4

# Contact modelling with the dual mortar method

Heretofore, the focus of the work was placed on the characterization of random rough surfaces and their statistics. The results addressed in the previous chapter are undoubtedly very useful sources of information, as they provide a deeper understanding of how different parameters affect the topography features. Moreover, the statistical characterisation, in particular the one concerned with Gaussian topographies, have been widely used in micromechanical models of rough surfaces, which provides a simple and concise approach to the evolution of the real contact area with the load. Models such as the GW-McCool (proposed by J. A. Greenwood, J. B. P. Williamson, *et al.* (1966) and later enhanced by McCool (1986)) or the BGT (proposed by Bush *et al.* (1975)) make use of the joint probability distributions of summits and curvatures of Gaussian surfaces. Nonetheless, this type of model possesses some limitations and are restricted to very simple conditions like frictionless and elastic contact. If one extends the problem to non-Gaussian rough surfaces, the problem of modelling micromechanical contact becomes even more challenging, with very few research works trying to approach this topic.

With the increasing computational capacity over the last few decades, numerical methods, such as the Finite Element Method (FEM), have gained a lot of popularity for solving mechanical problems as rough contact, for instance. This method gives an incomparable flexibility level to the rough contact problems and allows to simulate several types of boundary conditions or include other important physical phenomena such as plasticity, wear, thermal effects and large deformations. Despite being the most general tool for solving engineering problems, there are other alternative methods to FEM that are well suited for solving rough contact problems, like the Boundary Element Method (BEM). This method is well known for its low computational cost, since it only requires discretization of the surfaces in contact, being the bulk modelled with a set of fundamental analytical solutions. Being such a lightweight method, it allows to drastically increase the degrees of freedom (when compared with FEM) of the problem in analysis, and still being capable of dealing with the problem (Campañá *et al.*, 2008). One of the drawbacks of this model is still its limitation to elastic and frictionless problems. The interested reader is referred to Vakis *et al.* (2018) for a review of the numerical methods for solving rough contact problems explored in the last years.

**Remark 4.1 on the numerical method used for solving the rough contact problem.**
*Within the context of this work, only frictionless and elastic contact of self-affine random rough surfaces is analysed. A FEM framework is used in what might seem a not so appropriate decision since the BEM provides a way more reliable method for this type of problem. It should be mentioned that a complete FEM framework was available for the execution of the current work. Therefore, since the present work has a pioneering objective of studying the influence of non-Gaussian heigh distributions in rough contact, the most convenient solution became the one that most quickly allowed the beginning of the study. Additionally, one must note that the FEM framework is based around a nonlinear FE implementation and is equipped with a dual-mortar contact algorithm. Such tools provide greater robustness for treating geometric non-linearities and provide an incomparable precision in contact phenomena. This comes at the cost of greater computational expense, yet ensure great modelling accuracy and robustness.*

This chapter aims to present the fundamental aspects on which the FEM framework used is based. It starts with a fundamental introduction to the continuum solid mechanics for solving contact based on a dual mortar approach. Then the FE discretization is presented as well as the required solution algorithm for solving such type of problems. After the FEM framework used in the current work is presented, details are given on the definition of the *Representative Contact Element* (RCE), roughness model, material properties, boundary conditions, meshing process and the methodologies for computing the real contact area.

**Remark 4.2 on the FEM framework for contact modelling concepts.**
*In the following sections, only the most important ideas of the FEM contact modelling with the dual mortar method are introduced. For a more in-depth review of the concepts the interested reader is referred to the following references:*

- ***Nonlinear continuum mechanichs*** *— Holzapfel (2000), Bonet and Wood (2008) and Chaves (2013);*
- ***Contact mechanics*** *— Laursen (2003), Wriggers (2006) and Wriggers and Laursen (2010);*
- ***Finite element method*** *— Wriggers (2008) and Zienkiewicz* et al. *(2013);*
- ***Dual mortar methods for contact problems*** *— Popp (2012) and Carvalho (2018).*

## 4.1 Continuum mechanics

The classical continuum mechanics approach is considered in the current work, starting with the description of motion and deformation kinematics, as lustrated in Figure 4.1. Assuming that a body can accept an infinite number of configurations it should be defined, by analysis convenience, the *reference configuration*. It is considered that all the configurations hold the same Cartesian coordinate system. A deformable body in the reference configuration is defined by the Lipschitz open set $\Omega_0 \subset \mathbb{R}^d$, being a generic point $P \in \Omega_0$ defined as $\boldsymbol{X}$. The spatial dimension of the problem is given by $d$, that for the current framework assumes the value $d = 2,3$. To relate the reference configuration with a *current configuration*, after a deformation, a bijective nonlinear *deformation mapping function*

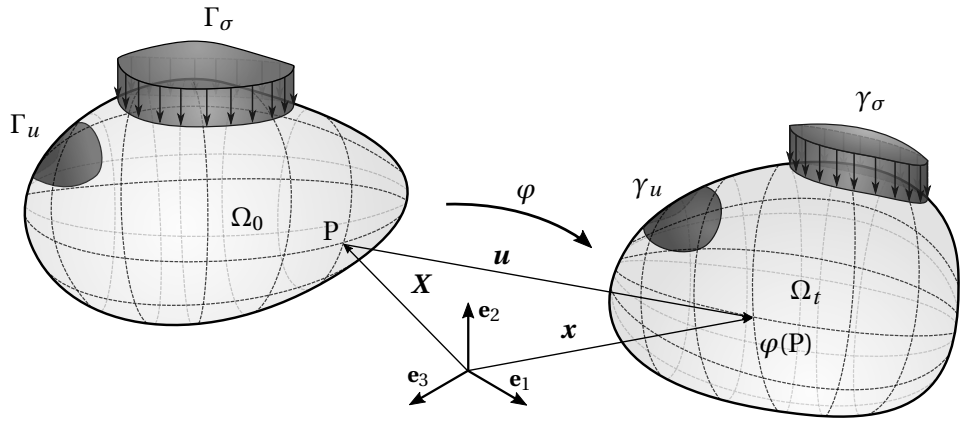


**Figure 4.1:** Reference and current configuration of a deformable body. Adapted from Couto Carneiro (2019).

$\varphi$ is used, viz.

$$\boldsymbol{x} = \varphi(\boldsymbol{X}, t). \tag{4.1}$$

for each time instant $t$. This function $\varphi$ maps the material points between configurations univocally not allowing the superposition nor the opening of gaps inside the material. The displacement vector field $\boldsymbol{u}(\boldsymbol{X}, t)$ comes written as

$$\boldsymbol{u}(\boldsymbol{X}, t) = \boldsymbol{x}(\boldsymbol{X}, t) - \boldsymbol{X}(t)\,. \tag{4.2}$$

In this description of motion the $\boldsymbol{X}$ is considered the independent variables, whereas $\boldsymbol{x}$ is the dependent variable as it a function of the displacement field $\boldsymbol{u}$. One can then write the position occupied by $\boldsymbol{X}$ in the current configuration through the Equation (4.2) as the addition to the reference configuration $\boldsymbol{X}(t)$ of the displacement field $\boldsymbol{u}(\boldsymbol{X}, t)$. If one assumes the *Lagrangian description* the reference configuration is considered and than the attention is given to $\boldsymbol{X}$. Alternatively, the *Eulerian description* is associated to the current configuration tacking a specific point $\boldsymbol{x}$.

In the reference configuration the boundary of a deformable body is denoted by $\partial\Omega_0$ and encompasses to open disjoint subsets: the *Neumann partition* $\Gamma_\sigma$ and the *Dirichlet partition* $\Gamma_u$. The disjointness property is written as

$$\Gamma_\sigma \cup \Gamma_u = \partial\Omega_0\,, \tag{4.3a}$$

$$\Gamma_\sigma \cap \Gamma_u = \emptyset\,. \tag{4.3b}$$

The analogue partitions in the current configuration are represented by $\gamma_\sigma$ and $\gamma_u$.

An quintessential quantity in the deformation of continuum media is the *deformation gradient*, hereafter represented by $\boldsymbol{F}$. It is a second-order two-point tensor that gives a fundamental measure of the deformation and strain of the body, mapping the vectors from the reference configuration to the current configuration. One writes $\boldsymbol{F}$ as the partial derivative between the the position in the current configuration $\boldsymbol{x}$ to the one in the reference configuration $\boldsymbol{X}$, viz.

$$\boldsymbol{F} = \frac{\partial \boldsymbol{x}(\boldsymbol{X}, t)}{\partial \boldsymbol{X}} = \boldsymbol{I} + \frac{\partial \boldsymbol{u}(\boldsymbol{x}, t)}{\partial \boldsymbol{X}}, \tag{4.4}$$

where the second-order identity tensor is given by $\boldsymbol{I}$. The Cartesian components of the $\boldsymbol{F}$ are given by

$$F_{ij} = \frac{\partial x_i}{\partial X_j} = \delta_{ij} + \frac{\partial u_i}{\partial X_j}, \tag{4.5}$$

where $\delta_{ij}$ is the Kronecker delta. An important measure given by the deformation gradient is its determinant denominated the *Jacobian J*, given by

$$J = \det \boldsymbol{F}\,. \tag{4.6}$$

The Jacobian represent the volume change of a particle, i.e., the ratio between the volume on the current and reference configurations,

$$\mathrm{d}V = J\mathrm{d}V_0\,. \tag{4.7}$$

The Jacobian in the reference configuration must satisfy $J = 1$, and during the deformation it should be observed $J > 0$. For a deformation where $J = 1$ the the volume is preserved and it is named *isochoric*.

### 4.1.1 Strain measures

From the deformation gradient tensor $\boldsymbol{F}$ alternative *strain measures* can be derived. One can split the effects of $\boldsymbol{F}$ in two components: a shape-change component (stretching and shearing) and a rotation component, that does influence the body deformation. Therefore, the *polar decomposition theorem* allow to write the deformation gradient as

$$\boldsymbol{F} = \boldsymbol{R}\boldsymbol{U} = \boldsymbol{V}\boldsymbol{R}\,, \tag{4.8}$$

where $\boldsymbol{R}$ is the local rotation tensor and $\boldsymbol{U}$ and $\boldsymbol{V}$ are, respectively, thee right and left stretch tensors—symmetric positive definite tensors. [1] Two common strain measures are the so called right and left *Cauchy-Green strain tensors*, denoted by $\boldsymbol{C}$ and $\boldsymbol{B}$, respectively. One can write these tensors as a function of $\boldsymbol{F}$

$$\boldsymbol{C} = \boldsymbol{F}^{\mathrm{T}}\boldsymbol{F}\,, \tag{4.9a}$$

$$\boldsymbol{B} = \boldsymbol{F}\boldsymbol{F}^{\mathrm{T}}\,, \tag{4.9b}$$

that can be related to the stretch tensors by

$$\boldsymbol{U} = \sqrt{\boldsymbol{C}}\,, \tag{4.10a}$$

$$\boldsymbol{V} = \sqrt{\boldsymbol{B}}\,. \tag{4.10b}$$

The right Cauchy-Green tensor possesses two particularly interesting features. On the one hand, it only depends on the reference configuration, whereas $\boldsymbol{F}$ is dependent on both reference and current configurations. On the other hand, being related to $\boldsymbol{U}$ it is a practical measure of the body deformations as it despises rigid body rotations. If one wants to ensure that a zero strain rate occurs at the reference configuration, the *Green-Lagrange strain tensor* $\boldsymbol{E}$ may be defined as

$$\boldsymbol{E} = \frac{1}{2}\left(\boldsymbol{C} - \boldsymbol{I}\right)\,. \tag{4.11}$$

A similar formulation can be applied to the current configuration using the left Cauchy-Green tensor $\boldsymbol{B}$.

[1] The stretch tensors are related by the rotation tensor: $\boldsymbol{V} = \boldsymbol{R}\boldsymbol{U}\boldsymbol{R}^{\mathrm{T}}$

### 4.1.2 Stress measures

Similarly to the strain measures, several *stress measures* can be defined within the context of nonlinear mechanics. One of the most common is the *Cauchy stress tensor* $\boldsymbol{\sigma}$, which relates the surface tension in the element area, of the current configuration, to the real internal force of the body,

$$\mathrm{d}\boldsymbol{f} = \boldsymbol{\sigma} \cdot \mathrm{d}A\boldsymbol{n}\,, \tag{4.12}$$

where $\boldsymbol{n}$ represents the normal vector to the current configuration's element area $\mathrm{d}A$. Alternately, the *first Piolla-Kirchoff tensor* $\boldsymbol{P}$ relates the surface element area in the reference configuration to the true internal force in the current configuration, i.e.,

$$\mathrm{d}\boldsymbol{f} = \boldsymbol{P} \cdot \mathrm{d}A_0\boldsymbol{N}\,, \tag{4.13}$$

where $\boldsymbol{N}$ represents the normal vector to the current configuration's element area $\mathrm{d}A_0$. This tensor is related to the Cauchy stress tensor by

$$\boldsymbol{P} = J\boldsymbol{\sigma} \cdot \boldsymbol{F}^{-\mathrm{T}}\,. \tag{4.14}$$

While the Cauchy stress tensor is a symmetric ($\boldsymbol{\sigma} = \boldsymbol{\sigma}^{\mathrm{T}}$), the same does is not verified for the first Piolla-Kirchoff tensor. To overcome this fact the *second Piolla-Kirchoff tensor* $\boldsymbol{S}$ is introduced, recovering the symmetry property, yet with a less clear interpretation,

$$\boldsymbol{S} = \boldsymbol{F}^{-1} \cdot \boldsymbol{P} = J\boldsymbol{F}^{-1} \cdot \boldsymbol{\sigma} \cdot \boldsymbol{F}^{-\mathrm{T}}\,. \tag{4.15}$$

### 4.1.3 Constitutive laws

The relations between the strain and stress measures are named *constitutive laws*. The strain energy function $\Psi$, or Helmholtz free-energy function, is often used to define the constitutive laws of different types of hyperelastic materials. This function should be defined ensuring that it is independent from rotation and it verifies the second law of thermodynamics. For hyperelastic laws, a pivotal relation enabled by the strain energy function is that one established between the second Piola-Kirchoff stress tensor $\boldsymbol{S}$ and the Green-Lagrange strain tensor $\boldsymbol{E}$,

$$\boldsymbol{S} = \frac{\partial \Psi}{\partial \boldsymbol{E}}\,. \tag{4.16}$$

The relation for each increment of stress and strain is given by a fourth-order constitutive tensor $\mathscr{C}$, written as

$$\mathscr{C} = \frac{\partial \boldsymbol{S}}{\partial \boldsymbol{E}}\,. \tag{4.17}$$

Both $\boldsymbol{S}$ and $\mathscr{C}$ are dependent on the model adopted and the type of problem in consideration (eg. hyperelasticity and viscoelasticity).

### 4.1.4 Fundamental conservation principles

In parallel with the previous continuum mechanics description, the mechanical framework is also described by the equilibrium conditions, namely the conservation of mass, the equilibrium of linear and angular momentum and the energy balances, given by

the fundamental laws of thermodynamics. One should not that the equilibrium of angular momentum only reduces to the symmetry conditions the Cauchy and second Piola-Kirchoff stress tensors. Since in this work the thermal phenomena can be neglected (only considering pure mechanical systems), the energy balances are redundant relative together with the linear momentum equilibrium.

**Conservation of mass**

The conservation of mass dictates that any given particle in the reference configuration must be conserved into the current configuration, even if volume changes are verified. The classic conservation o mass writes

$$\frac{\mathrm{d}m}{\mathrm{d}t} = \frac{\mathrm{d}}{\mathrm{d}t}\int_{\Omega_0} \rho_0 \, \mathrm{d}V_0 = \frac{\mathrm{d}}{\mathrm{d}t}\int_{\Omega_t} \rho \, \mathrm{d}V = 0 \,. \tag{4.18}$$

where $\rho_0$ and $\rho$ are the body density in the reference and current configuration, respectively, and $m$ is represents the mass of the body. Since, the body density is independent of time , through the Reynold's transport theorem one can write

$$\dot{\rho} + \rho \, \mathrm{div}\dot{\boldsymbol{u}} = 0 \,, \tag{4.19a}$$

$$\dot{\rho}_0 = 0 \,, \tag{4.19b}$$

where the operator $(\dot{\bullet})$ is the total time derivative, and $\mathrm{div}(\bullet)$ is the divergence of a vector that for the vector field $\dot{\boldsymbol{u}}$ writes

$$\mathrm{div}\boldsymbol{u} = \frac{\partial \dot{u}_1}{\partial x_1} + \frac{\partial \dot{u}_2}{\partial x_2} + \frac{\partial \dot{u}_3}{\partial x_3} . \tag{4.20}$$

**Equilibrium of linear momentum**

In this work, since the analysis is focused on quasi-static problems, the linear momentum is null. Therefore, Newton's second law, which relates the linear momentum with the external forces applied to a body, is reduced to the equilibrium of the external forces. The forces acting on body are divided in body forces $\boldsymbol{b}$ (forces per unit of volume in the current configuration) and the surfaces traction, denoted by $\boldsymbol{t}$ (forces per unit of boundary area in the current configuration). The equilibrium condition comes

$$\int_{\Omega_t} \boldsymbol{b} \, \mathrm{d}V + \int_{\partial\Omega_t} \boldsymbol{t} \, \mathrm{d}A = 0 \,, \tag{4.21}$$

Considering the Gauss divergence theorem, the Equation (4.21) can be rewritten into the local formulation of the equilibrium

$$\mathrm{div}\boldsymbol{\sigma} + \boldsymbol{b} = \boldsymbol{0} \,, \tag{4.22}$$

where $\boldsymbol{0}$ denotes the null vector—recall that the divergence of a second-order tensor results in a first-order tensor.

### 4.1.5 Strong form of the continuum solid mechanics problem

Up to now, the presented concepts, namely the Neummann and Dirichlet partition, the continuum mechanics formulation and the conservation principles, allow to formulate the strong form of the *Initial Value Boundary Problem* (IBVP), for solids under finite deformations. This formulation is established for a solid sub-domain in the current configuration $\Omega_t^i$, in a time domain comprised between 0 and $T$, where it must be verified:

**Problem 4.1 (Strong form of the IBVP of nonlinear solid mechanics).**
*On each sub domain $\Omega_t^i$, the momentum balance and the boundary conditions of the problem (Neumann and Dirichlet) is defined by*

$$\mathrm{div}\boldsymbol{\sigma}^i + \boldsymbol{b}^i = \mathbf{0}, \quad \text{in } \Omega_t^i \times [0,T], \tag{4.23a}$$

$$\boldsymbol{u}^i = \bar{\boldsymbol{u}}^i, \quad \text{in } \gamma_u^i \times [0,T], \tag{4.23b}$$

$$\boldsymbol{\sigma}^i \boldsymbol{n}^i = \bar{\boldsymbol{t}}^i, \quad \text{in } \gamma_\sigma^i \times [0,T], \tag{4.23c}$$

In Equations (4.33) $\bar{\boldsymbol{u}}^i$ and $\bar{\boldsymbol{t}}^i$ are the prescribed displacements and surface tractions, respectively. The previous description is expressed over time as a quasi-static system, since rate-dependent phenomena like plasticity may also be considered.

**Remark 4.3 on the formulation of continuum frictional contact.**
*In the following section the fundamental equations that describe a finite deformation contact problem are introduced, considering both normal and tangential contact constraints. Even knowing that the numerical simulations performed assumed a frictionless contact scenario, the following section aims to formulate a more generic problem, since the simplifications required to consider just normal contact constraints are straightforward.*

## 4.2 Continuum contact mechanics

The previous description was only concerned with nonlinear phenomena arising from the continuum deformation of solid bodies (geometry and constitutive laws). Since both Neumann and Dirichlet are established in advance, neither the prescribed displacements or the surface traction act as a source of nonlinearity. Instead, the possibility of contact interactions introduces additional nonlinear phenomena to the continuum mechanics formulation. Several different contact problems can be identified from a mathematical formulation point of view, such as the *Signorini* problem (contact between a rigid surface and an elastic body), self contact and contact between multiple bodies. In this work the general formulation of contact between two deformable bodies is assessed, allowing to introduce the fundamental concepts of the contact modelling characteristics employed in the used framework.

The general problem of two deformable bodies in unilateral contact is presented in Figure 4.3. The superscripts *s* and *m* stand for *non-mortar* and *mortar* bodies, respectively. [2]

[2] The notation *s* and *m* follows that classical contact mechanics denomination of surfaces in contact, namely, *slave* and *master* surfaces.

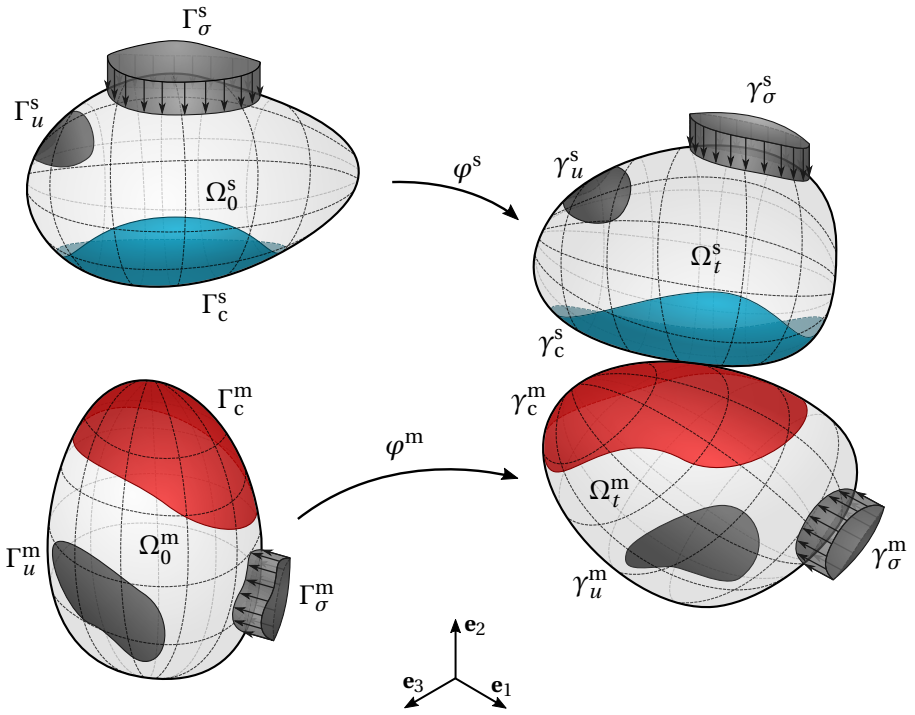


**Figure 4.2:** Two deformable bodies in unilateral contact and the reference and current configuration. Adapted from Carvalho (2018).

Considering that all bodies are under potential contact, a new domain boundary is introduced — the denominated potential contact boundary, and represented by $\Gamma_{\mathrm{c}}$ and $\gamma_{\mathrm{c}}$, in the reference and current configuration, respectively. (cf. Figure 4.3). The Equations (4.24) can be rewritten to encompass this new domain, viz.

$$\Gamma^i_{\sigma} \cup \Gamma^i_u \cup \Gamma^i_{\mathrm{c}} = \partial\Omega^i_0 \,, \tag{4.24a}$$

$$\Gamma^i_{\sigma} \cap \Gamma^i_u = \Gamma^i_{\sigma} \cap \Gamma^i_{\mathrm{c}} = \Gamma^i_{\mathrm{c}} \cap \Gamma^i_u = \emptyset \,. \tag{4.24b}$$

The equations apply for both bodies in unilateral contact—$i \in [s, m]$. One must distinguish the *potential contact surface* form the *active contact surface* $\Gamma_{\mathrm{a}} \subseteq \Gamma_{\mathrm{c}}$. It is considered that regions that belong to the potential contact surface, but not to the active contact surface to be part of the Neumann boundary—$\Gamma_{\mathrm{c}} \setminus \Gamma_{\mathrm{a}} \subset \Gamma_{\sigma}$.

### 4.2.1 Contact kinematics

The potential interaction between surfaces contact bodies is defined by means of kinematic quantities. For reference, one of the potential contact surfaces should be used to define such quantities. In the following description, the non-mortar potential contact boundary $\gamma^{\mathrm{s}}_{\mathrm{c}}$ has been selected o parameterise the contact kinematics—as a prelude to the mortar-based discretisation. The fundamental measure of proximity between contact bodies is the so-called *gap function* $g$, defined as the distance between a point $\boldsymbol{x}^{\mathrm{s}} \in \gamma^{\mathrm{s}}_{\mathrm{c}}$ and its projection to the mortar side. The projection is determined along the unit normal of the non-mortar surface $\boldsymbol{\eta}(\boldsymbol{x}^{\mathrm{s}}, t)$, resulting in the projected point $\hat{\boldsymbol{x}}^{\mathrm{m}} \in \gamma^{\mathrm{m}}_{\mathrm{c}}$ , in the mortar

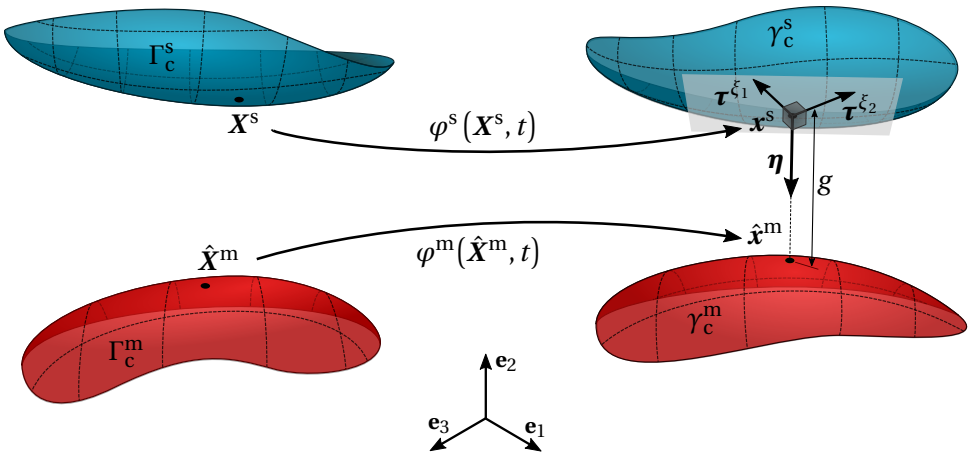


**Figure 4.3:** Graphical representation of the gap function. Adapted from Carvalho (2018).

surface—thus, adopting a ray-tracing approach. One can define mathematically the gap function as

$$g(\boldsymbol{x}^s,t) = -\boldsymbol{\eta}(\boldsymbol{x}^s,t)\cdot\left[\boldsymbol{x}^s - \hat{\boldsymbol{x}}^m(\boldsymbol{x}^s,t)\right]. \tag{4.25}$$

whereas the gap vector comes

$$\boldsymbol{g}(\boldsymbol{x}^s,t) = \boldsymbol{x}^s - \hat{\boldsymbol{x}}^m(\boldsymbol{x}^s,t). \tag{4.26}$$

Another kinematic quantity used in the description of the unilateral contact is the relative tangential velocity. This variable has the purpose to allow the characterization of the tangential contact. Using the difference of material velocities, the relative tangential velocity $\boldsymbol{v}^\tau$ is defined as the projection of the time derivative of the gap vector $\dot{\boldsymbol{g}}$ in the tangential direction

$$\boldsymbol{v}^\tau = \left(\boldsymbol{I} - \boldsymbol{\eta}\otimes\boldsymbol{\eta}\right)\dot{\boldsymbol{g}}, \tag{4.27}$$

where $(\bullet)\otimes(\bullet)$ is the dyadic operator that for a first order tensor writes $\boldsymbol{\eta}\otimes\boldsymbol{\eta} = \boldsymbol{\eta}\cdot\boldsymbol{\eta}^{\mathrm{T}}$. The definition of Equation (4.27) is only applicable for points in contact.

### 4.2.2 Contact constraints

Contact conditions can be established, based on the previous defined kinematic quantities. In advance, the establishment of the contact constraints requires a compatible mathematical description to encompass both kinematic quantities and forces in the same fashion. Therefore, the contact tractions are decomposed in a normal a tangential components. For the contact traction vector acting in the current non-mortar contact region $\gamma_c^s$

$$\boldsymbol{t}_c^s(\boldsymbol{x}^s,t) = p^\eta\boldsymbol{\eta} + \boldsymbol{t}^\tau, \tag{4.28}$$

where $p^\eta$ represents the contact normal pressure and $\boldsymbol{t}^\tau$ the tangential contact traction — that is null for a frictionless contact setup. The linear conservation of momentum gives, that the surface traction on the mortar side has to be the inverse of the analogue quantities in the non-mortar side, i.e.,

$$\boldsymbol{t}_c^m(\hat{\boldsymbol{x}}^m,t) = -\boldsymbol{t}_c^s(\boldsymbol{x}^s,t). \tag{4.29}$$

**Normal contact constraints**

In the normal direction the contact constraints make sure that the geometrical condition of non-penetration is accomplished and that the interaction between surfaces has only a compression nature (non-adhesive contact). One can look at Equation (4.25) and verify that, due to sign convention, non-contact points hold a positive gap value $g > 0$ and shall verify $p^\eta = 0$. Whereas for points in contact (active contact boundary) the gap assumes an expected null value $g = 0$ and the contact pressure $p^\eta < 0$. This considerations lead to the definition of the so-called *Karush-Kuhn-Tucker* (KKT) conditions, also refered to as the *Hertz-Signorini-Moreau* (HSM) conditions, which write

$$g(\boldsymbol{x}^\mathrm{s}, t) \geq 0\,, \tag{4.30a}$$

$$p^\eta(\boldsymbol{\eta}, \boldsymbol{t}_\mathrm{c}^\mathrm{s}) \leq 0\,, \tag{4.30b}$$

$$p^\eta(\boldsymbol{\eta}, t)\, g(\boldsymbol{x}^\mathrm{s}, t) = 0\,. \tag{4.30c}$$

These conditions apply to the points throughout the non-mortar domain $\boldsymbol{x}^\mathrm{s} \in \gamma_\mathrm{c}^\mathrm{s}$. The first relation guarantees the non-penetration assumption and the second imposes the existence of only negative stresses coming from contact. The third condition, often named *complementary condition*, maintains the aforementioned relation between $g$ and $p^\eta$, i.e., for contact the pressure is necessarily negative and for a non-contact situation the contact pressures are not verified. In Figure 4.4a a graphical representation of the KKT conditions is shown.

**Frictional contact constraints**

To encompass the frictional contact in the unilateral contact case the *Coulomb's friction law* is often used. This classical approach can be used to defined the contact constraints by introducing the coefficient of friction $\mu$. The resultant constraint conditions can be stated as follows

$$\psi(\boldsymbol{t}^\tau, p^\eta)) \equiv \|\boldsymbol{t}^\tau(\boldsymbol{x}^\mathrm{s}, t)\| - \mu|p^\eta(\boldsymbol{x}^\mathrm{s}, t)| \leq 0\,, \tag{4.31a}$$

$$\boldsymbol{v}^\tau(\boldsymbol{x}^\mathrm{s}, t) + \beta \boldsymbol{t}^\tau(\boldsymbol{x}^\mathrm{s}, t) = \boldsymbol{0}\,, \tag{4.31b}$$

$$\beta \geq 0\,, \tag{4.31c}$$

$$\psi(\boldsymbol{t}^\tau, p^\eta)\beta = 0\,. \tag{4.31d}$$

In this conditions two new quantities were introduced: the *slip function*, denoted by $\psi(\boldsymbol{t}^\tau, p^\eta)$, and the $\beta$ as a scalar parameter. The Equation (4.31a) imposes that the tangential contact traction $\boldsymbol{t}^\tau$ is limited by a maximum value defined as the product between the coefficient of friction $\mu$ and the contact pressure $p^\eta$. From this condition and taking into consideratio the *complementary condition* given by Equation (4.31d), the slip function value splits the frictional contact formulation in two difference scenarios:

- *Stick condition* — $\psi(\boldsymbol{t}^\tau, p^\eta) < 0$

  The tangential contact traction $\boldsymbol{t}^\tau$ is smaller than the limit by $\mu p^\eta$ and, from te complementary condition, $\beta = 0$. Therefore, at the light of Equation (4.31b) the there is no relative tangential velocity as $\boldsymbol{v}^\tau = 0$.

- *Slip condition* — $\psi(\boldsymbol{t}^\tau, p^\eta) = 0$

In this scenario the tangential contact traction $\boldsymbol{t}^{\tau}$ has matched the limiting value $\mu p^{\eta}$. Also, the complementary condition in pair with Equation (4.31c) imposes that $\beta$ can assume values greater zero, meaning that the Equation (4.31b) allows the tangential relative motion to occurs, i.e., $\boldsymbol{v}^{\tau} > 0$.

The graphical representation of the Coulomb's friction law for one dimensional sliding is show on Figure 4.4b. It should be noted that both KKT and Coulomb's conditions describe non-smooth and multivalued constraints at the origin.

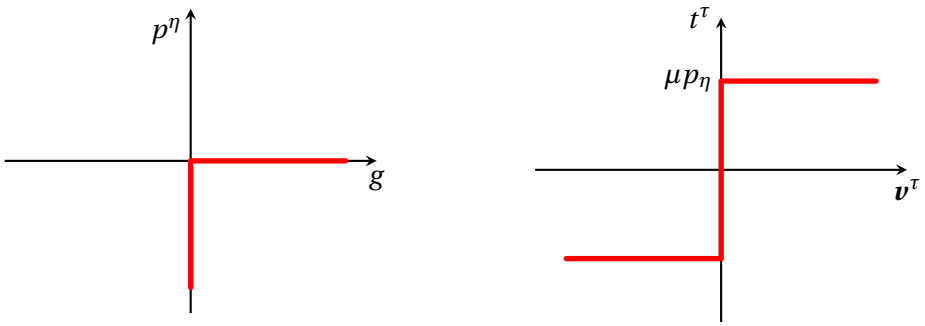


**(a)** KKT conditions **(b)** Coulomb's friction law

**Figure 4.4:** Graphical representation of the contact constrains in normal and tangential directions, i.e., Karush-Kuhn-Tucker conditions and Coulomb's friction law, respectively. Adapted from Carvalho (2018).

### 4.2.3 Strong form of the finite deformation frictional contact

At this point, one can extend of equations defined on Section 4.1.5, for the generic IBVP of continuum solid mechanics, to encompass the finite deformation frictional contact. Therefore, for each sub-domain $\Omega_t^i$ of the current configuration, the deformed solution of this problem is stated by:

**Problem 4.2 (Strong form of the IBVP of finite deformation frictional contact).** *On each sub domain $\Omega_t^i$, the momentum balance and the boundary conditions of the problem (Neumann and Dirichlet) are defined by*

$$\operatorname{div}\boldsymbol{\sigma}^i + \boldsymbol{b}^i = \boldsymbol{0}, \quad \text{in } \Omega_t^i \times [0,T], \tag{4.32a}$$

$$\boldsymbol{u}^i = \bar{\boldsymbol{u}}^i, \quad \text{in } \gamma_u^i \times [0,T], \tag{4.32b}$$

$$\boldsymbol{\sigma}^i \boldsymbol{n}^i = \bar{\boldsymbol{t}}^i, \quad \text{in } \gamma_\sigma^i \times [0,T], \tag{4.32c}$$

*and the contact constraints in the normal and tangential directions,*

$$g \geq 0\,, \quad p^{\eta} \leq 0\,, \quad p^{\eta} g = 0\,, \quad \text{in } \gamma_{\mathrm{c}}^{\mathrm{s}} \times [0,T]\,, \tag{4.33a}$$

$$\psi \leq 0\,, \quad \boldsymbol{v}^{\tau} + \beta \boldsymbol{t}^{\tau} = \boldsymbol{0}\,, \quad \beta \geq 0\,, \quad \psi\beta = 0\,, \quad \text{in } \gamma_{\mathrm{c}}^{\mathrm{s}} \times [0,T]\,. \tag{4.33b}$$

### 4.2.4 Weak form of the contact formulation

The following section aims to obtain the weak formulation of the frictional contact problem, following the logical process to the final finite element model derivation. One shall first define the solution space $\mathcal{U}^i$ and the weighting space $\mathcal{V}^i$ defined as

$$\mathcal{U}^i \equiv \left\{ \boldsymbol{u}^i \in \left[ H^1\left(\Omega_t^i\right) \right]^d \mid \boldsymbol{u}^i = \bar{\boldsymbol{u}}^i \text{ in } \gamma_u^i \right\}, \tag{4.34}$$

$$\mathcal{V}^i \equiv \left\{ \delta\boldsymbol{u}^i \in \left[ H^1\left(\Omega_t^i\right) \right]^d \mid \delta\boldsymbol{u}^i = \boldsymbol{0} \text{ in } \gamma_u^i \right\}, \tag{4.35}$$

where $H^1\left(\Omega_0^i\right)$ defines the Sobolev space, which is the space of all square integrable functions on a given domain. The notation shorthand $\mathcal{U} \equiv \mathcal{U}^{\mathrm{s}} \times \mathcal{U}^{\mathrm{m}}$ and $\mathcal{V} \equiv \mathcal{V}^{\mathrm{s}} \times \mathcal{V}^{\mathrm{m}}$ is employed in what follows. The application of the *Principle of Virtual Work* (PVW) to the momentum balance equations (4.33) and with a virtual displacement field $\delta\boldsymbol{u}$, results in

$$\delta\Pi_{\mathrm{int}}(\boldsymbol{u}, \delta\boldsymbol{u}) - \delta\Pi_{\mathrm{ext}}(\delta\boldsymbol{u}) + \delta\Pi_{\mathrm{c}}(\boldsymbol{u}, \delta\boldsymbol{u}) = 0\,, \quad \forall \delta\boldsymbol{u} \in \mathcal{V}\,, \tag{4.36}$$

where $\delta\Pi_{\mathrm{int}}$ and $\delta\Pi_{\mathrm{ext}}$ denote the *internal* and *external* virtual work, respectively. The symbol $\delta\Pi_{\mathrm{c}}$ represents the virtual work of contact forces. All these quantities are defined as

$$\delta\Pi_{\mathrm{int}}(\boldsymbol{u}, \delta\boldsymbol{u}) = -\sum_{i \in \{\mathrm{s},\mathrm{m}\}} \left[ \int_{\Omega_t^i} \boldsymbol{\sigma}^i : \nabla_x\left(\delta\boldsymbol{u}^i\right) \, \mathrm{d}\Omega_t^i \right], \tag{4.37a}$$

$$\delta\Pi_{\mathrm{ext}}(\delta\boldsymbol{u}) = -\sum_{i \in \{\mathrm{s},\mathrm{m}\}} \left[ \int_{\Omega_t^i} \boldsymbol{b}^i \cdot \delta\boldsymbol{u}^i \, \mathrm{d}\Omega_t^i + \int_{\gamma_\sigma^i} \boldsymbol{t}^i \cdot \delta\boldsymbol{u}^i \, \mathrm{d}\gamma_\sigma^i \right], \tag{4.37b}$$

$$\delta\Pi_{\mathrm{c}}(\boldsymbol{u}, \delta\boldsymbol{u}) = -\int_{\gamma_{\mathrm{c}}^{\mathrm{s}}} \boldsymbol{t}_{\mathrm{c}}^{\mathrm{s}} \left(\delta\boldsymbol{u}^{\mathrm{s}} - \delta\hat{\boldsymbol{u}}^{\mathrm{m}}\right) \, \mathrm{d}\gamma_{\mathrm{c}}\,. \tag{4.37c}$$

In Equation (4.37a) the operator $(\bullet) : (\bullet)$ denotes the tensor double contraction, that for a two generic second-order tensors $\boldsymbol{A}$ and $\boldsymbol{B}$ writes

$$\boldsymbol{A} : \boldsymbol{B} \equiv \sum_i \sum_j A_{ij} B_{ij}\,. \tag{4.38}$$

In turn, the spatial gradient of a virtual displacement vector field $\nabla_x(\bullet)$ is obtained by

$$\nabla_x(\delta\boldsymbol{u}) = \sum_{i=1}^{3} \sum_{j=1}^{3} \frac{\partial \delta u_j}{\partial x_i} \, \boldsymbol{e}_i \otimes \boldsymbol{e}_j\,. \tag{4.39}$$

The symbol $\delta\hat{\boldsymbol{u}}^{\mathrm{m}}$ used in Equation (4.37c) represents the virtual displacement of the projected point in the mortar side.

**Enforcement of the contact constraints**

The mortar finite element method for contact often pursues a *Lagrange multiplier*-based approach to enforce the contact constraints. This technique is applied to the current problem by defining the Lagrange multiplier vector $\boldsymbol{\lambda}$ as the negative contact traction on the mortar side,

$$\boldsymbol{\lambda} = -\boldsymbol{t}_{\mathrm{c}}^{\mathrm{s}}\,. \tag{4.40}$$

Similarly to the decomposition of the traction vector into a normal and a tangential components (cf. Equation (4.28)), the Lagrange multiplier vector $\boldsymbol{\lambda}$ can also be decomposed in a same fashion,

$$\boldsymbol{\lambda} = \lambda^{\eta}\boldsymbol{\eta} + \boldsymbol{\lambda}^{\tau} \,. \tag{4.41}$$

Equation (4.40) allows to rewrite the Equation (4.37c), i.e., the virtual work due to contact interactions as

$$\delta\Pi_{\mathrm{c}}\left(\boldsymbol{u}, \delta\boldsymbol{u}\right) = \int_{\gamma_{\mathrm{c}}^{\mathrm{s}}} \boldsymbol{\lambda}\left(\delta\boldsymbol{u}^{\mathrm{s}} - \delta\hat{\boldsymbol{u}}^{\mathrm{m}}\right) \,\mathrm{d}\gamma_{\mathrm{c}} \,. \tag{4.42}$$

In order to formulate the weak form of a mortar-based frictional contact problem, an appropriate solution space for the Lagrange multiplier has to be defined. Denoting the solution space of the Lagrange multiplier vector $\boldsymbol{\lambda}$ as $\mathcal{M}(\boldsymbol{\lambda})$ it is defined as the dual space of the restriction of the solution space $\mathcal{U}^{\mathrm{s}}$ to the potential contact boundary $\gamma_{\mathrm{c}}^{\mathrm{s}}$, constrained to ensure the non-penetration and frictional constraints in a weak sense. The interested reader is referred to Hüeber (2008) for a complete mathematical definition of the solution space of $\boldsymbol{\lambda}$. Being the contact constraints imposed as variational inequities [3], one can write the weak form of IBVP for frictional contact as follows:

**Problem 4.3 (Weak form of the IBVP of finite deformation frictional contact).**
*The solution for the kinematically admissible displacement field $\boldsymbol{u} \in \mathcal{U}$ and the Lagrange multiplier vector $\boldsymbol{\lambda} \in \mathcal{M}(\boldsymbol{\lambda})$, for all $t \in [0, T]$, must verify the PVW*

$$\delta\Pi_{\mathrm{int}}\left(\boldsymbol{u}, \delta\boldsymbol{u}\right) - \delta\Pi_{\mathrm{ext}}\left(\delta\boldsymbol{u}\right) + \int_{\gamma_{\mathrm{c}}^{\mathrm{s}}} \boldsymbol{\lambda}\left(\delta\boldsymbol{u}^{\mathrm{s}} - \delta\hat{\boldsymbol{u}}^{\mathrm{m}}\right) \,\mathrm{d}\gamma_{\mathrm{c}} = 0 \,, \quad \forall\delta\boldsymbol{u} \in \mathcal{V} \,, \tag{4.43}$$

$$\int_{\gamma_{\mathrm{c}}^{\mathrm{s}}} g\left(\delta\lambda^{\eta} - \lambda^{\eta}\right) \,\mathrm{d}\gamma_{\mathrm{c}}^{\mathrm{s}} \geq 0 \,, \quad \forall\delta\boldsymbol{\lambda} \in \mathcal{M}\left(\boldsymbol{\lambda}\right) \,, \tag{4.44}$$

$$\int_{\gamma_{\mathrm{c}}^{\mathrm{s}}} \boldsymbol{v}^{\tau} \cdot \left(\delta\boldsymbol{\lambda}^{\tau} - \boldsymbol{\lambda}^{\tau}\right) \,\mathrm{d}\gamma_{\mathrm{c}}^{\mathrm{s}} \leq 0 \,, \quad \forall\delta\boldsymbol{\lambda} \in \mathcal{M}\left(\boldsymbol{\lambda}\right) \,. \tag{4.45}$$

**Remark 4.4 on the simplification of the finite element formulation.**
*As mentioned in Remark 4.3 the previous description was focused on a more generic contact problem formulation, with both normal and tangential contact constraints. In the following section, the finite element approximation is introduced considering only the normal contact constraints, since the numerical works only focus on such case.*

## 4.3 Finite element approximation

Having derived the weak form of the finite deformation contact problem one can discretize such formulation in the light of the finite element method. The description shall focus only on the fundamental concepts of the mortar-based FEM for contact problems and the interested reader is referred to one of the sources presented in Remark 4.2 for more comprehensive treatments. The finite element discretization generally concerns obtaining an approximate solution for the displacement field (the primary value). With this

[3] The reader is referred to Kikuchi and J. T. Oden (2001) to a more in-depth approach of the topic.

approxmation, the finite dimensional spaces for both displacement and virtual displacement fields came denoted by $\mathcal{U}^h \subset \mathcal{U}$ and $\mathcal{V}^h \subset \mathcal{V}$. [4] The FEM approximation implies the division of the domain $\Omega = \Omega_t^{\mathrm{s}} \cup \Omega_t^{\mathrm{m}}$ in $n^e$ subdomains $\Omega_e \subset \Omega^h$, that verify

$$\Omega \approx \Omega^h \equiv \bigcup_{e=1}^{n^e} \Omega_e \,. \tag{4.46}$$

The solutions should be found at discrete points that correspond to the nodes that connect with each other forming a finite element mesh. The finite dimension subsets $\mathcal{U}^h$ and $\mathcal{V}^h$ are composed by basis functions with compact support and meet the differentiability requirements required by the weak form, cf. Equation (4.43). This approximation functions, also called *interpolation* or *shape functions*, are expressed in a element basis, being mapped to the parameter space:

$$\boldsymbol{\xi} = (\xi_1, ..., \xi_d) \,. \tag{4.47}$$

Using an isoparametric approach, it dictates that these functions are used to parametrize both displacement solution and the geometry in each subdomain $\Omega_e$. One shall mention that throughout this work the mortar approach is completely independent of the remaining quantities (eg. internal loads and external forces).

The field variables and boundary geometry are interpolated using shape functions of dimensions $d-1$. Contact interactions are evaluated at $\gamma_{\mathrm{c}}^i$, which means that a convenient relation can be established between the finite element discretization and the contact interface elements. One writes the boundary geometry interpolation as

$$\boldsymbol{x}^{\mathrm{s}} \approx \left\{\boldsymbol{x}^{\mathrm{s}}\right\}^h\Big|_{\left\{\gamma_{\mathrm{c}}^{\mathrm{s}}\right\}^h} = \sum_{k=1}^{n^{\mathrm{s}}} N_k^{\mathrm{s}}\left(\boldsymbol{\xi}^{\mathrm{s}}\right)\mathbf{x}_k^{\mathrm{s}} \,, \tag{4.48a}$$

$$\boldsymbol{x}^{\mathrm{m}} \approx \left\{\boldsymbol{x}^{\mathrm{m}}\right\}^h\Big|_{\left\{\gamma_{\mathrm{c}}^{\mathrm{m}}\right\}^h} = \sum_{l=1}^{n^{\mathrm{m}}} N_l^{\mathrm{m}}\left(\boldsymbol{\xi}^{\mathrm{m}}\right)\mathbf{x}_l^{\mathrm{m}} \,, \tag{4.48b}$$

and in a same fashion the field variables

$$\boldsymbol{u}^{\mathrm{s}} \approx \left\{\boldsymbol{u}^{\mathrm{s}}\right\}^h\Big|_{\left\{\gamma_{\mathrm{c}}^{\mathrm{s}}\right\}^h} = \sum_{k=1}^{n^{\mathrm{s}}} N_k^{\mathrm{s}}\left(\boldsymbol{\xi}^{\mathrm{s}}\right)\mathbf{d}_k^{\mathrm{s}} \,, \tag{4.49a}$$

$$\boldsymbol{u}^{\mathrm{m}} \approx \left\{\boldsymbol{u}^{\mathrm{m}}\right\}^h\Big|_{\left\{\gamma_{\mathrm{c}}^{\mathrm{m}}\right\}^h} = \sum_{l=1}^{n^{\mathrm{m}}} N_l^{\mathrm{m}}\left(\boldsymbol{\xi}^{\mathrm{m}}\right)\mathbf{d}_l^{\mathrm{m}} \,. \tag{4.49b}$$

In this formulation, $n^{\mathrm{s}}$ and $n^{\mathrm{m}}$ represent the number of nodes in the non-mortar and mortar sides, accordingly. The symbol $\left\{\gamma_{\mathrm{c}}^i\right\}^h$ denotes both discretized subdomains (mortar and non-mortar). The shape functions are denoted by $N(\boldsymbol{\xi}^i)$ and $\mathbf{x}$ and $\mathbf{d}$, the nodal coordinates and displacements, respectively. In the current work, the Lagrange multiplier vector $\boldsymbol{\lambda}$ is approximated based on the Lagrange multiplier space $\mathcal{M}^h \subset \mathcal{M}$ , and is obtained by interpolation on the non-mortar side, writing

$$\boldsymbol{\lambda} \approx \boldsymbol{\lambda}^h = \sum_{j=1}^{n^{\lambda}} \Phi_j\left(\boldsymbol{\xi}^{\mathrm{s}}\right)\mathbf{z}_j \,, \tag{4.50}$$

[4] Henceforth, the superscript $h$ will be used to represent a FE discretized variable.

where $\Phi_j$ denotes the Lagrange multiplier interpolation function, $n^\lambda$ is the number of nodes on the non-mortar side with additional degrees of freedom due to the Lagrange multiplier, and $\mathbf{z}_j$ si the nodal values of the Lagrange multipliers.

By introducing the finite element mortar discretization in the weak form of the problem (Equation (4.43)), two fundamental entities of the mortar methods arise: the so-called *first mortar coupling matrix* **D** and the *second mortar coupling matrix* **M**. The matrix elements are defined as follows

$$\mathrm{D}_{jk} = \int_{\{\gamma_\mathrm{c}^\mathrm{s}\}^h} \Phi_j(\boldsymbol{\xi}^\mathrm{s}) N_k^\mathrm{s}(\boldsymbol{\xi}^\mathrm{s}) \, \mathrm{d}\gamma_\mathrm{c}^\mathrm{s}, \quad \text{for } j = 1,...,n^\lambda, \; k = 1,...,n^\mathrm{s}; \tag{4.51}$$

$$\mathrm{M}_{jl} = \int_{\{\gamma_\mathrm{c}^\mathrm{s}\}^h} \Phi_j(\boldsymbol{\xi}^\mathrm{s}) N_k^\mathrm{m}(\hat{\boldsymbol{\xi}}^\mathrm{m}) \, \mathrm{d}\gamma_\mathrm{c}^\mathrm{s}, \quad \text{for } j = 1,...,n^\lambda, \; l = 1,...,n^\mathrm{m}. \tag{4.52}$$

It should be noted that the first mortar coupling matrix **D** is only related to the non-mortar quantities, whereas the second matrix **M** involve terms of both non-mortar and mortar sides. The evaluation of these *mortar integrals* requires the application of intricate numerical integration schemes and some examples can be found in Popp (2012), Farah *et al.* (2015) and Carvalho (2018). In the particular problem setup considered in this work, the *element-based* integration of the mortar integrals exhibits superior computational advantage without severely impinging upon the accuracy (Farah *et al.*, 2015)

**Remark 4.5 on the applicability of the second coupling matrix.**
*In the numerical studies performed within the context of this work, only the non-mortar side has Lagrange degrees of freedom to be determined (node displacements and Lagrange multipliers values), since the non-mortar side is considered to be flat and rigid. With this in mind, the second mortar coupling matrix* **M** *does not have to be computed since it encompasses the Lagrange multiplier values on the mortar side. This simplification introduces a significant improvement in computational performance. One can look at the mortar Lagrange multiplier values at the mortar side as prescribed quantities since one knows in advance their value—zero.*

### 4.3.1 Dual Lagrange multipliers and discrete constraints

The discrete Lagrange multiplier space $\mathcal{M}^h$ has to be properly defined. Due to the intricate mathematical formulation, the current section only aims to present the general ideas. The classical approach to the choice of Lagrange multipliers is the standard Lagrange multipliers where the boundary displacement interpolation functions $N_j^\mathrm{s}$ are used as Lagrange multiplier interpolation function $\Phi_j$. This option generates global couplings between displacements and Lagrange multipliers. An alternative approach, proposed by Wohlmuth, 2000, is to use the dual Lagrange multipliers. This method relies on the so-called *bi-orthogonality condition*, that writes

$$\int_{\{\gamma_\mathrm{c}^\mathrm{s}\}^h} \Phi_j(\boldsymbol{\xi}^\mathrm{s}) N_k^\mathrm{s}(\boldsymbol{\xi}^\mathrm{s}) \, \mathrm{d}\gamma_\mathrm{c}^\mathrm{s} = \delta_{jk} \int_{\{\gamma_\mathrm{c}^\mathrm{s}\}^h} N_k^\mathrm{s}(\boldsymbol{\xi}^\mathrm{s}) \, \mathrm{d}\gamma_\mathrm{c}^\mathrm{s}. \tag{4.53}$$

This approach introduces two main advantages. First, the first coupling mortar matrix **D** becomes diagonal, localizing the coupling conditions. Second, normal contact contstraints of the weak form Equation (4.44) becomes decoupled, that becomes a set of

point-wise conditions for all nodes in the non-mortar side — $j = 1, ..., n^{\mathrm{s}}$. It writes

$$\tilde{g}_j \geq 0\,, \tag{4.54a}$$

$$z_j^{\eta} \geq 0\,, \tag{4.54b}$$

$$\tilde{g}_j z_j^{\eta} = 0\,. \tag{4.54c}$$

The discrete weighted gap, denoted by $\tilde{g}$

$$\tilde{g}_j\left(\boldsymbol{\xi}^{\mathrm{s}}\right) = \int_{\{\gamma_{\mathrm{c}}^{\mathrm{s}}\}^h} \Phi_j\left(\boldsymbol{\xi}^{\mathrm{s}}\right) g^h\left(\boldsymbol{\xi}^{\mathrm{s}}\right)\, \mathrm{d}\gamma_{\mathrm{c}}^{\mathrm{s}}\,. \tag{4.55}$$

The simplification of the contact problem only to normal contact constraints implies that the tangential component of the Lagrange multiplier vector $\boldsymbol{\lambda}^{\tau}$ becomes null.

Even though the application of the dual interpolation functions in the definition of the weighted gap leads to the popular pointwise decoupling of the contact constraints, it is often useful to employed distinct weighting functions, due to the positivity-requirement classical in computational contact mechanics. In this work, a Petrov-Galerkin approach is pursued in the definition of the weighted gap, by using the standard shape functions as gap weighting functions. This permits avoiding the negative part of the dual interpolation functions and thus eliminate the possibility to detect false positive active contact nodes (Popp *et al.*, 2013).

### 4.3.2 Primal-Dual active set strategy

The previous formulation for the normal contact problem has additional sources of non-linearities when comparing with the classic non-linear solid mechanics problem, due to the contact inequality constraints. This adversity is treated by reformulating these nodal constraints using the *Nonlinear Complementary* (NPC) function. For a frictionless contact the NPC function in the normal direction is defined as Hüeber and Wohlmuth (2005)

$$C_j^{\eta}(\mathbf{d},\, \mathbf{z}) = z_j^{\eta} - \max\left\{0,\; z_j^{\eta} - c^{\eta}\tilde{g}_j\right\}, \quad c^{\eta} > 0\,. \tag{4.56}$$

where $c^{\eta}$ is the normal complementary parameter, which proves to have influence in the convergence rate and not in the precision of the method. Therefore, the NPC function can be used to replace the Equations (4.54) into a more convenient form, i.e., by verifying the following

$$C_j^{\eta} = 0, \quad j = 1, ..., n^{\mathrm{s}}\,. \tag{4.57}$$

In Figure 4.5 the NPC function is presented, where one sees that its is equivalent to the KKT conditions. One can also easly distinguish between *active* and *inactive* contact branches. The biggest advantage of this type of constraints imposition is that it allows treating the KKT conditions as non-linear equations, passable to be soaked into a loop that leads with all sources of non-linearities of the problem.

## 4.4 A contact homogenisation approach to rough contact

This section outlines the computational contact homogenisation approach to rough contact, based on the dual mortar-based finite element implementation described earlier. This strategy relies on the definition of the *Representative Contact Element* to be presented in detail in the next sections.

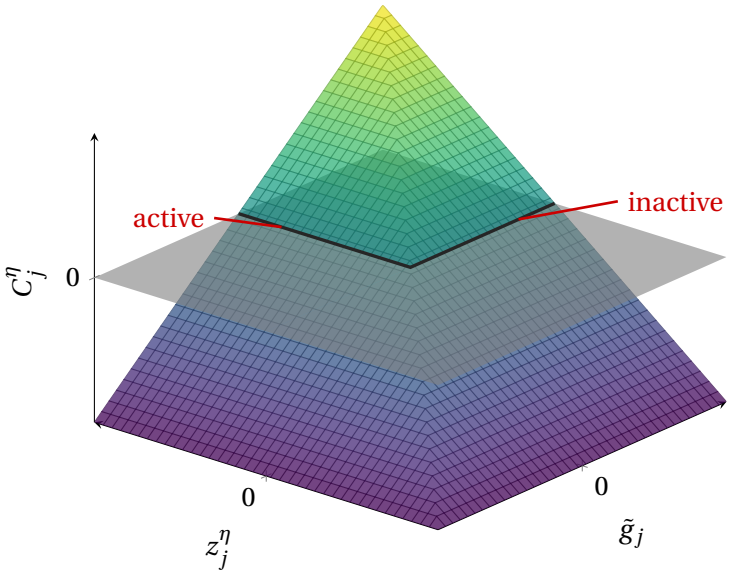


**Figure 4.5:** Nodal complementarity function $C_j^\eta$ for the normal contact constraints (with $c^\eta = 1.$). Adapted from Carvalho (2018).

### 4.4.1 Representative Contact Element

The modelling of micromechanical contact problems with the Finite Element Method requires the definition of the so-called *Representative Contact Element* (RCE). The RCE shall be chosen such that it is capable represent the macro behaviour of the system in study. Therefore, parameters and dimensions have to be established in order to obtain an RCE with statistical representativeness.

**RCE Geometry**

One must start by defining the geometry of the RCE. The class of contact problems studied in this work are encompassed by the same class the *Signorini* type of problems. These simplify the contact problem to two bodies in contact where one of them is considered rigid and the other deformable and elastic. The deformable body (RCE) is considered to be the one that possesses the rough surface and contacts against a rigid flat surface. The RCE assumes a form of a parallelepiped for the tridimensional case or a rectangle in a bi-dimensional problem, with a rough boundary in one of the faces. The dimensions of RCE will be defined ahead. A schematic representation of the RCE for both 2D and 3D cases is presented in Figure 4.6.

**RCE parameters**

A representative element for rough contact has to be established in order to perform numerical studies with the guarantee that results can be representative of the case in study—at least on average. Some studies on the representativeness of a rough element have been made in the past years, yet only concerning Gaussian topographies. Yastrebov, Anciaux, *et al.* (2012) have performed numerical studies on a representative element for rough surface contact problems, yet concerning a Boundary Element Method (BEM) framework, resulting in the definition of *Representative Self-affine Surface Element* (RSSE).

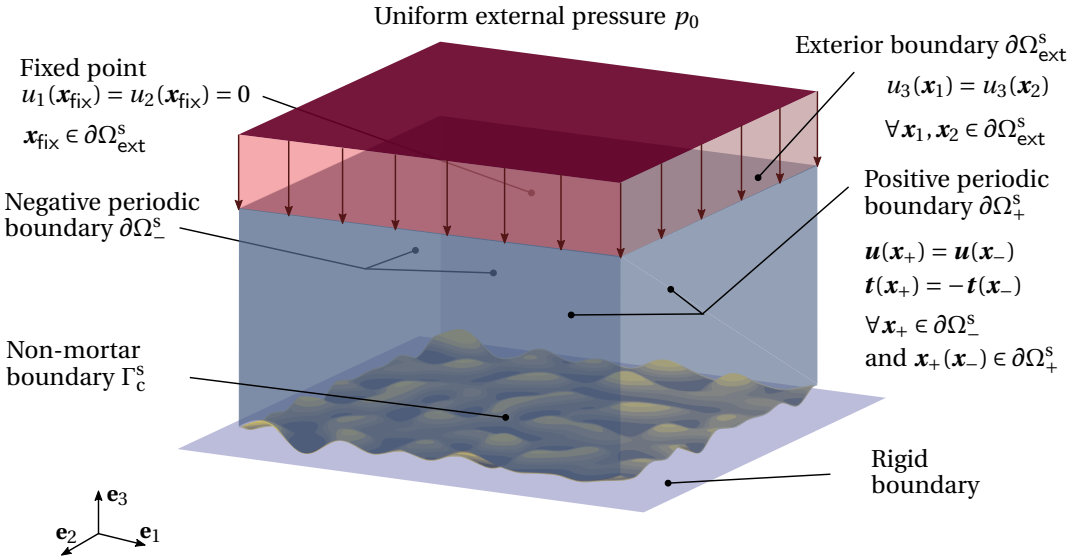


**(a)** 3D model

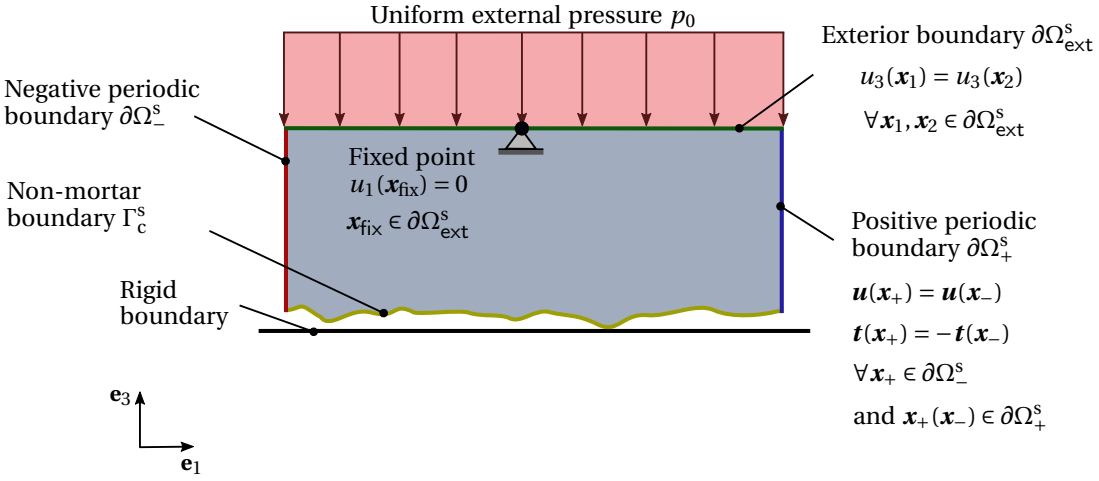


**(b)** 2D model

**Figure 4.6:** Numerical model setup used for simulation the RCE with the FEM, in two and three dimensions. Adapted from Couto Carneiro (2019).

Within the context of FEM, up to recently, only studies concerning the influence of the height of the RCE blocks have been made (Temizer and Wriggers, 2008; De Lorenzis and Wriggers, 2013). More recently in the work of Couto Carneiro (2019), posteriorly extended in Couto Carneiro *et al.* (2020), the definitions of a statistically representative contact element have been assessed with focus on 2D RCEs.

The goal of the previous works was to define a set of parameters, such that they can consistently give the response of the prescribed system, defined by the wavelength ratio $\lambda_l/\lambda_s$ and Hurst exponent $H$, considering fractal-only surfaces with a Gaussian heigh distribution. The parametric studies focused on the convergence with mesh size, length, height and number of realisations. All the numerical procedures are conveniently described in both works and the interested reader is referred to them for more details. In short, it resulted in the definitions of a set of rules of thumb that intent to describe a complete 2D RCE, in the case of Gaussian profiles considering only the elastic behaviour and subjected to normal, frictionless and non-adhesive contact:

$$\lambda_s/\Delta x \geq 8\,; \tag{4.58a}$$

$$L/\lambda_l \geq 8\,; \tag{4.58b}$$

$$H_{\text{sub}}/\sigma_z \geq 160\,; \tag{4.58c}$$

$$H_{\text{r}}/\sigma_z \geq 40\,; \tag{4.58d}$$

$$\text{Number of realizations} \geq 20\,. \tag{4.58e}$$

The first condition (4.58a) refers to the mesh size of the RCE and is presented in terms of the smallest wavelength $\lambda_s$ since this is the most affected by the discretization of the mesh. The condition states that the mesh should be such that mesh increment $\Delta x$ is at least 8 smaller than $\lambda_s$. The following conditions (4.58b) and (4.58c), refer to the length $L$ and height of the substrate $H_{\text{sub}}$ of the 2D RCE, respectively. The length size is measured in relation to the longest wavelength and it is proposed that it must be equal or superior in 8 times the $\lambda_l$ value. In turn, the height of the substrate is referred in order to the standard deviation of heights or RMS height, if one recalls that $z_{\text{rms},x} = \sigma_z$. The height of a fine resolution near the contact interfaces $H_{\text{r}}$ is also defined in relation to the RMS height—to resolve the high-stress gradients. One must remember that from Equation (2.16a) and (2.34a) the standard deviation of height can be written as $\sigma_z = \sqrt{m_0}$—this nomenclature is also used is works on this field, such as in Couto Carneiro *et al.* (2020). Finally, a minimum number of 20 realizations is considered to be sufficient to overcome the effects of randomness in each individual realisation.

**Remark 4.6 on RCE parameters for non-Gaussian rough surfaces.**
*As it has been recurrent in this research topic, past experiments have been made considering Gaussian surfaces. Due to the lack of studies on the field of non-Gaussian rough surfaces, one should accept the Gaussian results as a decent approximation of the RCE parameters in this case. In this study, Weibull rough surfaces are considered and then it is believed that no loss of representativeness should be seen for values near the Gaussian case, such as $C = 3{,}602$ and $C = 2$. If extreme cases are considered, like $C = 1$ representativeness may be lost, yet the relative behaviour of the surfaces is still captured, fulfilling the main goal of the study.*

### 4.4.2 Boundary conditions

In order to obtain a feasible set of boundary conditions to the RCE a few considerations have to be made—the further advances should be read with the help of Figure 4.6. Within the dual mortar methodology, the rough boundary is picked as the non-mortar boundary while the mortar side is set as the rigid flat boundary. This definition allows to explicitly obtain the values of the Lagrange multipliers for the rough contact, thus directly leading with the pressure distribution due to contact. In order to follow the concept of the RCE, periodic conditions have to be assigned to the faces of the deformable block. This principle is valid inasmuch as the micromechanical problem continues relatively small to the macroscopic situation that is trying to replicate. The periodicity must also be guaranteed in the rough surface, keeping the consistency of the imposed boundary conditions—a condition that is already satisfied by the nature of the topography generation process based on FFT. Finally, the periodic condition implies, in the boundaries of the deformable block, denoted by $\partial\Omega^{\mathrm{s}}_{+}$ and $\partial\Omega^{\mathrm{s}}_{-}$, for positive and negative boundaries, respectively, tthe following conditions for displacements

$$\boldsymbol{u}(\boldsymbol{x}_{-}) = \boldsymbol{u}(\boldsymbol{x}_{+}), \quad \text{for } \boldsymbol{x}_{+} \in \partial\Omega^{\mathrm{s}}_{+}, \text{ and } \boldsymbol{x}_{-}(\boldsymbol{x}_{+}) \in \partial\Omega^{\mathrm{s}}_{-}\,, \tag{4.59}$$

and for the surfaces tractions it must be verified

$$\boldsymbol{t}(\boldsymbol{x}_{-}) = -\boldsymbol{t}(\boldsymbol{x}_{+}), \quad \text{for } \boldsymbol{x}_{+} \in \partial\Omega^{\mathrm{s}}_{+}, \text{ and } \boldsymbol{x}_{-}(\boldsymbol{x}_{+}) \in \partial\Omega^{\mathrm{s}}_{-}\,. \tag{4.60}$$

Relatively to the top boundary of the deformable block, here denominated $\partial\Omega^{\mathrm{s}}_{\mathrm{ext}}$ the same amount of vertical displacement $\bar{u}_3$ must be verified in all nodes on this domain. To avoid rigid body motions in planar directions, that can occur in certain less stable force balances, an arbitrary node $\boldsymbol{x}_{\mathrm{fix}} \in \partial\Omega^{\mathrm{s}}_{\mathrm{ext}}$ is considered to be only able to move vertically (perpendicularly to the contact interface). The rough block is loaded by a uniform pressure $p_0$ also at the top boundary, which is incrementally added to the model during the solving stage. For each increment, the equilibrium of the model is founded and the solutions for a certain fraction of $p_0$ determined—this incremental procedure is fundamental for obtaining the area-pressure curves, as it will be further investigated on the numerical studies discussion. The contact condition requires that, at least, one node is in contact in the initial configuration. Such condition is imposed when pre-processor the realization, imposing that at least a bit portion of the rough surface is penetrating the flat boundary—several strategies can be used, for instance, a certain fraction of the RMS heigh or a fraction of the maximum summit/peak of the topography. The 2D simulations follow the same conditions here exposed with the additional plane strain condition—one of the dimensions is considered greater than the others, e.g. the case of a strong anisotropic topography.

### 4.4.3 Materials

Due to the nature of the Signorini problem only the deformable body has a material assigned. In this work, only the elastic domain was considered and in order to keep a practical application of the results the conventional properties of the steel were considered. Note that, in Chapter 2 both Figure 3.14 and Table 3.2 the skewness and kurtosis values were analysed for machined surfaces, where steel as a predominance. The elastic

properties of the deformable body are presented in Table 4.1. Within the nonlinear finite element implementation employed in the present work, elasticity is modelled by means of the *Hencky* material model. To the rigid body no material needs to be assigned as the rigid condition implies the consideration of *infite stiffness* to the contact problem.

**Table 4.1:** Elastic properties of the rough block used throughout the tests.

| Material | $E$ /GPa | $\nu$ |
|---|---|---|
| Steel | 210 | 0.3 |

### 4.4.4 Roughness properties

As it was seen in Chapter 2 the topographies in the study are considered to be self-affine being the fractal features of the surface assigned through the Hurst exponent $H$ and the wavelengths that limit the PSD, i.e., the large and short cut-off wavelength $\lambda_l$ and $\lambda_s$ and the roll-off frequency $\lambda_r$—cf. Figure 2.12 for a recall on these quantities. In the previous numerical studies of the statistics of non-Gaussian rough surfaces, a very convenient simplification was done in order to reduce the degrees of freedom of the studies: it was considered only the fractal part of the PSD. This simplification allows to use the wavelength ratio $\lambda_l/\lambda_s$ as an input parameter the second input parameter to define the PSD of a rough surface. The ratio $\lambda_l/\lambda_s$ can also be used to define specific properties of a rough topography like the RMS slope, which has a crucial role in controlling the overall smoothness of the surface. This parameter has a crucial importance on the convergence of the FE mesh. A common procedure is to prescribe a certain value of the RMS slope and to compute the scaling factor that satisfies it through the spectral moments. The expression required for the surfaces' case have been already exposed in Section 3.2.5, from Equations (3.35) to (3.37). In a similar fashion, for a rough profile, the power spectral density of a self-affine, given by Equation (2.50), can be written in its discrete version as

$$\hat{\Phi}^{\theta}\left[k=\frac{p}{N}\Omega_s\right]=\begin{cases}\hat{C}_0' & , \quad k_l \le k < k_s \\ \hat{C}_0'\left(\dfrac{k_r}{k}\right)^{1+2H} & , \quad k_r \le k \le k_s \\ 0 & , \quad \text{elsewhere}\,.\end{cases} \tag{4.61}$$

where $\hat{C}_0'$ is a discrete scale constant. One should note that the discrete PSD is obtained by sampling the continuous version and dividing it by the sampling length $l_s$. Therefore, for a aliasing free samples it follows

$$\hat{\Phi}^{\theta}[q]=\frac{1}{l_s}\Phi_{\theta}\left(\frac{q}{N}\Omega_s\right), \qquad q=0,1,2,....,N/2\,. \tag{4.62}$$

Using this relation in the definition of the spectral moments (Equation (2.32)) one can obtain the analytical expressions of the zeroth, second and fourth order moments, needed to compute $\alpha$, as it was written in Equation (2.37). The spectral moments and the Nayak


**Figure 4.7:** LINKS logo.

parameter come written for a rough profile as

$$m_0 = \frac{l_s \hat{C}_0' k_r}{\pi}\left(1-\xi+\frac{1-\zeta^{-2H}}{2H}\right); \tag{4.63a}$$

$$m_2 = \frac{l_s \hat{C}_0' k_r^3}{\pi}\left(\frac{1-\xi^3}{3}+\frac{\zeta^{2-2H}-1}{2-2H}\right); \tag{4.63b}$$

$$m_4 = \frac{l_s \hat{C}_0' k_r^5}{\pi}\left(\frac{1-\xi^5}{5}+\frac{\zeta^{4-2H}-1}{4-2H}\right); \tag{4.63c}$$

$$\alpha = \left(1-\xi+\frac{1-\zeta^{-2H}}{2H}\right)\left(\frac{1-\xi^5}{5}+\frac{\zeta^{4-2H}-1}{4-2H}\right)\Big/\left(\frac{1-\xi^3}{3}+\frac{\zeta^{2-2H}-1}{2-2H}\right)^2. \tag{4.63d}$$

In this equations the wavelengths are arranged in a form of wavelength ratios being $\xi = \lambda_r/\lambda_l$ and $\zeta = \lambda_r/\lambda_s$. One verifies from these equations that, despite being used for the computation of the parameters, both the scaling factor $\hat{C}_0'$ and the sampling length $l_s$ are not contained in the $\alpha$ analytical expression, being written only as a function of the wavelengths ratios and the Hurst exponent $H$. Recent studies have used surfaces with RMS slope of 0.1, verifying good physical results (Pei *et al.*, 2005; Yastrebov, Anciaux, *et al.*, 2012, 2015), being this value also employed in the numerical studies of this work.

### 4.4.5 Numerical framework for rough contact analysis

In this section, the focus is placed on the fundamental aspects of the FEM modelling of rough contact based on the dual mortar approach introduced previously. The numerical studies were based on two different tools that combined together provide a feasible and versatile framework for such class of problems. The FEM calculation process is carried out by the `Fortran` in-house code denominated `LINKS` (Large Strain Non-Linear Analysis of Solids Linking Scales) (Figure 4.7) developed by the research group CM2S (Computational Multi-Scale Modelling of Solids ans Structures)—details on this code can be found in Reis (2014) and Lopes (2019), for instance. This code can robustly deal with several advanced computational problems, such as contact, and is equipped with an implicit solver for small and large strains, capable of modelling general constitutive models. The rough contact problem is specifically treated with a pre- and post-processor named `LINKS-RC`, and implemented in `Python`—for details on the implementation the reader is referred to Couto Carneiro (2019). This tool has already been introduced in Section 3.1.2 where the generation of Gaussian and non-Gaussian rough topographies was tackled. In fact, the topography generation process constitutes a pre-processing stage *per si*, yet additional steps are required for setting up the model, as will be described in the current chapter.

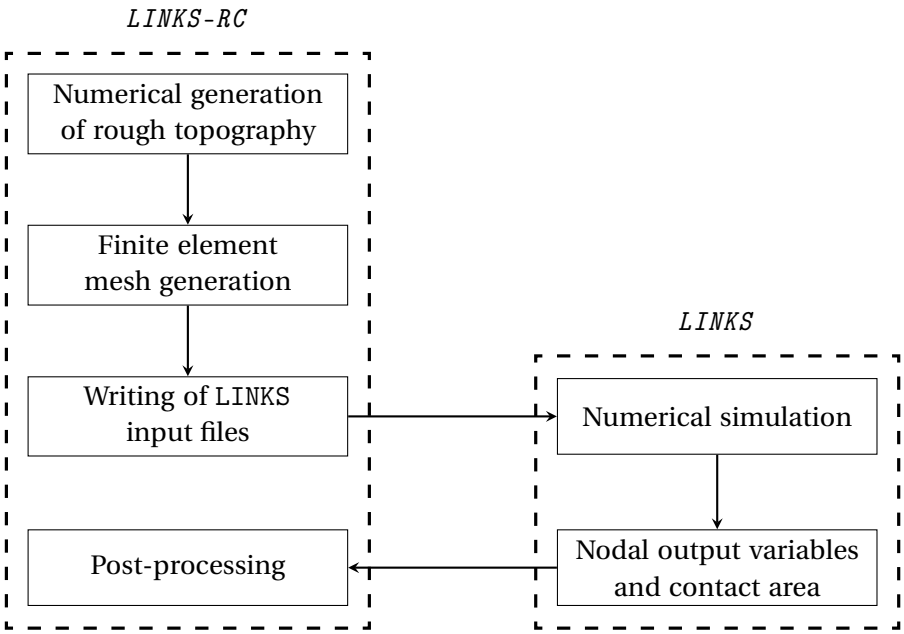


**Figure 4.8:** General framework of numerical tools used to process rough contact.

An overview of the framework for rough contact is schematically shown in Figure 4.8. As seen, the process starts with the LINKS-RC module where the numerical generation of random rough surfaces is done, being followed by a FEM mesh generation process. The LINKS input file can be then generated for several configurations with different topography properties. Is also possible to obtain different realizations for the same rough topography set of features, allowing to overcome the random character of these problems. After the numerical solution is obtained with LINKS, both contact area fraction and a list of nodal output variables are recovered and can be then treated with LINKS-RC's post-processing features.

### 4.4.6 Meshing process

Micromechanical contact of rough surfaces, due to its dependence on the geometric details, requires particular attention to the mesh generation process. In this type of phenomenon, the majority of the interesting mechanical behaviours occurs in a thin boundary layer near the contact interface, therefore requiring a really fine discretization in order to capture the most interesting results. Nevertheless, the mesh does not have to be as fine throughout all the RCE height as the one used to discretise the rough features. To embrace these requirements and reduce the computational cost, as a more discrete mesh also translates into a more expensive numerical study, the mesh should get coarser as one moves away from the rough boundary. Different strategies can be employed to perform such size reduction. One can simply apply a gradient on the element characteristic length reducing this dimension along with the height of the block. Alternatively, structured mesh transitions are typically applied to this type of problems, such as the ones used in Stupkiewicz (2007) and Yastrebov (2013). These transitions take advantage of

compacting schemes techniques merging a certain number of elements to a single one, adopting different configurations according to the element implemented.

In the current work, two different strategies are used to optimize the transition scheme having in mind two main goals. On one hand, the reduction of transitions layers, i.e., the capacity to transition the number of elements in the small number of layers possible. On the other hand, the reduction of the overall number of elements used in the transition, thus reducing the computation cost. For the 3D simulations a transition scheme 9 to 1 was used, based on 3 different type of elements. The transitions layer is constituted by:

- 8-node hexahedral element (HEXA8-FBAR) — 1 element;
- 5-node pyramidal element (PYRA5) — 4 elements;
- 6-node wedge element (WEDGE6) — 4 elements.

The remaining elements of the 3D mesh are also the hexahedral ones (HEXA8-FBAR). In the 2D case, the transition scheme is 3 to 1 yet with a more simple methodology since only one type of element is used. The 2D mesh is completely made out of 4-node quadrangular bilinear elements (QUAD4-FBAR). In Figure 4.9 two examples of the FE meshes generated for both 2D and 3D cases are presented. The type of elements employed in each mesh is depicted as well as the transition scheme. The 3D FE transition scheme is detailed in Figure 4.10.

It should be noted that *F-bar* elements in order avoid the occurrence of *volumetric locking*, which is more likely to happen for large strains in low order standard finite elements, ensuring more precise results. The *F-bar* techniques consists in splitting the deformation gradient in a volume-preserving component (*isochoric*) and a purely dilatational component (*volumetric*). While the isochoric component is computed in the Gauss point where the stress tensor will be established, the volumetric component is computed at the centroid of the element. One should also resemble that the problems appointed before could have been also solved if high order elements were considered. Nonetheless, the computational cost associated with this option is considerable and the more simple approach of linear elements favours the selected choice.

Finally, one should mention that the FE mesh in the rough boundary has to be the smoothest as possible to favour the good application of the numerical method. Yet, one cannot refine the generated surface by increasing the number of elements, neither by interpolating more points in between the generated ones, since it would not preserve the surfaces imposed PSD. A consistent discretization has to be employed during the numerical framework and therefore the smoothness of the mesh is defined in the surface generation process.

### 4.4.7 Computation of the real contact area

A fundamental aspect of the FE methodology for analysing the mechanical behaviour of rough contact is how the real contact area is evaluated. To obtain the evolution of the real contact area as a function of the external load applied to the RCE its value has to be calculated for each load increment. A first approach to the real contact area is that the real contact area can be computed as the fraction of the nodes that have non-zero pressure, for a given increment. Despite being a geometrically correct approach it

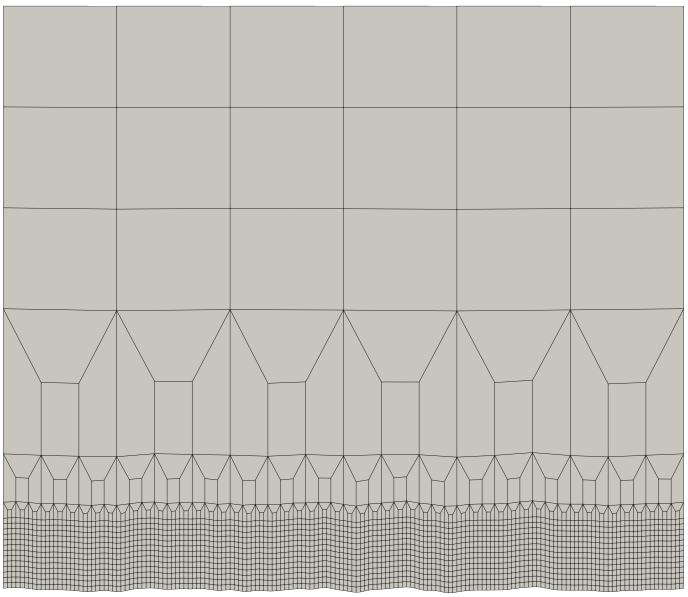

**(a)** 2D FE mesh

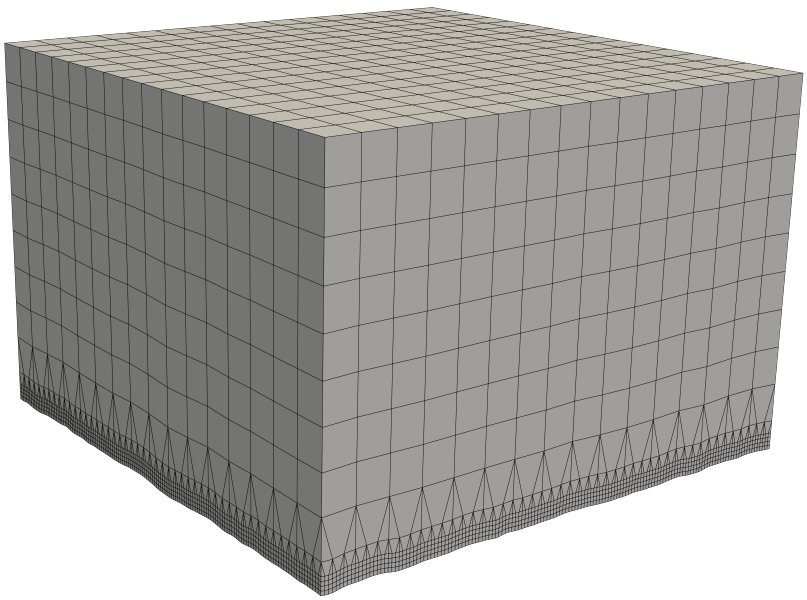

**(b)** 3D FE mesh

**Figure 4.9:** Illustrative examples of the finite element meshes generated by the `LINKS-RC` module for both 2D and 3D cases.

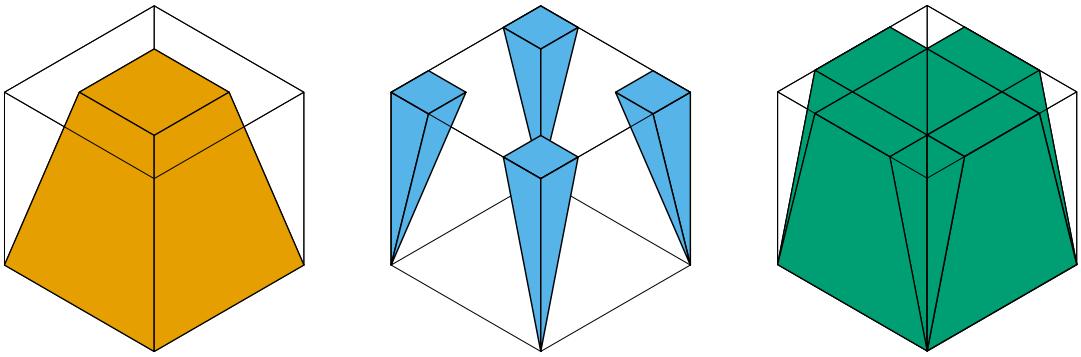

**(a)** 1 element HEXA8-FBAR **(b)** 4 elements PYRA5 **(c)** 4 elements WEDGE6

**Figure 4.10:** Finite elements employed in the mesh transition.

is highly dependent on how refined the rough boundary is. Two different strategies can be used to compute the numerical real contact area. The first one relies on summing all the boundary areas of the nodes that are in contact, i.e., belong to the active set, such that the contact area fraction is the proportion of active nodes relative to the total number of rough nodes. This area value is commonly called *node-based*, being also referred as *upper bound* area. The second strategy for computing the real contact area is the so-called *element-* or *segment-based* and states that the area of an element is summed only if all the nodes of the element belong to the active set. This methodology tends to underestimate the real contact area, justifying the parlance *lower bound*. To illustrate both methodologies the Figure 4.11 is introduced, where one can see that both techniques can lead to significatively different values of area. A practical measure to obtain a more accurate value is by simply average the upper and lower bound. This methodology that was implement in this work due to is simplicity and applicability. One must note that further developments in this topic, namely, the work of Yastrebov, Anciaux, *et al.* (2017a), a correction to the node-based area is proposed. Denoting the node-based area by $A_{\text{node}}$, the discrete contact perimeter by $S_d$ and the grid spacing (equal in both directions) by $\Delta x$, the correct area $A_{\text{cor}}$ comes as

$$A_{\text{cor}} = A_{\text{node}} - \frac{\pi - 1 + \ln 2}{24} S_d \Delta x \,. \tag{4.64}$$

In the previous equation, the contact perimeter $S_d$ is computed as the product between $\Delta x$ and the number of transitions between active and inactive nodes in both directions of the contact mesh. This strategy strongly accelerates the convergence of the real contact area, yet is only applicable to 3D problems.

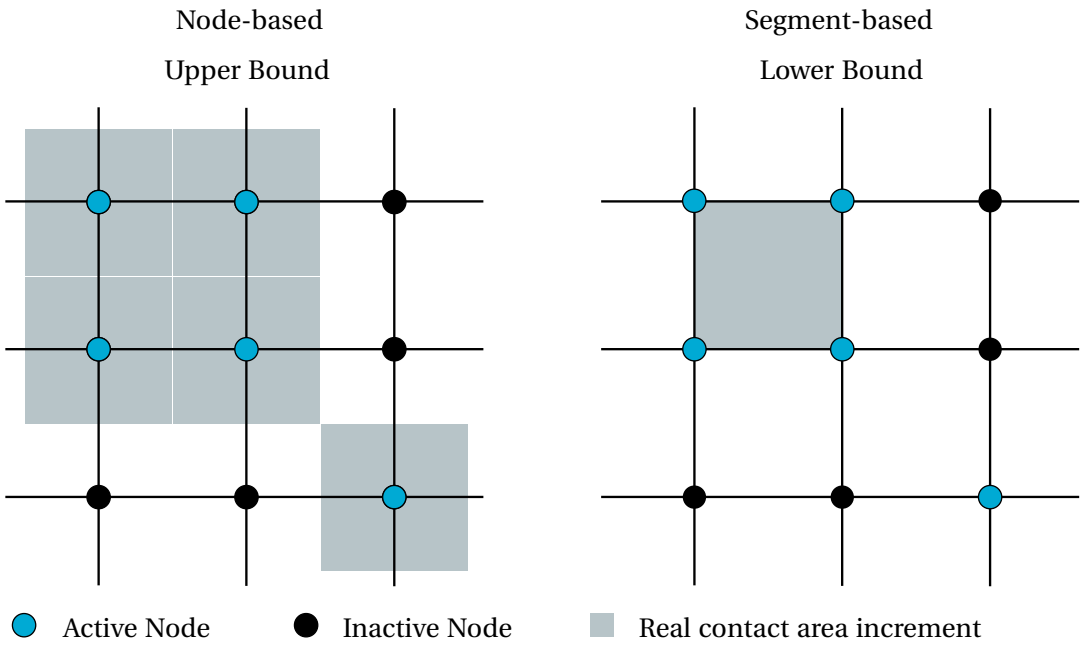


**Figure 4.11:** Strategies for computation of the real contact area. In this example the

*Page intentionally left blank*

# Chapter 5

# Finite element analysis of non-Gaussian rough contact

In the previous chapter, a review on the FEM approach to rough contact adopted in the present work was presented. The particular problem to be analysed was also carefully addressed, highlighting the principal characteristics of the contact problem to solve, introducing the notion of RCE, meshing techniques and area computational strategies. The required conditions to perform FE studies on the elastic and frictionless rough contact were depicted, as well. The current chapter aims to address the numerical work that has been done on the characterization of the micromechanical behaviour of non-Gaussian rough surfaces, using the FEM framework. The results obtained are discussed around the real contact area evolution and the contact pressure distribution. For this reason, an initial section is dedicated to the introduction of the phenomena based on the well-known Gaussian results. The focus is then allocated to the numerical studies, starting with the initial mesh convergence study to validate the framework, and delving into more specific studies to explore the effects on non-Gaussianity and the topography's parameters.

## 5.1 Contact area evolution and contact pressure distribution

When to rough surfaces first get in contact, only a few regions on the interface are actually in touch. Consequently, the observed real contact area is smaller than the apparent, or nominal, contact area. For several applications, the knowledge of the real contact area is crucial, therefore it is important to characterize its relation with applied external pressure. It is known that the contact between two elastic Gaussian rough surfaces under frictionless and non-adhesive conditions can be reduced to the contact of an equivalent rough surface with a rigid flat plane (K. L. Johnson, 1985). In the past decades, the modelling of rough contact has attracted several concerted efforts, with many authors focusing on this topic. Since the contact of rough surfaces is inherently three-dimensional, the majority of the analytical solutions are proposed in 3D, as well. Also, the majority is concerned with Gaussian rough surfaces, and do not contemplate other types of height distributions. The first class of analytical models, named *asperity-based models* have started with the work of J. A. Greenwood, J. B. P. Williamson, *et al.* (1966), commonly named Greenwood and Williamson model (GW), that assumed summits as spherical asperities with the same

radius of curvature. Using Hertz's theory, the contact area and load, between surfaces and reference plane, can be obtained as a function of the separation. This work was enhanced by McCool (1986) (GW-McCool model) to incorporate the results from Nayak's theory (Nayak, 1971) and to more accurately compute other relevant quantities. The work of Bush *et al.* (1975) (BGT) proposed the most general asperity-based model, which has taken into account the change of curvatures of the asperities with the height, by modelling the summits as elliptic paraboloids. A simplification to this model was introduced by J. Greenwood (2006), originating the Greenwood-Williamson Simplified Elliptic model (GW-SE), by approximating the asperities as spheres with an effective average curvature. All these models are only able to predict area values on a small range of lower pressures, in a region known as *light-contact*. In Figure 5.1 the contact area evolution predicted by the introduced models is presented, for three different values of Nayak's parameter $\alpha$. In this figure, one verifies the typical linear behaviour associated with Gaussian topographies that only remains true within very small ranges of external pressure. This linearity is commonly associated with the superposition of the contact of the asperities since it is known from Hertz's theory that a single asperity in contact does not have a linear contact area evolution. However, within a rough surface and for very small pressure increments the balance between the contribution of all asperities in contact results in an approximately linear evolution. One also sees that the contact area evolution curves are strongly associated with the value of $\alpha$, with higher area values being predicted for lower $\alpha$ for the same normalised external pressure. This effect is strongly related to the distribution of the summit heights distribution, as was seen in Figure 3.1. This is a classical result of asperity-based models of Gaussian surfaces and has been proved numerically (Yastrebov, Anciaux, *et al.*, 2015).

Despite relying upon several approximations, one of the drawbacks of this type of models is not being capable of modelling *full-contact* conditions, i.e., the contact area evolution up to the nominal value of area is achieved. The Perssons's model, introduced in Persson (2001a,b), is the most acknowledged model inside the contact *fractal models*. This model has the ability of modelling multi-scale roughness features and does not rely on Hertz's theory for point contact. It is based on the evolution of the contact pressure distribution with increasing magnification and despite the criticism on the original formulation, the model gives an appropriate trend on the contact evolution on a Gaussian rough surface. In Figure 5.2 the evolution of the contact area is depicted up to full-contact alongside state-of-the-art numerical results from Yastrebov, Anciaux, *et al.* (2017b). One verifies that a certain underestimation of the real contact area is associated with this model, yet the evolution trend is almost perfectly captured. The evolution of Gaussian topographies up to full-contact in Gaussian topographies is represented by a non-linear behaviour, verifying a reduction in the area growth rate with the increase of the external pressure. This can be easily seen by looking at the asymptotic evolution of Persson's model that requires almost half of the external pressure to reach full contact conditions when comparing with the original model curve.

The Persson's model can also predict the contact pressure distribution for a given value of external pressure. The quantity gives important information on the behaviour of the surfaces in contact and should reflect the area at a given value of external pressure. In

Figure 5.3 the contact pressure distribution for a given value of four different values of external pressure is presented. It is seen that with the increase of the external pressure, the integral of the probability density of contact stresses increases and tends to move towards higher stress values. In fact, the higher the external pressure the more similar to a normal distribution the contact pressure distribution becomes, as it tends to reproduce the shape of the height distribution.

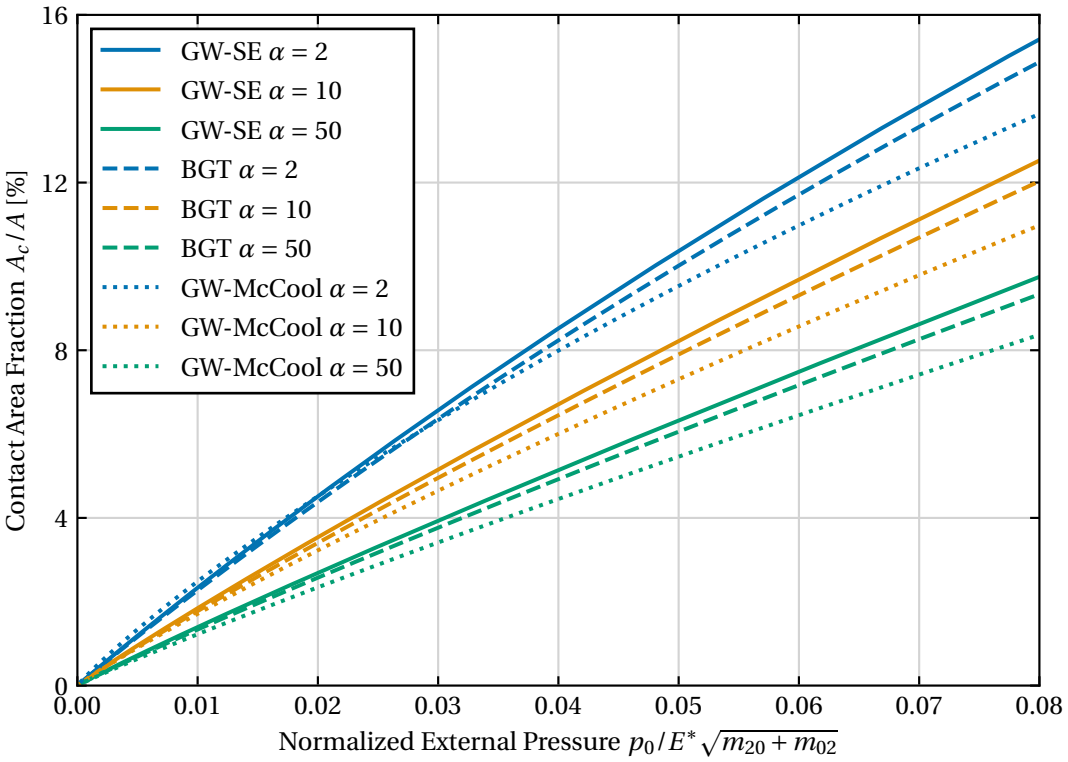


**Figure 5.1:** Comparison of the real contact area evolution between different asperity-based models for different values of Nayak's parameter $\alpha$, in the light-contact region.

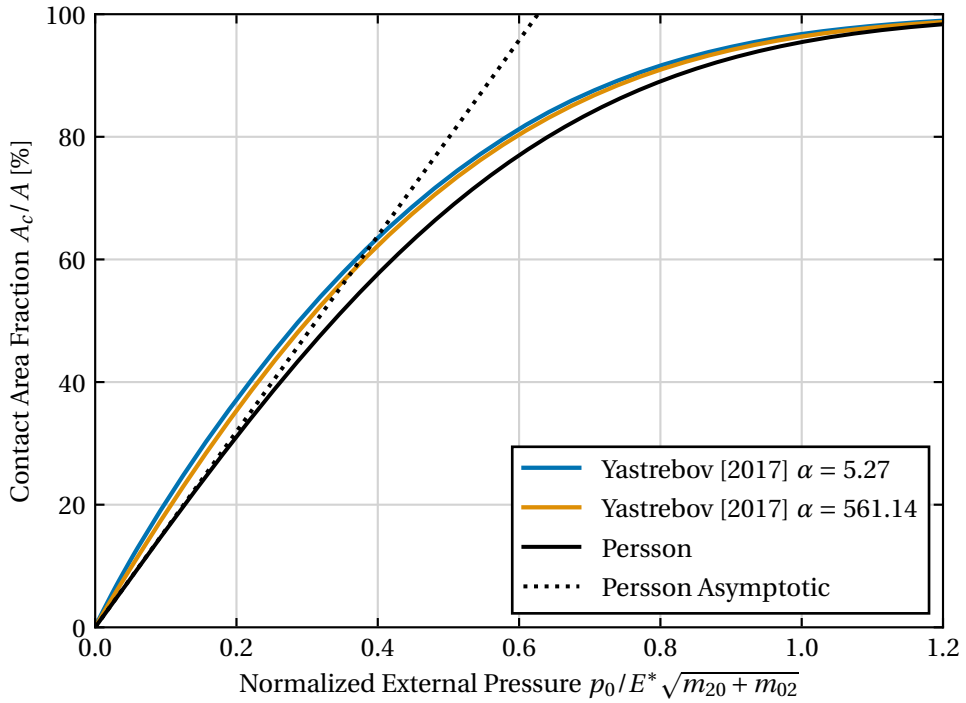


**Figure 5.2:** Comparison of the real contact area evolution between Persson's model and numerical results from Yastrebov, Anciaux, *et al.* (2017b), in the full-contact region.

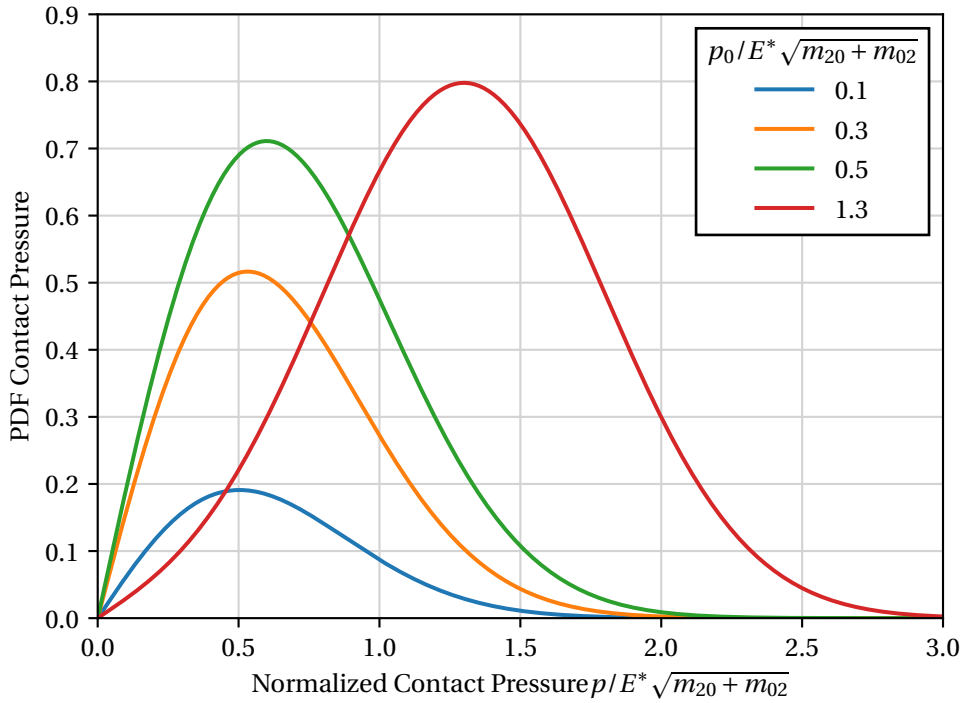


**Figure 5.3:** Comparison of contact pressure distribution for different values of normalized external pressure.

## 5.2 Mesh convergence study on the 2D FEM Analysis

The first 2D FEM study targets the mesh convergence of the real contact area fraction of non-Gaussian surfaces. Despite the purpose of the current work is not the definition of an RCE for analysing non-Gaussian rough surfaces, the mesh discretization has some capacity of changing previous observations (Couto Carneiro *et al.*, 2020). This thesis comes especially due to the fact that surfaces with positively skewed height distributions (as the ones produced by the Weibull Minimum distribution) tend to have higher summits (with higher curvatures), that may suffer large deformation and in which the poor discretization of the mesh may be significant. In addition, is also paramount to verify that the framework for FE analysis shows convergence with mesh refinement, under the present circumstances. [1] Therefore, as a starting point for the numerical studies, the evaluation of the effect of the mesh discretization was assessed by means of the parameter $\lambda_s/\Delta x$. Within this type of numerical studies, two distinct blocks can be outlined to describe the study setting. The first block is concerned with the roughness model of the surface, i.e., the properties that completely define the PSD and the height distribution of the rough surface. In turn, the second block is dedicated to the definition of the RCE in use and it contains the properties that have been shown in Section 4.4.1. These two blocks constitute the conditions of the 2D numerical study on the mesh convergence and for this study were set to: [2]

**Study 5.1 (Conditions of the convergence 2D FEM study).**

***Roughness Model***

| | |
|---|---|
| *RMS slope:* | $z'_{rms,x} = 0.1$ |
| *Wavelength ratio:* | $\lambda_l/\lambda_s = 8$ |
| *Hurst exponent:* | $H = 0.8$ |
| *Height distribution:* | *Weibull Max. and Min.* |
| *Shape parameter:* | $C = 1$ |

***RCE parameters***

| | |
|---|---|
| *Mesh:* | $\lambda_s/\Delta x \in [4, 8, 16, 32, 64]$ |
| *Length:* | $L/\lambda_l = 8$ |
| *Substrate height:* | $H_{\text{sub}}/\sigma_z = 500$ |
| *Fine mesh height:* | $H_r/\sigma_z = 40$ |
| *Number of realizations:* | $= 30$ |

Starting with the roughness model block, one verifies that the RMS slope was set to a value of 0.1 as was stated in Section 4.4.4. The value of the wavelength ratio $\lambda_l/\lambda_s$ was set to 8 since, in the work of Couto Carneiro *et al.* (2020), it was proved that the smaller the spectra bandwidth the higher the tendency for different mesh sizes to diverge. Respectively, to the Hurst exponent the value was defined for a value of $H = 0.8$ for numerical convenience (cf. Remark (5.1). The height distribution was modelled using

[1] This consideration may be better understood if ones revisits Figure 3.19.

[2] This scheme type for the definition of the simulation conditions will be followed in the current work.

the Weibull function in both Maximum and Minimum forms, as previously introduced (cf. Section 3.2.1). The shape parameter $C$ was carefully selected to reproduce the more distinct case relative to the Gaussian scenario, thus the value of 1 was defined.

**Remark 5.1 on the applicability of the Hurst value for the convergence study.**
*As mentioned, the Hurst value was defined to the value of $H = 0.8$, for numerical convenience. It should be noted that in the work of Couto Carneiro* et al. *(2020) it was verified, for Gaussian rough surfaces, that lower values of $H$ tend to have slower convergence rates. This means that a choice for a lower value of the Hurst exponent would probably constitute a better scenario for a mesh convergence study. Nonetheless, it should be kept in mind that the goal of this study is not the definition of an RCE for non-Gaussian surfaces. Furthermore, the chosen value of $H$, despite not being the critical case for mesh convergence, allows obtaining good results from which conclusions on the mesh convergence can be drawn.*

Regarding the definition of the RCE parameters the values are chosen are in tune with the results previously presented in Section 4.4.5. The parameter $\lambda_s/\Delta x$ was varied between 4 and 64 in order to verify its influence of the final results. In Figure 5.4 three examples of meshes with different values of $\lambda_s/\Delta x$ are shown. Moreover, the substrate height was set to a value of $H_{\text{sub}}/\sigma_z = 500$ to guarantee the modelling of the bulk, and by the fact that it does not represent a meaningful increase in the computational time. Also, the number of realizations was increased to 30 allowing for a better representation of the convergence results. These conditions have resulted in RCEs with a significantly different number of nodes and elements, as depicted in Table 5.1. The number of nodes increases exponentially with the mesh discretization which is also reflected in the computational time required. The average time of each case is presented in Table 5.2. Considering the 30 realizations for each case, the total simulation time was about 275 hours (around 11 days). To massively reduce the computation time, multiple realisations are solved in parallel in a desktop workstation. A reduction in the computational time can be obtained by using multiple cores yet memory usage requirements also increase creating a limitation on the maximum number of simulations running in parallel.

**Table 5.1:** Number of elements and nodes per each RCE, for each value of $\lambda_s/\Delta x$ considered in the 2D FEM convergence study.

| $\lambda_s/\Delta x$ | No. Nodes | No. Elements |
|---|---|---|
| 4 | 2854 | 2700 |
| 8 | 10647 | 10340 |
| 16 | 39003 | 38418 |
| 32 | 150963 | 149796 |
| 64 | 593763 | 591432 |

**Table 5.2:** Average computational time (in minutes) required to perform a 2D FEM convergence study.

| Height Distribution | $\lambda_s/\Delta x$ | Average computational time / min |
|---|---|---|
| Weibull Maximum | 4 | $\approx 1$ |
| | 8 | $\approx 3$ |
| | 16 | $\approx 10$ |
| | 32 | $\approx 48$ |
| | 64 | $\approx 239$ |
| Weibull Minimum | 4 | $\approx 1$ |
| | 8 | $\approx 2$ |
| | 16 | $\approx 9$ |
| | 32 | $\approx 40$ |
| | 64 | $\approx 197$ |

### 5.2.1 Discussion of results

The results of this numerical study are very interesting and show some important details, which will be discussed hereafter. Firstly, the analysis places focus on the results up to the full contact region, i.e., considering the evolution of the area from 0 almost up to 100% of relative area fraction—the ratio between the real contact area $A_c$ and the nominal contact area $A$. In addition, the evolution of the area is evaluated by both methods refereed in the Section 4.4.7, namely the node-based (upper-bound) and the segment-based (lower-bound), and therefore ensuring a more methodized framework. Figures 5.6 and 5.6 show the results of the numerical study on the convergence of the mesh for both Weibull Maximum and Weibull Minimum cases. The curves of both distributions show convergence with the mesh refinement, i.e., with the increase the value of $\lambda_s/\Delta x$. Also, both strategies for area evaluation seem to be in tune with what was advanced in Section 4.4.7. While the upper-bound area seems to overestimate the real contact area and the refinement of the mesh results in lower values of the real contact area, the inverse is verified for the lower area where a fine mesh increases the value of the area, indicating the underestimation of this method.

A straightforward method to evaluate the convergence is by computing the error relative to the most refined case—$\lambda_s/\Delta x = 64$ case. By doing so, one obtains a easier visualization of the convergence results as it is seen in the inset graphs of Figures 5.6 and 5.6. Regarding the Weibull Maximum's curves (Figure 5.6) the convergence of the results is once again highlighted. It is seen that the curve with $\lambda_s/\Delta x = 4$ presents the largest value of relative error and stands out particularly for the upper-bound area. The remaining results verify smaller differences, emphasising the asymptotic convergence towards the case $\lambda_s/\Delta x = 64$ . On the other hand, Weibull's minimum results show less smooth error curves with increasing pressure, yet without impinging upon the overall convergence at any time. In order to explore the lack of smoothness of these results, one must first note that for both heigh distribution cases the errors tend to reduce with the increase of the

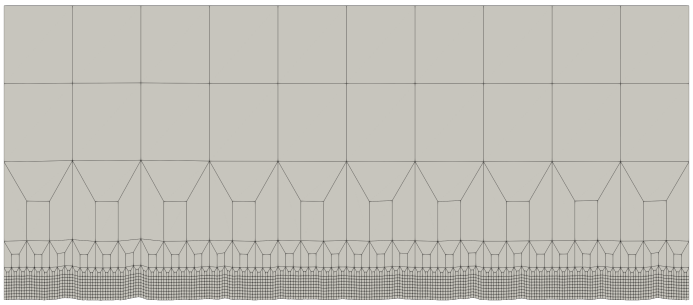

**(a)** $\lambda_s/\Delta x = 4$

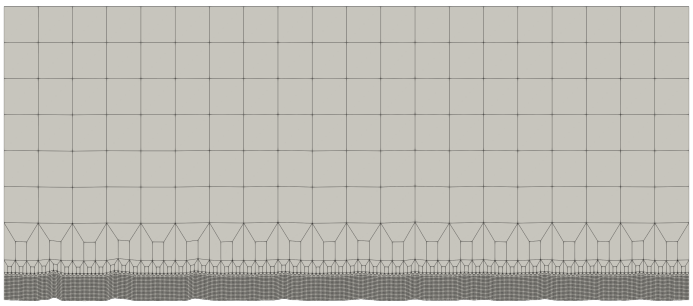

**(b)** $\lambda_s/\Delta x = 8$

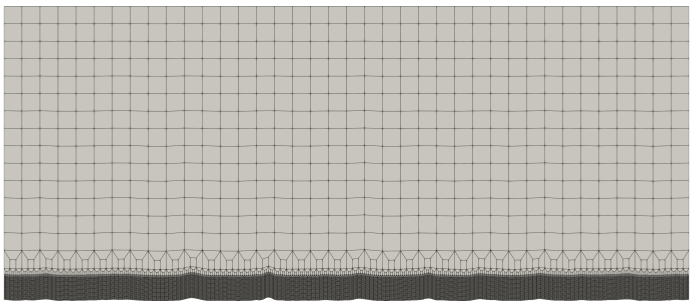

**(c)** $\lambda_s/\Delta x = 16$

**Figure 5.4:** Illustrative examples of different mesh sizes used in the convergence study.

external pressure. For lower values of normalized external pressure, approximately up to $p_0/E^*\sqrt{m_2} \approx 0.2$, it is verified that relative errors are significatively with maximum values above the 10% limit, that tend to be even higher for the lower the external pressure. The sources of error, in this case, can be well-identified beforehand. The first error concerns the spatial approximation error associated with the FEM, which decreases for finer meshes. A second source of error, and probably the one that affects the most in lower-pressure areas, is the resolution from which the real contact area is computed. During the low pressure stage, the RCE has a restricted number of nodes in contact making this region very sensitive to variations on the number of nodes in contact. Thus small variations

in the number of active nodes ensure large area errors. Additionally, from the statistical studies of Chapter 3, it is known that Weibull Minimum have the outliers located at higher heights, which constitute the first regions to contact. In such cases the errors are even larger due to the lack of o contact nodes, being the reason why the error curves of the Weibull Minimum distribution possesses amplified errors with less a smooth progression. The decaying behaviour of the errors curves is then justified by the increasing number of contact nodes, which tends to mitigate the area resolution issues.

Although the full contact results already show mesh convergence, the analysis on the light contact region is also very important from an engineering point of view—the region concerning the first micromechanical contact phenomena where low values of real contact area fraction are verified (approximately up to 20%). In this region, the real contact area evolution must also verify mesh convergence, as it constitutes an important domain of numerous contact problems and several works have tried to model such behaviour. Therefore, further numerical studies on non-Gaussian rough surfaces should also verse on the light contact region, especially taking into account that approximate analytically inspired solutions can be derived. The light contact region of this study is presented on Figure 5.7, for both upper- and lower-bound areas, following the same scheme as the previous results. Both Weibull distributions are presented on the same graph. [3] These plots reiterate the previously taken conclusion before since all the cases show convergence and the convergence direction is in tune with area evaluation methodology. A detail that is more noticeable in this case is that convergence of the average contact area fraction is not monotonic, insofar as decreasing the mesh size does not necessarily imply exclusively increasing or decreasing area.

So far, two different techniques have been used to evaluate the real contact area, and it was verified that the real contact area values end up being over or underestimated, if one considers the node-based or the segment-based methodology, respectively. A practical way to deal with this problem is by averaging upper and lower area values, thus correcting both errors. This technique has already been employed in the works of Couto Carneiro (2019) and Couto Carneiro *et al.* (2020) constituting a feasible approach to real contact area computation even when comparing with Yastrebov's method (cf. Section 4.4.7) (Yastrebov, Anciaux, *et al.*, 2017a). The real contact area evolution computed through the average area method is presented in Figure 5.8 up to full contact, being the light contact region highlighted in Figure 5.9. In the full contact representation, the numerical curves are almost superimposed, being difficult to track a mesh convergence tendency. Nonetheless, if ones looks into the representation of the error, one verifies that by averaging the results one obtains astonishing improvements, even for coarser meshes such as $\lambda_s/\Delta x = 4$. It can be seen that by using the average technique one is increasing the rate at which the results converge with mesh size. Therefore, by using this methodology one can relax the refinement conditions without a loss of physical meaning to the global problem, strongly reducing the computational cost. The results on the light contact region also highlight these conclusions. One verifies that Weibull Maximum curves tend to converge faster than Weibull Minimum's. This may not only be justified by the proper characteris-

[3] In Figures 5.6 and 5.6 the light contact region is highlighted by a grey rectangle, so one can easily identify the region that Figure 5.7 is showing.

tics of the topographies but also by the lack of nodes in contact for lower pressures that increase the errors for such domains—as it was previously described.

In summary, the presented convergence study has led to some important conclusions. A first objective, which was the validation of FEM framework for analysing contact of non-Gaussian rough surfaces, was accomplished with success, paving the way for broader spectrum studies. [4] Secondly, the mesh convergence was verified for the selected case being analysed a wide range of the parameter $\lambda_s/\Delta x$. One also has concluded that by averaging both area computation methods one obtains the convergence faster and compensates the errors. For this reason, one can use a lower discretization guaranteeing a good compromise between the representativeness of the contact phenomena and computational time. It was determined that the value proposed in the work of Couto Carneiro *et al.* (2020) for Gaussian surfaces can be also employed for non-Gaussian surfaces with great confidence— $\lambda_s/\Delta x = 8$ (cf. Section 4.4.1).

**Remark 5.2 on the applicability of the convergence study.**
*When studying mesh convergence, the common procedure constitutes of considering just one topography realization and analysing it under mesh refinement. This way, one could capture the mesh convergence independently of the realization considered, with the proviso that different realizations would probably lead to different real contact area values—yet it would remain strictly valid for the sake of mesh convergence. In the current work, however, the convergence study was made taking into account the randomness of rough surfaces, thus* 30 *realizations were generated for each $\lambda_s/\Delta x$ considered. At first glance, this procedure may seem unnecessary and entails additional computational costs. However, due to the implementation of the non-Gaussian surface's generation algorithm and the fact the mesh discretization is defined when generating the topographies (cf. Section 4.4.6), surfaces with the same random seed (the number used to initialize the generation of the Gaussian rough surface) originate different realizations for different mesh sizes. To overcome this issue, a different approach could have been pursued. In order to guarantee the same non-Gaussian realization at different mesh discretization, a refined mesh (with high $\lambda_s/\Delta x$ ) would need to be generated. After that, by systematically merging elements, one could obtain coarser meshes, yet with the same realization and spectral properties. Such process, even knowing its simplicity, would result in a laborious task with a not so considerable benefit. For this reason and due to the fact that the main focus of the work is not the definition of an RCE, the aforementioned procedure involving the average of multiple realisations was contemplated with all the acknowledged vulnerabilities.*

[4] Studies with non-Gaussian rough surfaces have never been done with the FEM framework (`LINKS` and `LINKS-RC`) up to the current work.

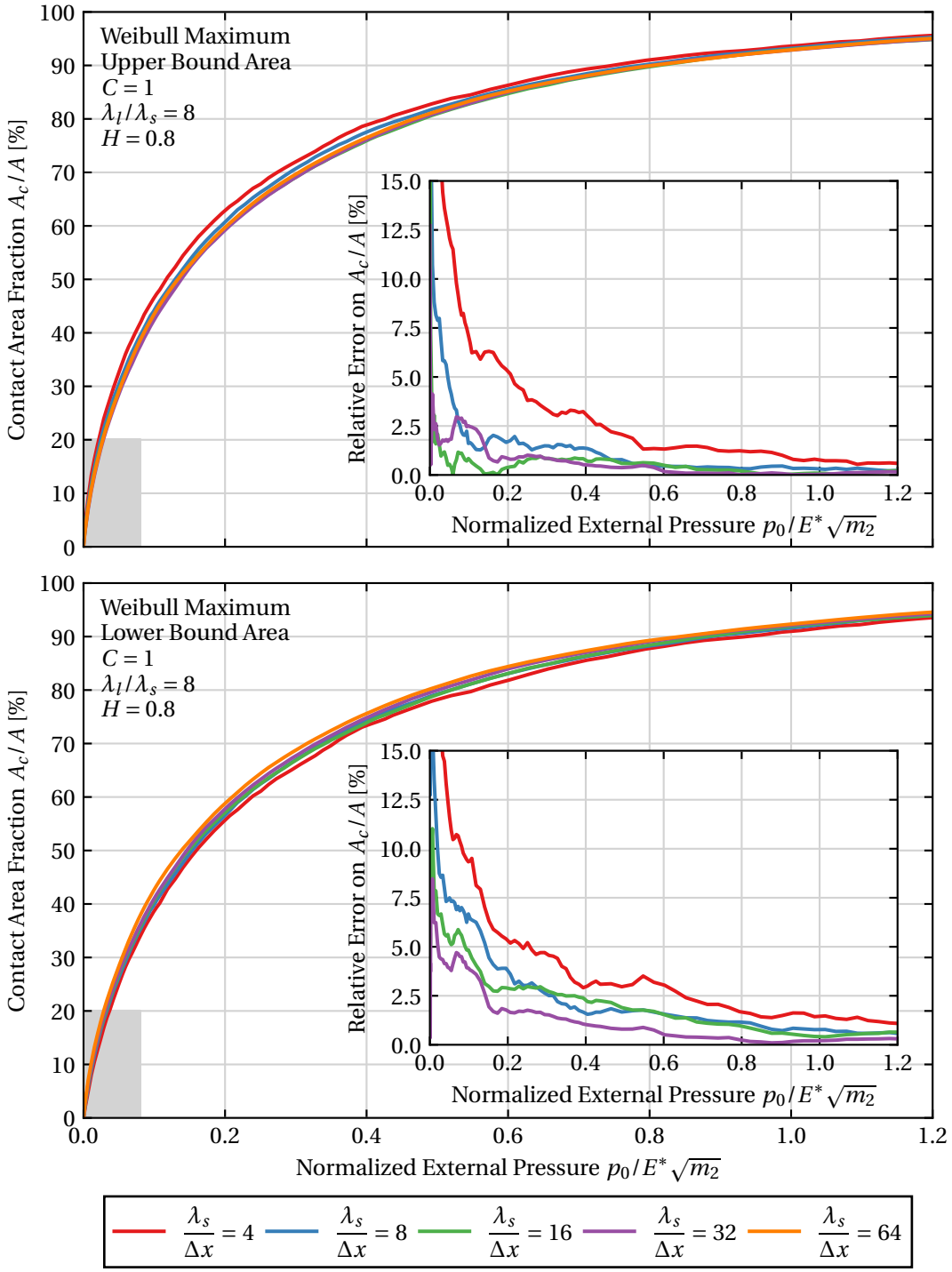


**Figure 5.5:** Influence of the mesh refinement on the contact area fraction $A_c/A$ evolution up to full contact of a Weibull Maximum height distribution, for a value of the shape parameter $C = 1$, evaluated for both upper-bound and lower-bound values of area. The error of the curves relatively to to the most refined case, $\lambda_s/\Delta x = 64$, are presented on the insetted graph.

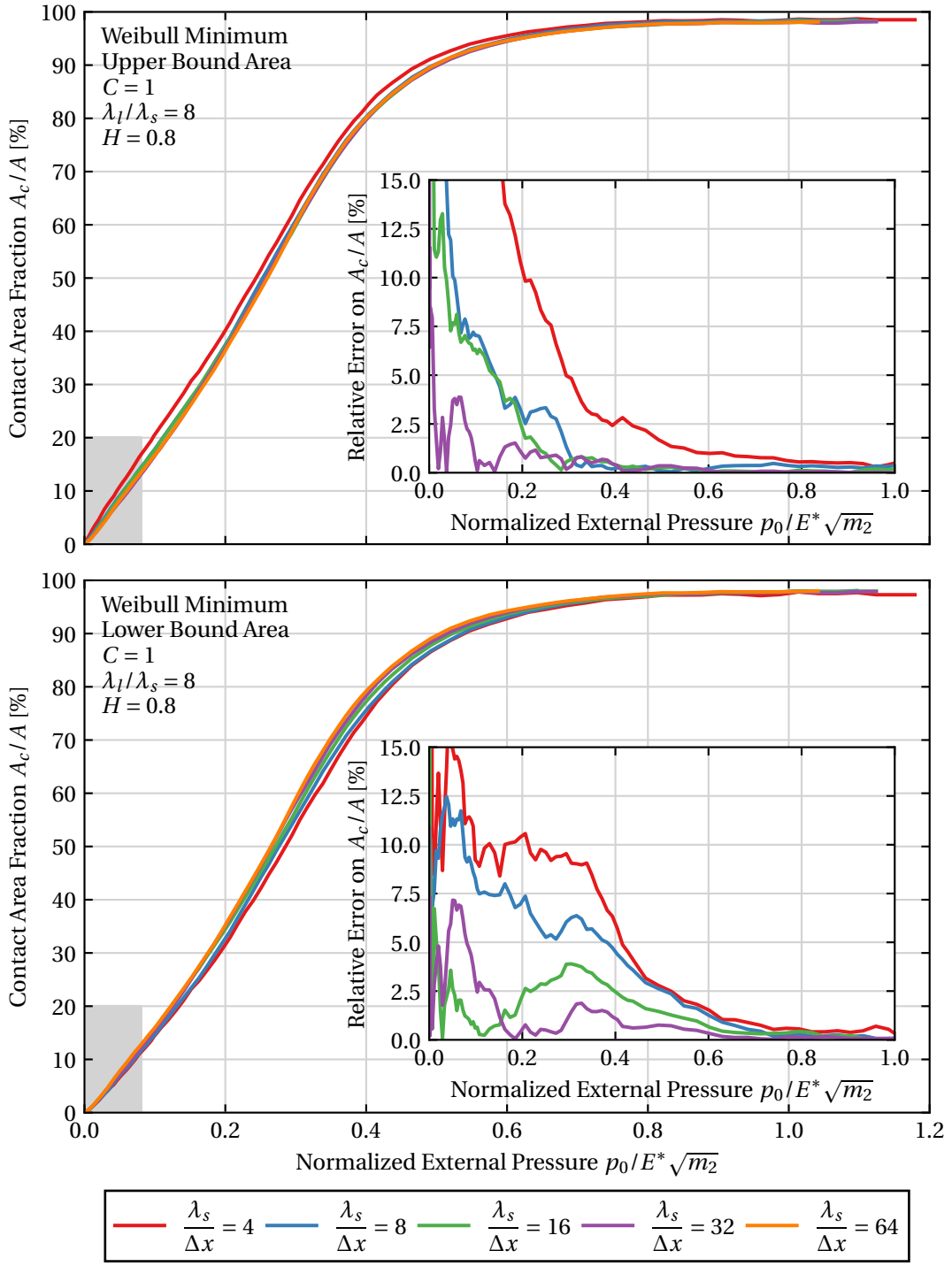


**Figure 5.6:** Influence of the mesh refinement on the contact area fraction $A_c/A$ evolution up to full contact of a Weibull Minimum height distribution, for a value of the shape parameter $C = 1$, evaluated for both upper-bound and lower-bound values of area. The error of the curves relatively to to the most refined case, $\lambda_s/\Delta x = 64$, are presented on the insetted graph.

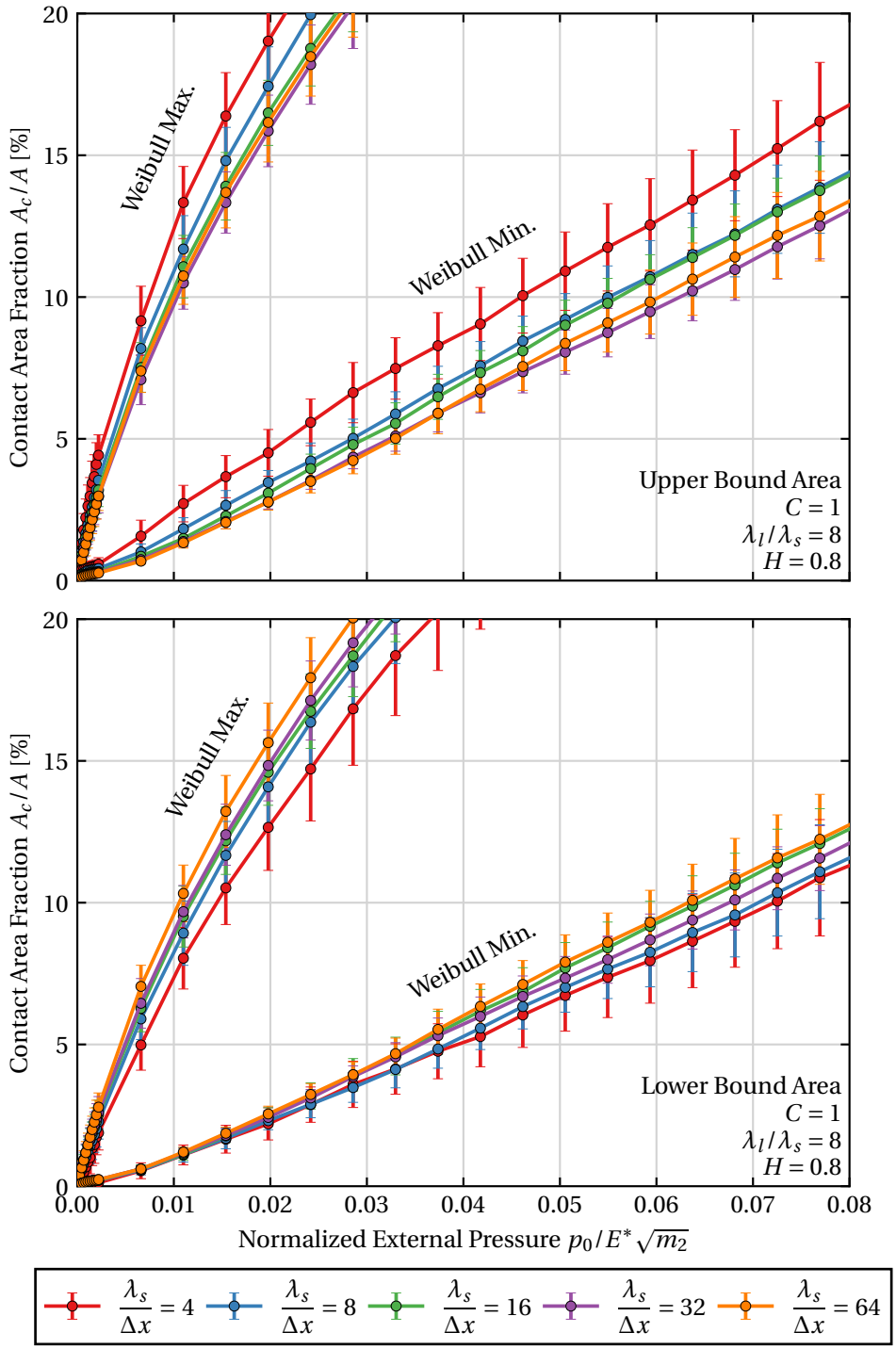


**Figure 5.7:** Influence of the mesh refinement on the contact area fraction $A_c/A$ evolution in light contact of a both Weibull height distributions, for a value of the shape parameter $C = 1$, evaluated for both upper-bound and lower-bound values of area.

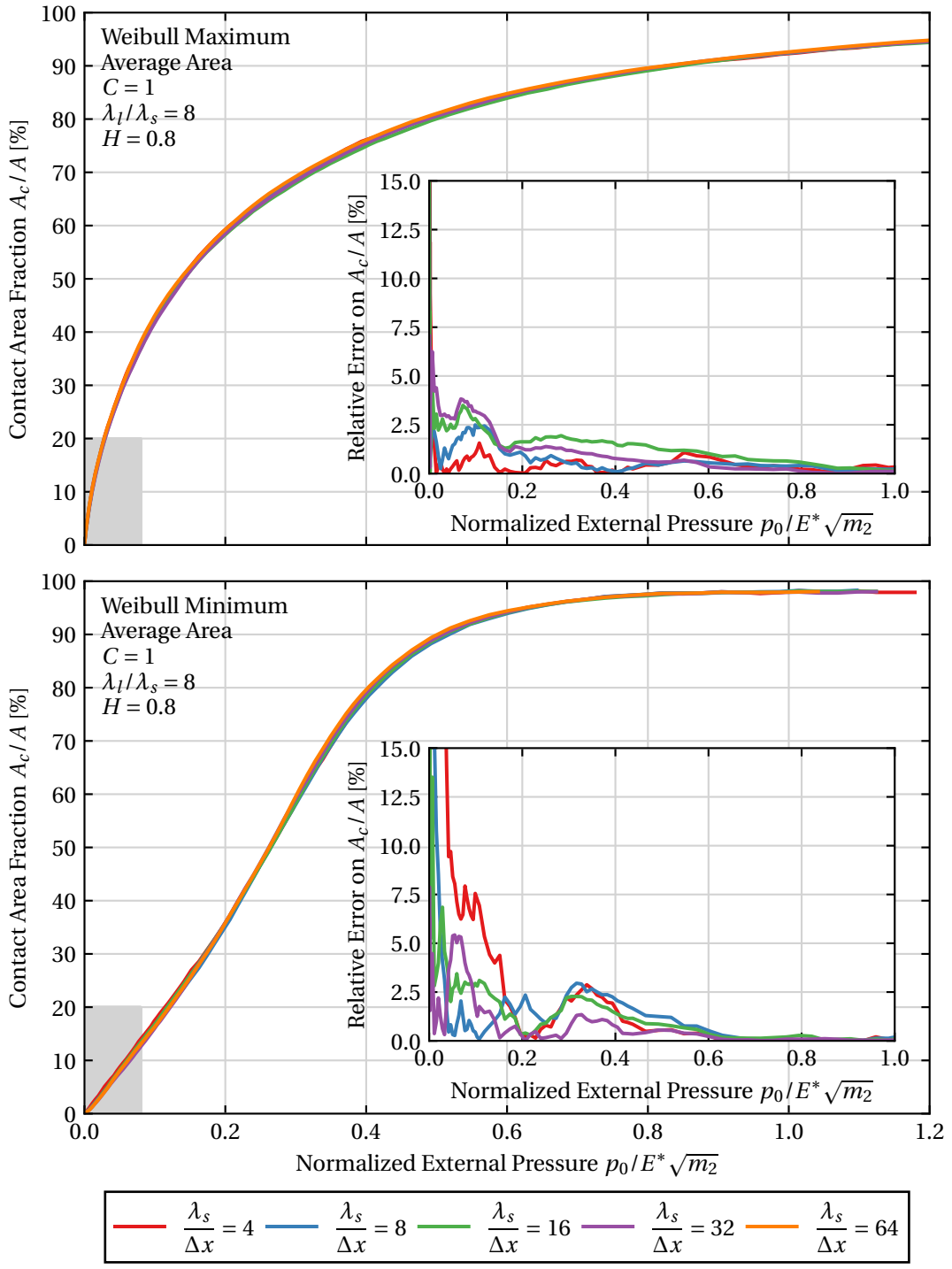


**Figure 5.8:** Influence of the mesh refinement on the contact area fraction $A_c/A$ evolution up to full contact of both Weibull height distributions, for a value of the shape parameter $C = 1$, evaluated by the average value of area. The error of the curves relatively to to the most refined case, $\lambda_s/\Delta x = 64$, are presented on the insetted graph.

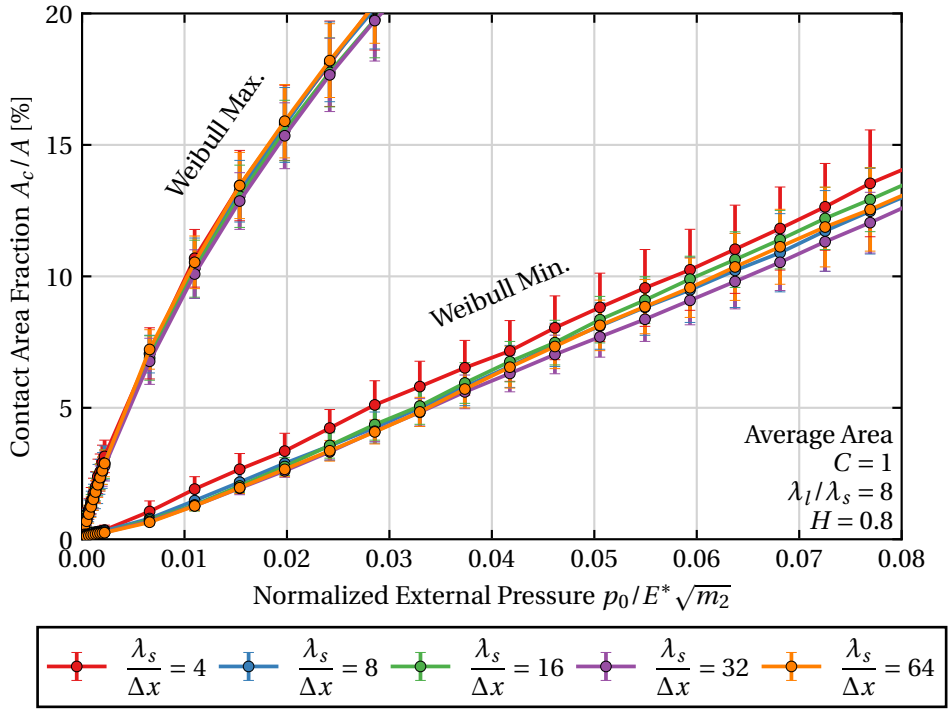


**Figure 5.9:** Influence of the mesh refinement on the contact area fraction $A_c/A$ evolution in light contact of both Weibull height distributions, for a value of the shape parameter $C = 1$, evaluated by the average value of area.

## 5.3 Study on non-Gaussian rough contact of 2D topographies

After the preliminary study for assessing the overall validity of the framework under mesh convergence, the major goal of the work is to inspect the behaviour of random non-Gaussian rough topographies under purely elastic contact. With this study, it was intended to initially characterize the behaviour of non-Gaussian rough surfaces, specifically by looking at the evolution of the real contact area and the contact pressure distribution. Thus, following the same approach has in Chapter 3, where a numerical investigation on non-Gaussian rough surfaces statistics was performed, the results are analysed at the light of the properties used to parametrize the final topography. For computational convenience, the study is undertaken in a 2D setting with rough profiles, yet knowing that the results for pure 3D rough surfaces have an intrinsically higher value. This study intends to cover a wide range of properties and thus creating a proper set of conclusions on non-Gaussian rough surfaces, enabling opportunities for further studies and developments on the topic. The parameters considered as input variables to combine are presented in Table 5.3. A total value of 80 cases resulting from the combination of all the parameter values have been considered.

Since in the previous section Section 5.2 one has verified good convergence properties for the given parameters with the mesh refinement $\lambda_s/\Delta x = 8$ being adequate if one considers the average area, the same set of conditions was employed. Only, the number

**Table 5.3:** Variables considered for the 2D FE study on non-Gaussian rough surfaces modelled with the Weibull distribution. The studied cases result from a combination of theses variables, making a total of 80 different cases.

| Height Distribution | $C$ | $\lambda_l/\lambda_s$ | $H$ |
|---|---|---|---|
| Weibull Maximum | 1 | 8 | 0.2 |
| | 1.2 | 16 | |
| | 1.5 | 32 | |
| Weibull Minimum | 2 | | 0.8 |
| | 3.602 | 64 | |

of realizations was decreased in order to diminish the computational cost and therefore extend the study to more parameters. The presented numerical setup resulted in 1600 different RCEs that were properly generated and simulated. [5] In sum, the conditions of the 2D FEM study on non-Gaussian rough surfaces are written as

**Study 5.2 (Conditions of the numerical 2D FEM study).**

***Roughness Model***

| | |
|---|---|
| *RMS slope:* | $z'_{rms,x} = 0.1$ |
| *Wavelength ratio:* | $\lambda_l/\lambda_s \in [8, 16, 32, 64]$ |
| *Hurst exponent:* | $H \in [0.2, 0.8]$ |
| *Height distribution:* | *Weibull Max. and Min.* |
| *Shape parameter:* | $C \in [1, 1.2, 1.5, 2, 3.602]$ |

***RCE parameters***

| | |
|---|---|
| *Mesh:* | $\lambda_s/\Delta x = 8$ |
| *Length:* | $L/\lambda_l = 8$ |
| *Substrate height:* | $H_{\text{sub}}/\sigma_z = 500$ |
| *Fine mesh height:* | $H_r/\sigma_z = 40$ |
| *Number of realizations:* | $= 20$ |

These conditions have resulted in different mesh sizes of the RCEs, which were also reflected in the computation time required as presented in Table 5.4. For the sake of clarity, the different values of the shape parameter were averaged for each pair of $\lambda_l/\lambda_s$ and $H$, since the spectral properties have a more meaningful impact on computational time. An exponential increase with $\lambda_l/\lambda_s$ is verified as it is associated with the mesh size ($L/\lambda_l = 8$), yet it is also worth noting that the topographies with higher Hurst exponent tend to require more computational time. In total, the computational time allocated was

[5] In truth, a total number of 2000 cases were simulated in this study since, in the initial setup, a wavelength ratio of $\lambda_l/\lambda_s = 128$ was also considered. Nevertheless, some of the realizations with this bandwidth failed during the contact simulations, reducing the total number of realizations available for each case. Hence, it was preferred to omit these results rather than draw conclusions from results with possible low representativeness.

about 583 hours (around 24 days). The true computation time is significantly shorter, due to the execution of multiple parallel calculations.

**Table 5.4:** Average computational time (in minutes) required to perform a 2D FEM study—averaged for each pair of $\lambda_l/\lambda_s$ and $H$.

| Height Distribution | $\lambda_l/\lambda_s$ | $H$ | Average computational time / min |
|---|---|---|---|
| Weibull Maximum | 8 | 0.2 | 2 |
| | | 0.8 | 3 |
| | 16 | 0.2 | 5 |
| | | 0.8 | 8 |
| | 32 | 0.2 | 11 |
| | | 0.8 | 27 |
| | 64 | 0.2 | 29 |
| | | 0.8 | 102 |
| Weibull Minimum | 8 | 0.2 | 2 |
| | | 0.8 | 2 |
| | 16 | 0.2 | 4 |
| | | 0.8 | 7 |
| | 32 | 0.2 | 11 |
| | | 0.8 | 23 |
| | 64 | 0.2 | 27 |
| | | 0.8 | 87 |

In the following sections, the obtained results will be extensively discussed. Each of the parameters considered in this study (cf. Table 5.3) are depicted by means of real contact area evolution and the contact pressure distribution. The discussion starts with the distinction between different Weibull topographies under rough contact, being followed by the effect of the shape parameter. Then, the impact of the spectral properties, wavelength ratio $\lambda_l/\lambda_s$ and the Hurst exponent, is analysed.

### 5.3.1 General behaviour of Weibull rough surfaces

As a first step into the analysis of the results, one can start by analysing the overall impact that different height distributions have on contact behaviour. Therefore, both Weibull Maximum and Minimum distributions will be analysed in terms of the evolution of the real contact area and the contact pressure distribution for a single combination of spectral and height distribution properties.

**Real contact area fraction**

In Figure 5.10 the real contact area evolution $A_c/A$ as a function of the normalized external pressure $p_0/E^*\sqrt{m_2}$ is presented for both height distributions, considering the shape parameter $C = 1$. The option for this shape parameter value relies on the fact that is the one that most evidence the difference between the distributions since it is the value that produces a higher absolute skewness value. To clarify and isolate the effect of the height

distributions only a pair of spectral properties was considered ($\lambda_l/\lambda_s = 16$ and $H = 0.8$) when plotting the results—the same conclusions can be achieved with any other combination of properties. In addition to the two Weibull curves, also two distinct Gaussian results are also presented in the Figure 5.10. The first one is simply the result of a similar numerical simulation with a Gaussian topography obtained with the same conditions of the current study. Secondly, Persson's model is also presented as it is an exemplarily model capable of predicting the behaviour of a rough surface up to full contact. The differences between the numerical and the theoretical model are expected and it is well known that Perrson's model underestimates the area values for lower values of external pressure (Pei *et al.*, 2005; Hyun *et al.*, 2004; C. Yang and Persson, 2008). The first graph (top) shows the full evolution of the real contact area, almost up to 100%, whereas the second (bottom) shows a detail of the first, concerning the evolution on the lower values of area and external pressure.

One should first start by analysing the Gaussian case and from there analyse the other results. Despite being slightly different, the Gaussian results (numerical and Persson's model) show that for light contact a nearly linear relation is recovered. One must note that at the onset of the contact area evolution, the phenomenon is dominated by the increasing number of contact clusters and the growing area of existing clusters. While for light external forces the contact increase with the increase of contact zones, for higher values of pressure the phenomenon becomes more complex, with the area evolution being due to the expansion and coalescence of the existing contact areas. This is why at the first stage the evolution is faster with several clusters entering in contact, whereas for higher values of pressure the area increase requires more pressure to reach the regions of the topography.

The Weibull distributions case show interesting area evolutions that points out some of the features of these type of topographies. For the Weibull maximum distribution, one verifies a very fast growth in area for lower values of pressures, following a nonlinear dependence with the external pressure. Looking at the statistical results from Chapter 3 one gets support and justification for these observations. This type of topographies is dominated by a significant proportion of positive heights, which lead to several summits with high topography height—the so-called *plateau*. During light contact, a substantial number of summits will immediately come into contact and with the increase of the external pressure even more contact clusters appear. Additionally, one has seen that the higher height summits tend to have lower curvatures (cf. Figure 3.25). The superposition of these two aspects leads to the fast-paced growth of the area, which is substantially superior to the Gaussian case. However, when in almost full contact conditions it is seen that growth rate severely reduces being the curve overtaken by the Gaussian curve at some point. This is due to the already mentioned outliers of this specific type of distribution (deep valleys), which have even lower heights, then requiring more pressure to reach full contact.

On the other hand, the Weibull Minimum distribution shows a slower increase in area in the light contact region being these values below the Gaussian. Similarly to the Weibull Maximum, also these results can be analysed in light of the conclusions from Chapter 3. One has seen that in this type of topographies the majority of the heights have low values, therefore meaning the first contact spots are in fact outliers values—steep peaks.

In addition, the scarce higher height summits also tend to have higher curvatures (cf. Figure 3.25) which reduces the contact area growth with increasing pressure even more. However, with the increase of external pressure, the growth rate starts to change as more contact spots—the bottom *plateau*, with progressive lower curvatures, enter in contact. It goes up to a point where the majority of the heights are in contact and where a fast increase in area is verified, due to the substantial increase in the number of contact spots. This evolution in the area is so dramatic that Weibull Minimum overtakes Weibull Maximum for the same value of normalized external pressure. It then decelerates once more, requiring progressively additional force to increase the contact area.

**Contact pressure distribution**

One can assess and compare the contact distribution numerical results from two different perspectives: by a fixed value of external pressure or by a fixed value of real contact area. In Figure 5.11 two different curves of contact area evolution of both Weibull distributions are presented, with the same conditions ($C = 1$, $\lambda_l/\lambda_s = 64$ and $H = 0.2$). This graph intends to depict the points from which the contact pressure will be analysed and the distributions compared. Whereas top graph shows in these curves several points with same value of normalized external pressure ($p_0/E^*\sqrt{m_2} \in [0.06, 0.2, 0.4, 0.7]$), the bottom graph shows points with approximately the values of area ($A_c/A = [20, 40, 70, 90]\%$). The resultant contact pressure distributions are presented in Figure 5.12 and in Figure 5.13 for fixed value of external pressure and a fixed value of area fraction, respectively. Additional distributions with $C = 1.2$ are included to endorse the conclusions in different formats of the height distribution. Only non-zero values of the contact pressure are considered, such that the integral of the probability distribution including the Dirac delta at zero pressure is equal to one. Also, in this Figure 5.12 (fixed external pressure) the Persson's model pressure distribution is presented (black dotted-line) as well as the external pressure value (gray dashed-line).

Starting by analysing the results for a fixed value of external pressure (Figure 5.12), one must denote that the contact pressure distribution should reflect the contact area at each pressure increment. Bearing this in mind, the external pressure values have been chosen to highlight this fact. When $p_0/E^*\sqrt{m_2} = 0.06$ one sees that Weibull Maximum presents a much more developed contact pressure distribution, with a considerable amount of lower pressures values, showing the superior area fraction—recall that the integral of the curve excluding the zero must be equal to the contact area fraction. In this case, the Weibull Maximum already has a significant number of contact clusters that possess several summits in contact thus having much more expression of the contact pressure distribution. In turn, Weibull Minimum has just a few contact spots, having a more spread contact pressure distribution. For $p_0/E^*\sqrt{m_2} = 0.2$, Weibull Minimum distribution approximates the Weibull Maximum case and a more developed contact pressure distribution is verified, yet with still noticeable less area. In this case, the Gaussian result becomes less similar to the Weibull contact pressure probability density function, a signal that reflects the effect of non-Gaussianity in this type of distribution. The histogram of $p_0/E^*\sqrt{m_2} = 0.4$ has been chosen to highlight a pressure value where area fractions are very similar in both Weibull cases (cf. Figure 5.11). A visual inspection of the distributions allows validating the hypothesis of similar contact area fractions. For the last value of external pressure,

$p_0/E^*\sqrt{m_2} = 0.7$, one expects the Weibull Minimum to demonstrate a superior area, as seen on Figure 5.11, yet it is visually hard to do so and the reasons are twofold. First, the relative differences in area fraction for this value of external pressure are not as large as in the first pressure values (cf. Figure 5.11). Second, Weibull Minimum distribution tends to have higher outliers contact pressures values, thus having superior probability density in the extremely high-pressure values not depicted in the figures under analysis.

The following expresses some general observations that are evidenced by these results. The contact pressure distribution graphs verify a right shift that is proportional to the increase of the external pressure. It is a well known and logical result (Persson's model predicts it for the Gaussian case) since the equilibrium on the RCE should be kept, therefore meaning that contact pressure values should compensate the increase of the external force. An interesting aspect of the Weibull contact pressure distributions is that they verify different mode values, which are located to the right or left of the external pressure, depending on whether one is referring to Weibull Maximum or Weibull Minimum. It is seen that contact pressure distribution intersect each other on a point of pressure very similar to the external pressure value. While Weibull Maximum has a great portion of contact stress above the average, Weibull Minimum verifies the opposite yet may counterbalance this effect by the existence of outlier higher contact pressure values. It is a quite intriguing behaviour with a not so obvious answer and that might be a topic for further investigations.

The same contact distributions can be now explored for the same value of area fraction by looking at Figure 5.13. The first two values of area fraction ($A_c/A \approx 20\%$ and $A_c/A \approx 40\%$) highlight curious differences in the contact pressure distributions. While for Weibull Maximum a large fraction of lower contact pressures are verified, the Weibull Maximum distribution has a wider range of contact pressures that extend up to higher values of topography height, and the probability of observing these very large pressure is greater. This might indicate several particularities in the deformation procedure of such antagonistic height distributions. It is tempting to justify this type of phenomena with some physical intuitions however, it should be left to future work. The higher values of area fraction ($A_c/A \approx 70\%$ and $A_c/A \approx 90\%$) indicate that for higher values of the external pressure the contact pressure distributions are increasingly more symmetric in the analysed pressure range, as previously observed. This is endorsed by the observation that in full contact, the contact pressure distribution is highly correlated with the full height distributions—which are symmetric for the Weibull Minimum and Maximum scenarios discussed in the present work.

**Remark 5.3 on convergence of the distribution to zero.**
*One must note that phenomenologically speaking contact pressure distributions should verify a trend toward zero for higher and lower values of contact pressure. This type of behaviour of the contact pressure distributions is evident and is observable in Persson's model. However, on the previously presented results, Figures 5.12 and 5.13, the histograms do not verify this effect for lower values of pressure. For certain external pressure values the mode value can even be the value nearest to zero—cf. Figure 5.11 for* $p_0/E^*\sqrt{m_2} = 0.06$. *The reason for this imprecision might have a few different origins. With the current framework, it was verified that mesh refinement has a significant impact on it, meaning that more refined mesh improves the results of the contact pressure distribution. However, in general terms, the contribution to the final results was not that great meaning for the purpose of the current work the mesh size considered is enough to capture trends and inspect how non-Gaussianity affects the contact pressure distribution.*

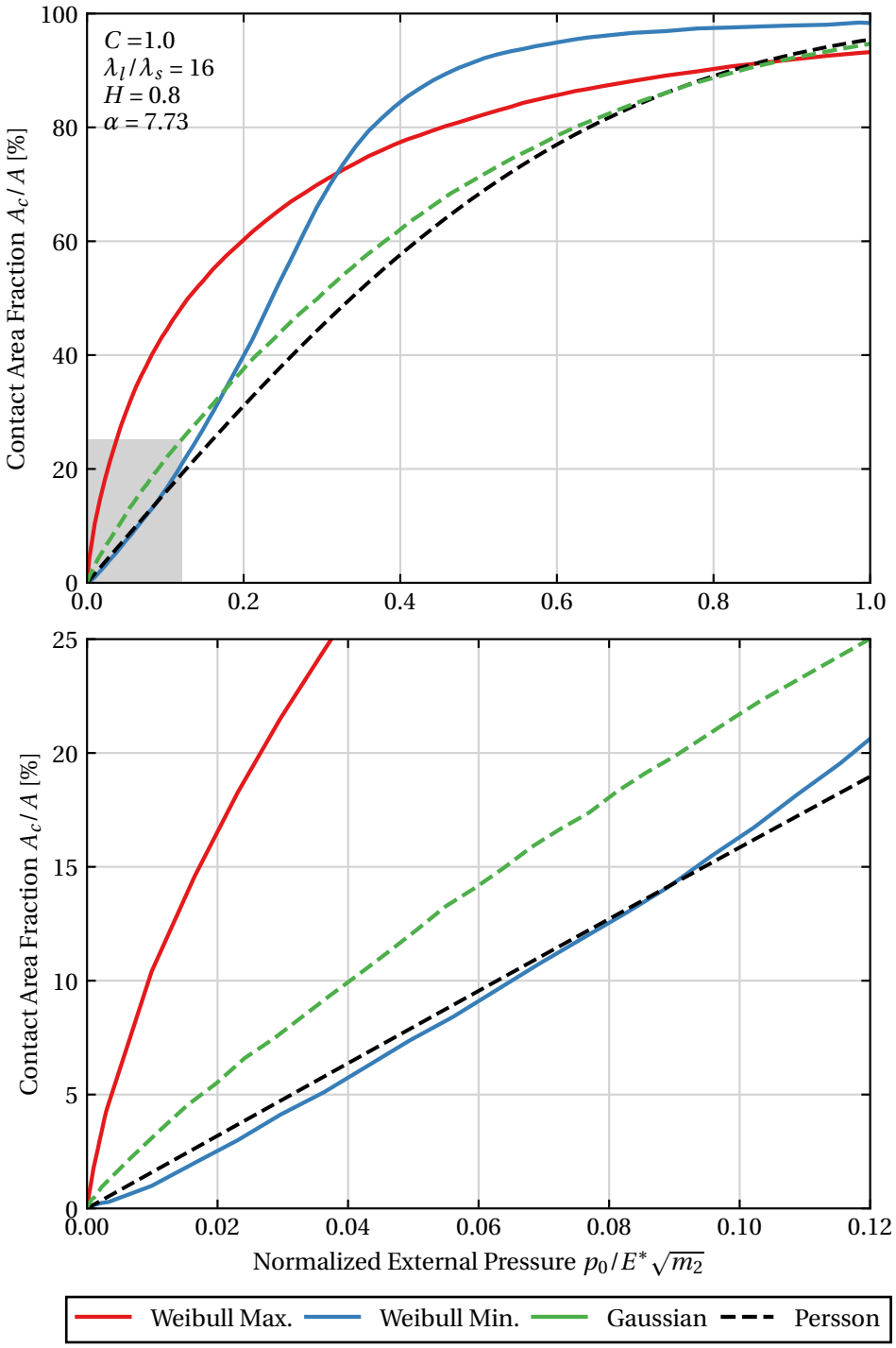


**Figure 5.10:** Comparison of the contact evolution curve for different Weibull distributions (Weibull Maximum and Minimum), for the particular case of $C = 1$, $\lambda_l/\lambda_s = 16$ and $H = 0.8$. Gaussian results are also plotted— numerical result and Persson's model

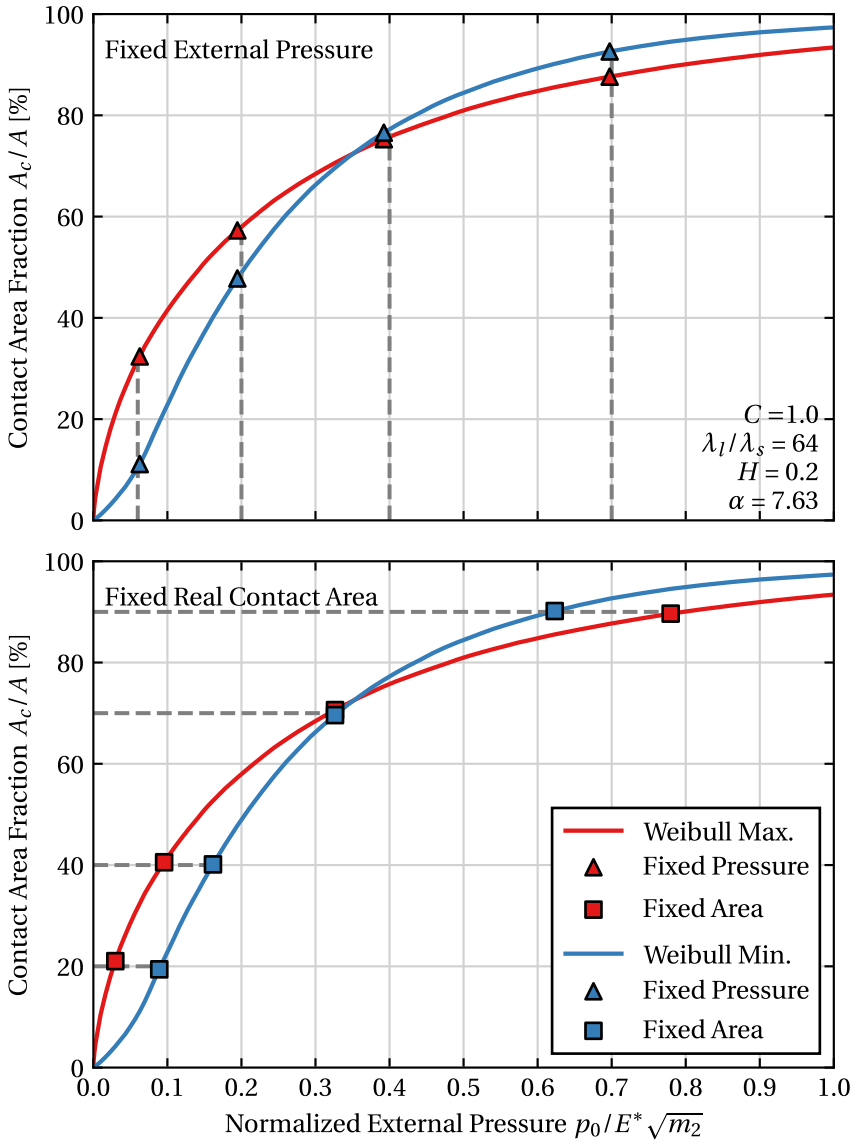


**Figure 5.11:** Fixed values of the normalized external pressure $p_0/E^*\sqrt{m_2}$ and the contact area fraction $A_c/A$, presented in the contact evolution curve for different Weibull distributions (Weibull Maximum and Minimum), for the particular case of $C = 1$, $\lambda_l/\lambda_s = 32$ and $H = 0.2$.

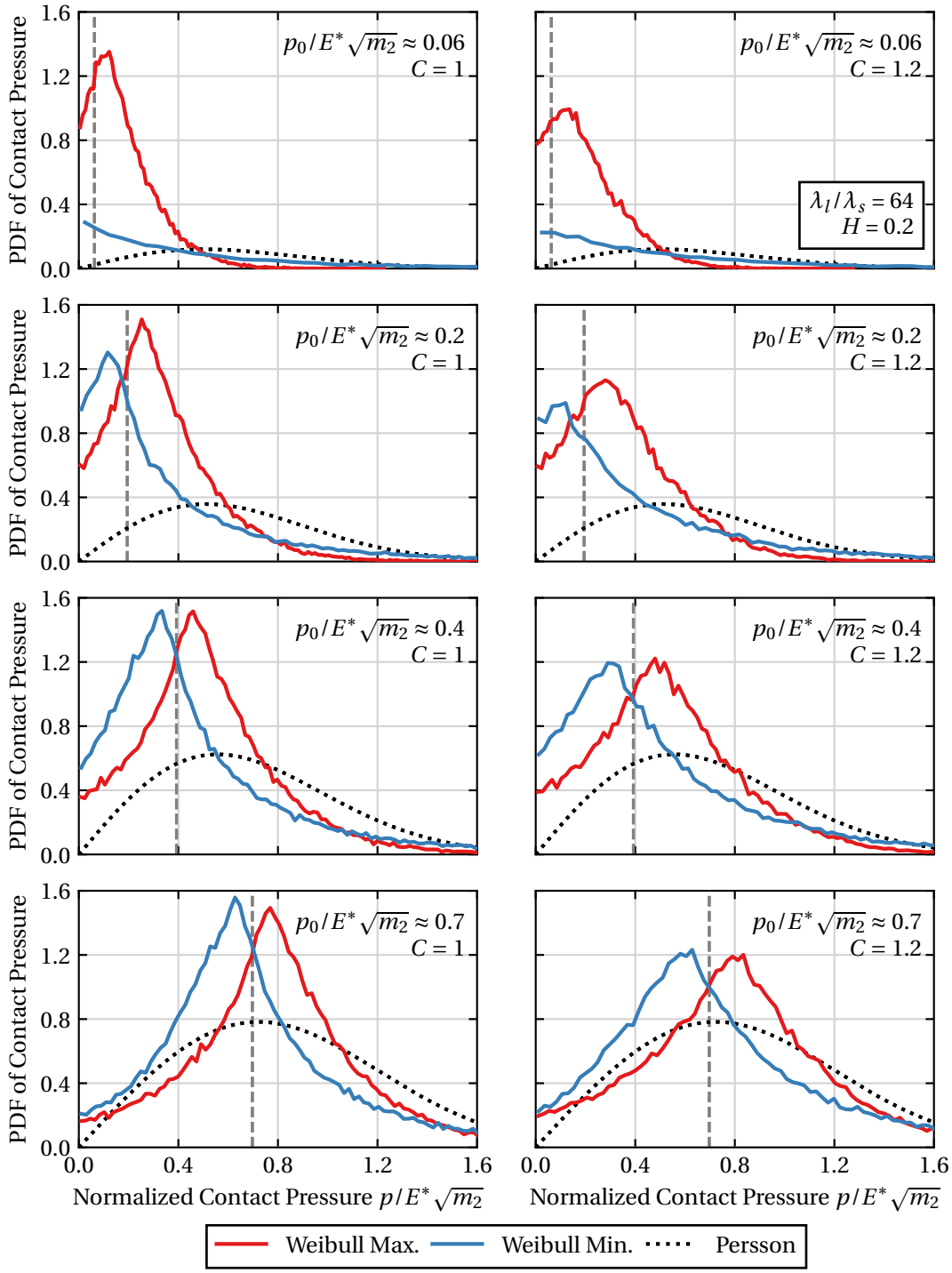


**Figure 5.12:** Comparison between the contact pressure distribution of the Weibull Maximum and Minimum cases, over four different values of normalized external pressure $p_0/E^*\sqrt{m_2}$, and for two different shape parameter $C$ cases. The Gaussian result is presented through Persson's model solution and the value of the increment is presented as a vertical and grey dashed-line.

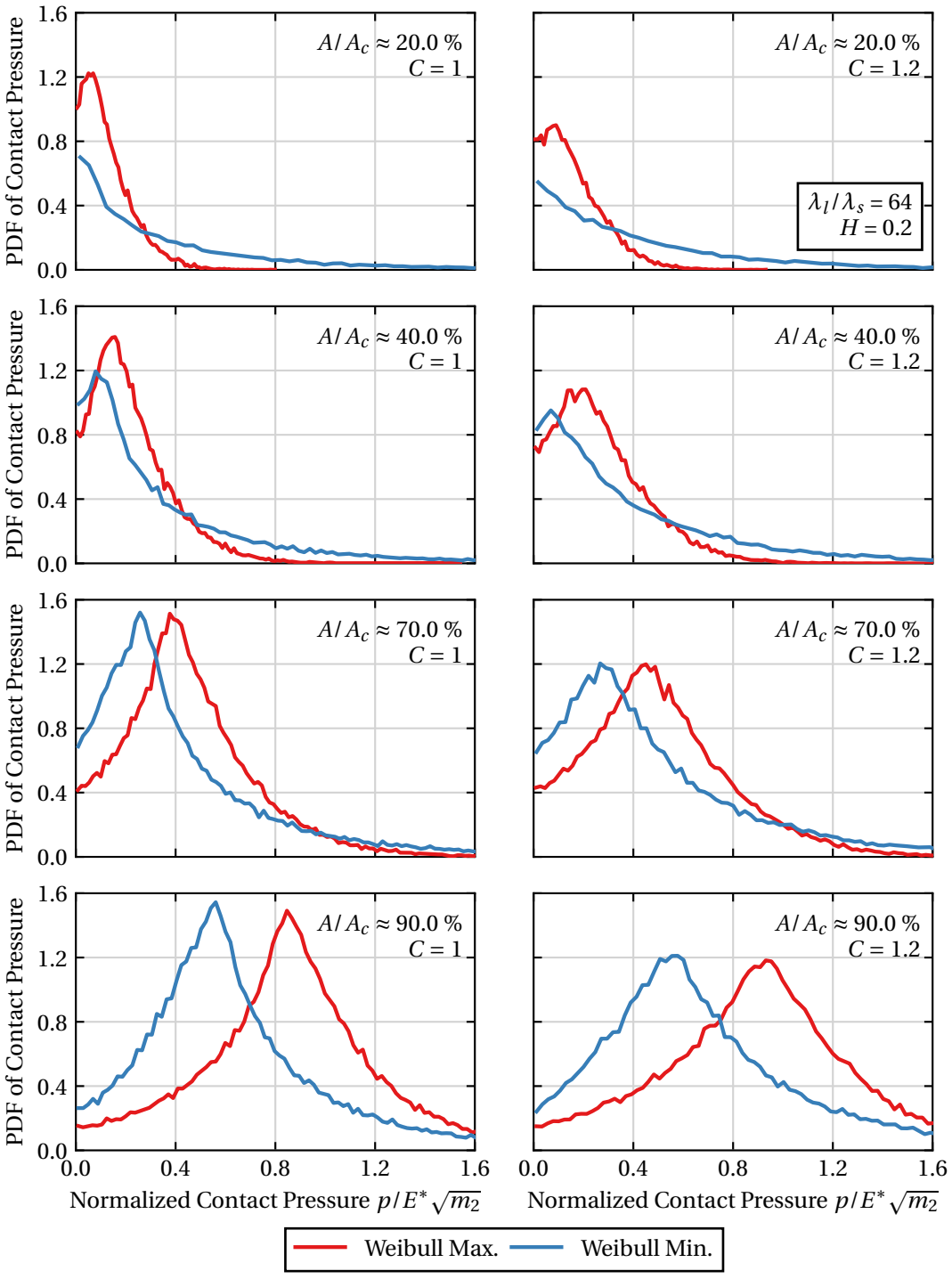


**Figure 5.13:** Comparison between the contact pressure distribution of the Weibull Maximum and Minimum cases, over four different values of contact area fraction $A_c/A$, and for two different shape parameter $C$ cases.

### 5.3.2 Influence of the shape parameter

One can isolate the effect of the shape parameter $C$ for each on the Weibull distributions considered and verify how this parameter affects both area evolution curves and contact pressure distribution. Specific spectral properties are chosen to evidence only the effect of $C$, however, all the conclusions can be extended to other spectral combinations.

**Real contact area evolution**

In Figure 5.14 and 5.15, the influence of the shape parameter $C$ on the evolution of the area fraction is depicted for Weibull Maximum and Weibull Minimum, respectively. The results are shown for different values of the wavelength ratio $\lambda_l/\lambda_s$ but only considering a Hurst exponent value of 0.2. The Perssons's model theoretical curve is plotted for reference.

Starting with the Weibull Maximum cases, one verifies that the shape parameter has a significant impact on the area fraction evolution. Generally speaking, the lower the value of $C$ the higher the contact area fraction is for any value of external pressure. This is seen in the light contact region since the lower values of $C$ reflect more left-skewed height distributions. The statistical results from Chapter 3 also justify these results, since lower $C$ values mean more concentration of higher summits (cf. Figure 3.20) that directly translate into more contact clusters and therefore a higher value of the area for initial external pressure values. The curvature of the asperities also give useful information and from Figure 3.25 one has seen that topographies whit lower $C$ values, tend to have lower expected mean curvatures when comparing with the topography global curvature value. The influence of the shape parameter is not uniform, insofar as $C$ leads to distinct changes in the area fraction for different values of external pressure. It is seen that from the start the shape parameter effect tends to progressively dilate the difference in the area in the light contact region, a phenomenon that is dominated by the previously mentioned topography characteristics. However, from a certain value of external pressure, this divergent trend of the different curves tends to cease and convergence of the curves starts to be observed. The reason for this has already been addressed and has to do with the outlier heights that tend to be deeper for lower $C$ values. It means that topography with a lower $C$ value will need a higher external force to reach the full contact condition. This condition even leads to a slight inversion of the curves relative position that in the presented case occurs near to $p_0/E^*\sqrt{m_2} = 0.8$. Overall, the decrease of $C$ hastens the area fraction evolution at small pressures due to the high concentration of summits, but hinders it at larger pressures because of the deep valleys that need to be flattened. These observations are verified for any spectrum bandwidth tested, which show no evident influence in this type of distribution. It is surprising that the area fraction of this non-Gaussian topography can easily be overestimated by a factor of two (or even more), relative to the nearly Gaussian case $C = 3.602$. This observation stresses the need for an accurate characterisation of the height distribution of rough topographies, in order to achieve relatively accurate predictions of the contact area-related behaviour.

One can now look into the Weibull Minimum area evolution curves (Figure 5.15). The more complex behaviour of this type of curves is well evidence highlighting an interesting dependence of the shape parameter $C$ but also on the wavelength ratio $\lambda_l/\lambda_s$—a topic which will be discussed later in this work. For very light contact conditions, one verifies

that the lower the $C$ the lower the area fraction. In this region, the contact evolution is almost totally dependent on the outlier values of the Weibull Minimum distribution as they are responsible for the first contact cluster to form. It is known that the more right-skewed the height distribution the more prominent, scarcer and sharper the summits are—cf. Figure 3.26. This translate into lower values of the area and slow growth in the first external pressure increments. However, in the light contact region, there can be observed a point where the contact area evolution accelerates strongly and grows to larger area fractions relative to higher $C$ values. For the same bandwidth ratio, this *inflection point* seems to occur for smaller pressures. Moreover, it seems to be heavily dependent on the bandwidth ratio, with larger ratios producing earlier inflections and steeper growths. This is in great contrast with the Weibull Maximum, where a monotonic dependence of the contact area with $C$ was observed in the light contact region, whereas for the Weibull maximum this is not strictly verified. With the increase of the external pressure, the area evolution becomes affected by the lower heights range where the majority of heights of this type of topographies are located. It was seen that the lower the $C$ the more compact are the heights at the lower values therefore, when in contact, the more concentrated are the heights the more quickly the area will evolve when the compression stage reaches these regions.

The light contact region of the area evolution curve is paramount in this study and engineering practice. An interesting aspect that was raised by the previous results is that the shape parameter does not affect in the same magnitude the contact area evolution of both height distribution types. In fact, the previous results highlight a more dominant influence of the shape parameter $C$ for the Weibull Maximum rather than the Weibull Minimum version. To inspect this hypothesis, in Figure 5.16 the contact evolution of both Weibull distributions up to a value of pressure of $p_0/E^*\sqrt{m_2} = 0.10$ are presented—the spectral properties considered are $\lambda_l/\lambda_s = 32$ and $H = 0.2$. When looking at the results of both distributions in the same graph, the previous advanced statement is even more emphasized. The shape parameter seems to have visually more effect on the Weibull Maximum than in the Weibull Minimum. A different way to inspect this premise is by seeing how the area fraction evolves with the shape parameter for a specific value of external pressure. This type of approach is presented in Figure 5.17 for three different values of external pressure ($p_0/E^*\sqrt{m_2} \in [0.04, 0.06, 0.08]$ ) in the same spectral conditions of Figure 5.16. With this representation, the evolution trends with the $C$ shape parameter become much more evident. While Weibull Maximum presents a more abrupt decay that slows down with the increase of $C$, Weibull Maximum has a softer nearly linear increase with $C$. The explanation for different degrees of impact on light contact seems to be well supported by the topographies statistics explored in Chapter 2. In a light contact region, the features associated with the higher heights of the topography are the ones that play a major role in this phenomenon. For Weibull Maximum it is seen that both the heigh distribution and the summits height distribution are severely affected by the shape parameter, a reason why the evolution of real contact area come also affected in a major significance. On the contrary, in the Weibull Minimum cases, higher heights are basically dominated by outlier values that, even though being affected by the shape parameter, do not produce considerable changes on the area evolution curve. Actually, it is seen for the Weibull Minimum that the shape parameter has a major degree of influence for higher

values of external pressure and area (cf. Figure 5.15), since it is the region where the lower heights of the topographies have a remarkable impact.

**Contact pressure distribution**

Relatively to the contact pressure distribution, one can get a sense of the impact of the shape parameter $C$ by looking at Figure 5.18. In this figure the contact pressure distributions, for a fixed spectral case ($\lambda_l/\lambda_s = 64$ and $H = 0.2$) of both Weibull cases are plotted for four different values of external pressure—($p_0/E^*\sqrt{m_2} \in [0.05, 0.1, 0.4, 0.6]$). Only three different values of the shape parameter $C$ are presented to give a better visual perception of the results. Apart from past observations on the individual behaviour of Weibull Maximum and Minimum surfaces, these results highlight the difference in area and how it is reflected on the contact pressure distribution. In the histograms with the lower value of external pressure, $p_0/E^*\sqrt{m_2} = 0.05$, one verifies that Weibull Maximum has a more developed contact pressures distribution, with the histograms for different $C$ values reflecting their relation in area, i.e., the lower the shape parameter the higher the area. In turn, the Weibull Minimum has contact pressure distribution less developed due to a small number of contact nodes, which makes the distribution harder to visualize and interpret, yet one verifies that the histogram of $C = 3.602$ has a superior area which is in tune with the previous area evolution results.

In the remaining values of external pressure, the shape parameter seems to have a similar impact for both types of topographies. For instance, lets focus on the $C = 1$ and $C = 1.2$ histograms. The mode of both cases occurs for a very similar value of contact stress, yet has a significant difference in frequency that, inasmuch as the growth in the area is accompanied by a higher concentration of contact stresses around the mode. This hypothesis is verified for both Weibull Maximum and Minimum cases in the regions of higher concentration of contact stresses. Another interesting aspect to mention is that for $C = 3.602$ the contact pressure distribution is very close to theoretical results for the Gaussian case.

In the previous section (Section 5.3.1) it was advanced that the outliers of the contact pressure distributions might also have a particular role on the contact pressure distribution, specially for Weibull Minimum topographies. To explore the existence and effect of the outliers and also how they are affected by the shape parameter $C$ one can use the moments of a PDF. The first central order moment, i.e., the mean does not provide any new information since the mean of the contact pressure due to equilibrium conditions is directly related to the external pressure applied on the RCE. In turn, the standard deviation of the topography also does not provide any interesting information to this type of analysis. Therefore, one is typically left with the skewness and kurtosis of the contact pressure distribution that are presented in the Figures 5.19 and 5.20 as a function of the external pressure for the different Weibull distributions and values of the shape parameter. It must be noted that these graphs are not intended to represent an accurate evolution of the skewness and kurtosis with the external pressure, but only a relative comparison between height distributions and different $C$ values is intended—focus is placed on comparing the moments for different shape parameters at different pressures and not to analyse the evolution of the moments with pressure Both quantities seem to express similar conclusions on the role of the heigh distribution and the shape parameter. By

comparing both Weibull Maximum and Minimum cases, one concludes that the latter has a much greater predominance of outlier values on the contact pressure distribution, due to the substantially larger skewness and kurtosis. Additionally, the effect of the shape parameter seems to be equal for both cases: the lower the $C$ the higher the presence and influence of the outliers in the distribution. Nevertheless, the shape parameter has a smaller influence for Weibull Maximum when compared with Weibull Minimum, as can be seen in Figure 5.21. In this figure, the kurtosis of the contact pressure distribution is plotted as a function of $C$ for two different values of normalized external pressure. It is clearly evidenced that the presence of outliers in the Weibull Minimum case possesses a larger dependency of the shape parameter, whereas for Weibull Maximum a decreasing trend is verified with the increase of $C$. Finally, one must note that, while skewness gives a measure of how the distribution is spread relatively to a mean axis, the kurtosis is more sensible to the outlier values as it is a fourth-order moment. However, in these results, the outliers seem to have a significant weight (the kurtosis values reaches large values) that camouflages the real measure provided by the skewness and makes it also sensitive to the tails of distributions. This largely explains why both moments give similar results about the contact distribution shape.

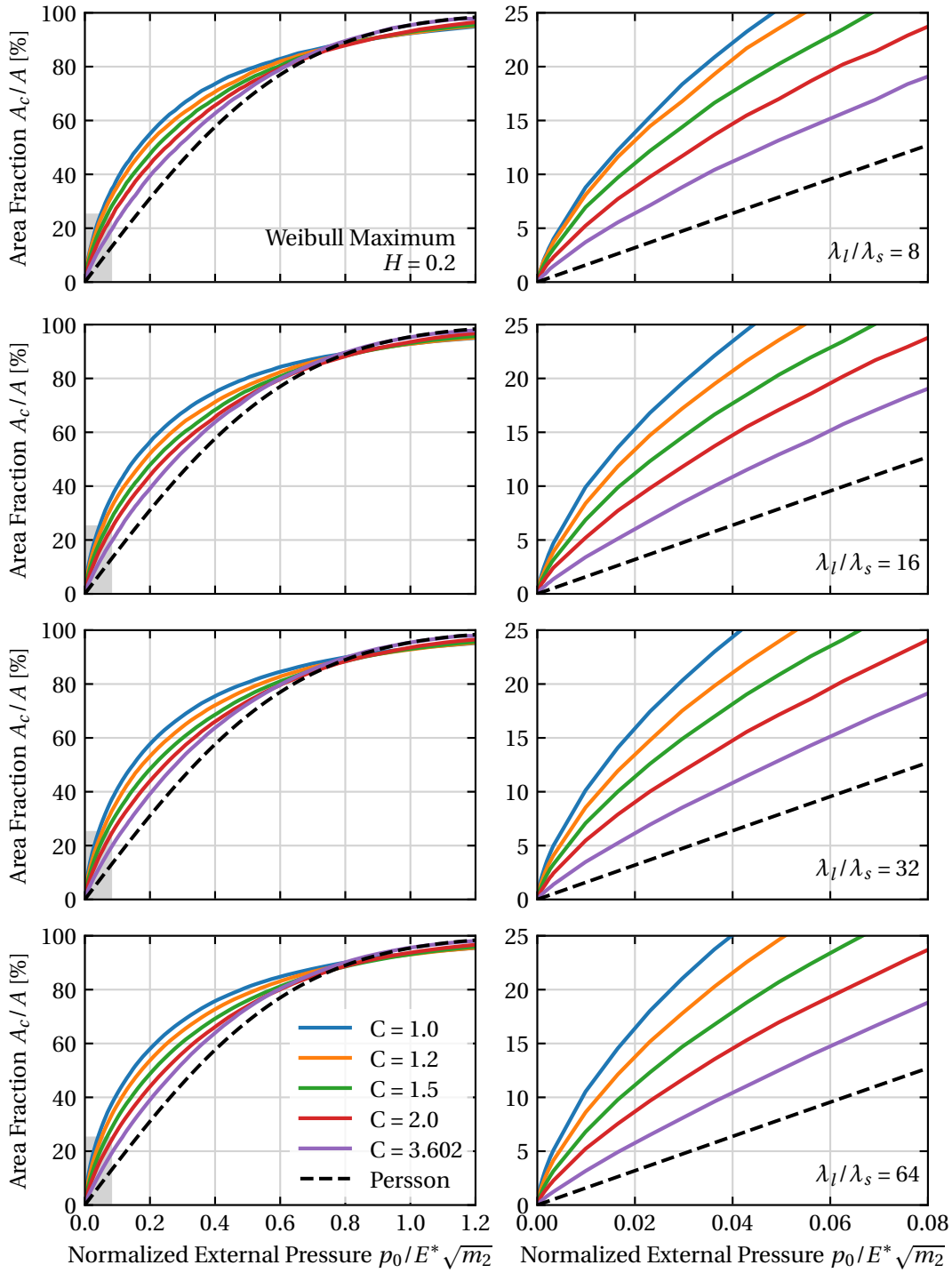


**Figure 5.14:** Comparison of the real contact area evolution of Weibull Maximum topographies for different shape parameter $C$ values.

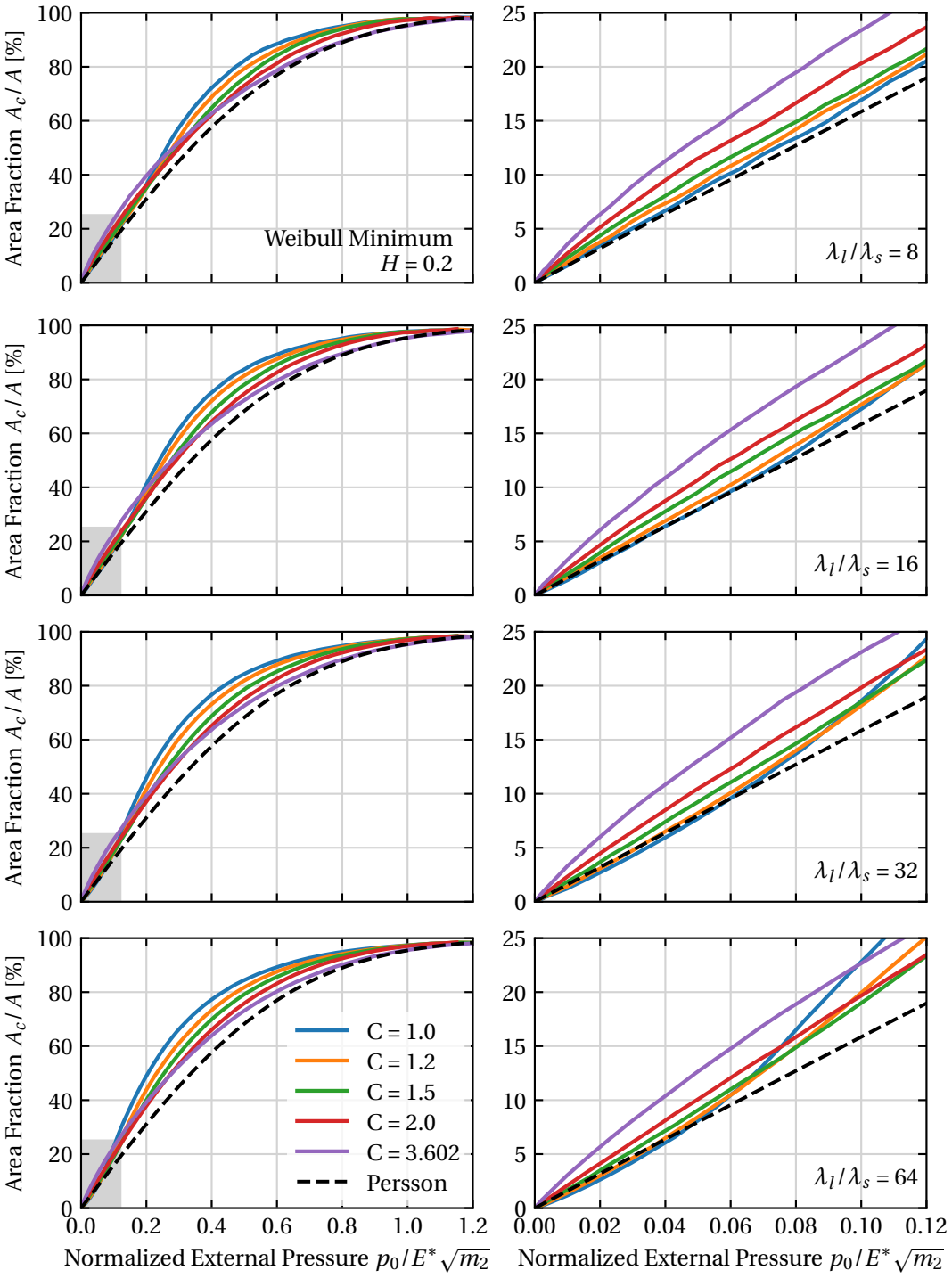


**Figure 5.15:** Comparison of the real contact area evolution of Weibull Minimum topographies for different shape parameter $C$ values.

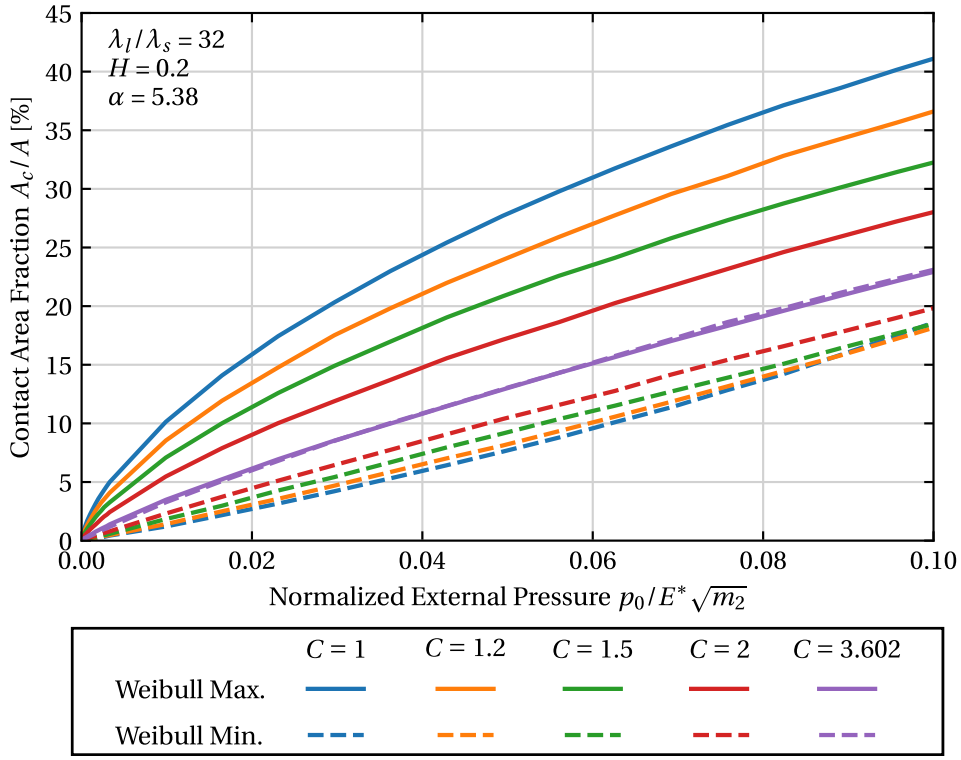


**Figure 5.16:** Comparison of the real contact area evolution of Weibull Maximum and Minimum topographies for different shape parameter $C$ values on the light contact region.

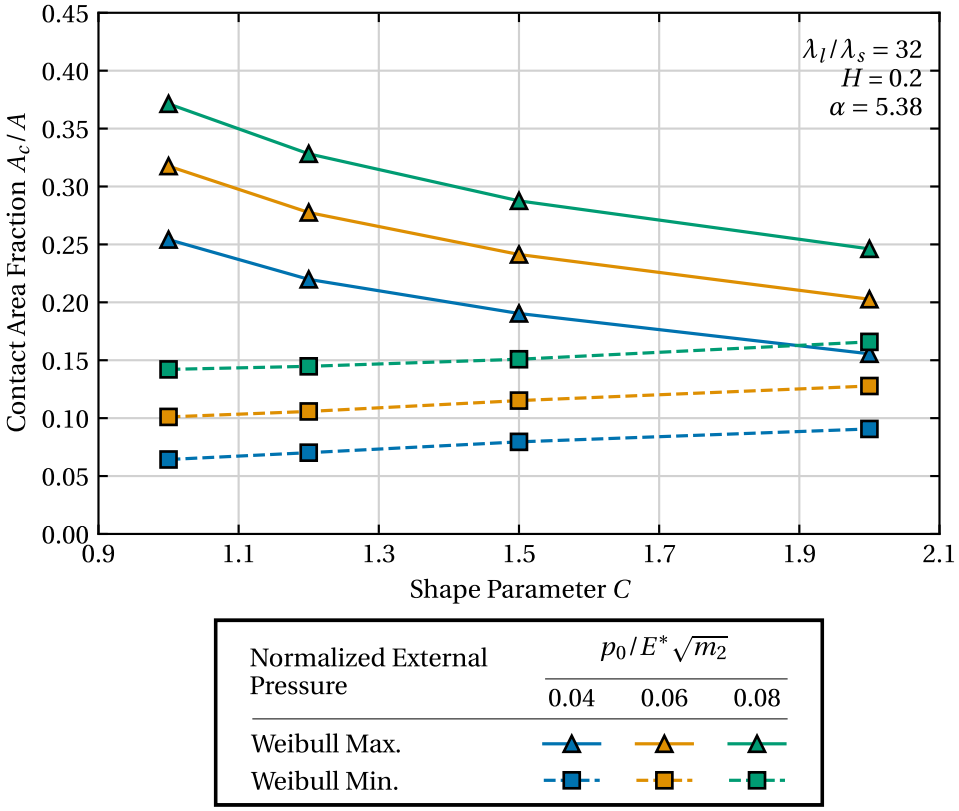


**Figure 5.17:** Evolution of the real contact area as function of the shape parameter $C$ for three different value of external pressure—for both Weibull cases.

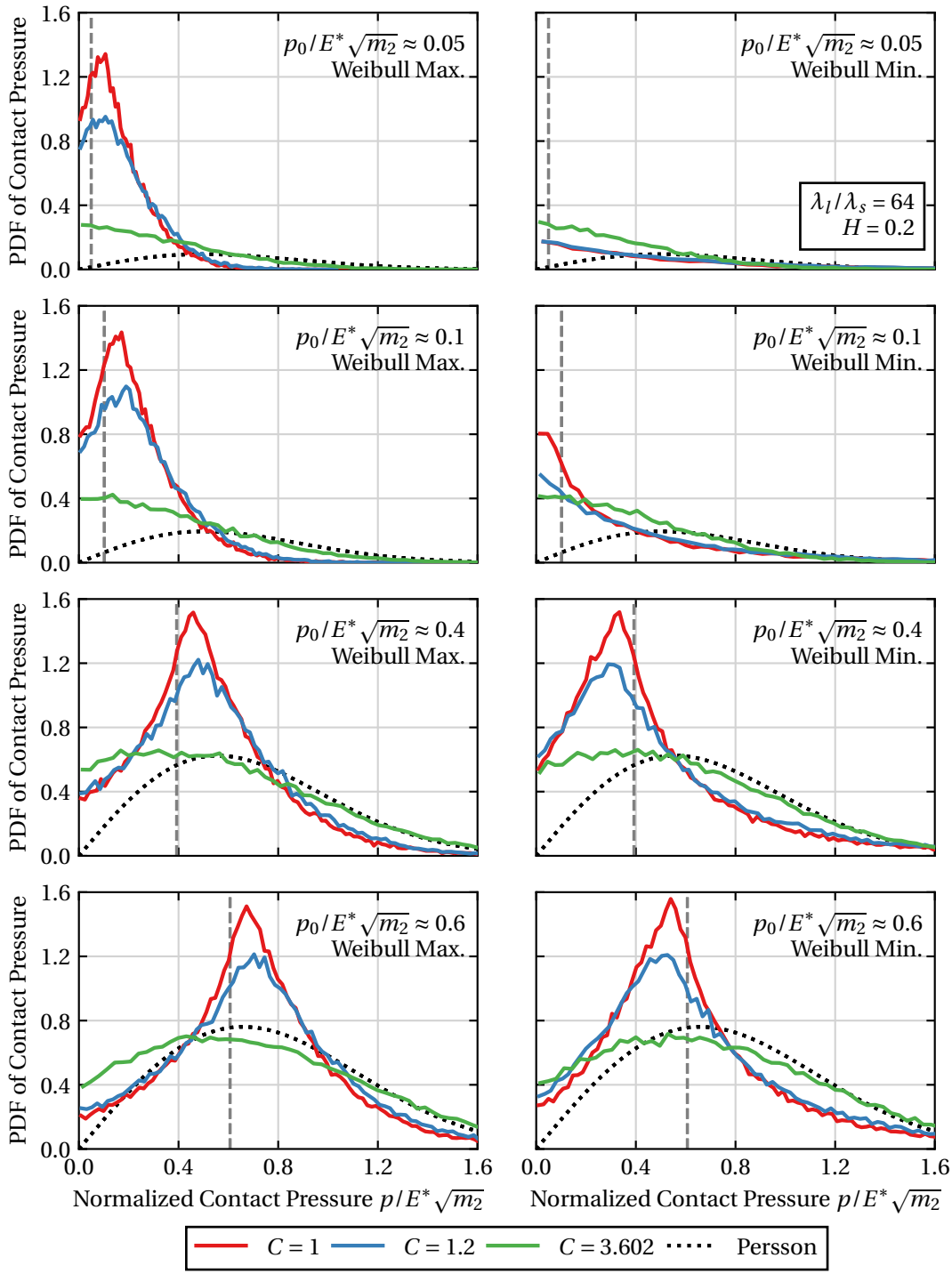


**Figure 5.18:** Comparison of the contact pressure distribution for different values of the shape parameter $C$, in both Weibull cases and over four different values of normalized external pressure $p_0/E^*\sqrt{m_2}$. The Gaussian result is presented through Persson's model solution and the value of the increment is presented as a vertical and grey dashed-line.

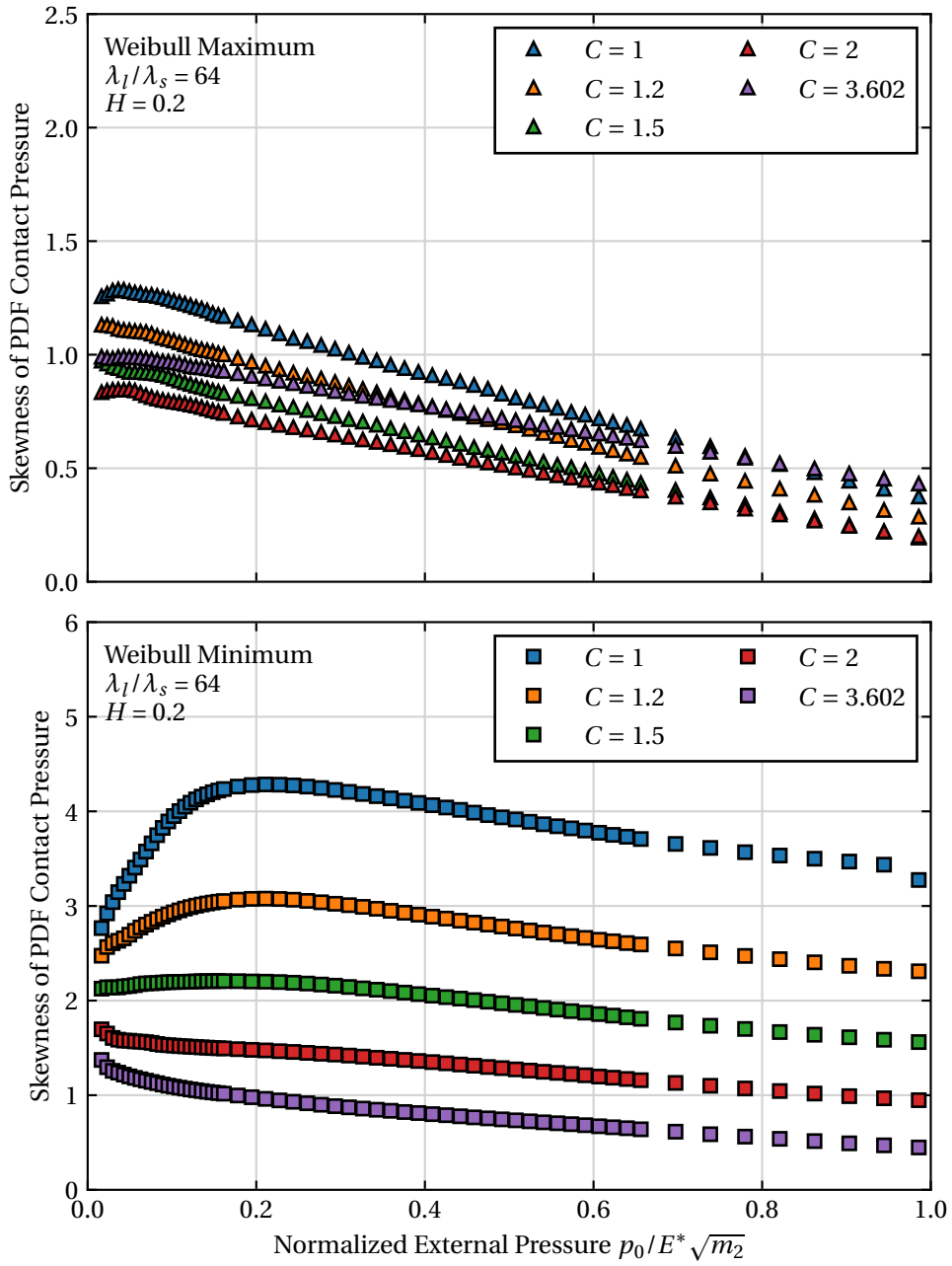


**Figure 5.19:** Comparison of the skewness of the contact pressure distribution (computed for each pressure increment) of the different shape parameter $C$ values for both Weibull cases.

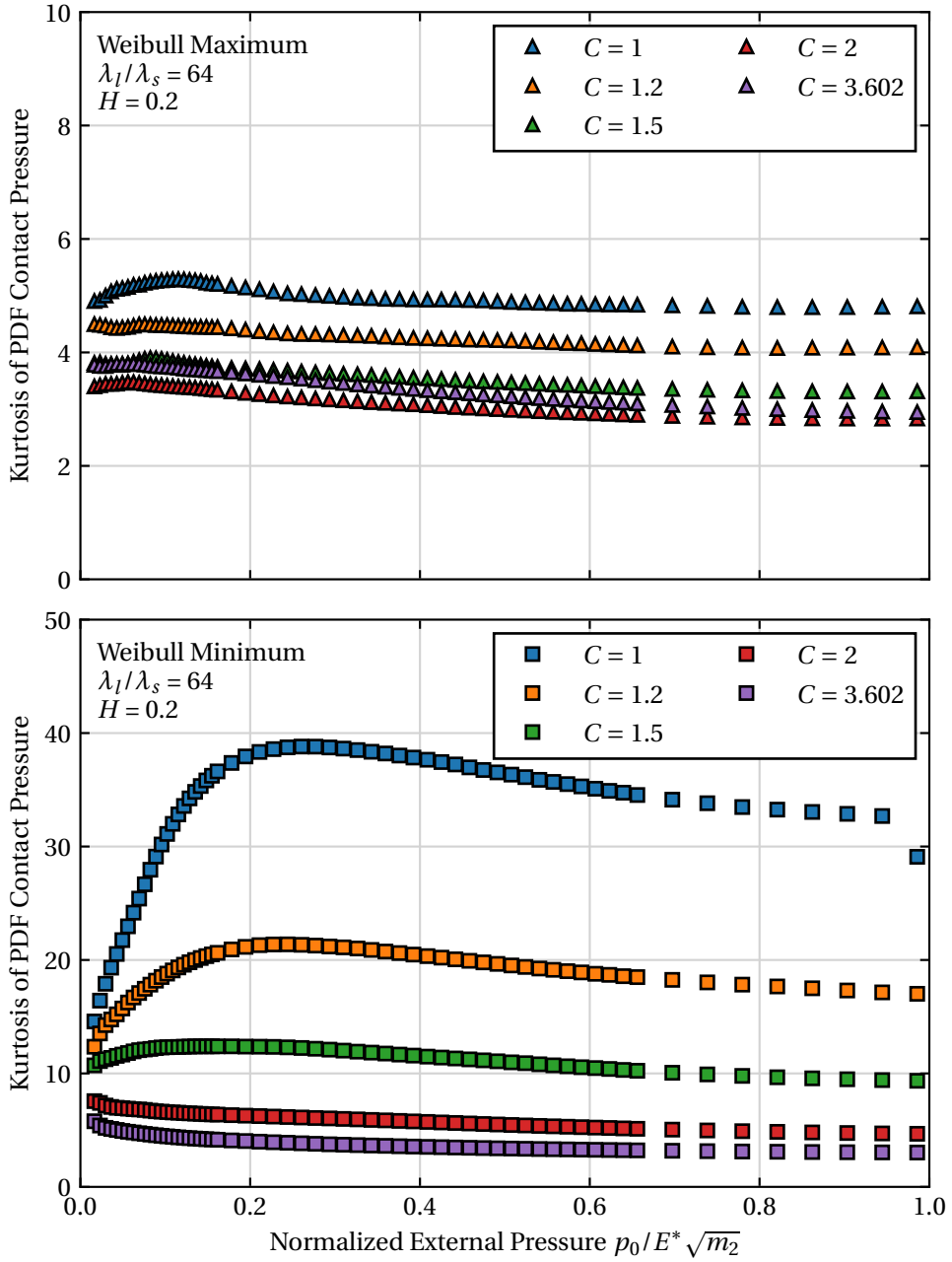


**Figure 5.20:** Comparison of the kurtosis of the contact pressure distribution (computed for each pressure increment) of the different shape parameter $C$ values for both Weibull cases.

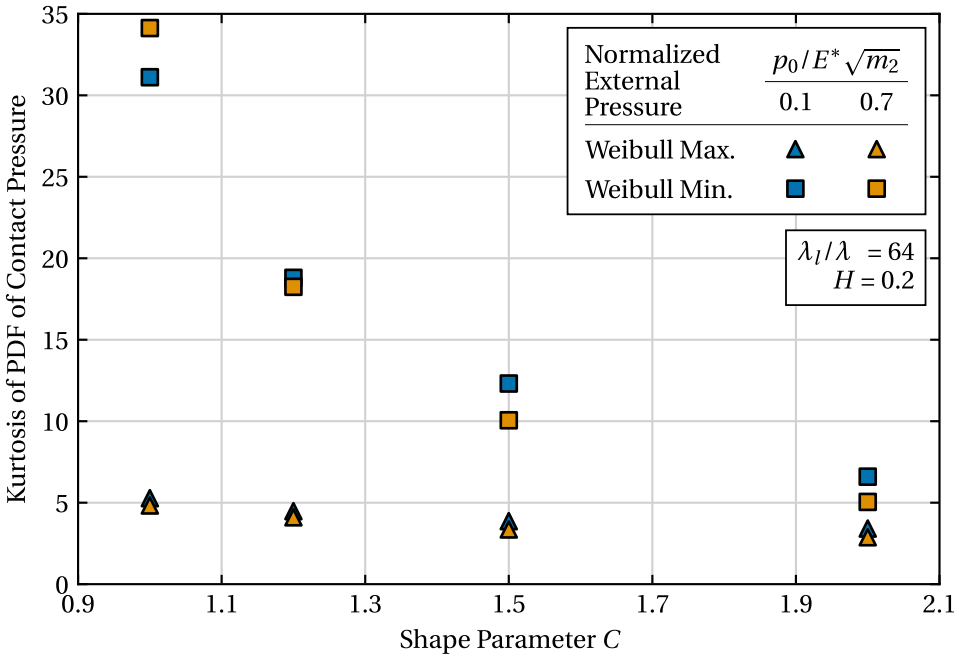


**Figure 5.21:** Comparison between the evolution of the kurtosis of the contact pressure distribution with the shape parameter $C$, for the Weibull Maximum and Minimum, computed for two different values of the external pressure.

### 5.3.3 Influence of the wavelength ratio

Moving on to the spectral properties, one can start by analyse the influence of the wavelength ratio $\lambda_l/\lambda_s$, also referred as the bandwidth of the PSD. Keeping the consistency of the previous sections, in the current the effect of $\lambda_l/\lambda_s$ on contact are evolution and contact pressure distribution is isolated and discussed.

**Real contact area evolution**

In Figures 5.22 and 5.23 the contact area evolution for different wavelength ratios is shown for both Weibull Maximum and Minimum, respectively. Different values of the shape parameter are considered, then the effect can be verified over different height distributions. A fixed value of the Hurst exponent is chosen, being the one that better highlights the impact of $\lambda_l/\lambda_s$.

Starting with the Weibull Maximum, at a first glance, the area evolution curve does not seem to severely affected by the wavelength ratio $\lambda_l/\lambda_s$, however, the results present some interesting features that require proper discussion. One must start by recalling the summit height distribution for a Gaussian case, that was presented in Section 3.1.1 and can be directly seen for several values of $\alpha$ in Figure 3.1. From this theory, one has seen that lower $\alpha$ (and consequent lower values of $\lambda_l/\lambda_s$ and $H$) lead to a higher concentration of higher summits. When in contact this characteristic means that surfaces with lower $\alpha$ tend to have higher contact area fractions. This result is captured in the well-known asperity based models (Carbone and Bottiglione, 2008) and also on several numerical studies such as Yastrebov, Anciaux, *et al.* (2017b). It was seen the summit height distribution of Weibull Maximum topographies reflects this aspect of the Gaussian theory, yet with a marked emphasis in higher height summits. For instance, in Figure 5.22, for $C = 2$, one verifies that this is still applicable for lower values of pressure, which is in agreement with the results presented in Figure 3.28. In these conditions, the differences between different curves are very small and tend to remain that way throughout all the external pressure values. However, it is verified that, for higher values of external pressure, curves with a higher wavelength ratio tend to have higher contact area fractions. With the decrease of $C$, the advanced hypothesis is even more evidenced. It is seen that in lower values of the shape parameter ($C = 1$ or $C = 1.2$, for example) the contact area fraction of the largest $\lambda_l/\lambda_s$ is higher—in contrast with the results expected for Gaussian topographies. The reason for this might be related to the density of summits of the topographies. As it was seen in Figure 3.35 the spectral properties have a huge influence on the density of summits with the increase of $\lambda_l/\lambda_s$ severely increasing the density of summits on the topographies. With this in mind, it can be understood that more summits lead to more contact clusters that, in the last instance, contribute to a higher area in these circumstances. The mean curvature results, previously shown in Figure 3.32, also express that lower values of $\lambda_l/\lambda_s$ tend to have lower expected mean curvatures values when comparing with the global curvature of the topography, for higher summit heights. This can add a slight contribution to the final response and sustain the superiority in the area of higher values of $\lambda_l/\lambda_s$.

The influence of the wavelength ratio $\lambda_l/\lambda_s$ on the Weibull Minimum topographies is depicted in Figure 5.23. For this type of topographies, the effect of $\lambda_l/\lambda_s$ is more evident. During the first increments of pressure, it is seen that the lower the bandwidth the higher the contact area. In these regions, the Gaussian logic seems to be well applied, as

the more frequency exists in the summits in contact the lower the area will be. The use of the statistical results on the initial increments, for this type of height distribution, is always a dubious task, since a poor statistical representation is obtained. However, this relation is kept not just for a small external pressure but is also influenced by the shape parameter. The closer the height distribution is to the Gaussian case (higher $C$) the wider is the region of external pressure where the lower value of $\lambda_l/\lambda_s$ has a dominant value of area. At a certain point, an inversion of the relative position of the curves with different $\lambda_l/\lambda_s$ values is observed. One sees, that higher values of $\lambda_l/\lambda_s$ become dominant in the medium contact area range, being this effect augmented by the shape parameter—lower $C$ induces higher differences for distinct values of $\lambda_l/\lambda_s$. The reasons for this might not be so simple and interpretable since, during the deformation process, several micromechanical phenomena occur that are not easily explained with a statistical approach. The trend of higher values of $\lambda_l/\lambda_s$ having higher area fraction is kept up to full contact conditions.

To evidence the impact of the wavelength ratio $\lambda_l/\lambda_s$ on the contact area, in Figures 5.24 and 5.25 the evolution $A_c/A$ is plotted as function of $\lambda_l/\lambda_s$ for fixed values of the normalized external pressure, for both light and full contact condition, respectively. The Hurst value is kept from the previous results and the shape parameter $C$ is considered to be 1 to represent the most contrasting result. In Figure 5.24 three different external pressure values under the light contact regime are considered ($p_0/E^*\sqrt{m_2} \in [0.01, 0.02, 0.03]$). The tendency for Weibull Maximum to increase the area with the increase of $\lambda_l/\lambda_s$ is well captured, as well as the opposite for Weibull Minimum. In Figure 5.25, the growing trend is once more presented, however, the main observation is concerned with the impact of $\lambda_l/\lambda_s$ on both Weibull cases. As it was seen before, but it is now clearly demonstrated, the wavelength ratio has a stronger impact on Weibull Minimum topographies.

**Contact pressure distribution**

The impact of the bandwidth $\lambda_l/\lambda_s$ in the contact pressure distribution is depicted in Figure 5.26 for both Weibull Maximum and Minimum cases. Four different values representing the normalized external pressure are considered. For the sake of clarity, only the extreme value of the wavelength ratio are plotted, i.e., $\lambda_l/\lambda_s = 8$ and $\lambda_l/\lambda_s = 64$. A single value of the shape parameter is consider ($C = 1$) as well as the Hurst exponent ($H = 0.2$). It can be generally stated that the increase in the roughness spectrum bandwidth is associated with a higher concentration of contact pressure around the mode. It was seen that the contact pressure PDF is differently skewed according to the type of height distribution. Therefore, with the increase of $\lambda_l/\lambda_s$ the contact pressure distribution tend to become closer to the external pressure value. For instance, in the Weibull Maximum case, the increase in $\lambda_l/\lambda_s$ slight moves the distribution to the left, whereas in Weibull Minimum the mode seems to move to the right.

The effect of $\lambda_l/\lambda_s$ on the outliers on the contact pressure distribution can be assessed through the kurtosis, as it was done in the previous section. In Figure 5.27 the kurtosis values, computed for the different values of $\lambda_l/\lambda_s$, at each increment of the external pressure, are shown. The considered properties are the same as in Figure 5.26. It can be seen that the higher the bandwidth $\lambda_l/\lambda_s$ the higher the presence of the outlier values on the contact pressure distribution. This impact is really meaningful in the Weibull Minimum case as it is seen that kurtosis reaches values over 250.

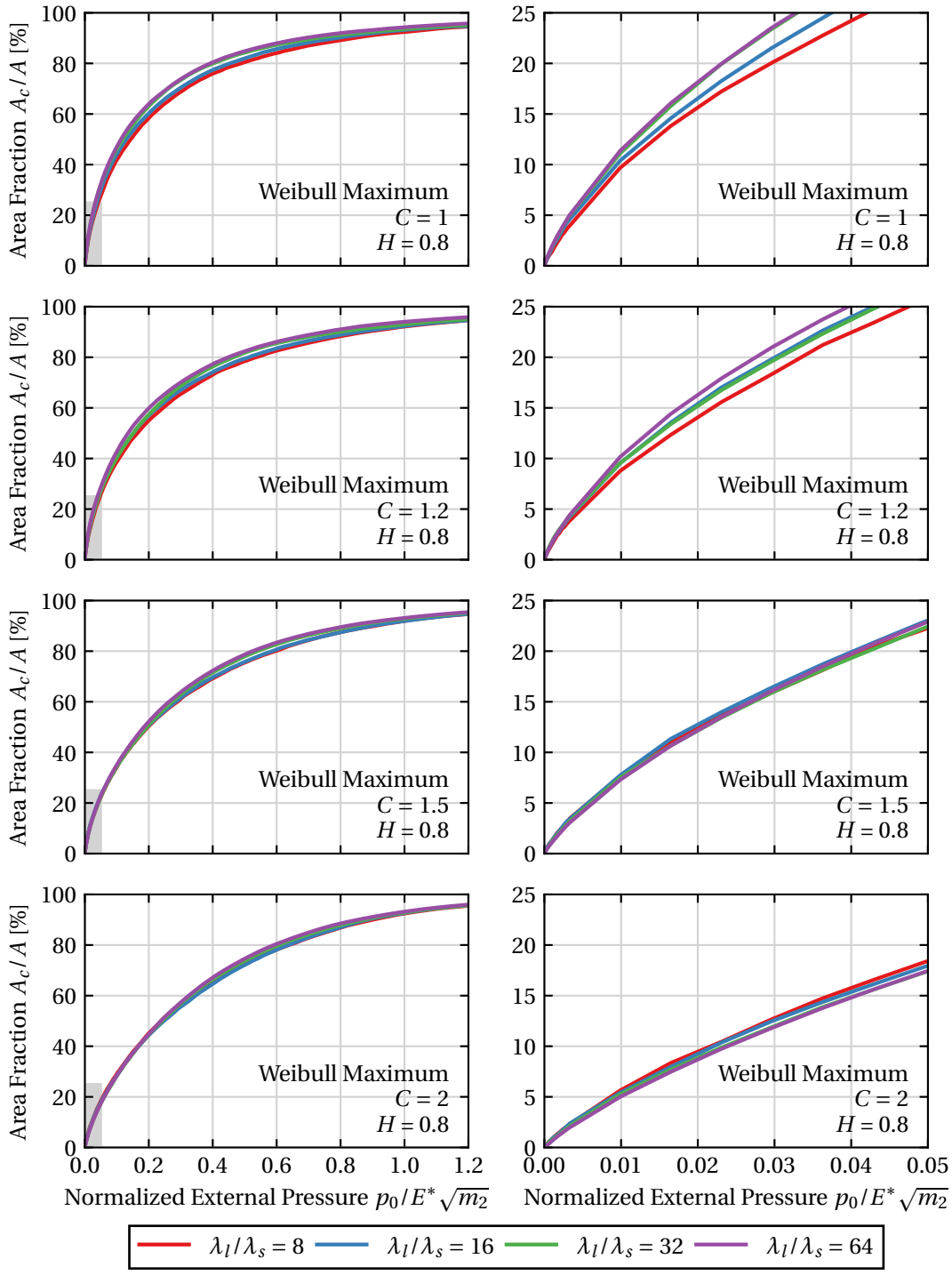


**Figure 5.22:** Comparison of the real contact area evolution of Weibull Maximum topographies for different values of the wavelength ratio $\lambda_l/\lambda_s$.

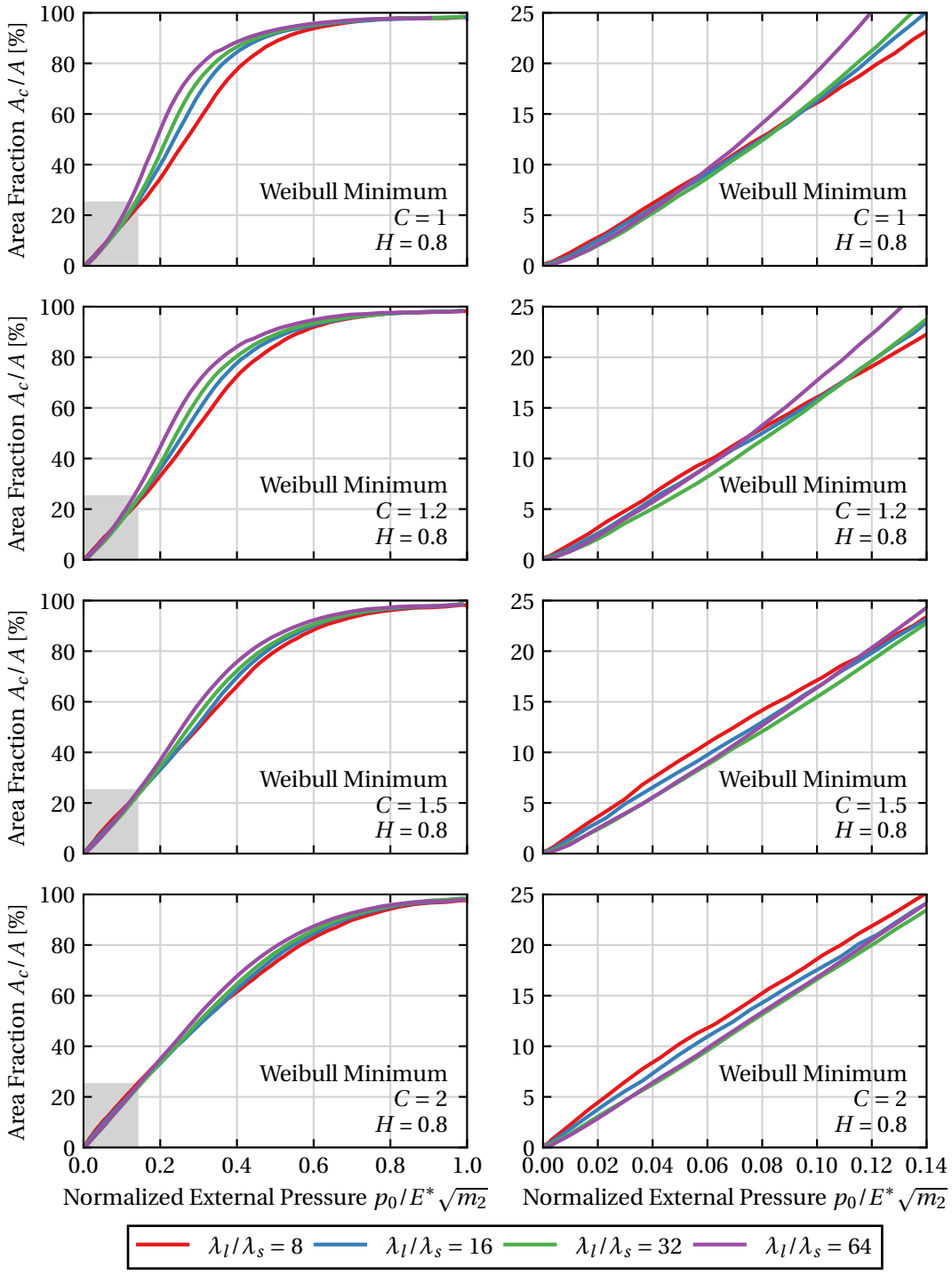


**Figure 5.23:** Comparison of the real contact area evolution of Weibull Minimum topographies for different values of the wavelength ratio $\lambda_l/\lambda_s$.

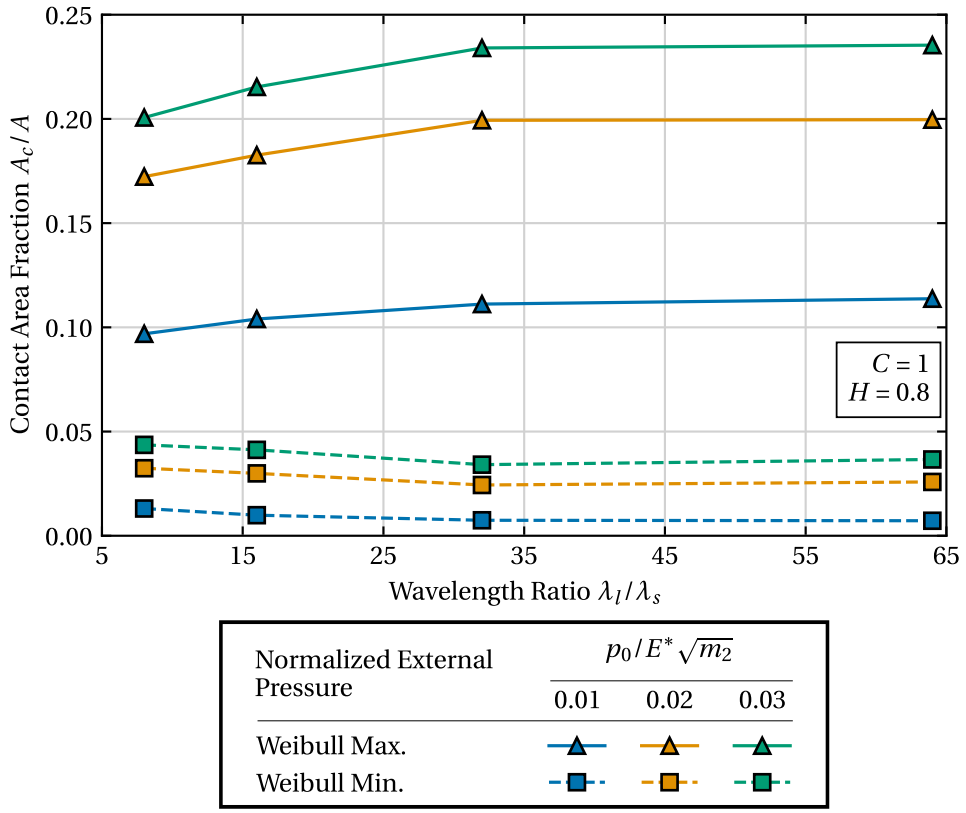


**Figure 5.24:** Evolution of the real contact area as a function of the wavelength ratio $\lambda_l/\lambda_s$ for three different external pressure values in the light contact domain—for both Weibull cases.

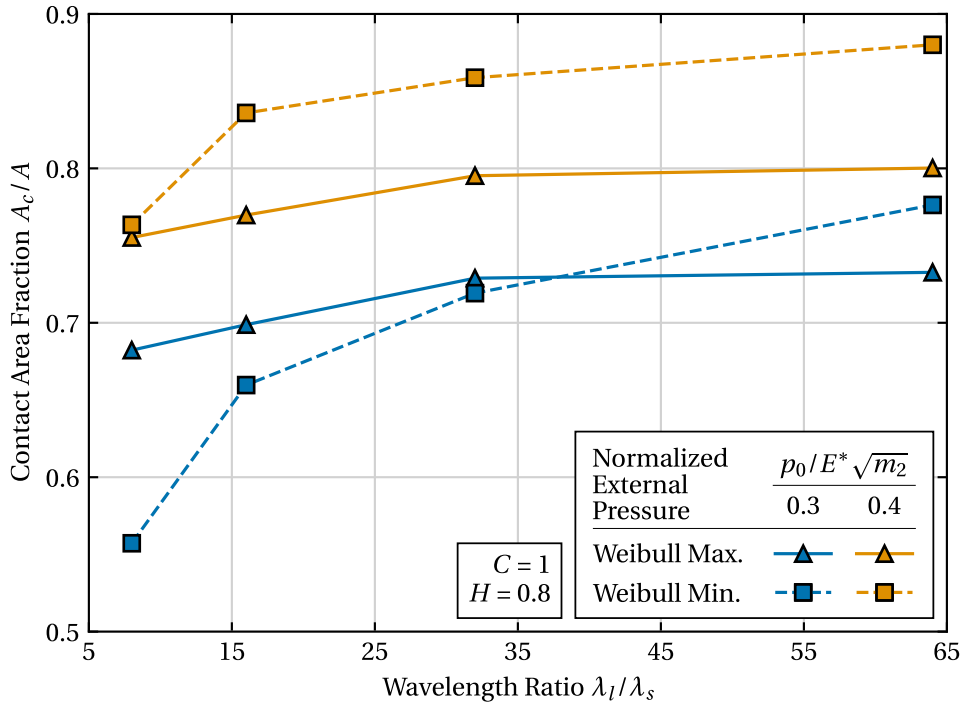


**Figure 5.25:** Evolution of the real contact area as function of the wavelength ratio $\lambda_l/\lambda_s$ for two different external external pressure values—for both Weibull cases.

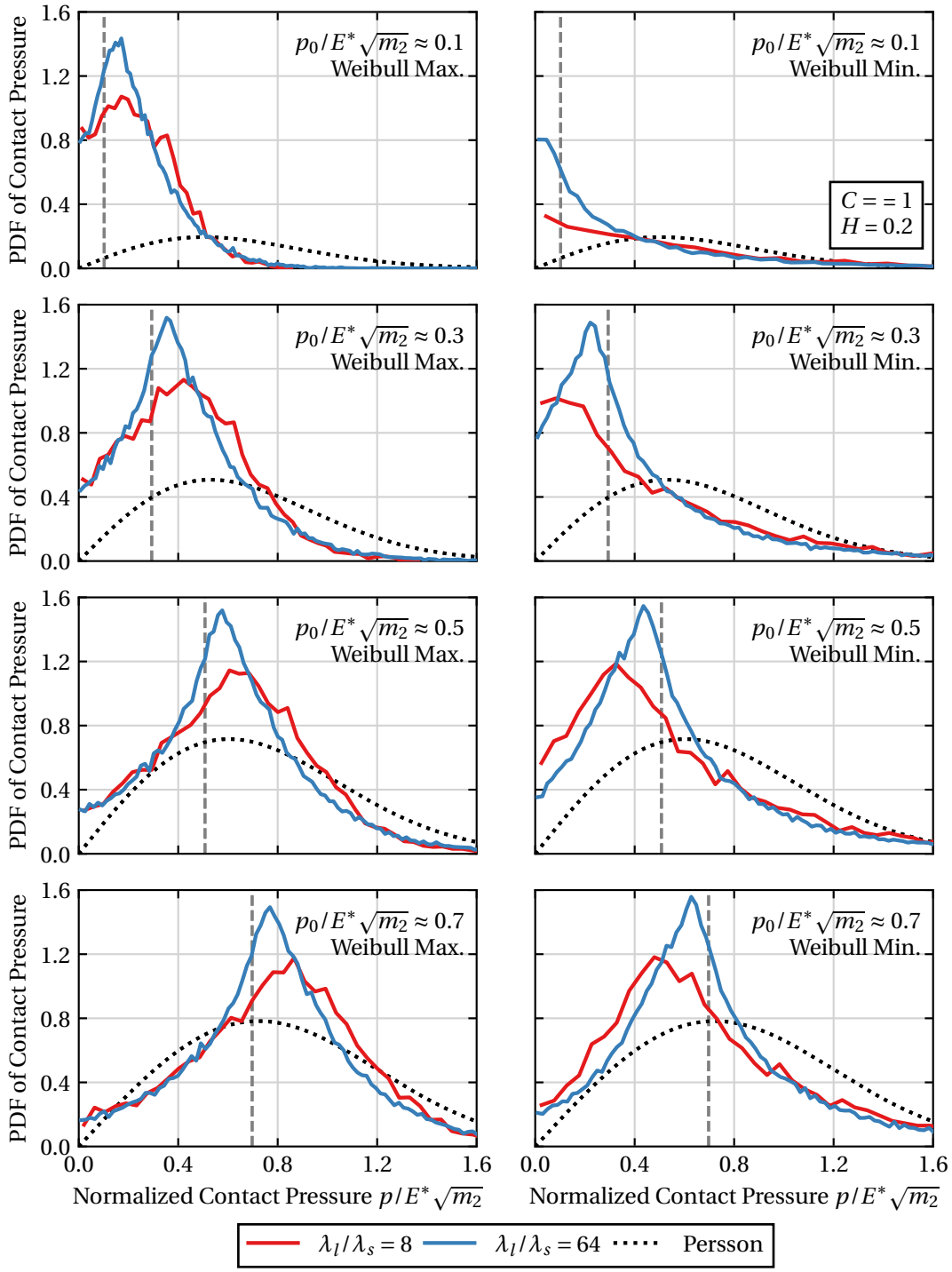


**Figure 5.26:** Comparison of the contact pressure distribution for two different values of the wavelength ratio $\lambda_l/\lambda_s$, in both Weibull cases and over four different values of normalized external pressure $p_0/E^*\sqrt{m_2}$. The Gaussian result is presented through Persson's model solution and the value of the increment is presented as a vertical and grey dashed-line.

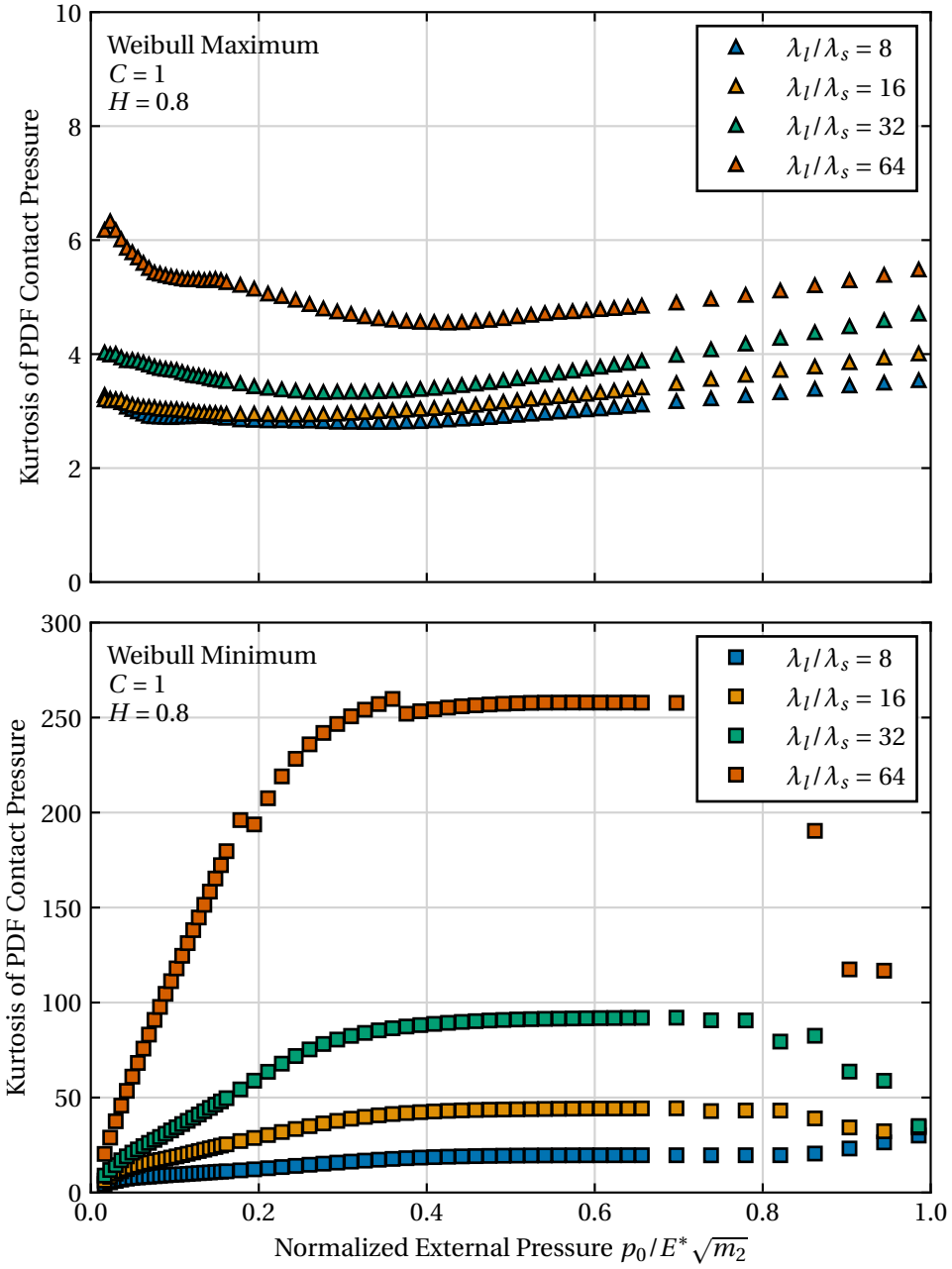


**Figure 5.27:** Comparison of the kurtosis of the contact pressure distribution (computed for each pressure increment) of the different wavelength ratio $\lambda_l/\lambda_s$ values for both Weibull cases.

### 5.3.4 Influence of the Hurst exponent

Finally, one can finish the analysis of the results with the effect of the Hurst exponent $H$. Both spectral properties are independently analysed to give a more in-depth analysis of their impact however, some of the conclusions and effects might be shared. The same scheme of the evolution of the area fraction and the contact pressure distribution is followed.

**Real contact area evolution**

The impact of the Hurst exponent $H$ on the evolution of the real contact area is isolated in Figure 5.28 and Figure 5.29, for both Weibull Maximum and Minimum scenarios, respectively. Different values of the shape parameter are considered yet only a wavelength ratio is presented ($\lambda_l/\lambda_s = 64$) to better inspect the effect of $H$.

The Weibull Maximum results (Figure 5.28) highlight a similar dependence on the Hurst exponent as it is for the wavelength ratio $\lambda_l/\lambda_s$. From the classical Gaussian results, it is known that higher values of $H$ lead to lower values of $A_c/A$ since the $\alpha$ also increases. In fact, this result was obtained for the nearly Gaussian case ($C = 3.602$) in the numerical simulations performed. However, with the addition of non-Gaussianity to the height distribution (a negative skewness in this case), the Hurst exponent starts to have the opposite effect. Only for the initial pressure increments, the Gaussian conclusions are applied. One sees that in the case of $C = 2$ the curves of different $H$ already become really close, but if one considers even lower values of the shape parameter like $C = 1.2$ or $C = 1.5$ it is verified that, except the very initial increments, the larger the Hurst exponent the higher the contact area fraction. The dominance in the area for the higher value the Hurst exponent is kept up to full contact. Similarly to the wavelength ratio, one can argue that the density of summits might play an important role in this case. As seen in Figure 3.35, higher values of the Hurst exponent lead to higher concentrations of summits which ultimately leads to a situation where the area tends to grow faster.

The opposite case, the Weibull Minimum distribution, shows also an evident dependency on the Hurst exponent, as presented in Figure 5.29. In light contact conditions, one verifies that the lower the Hurst exponent the higher the contact area fraction, which is in line with the results relative to Gaussian topographies. The initial contact on this type of topographies is dominated by higher height summits, whose contact area is severely affected by the predominance of higher frequencies. From a certain value of external pressure, an inversion on the Hurst curves is seen, with the $H = 0.8$ becoming the one with a higher value of contact area fraction. A possible justification for this dominance in the area might become also from the higher concentration of summits for topographies with higher Hurst values as seen in 3.35.

It is interesting to note that in this type of topographies the Hurst exponent can have a significant impact, yet it does not come in the same proportion in both Weibull cases. When comparing Figures 5.28 and 5.29, it is seen that Weibull Minimum tend to show higher deviations between the different Hurst values. To better explore the impact of $H$ on the different height distributions in Figure 5.30 the absolute difference between curve of $H = 0.8$ and the curve with $H = 0.2$ is plotted for different values of $C$ and considering $\lambda_l/\lambda_s = 64$. In the Weibull Maximum case, one verifies that the biggest difference for a

relatively lower value of external pressure with the maximum difference in the area being around 6% when $C = 1$. However, it is in the Weibull Minimum that the differences are more meaningful. The first part of these curves is concerned with the region where the curve $H = 0.2$ has a superior area and where the deviations tend to be smaller. The second part has bigger a longer (external pressure domain) impact, being reached difference values as high as 12%, for topographies with $C = 1$.

**Contact pressure distribution**

The effect of the Hurst exponent on the contact pressure distribution is presented in Figure 5.31 for both Weibull distributions. In this figure, the distributions of contact stress are plotted for four different values of external pressure, selected to cover a wider and representative range. The remaining properties were chosen in order to better highlight the influence of the Hurst exponent—$C = 1$ and $\lambda_l/\lambda_s = 64$. The analysis of these results flows into the same conclusions of the previous sections. The area has to be depicted on the contact pressure distributions and with the different Hurst values, this fact is applied. For instance, when $p_0/E^*\sqrt{m_2} = 0.1$ in the Weibull Minimum case, it is verified that $H = 0.2$ has a more developed contact pressure distribution which is tune with the results seen in Figure 5.28. The light contact in these conditions is slightly dominated by lower Hurst values, yet it is known that this fact only holds for small external pressures. For the remaining histograms, in both Weibull distributions, it is seen a dominance of the higher Hurst value ($H = 0.8$). This means that a higher area is translated into the contact stress distribution with a higher concentration of stresses around the mode value. One should note that unlike the previous properties (shape parameter $C$ and wavelength ratio $\lambda_l/\lambda_s$) the higher concentration of stress for higher $H$ is accompanied by a slight skew towards the direction of the heigh distribution—right for Weibull Maximum and left for Weibull Minimum. To complete the analysis of the distributions one has to inspect the effect of $H$ in tails of the stress distributions. In Figure 5.32 the computed value of kurtosis for each pressure increment is presented for the two values of the Hurst exponent, considering both Weibull cases. While in Weibull Maximum no clear evidence can be obtained between the different $H$ values, in the Weibull Minimum it is seen that higher Hurst have higher kurtosis values which is a signal of the higher predominance of high contact pressure values.

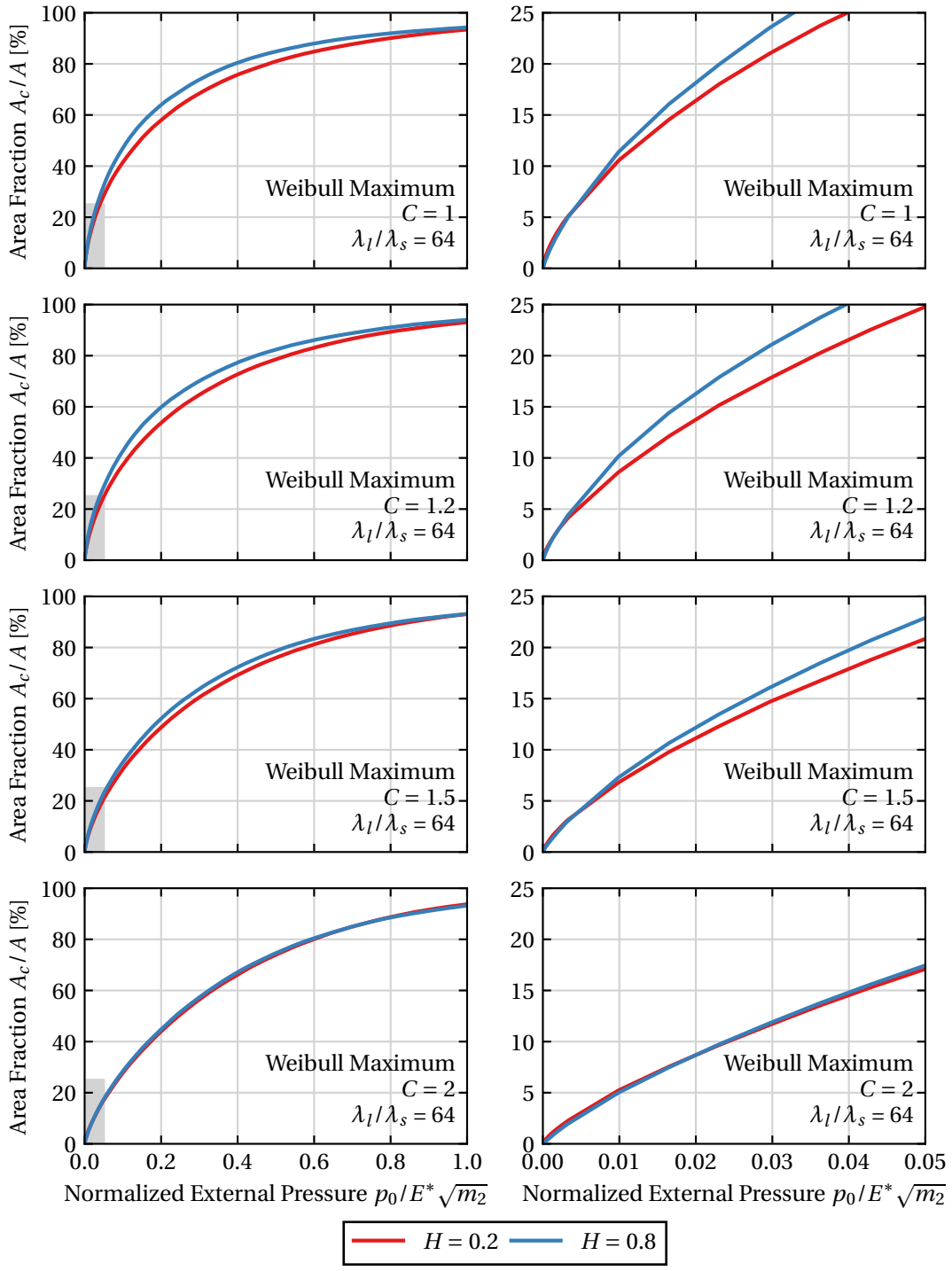


**Figure 5.28:** Comparison of the real contact area evolution of Weibull Maximum topographies for different values of the Hurst exponent $H$.

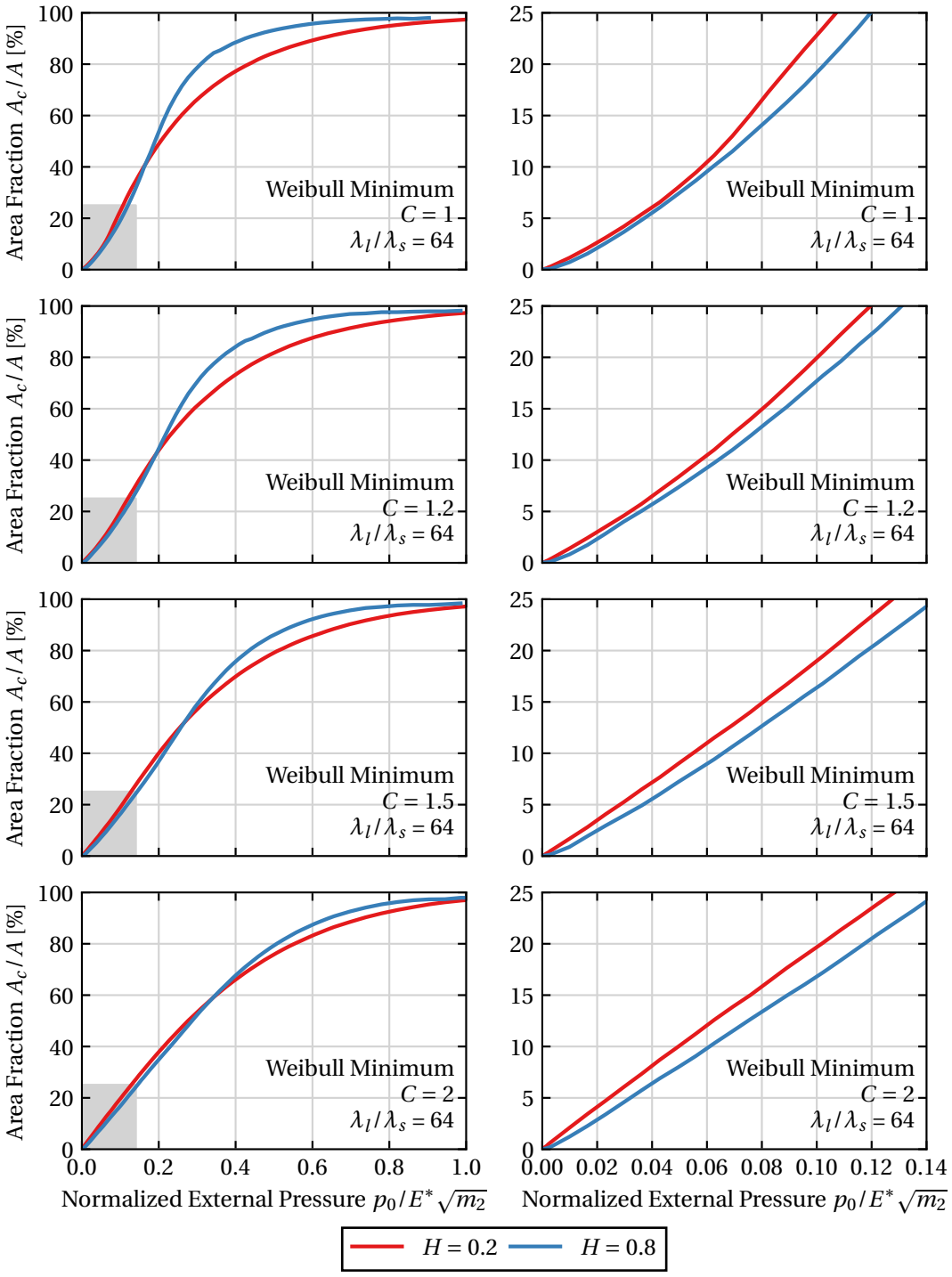


**Figure 5.29:** Comparison of the real contact area evolution of Weibull Minimum topographies for different values of the Hurst exponent $H$.

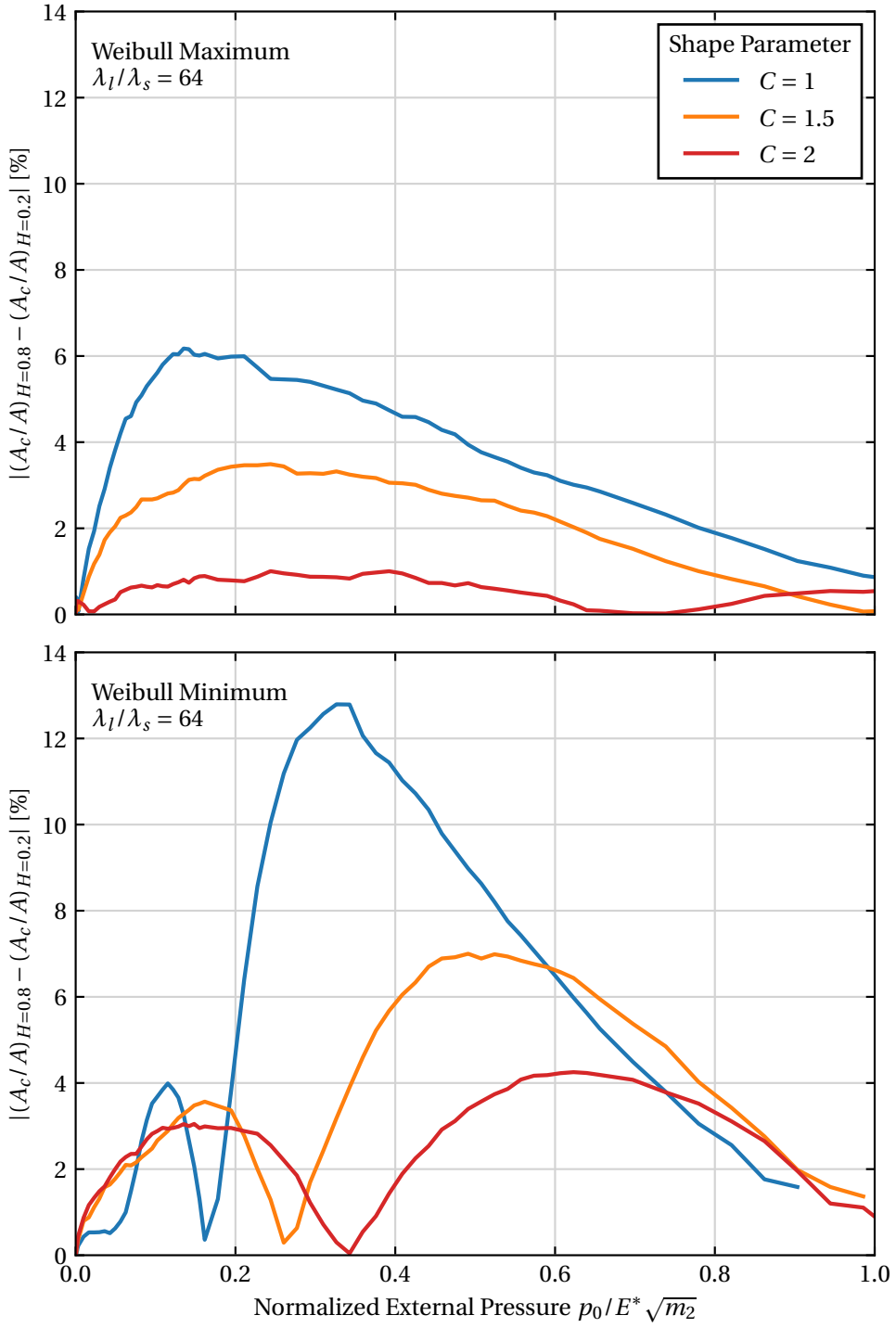


**Figure 5.30:** Absolute difference between the area fraction curves of $H = 0.8$ and $H = 0.2$, for different values of the shape parameter $C$ in both Weibull cases.

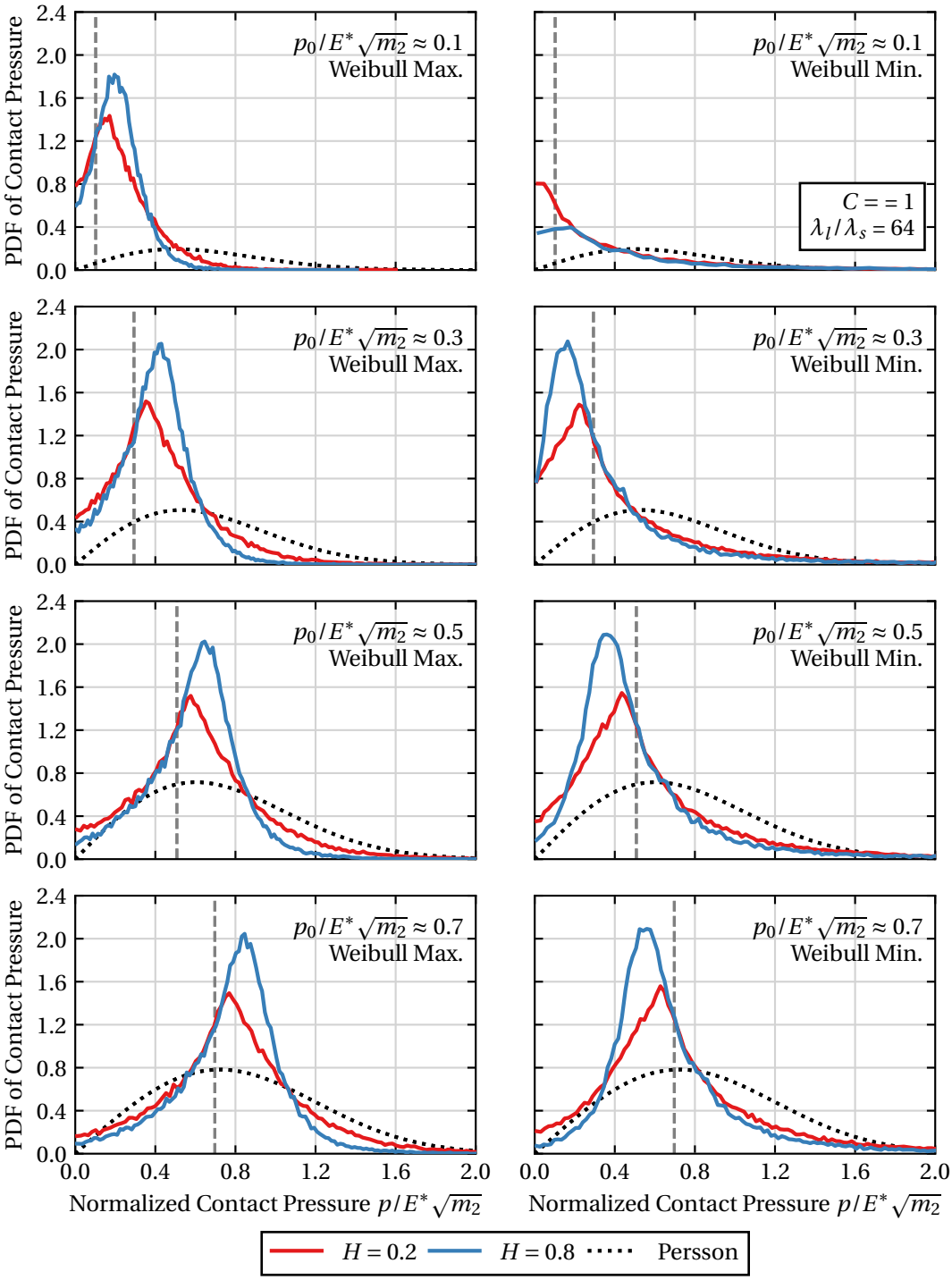


**Figure 5.31:** Comparison of the contact pressure distribution for the two different values of the Hurst exponent $H$, in both Weibull cases and over four different values of normalized external pressure $p_0/E^*\sqrt{m_2}$. The Gaussian result is presented through Persson's model solution and the value of the increment is presented as a vertical and grey dashed-line.

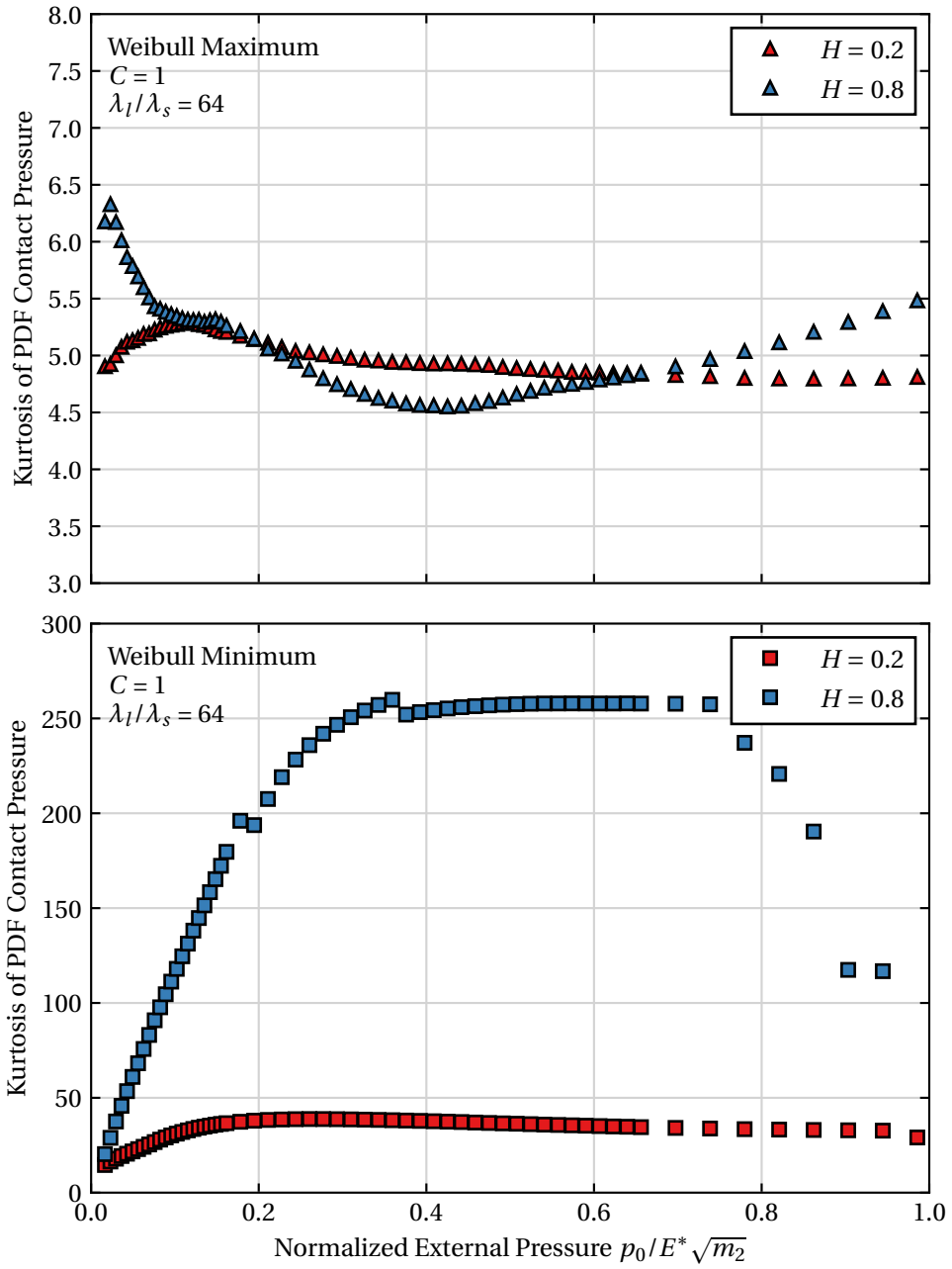


**Figure 5.32:** Comparison of the kurtosis of the contact pressure distribution (computed for each pressure increment) of the two different Hurst exponent $H$ values for both Weibull cases.

### 5.3.5 Modelling the real contact area evolution

The effect of the different properties that parametrize a non-Gaussian self-affine topography has been extensively discussed in the present chapter, yet no analytical treatment has been done to the obtained data in order to model the studied phenomena. In fact, the scope of the work is not o obtain a theoretical or numerical model to the evolution of the contact area on non-Gaussian topographies, but to study the resultant effects of this type of topographies and pave the way for future investigations. Nonetheless, fitting the obtained data to a proper selected function constitutes an effortless yet fruitful task, from where some additional observations on the results can be taken. In the fitting procedure, only the light contact portions of the results were considered, since the consideration of all the domains would lead to a more complex fitting function. Additionally, the light contact region is the more dominant domain on Gaussian contact models like the multiasperity models and standard engineering problems. The results were then truncated up to a maximum value of approximately $p_0/E^*\sqrt{m_2} \approx 0.12$ to incorporate both Weibull Maximum and Minimum results. From the Gaussian results, it has been seen through the past research work that in very initial contact conditions the behaviour is almost linear (Carbone and Bottiglione, 2008; Yastrebov, Anciaux, *et al.*, 2017b). In this work for example Figure 5.16, it has been also appointed that when the shape parameter is $C = 3.602$ a near-linear behaviour is obtained. Even so, the majority of the results have shown strongly non-linear behaviour with some results highlighting a concave down form, like the Weibull Maximum, or a concave up shape as in Weibull Minimum. Taking these considerations into account, a power-law function to model the contact evolution of both Weibull type of topographies has been chosen, that writes

$$\frac{A_c}{A} = a\left(\frac{p_0}{E^*\sqrt{m_2}}\right)^b , \tag{5.1}$$

were $a$ and $b$ are the fitting parameters. This function has great potential for modelling the current area evolution cases as one can obtain the linear case for $b = 1$, or both concave up and down if $b$ is bigger or smaller than 1, respectively.

The fitting procedure was made using the `Python3` package `SciPy` that easily performs the numerical regression using the non-linear least squares method. The power-law function (Equation (5.1)) resulted in impressive accurate results with every case being well modelled by such function—an average coefficient of determination $R^2$ of 0.9995 was obtained. The computed parameters $a$ and $b$ as well as the coefficient of determination $R^2$ values can be consulted Appendix A. A comparison between the numerical FEM results and the fitting function obtained is presented in Figure 5.33 were the precise fit can bee seen for both Weibull distributions—a particular spectral case was chosen ($\lambda_l/\lambda_s = 8$ and $H = 0.2$). In this graph, the region of external pressure and contact area fraction considered in this fitting process is also depicted. To ease the discuss around these results, a visual representation of the fitting parameters is showed in Figure 5.34 and Figure 5.35. Both graphics tend to highlight the different variables on which the contact area evolution is dependent, being the Figure 5.34 concerned with the dependency with the shape parameter $C$ and Figure 5.35 with the influence of $\lambda_l/\lambda_s$. The two graphs on top depict the Weibull Maximum cases while the two graphs on the bottom depict the Weibull Minimum. In turn, the different values of the Hurst exponent are presented in the columns,

i.e., the right side graphs show the results for $H = 0.2$ whereas the left side $H = 0.8$. These plots essentially compress the results and analysis presented in great detail in the previous sections.

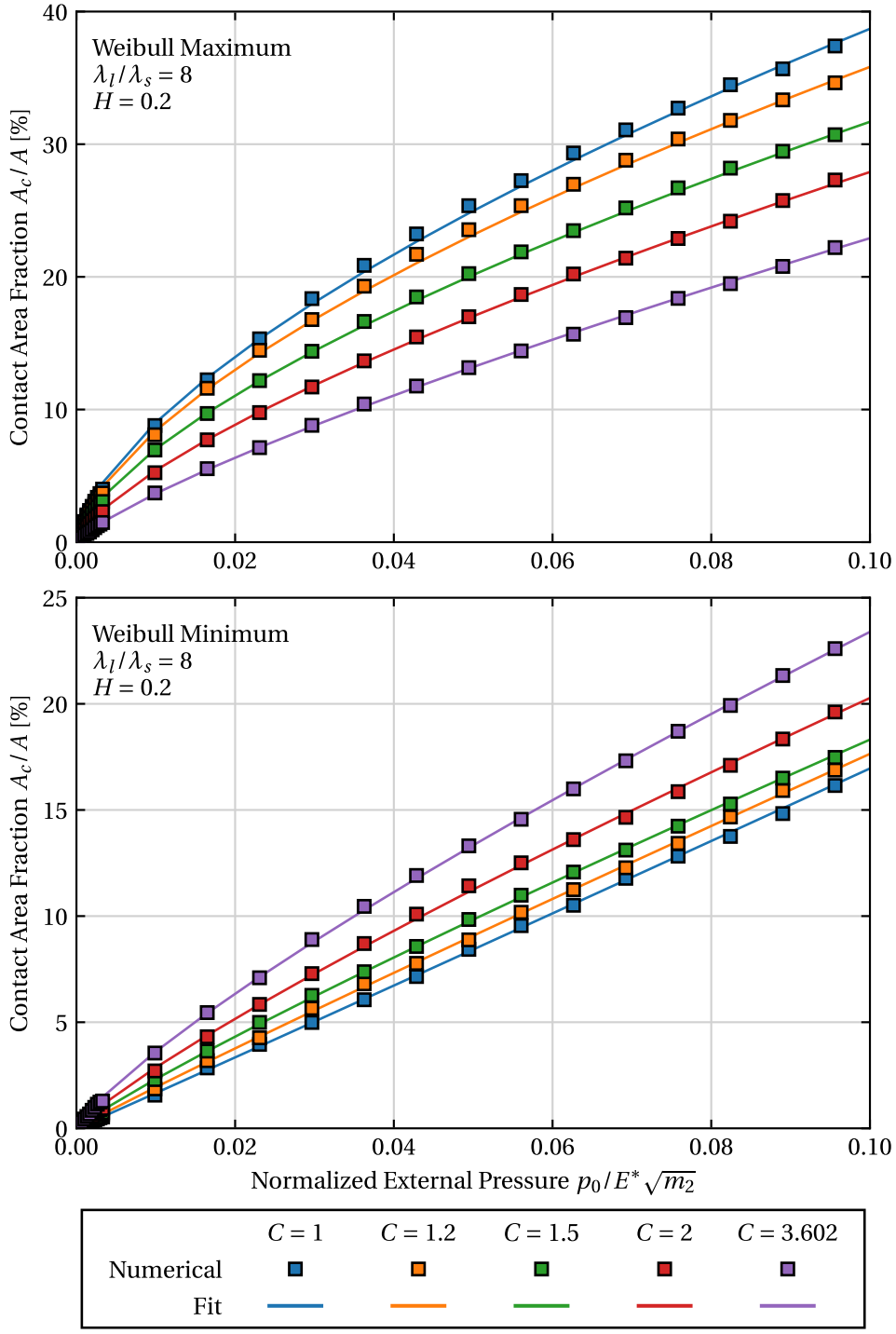


**Figure 5.33:** Comparison of the numerical FEM results and the power-law fitting function for the contact area evolution.

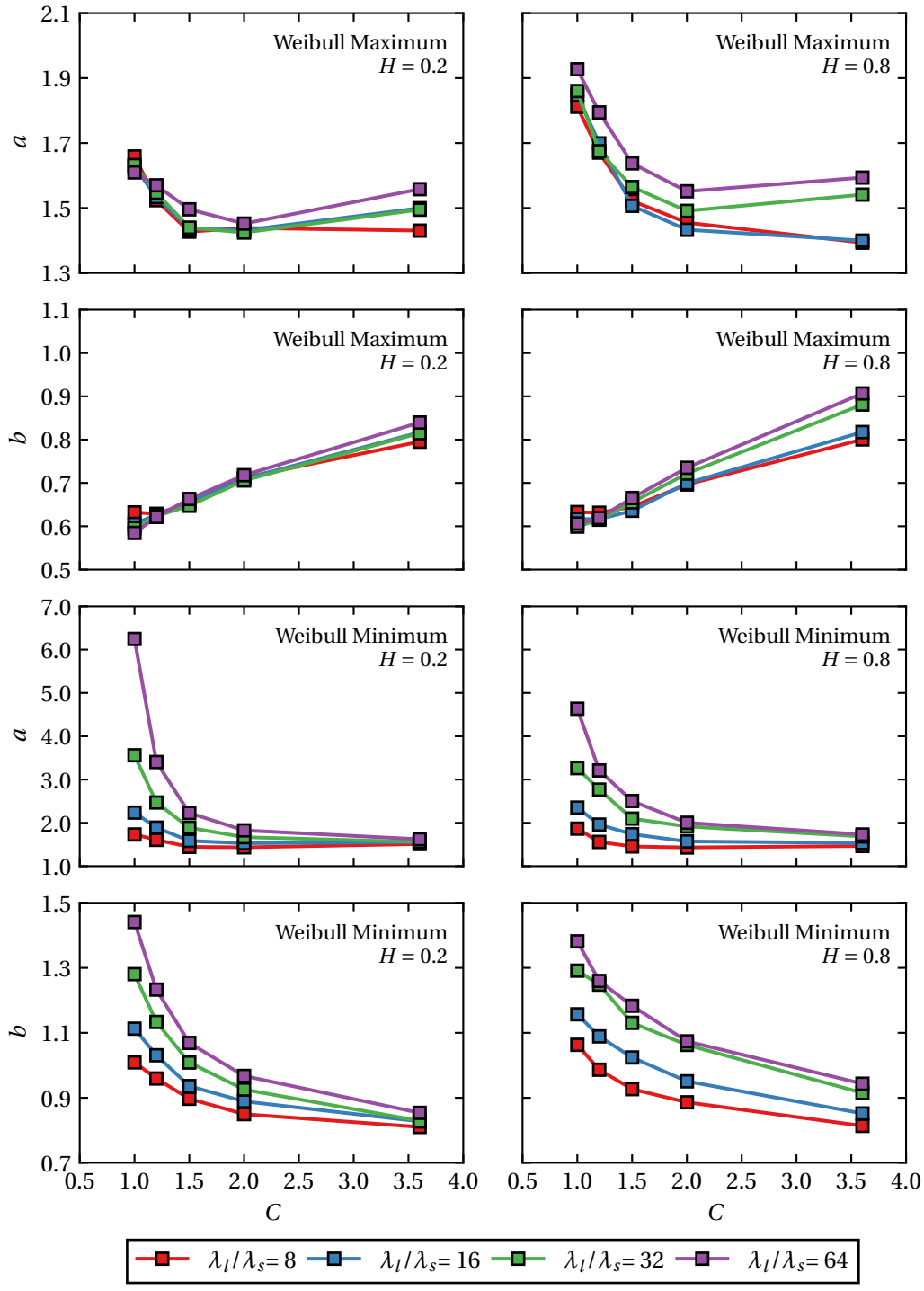


**Figure 5.34:** Fitting parameters $a$ and $b$ of the power-law function (Equation (5.1)) presented as a function of the shape parameter $C$ for different values of wavelength ratio $\lambda_l/\lambda_s$.

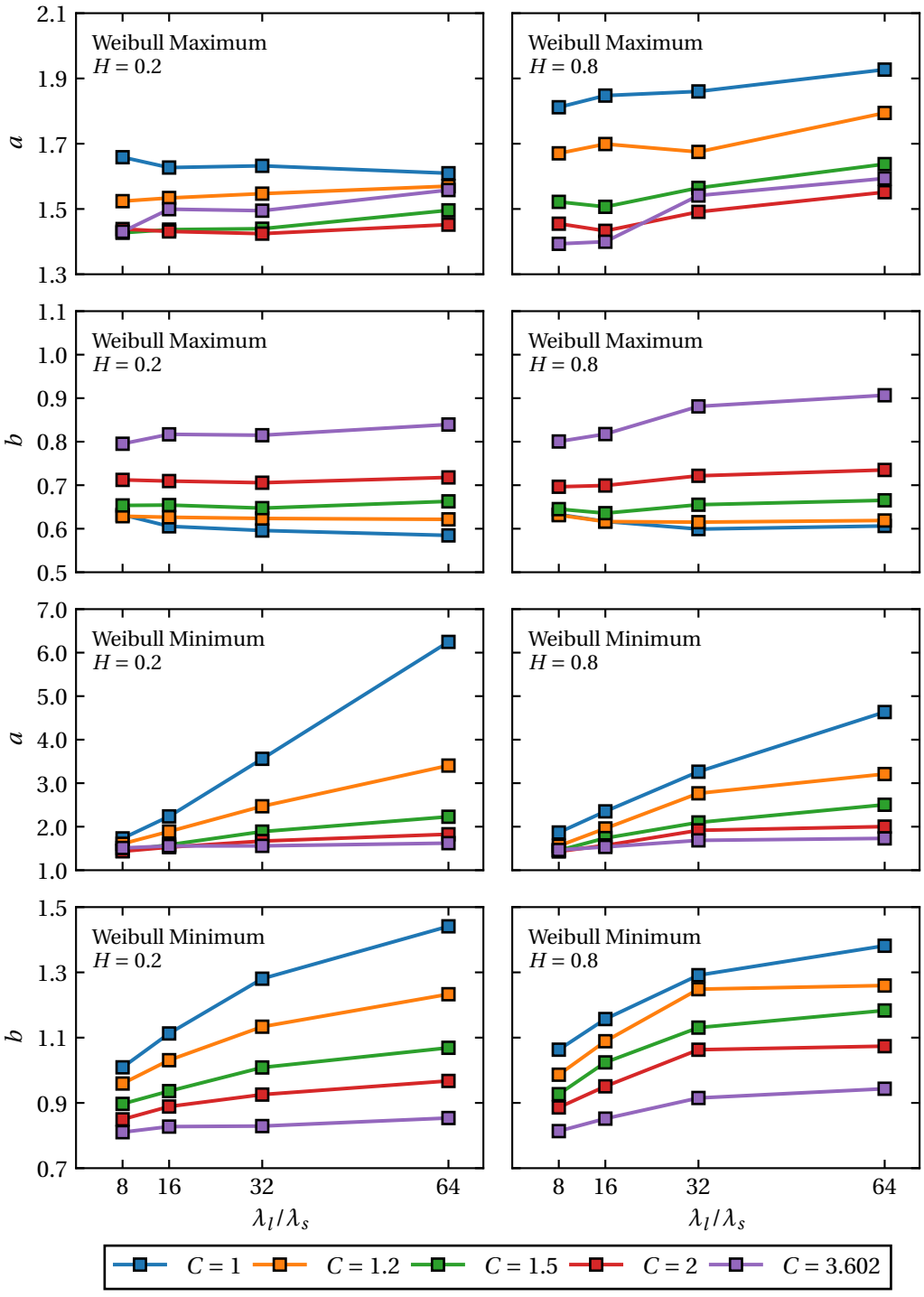


**Figure 5.35:** Fitting parameters $a$ and $b$ of the power-law function (Equation (5.1)) presented as a function of the wavelength ratio $\lambda_l/\lambda_s$ for different values of the shape parameter $C$.

## 5.4 Study on non-Gaussian rough contact of 3D topographies

The main topic on debate thought this work has been the impact of non-Gaussian height distributions on the contact of self-affine rough surfaces, which is a naturally 3D problem. Only in very peculiar conditions, its dimension size can be reduced, like extremely anisotropic topographies—even though it is possible to define a so-called *equivalent* profile of a given surface, in principle. However, due to computational limitations, 2D rough contact simulations still hold an important role on FE studies as they allow a fast a reliable method for obtaining important qualitative and quantitative information. The previous chapters have addressed several 2D simulations and, despite not providing a complete interpretation of the 3D rough contact phenomena, the study allowed to obtain a proper set of solid conclusions which must hold for the 3D case, in general. With the 3D analysis of rough contact, it is possible to obtain more useful and precise results that can be used to compare to the vast majority of the theoretical models and numerical data available in the literature. Additionally, a more direct relation with the topographies statistics, as studied in Chapter 3, is also obtained. Nonetheless, it also comes with a higher computational cost that tends to scale very quickly, particularly with the increase of the spectral content of the PSD—higher wavelength ratios $\lambda_l/\lambda_s$.

To complete the current study some 3D simulations were performed. This last study should be seen as an application of the 3D rough contact of non-Gaussian rough surfaces and act as a validation of some of the conclusions previously presented. The limitations of the 3D case only allow to select a very strict number of cases to simulate and even the RCE parameters have to be carefully chosen. Additionally, simulating topographies up to full contact conditions requires a considerable amount of computational requirements. For this reason, only the light conditions were explored in this study. Being paramount to test both Weibull distributions, two different shape parameter values were chosen—$C = 1.2$ and $C = 2$. These values have been selected with the goal on real engineering applications and, as one can see in Figure 3.14, they allow to cover a decent range of skewness and kurtosis values, thus retaining a practical interest. For the spectral parameters, one has to kept $\lambda_l/\lambda_s = 8$ and $H = 0.8$, since the higher the maximum frequency the more refined has to be the generated topography which translates into a more expensive simulation. The variables considered in this study are summarized in Table 5.5 where one sees that only a total of 4 cases were studied. Equally important is the definition of the RCE that have also to be cautiously selected. Both mesh size, the conditions on the length, discretisation and height of the substrate of the RCE have been relaxed to avoid high computation times. For the same reason, the high-resolution region has been defined as 5 times the spatial discretisation, comprising 5 layers of fine mesh near the rough boundary. To preserve a proper representativeness of the results, the number of realizations was kept in 20. The summary of the 3D FE study conditions is presented in Study 5.3.

These conditions have resulted in a 3D RCE with a total of 205579 nodes and 202400 elements. The average time of each simulated case is presented in Table 5.6, where it is seen that for each realization more than 10 hours were required to compute the final solution. Since for each case 20 realization were considered a total computational time of 1033 hours (around 43 days) was required. Once again, for practical considerations,

several cases are solved simultaneously to shave off the computation time down to reasonable practical values. When comparing these results with the 2D cases (cf. Table 5.4) it becomes clear the difference in the order of magnitude of 3D FE simulations.

**Table 5.5:** Variables considered for the 3D FE study on non-Gaussian rough surfaces modelled with the Weibull distribution. The studied cases result from a combination of theses variables, making a total of 4 different cases.

| Height distribution | $C$ | $\lambda_l/\lambda_s$ | $H$ |
|---|---|---|---|
| Weibull Maximum | 1.2 | 8 | 0.8 |
| Weibull Minimum | 2 | | |

**Study 5.3 (Conditions of the numerical 3D FEM study).**

***Roughness Model***

| | |
|---|---|
| *RMS slope:* | $z'_{rms,x} = 0.1$ |
| *Wavelength ratio:* | $\lambda_l/\lambda_s = 8$ |
| *Hurst exponent:* | $H = 0.8$ |
| *Height distribution:* | *Weibull Max. and Min.* |
| *Shape parameter:* | $C \in [1.2, 2]$ |

***RCE parameters***

| | |
|---|---|
| *Mesh:* | $\lambda_s/\Delta x = 7$ |
| *Length:* | $L/\lambda_l = 3$ |
| *Substrate height:* | $H_{\text{sub}}/\sigma_z = 300$ |
| *Number of fine mesh layers:* | $= 5$ |
| *Number of realizations:* | $= 20$ |

**Table 5.6:** Average computational time (in hours) required to perform a 3D FE simulation.

| Height distribution | $C$ | Average total time / h |
|---|---|---|
| Weibull Maximum | 1.2 | $\approx 16$ |
| | 2 | $\approx 14$ |
| Weibull Minimum | 1.2 | $\approx 11$ |
| | 2 | $\approx 11$ |

### 5.4.1 Discussion of results

After the simulations were performed the results were analysed and the area evolution curves were recovered. The area was computed using the method proposed by Yastrebov, Anciaux, *et al.* (2017a) as written in Equation (4.64). In Figure 5.36, the area evolution results are presented and compared to three different Gaussian solutions. The first one is obtained from the work of Yastrebov, Anciaux, *et al.* (2017b), which has available several numerical solutions and from where the curve with the same spectral properties of the

current study has been retrieved. This result has a particular interest since it has been obtained using the same area computation strategy and using a BEM framework, which has allowed the authors to employ more refined topographies on the study. Second, two theoretical models are shown: the already used Persson's model and the well know BGT multiasperity model (Bush *et al.*, 1975), being used in its asymptotic form. Additionally to the area evolution curves also the derivative of these curves is depicted, which is a common procedure that allows a more sound characterization of the results.

The simulation area curves truly resemble the 2D results obtained in 5.3. One verifies that, in Weibull Maximum topographies, the typical behaviour is characterized by a concave down curve that has a very steep initial gain in area that progressively tends to slow down. The derivative curves are very useful to depict these variations as one clearly sees that in the initial pressure increments the derivative assumes really large values that quickly decrease and tend to stabilize with the pressure increase. The Weibull Maximum results are also in accordance with the statistical data obtained and discussed in Chapter 3. Similar observations can be drawn for the Weibull Minimum area evolution curves. The low probability of higher height summits and the respective high curvature in this type of topographies corresponds to small values of area for the initial pressure increments. With the increase of pressure, growing derivate values are captured which emphasizes the concave-up curve type. The effect of the shape parameter is preserved for both Weibull cases, i.e., while for Weibull Maximum lower $C$ values lead to higher area values, Weibull Minimum topographies of lower $C$ tend to have the lower values of area. Comparing both Weibull cases some significant differences area captured. For instance, if one considers the curves of $C = 1.2$ it is verified that Weibull Minimum requires almost four times more external pressure value to reach the contact area fraction value of 20%

Regarding the comparison with the Gaussian solutions, it can be seen, that while Weibull Maximum topographies possess higher area values, Weibull Minimum tends to have inferior contact area, which is in tune with all the statistics observed here—this observation is better understood if the results from Yastrebov, Anciaux, *et al.* (2017b) are considered. The linear behaviour commonly associated with Gaussian rough contact analysis is inadequate for describing non-Gaussian topographies accurately. If the area curves are not enough to prove this point, a look into the derivatives (Figure 5.36b) evidence this fact. Despite not being constant, the derivate curves experience abrupt variations with pressure, which does not agree with the numerical Gaussian solution from Yastrebov, Anciaux, *et al.* (2017b). Surprisingly, the Weibull Minimum with $C = 2$ topographies exhibit the behaviour nearest to the linear evolution of the contact area with pressure, with an approximately constant throughout the loading range.

To end this analysis, one can also look at the contact pressure distribution results. In Figure 5.37 histograms of the contact pressure distribution of both Weibull cases as presented for several external pressure increments. As seen, the results in area should translate the contact area at the pressure increment that area analysed. This fact is seen in both Weibull topographies, with the histogram of $C = 1.2$ being the more dominant and well developed for Weibull Maximum and, in opposition, the less prominent for the Weibull Minimum case. Additionally, a visual representation of contact stresses is depicted, for the same values of external pressure of Figure 5.37 and considering $C = 2$, in Figures 5.38

and 5.39. By looking at these figures one can get some additional clear interpretations of the contact phenomena of this type of topographies. It is seen that the increase in pressure does not just increase the spatial frequency of the contact stresses but also their magnitude. The relation between the contact pressure distribution and the area is clearly seen as one can easily get an idea of how the area evolves with the increase of external pressure. Comparing both Weibull distributions it is also verified that, for the same pressure increment, Weibull Maximum has much more distributed contact pressure while in Weibull Minimum the equilibrium has to be done in smaller contact clusters. This is the reason why in Weibull Minimum topographies the magnitude of the contact stresses tends to be vastly superior.

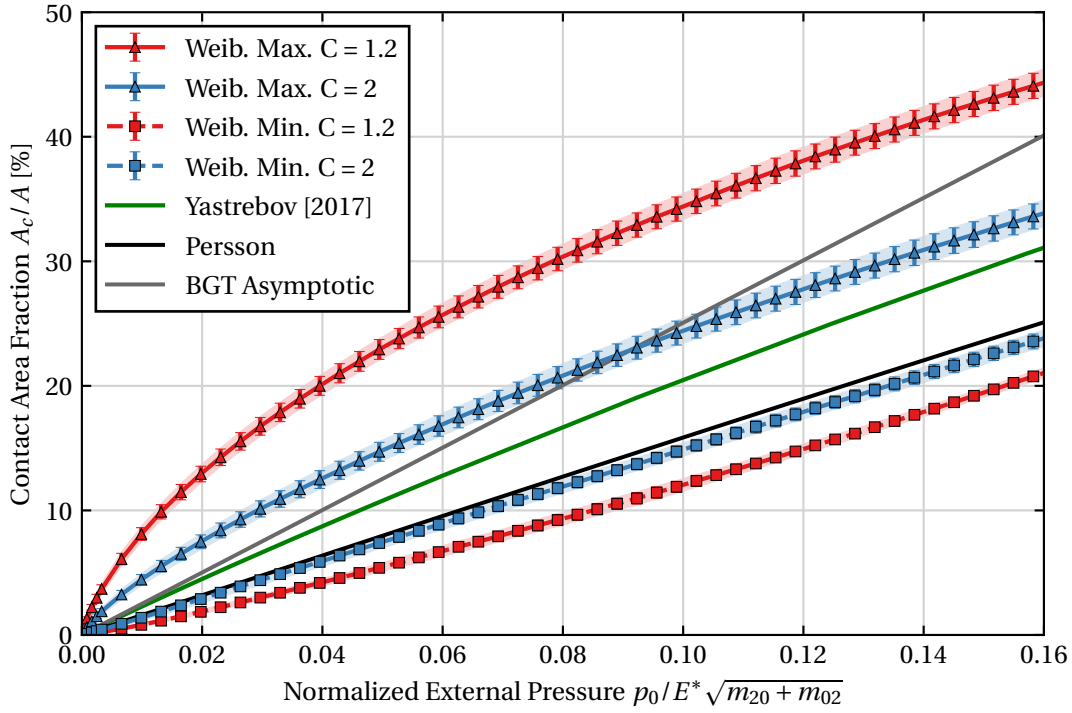


**(a)** Contact evolution curves.

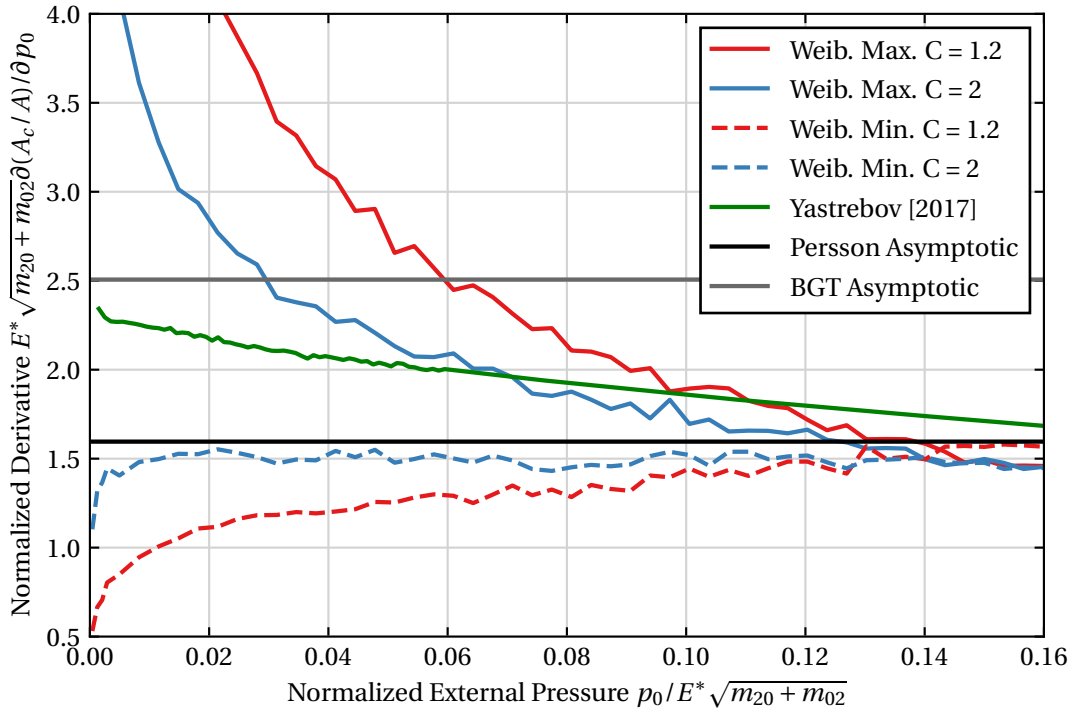


**(b)** Normalized derivative of the contact area curves.

**Figure 5.36:** Results for the real contact area and respective derivative from the 3D FEM study and comparison with three different Gaussian results.

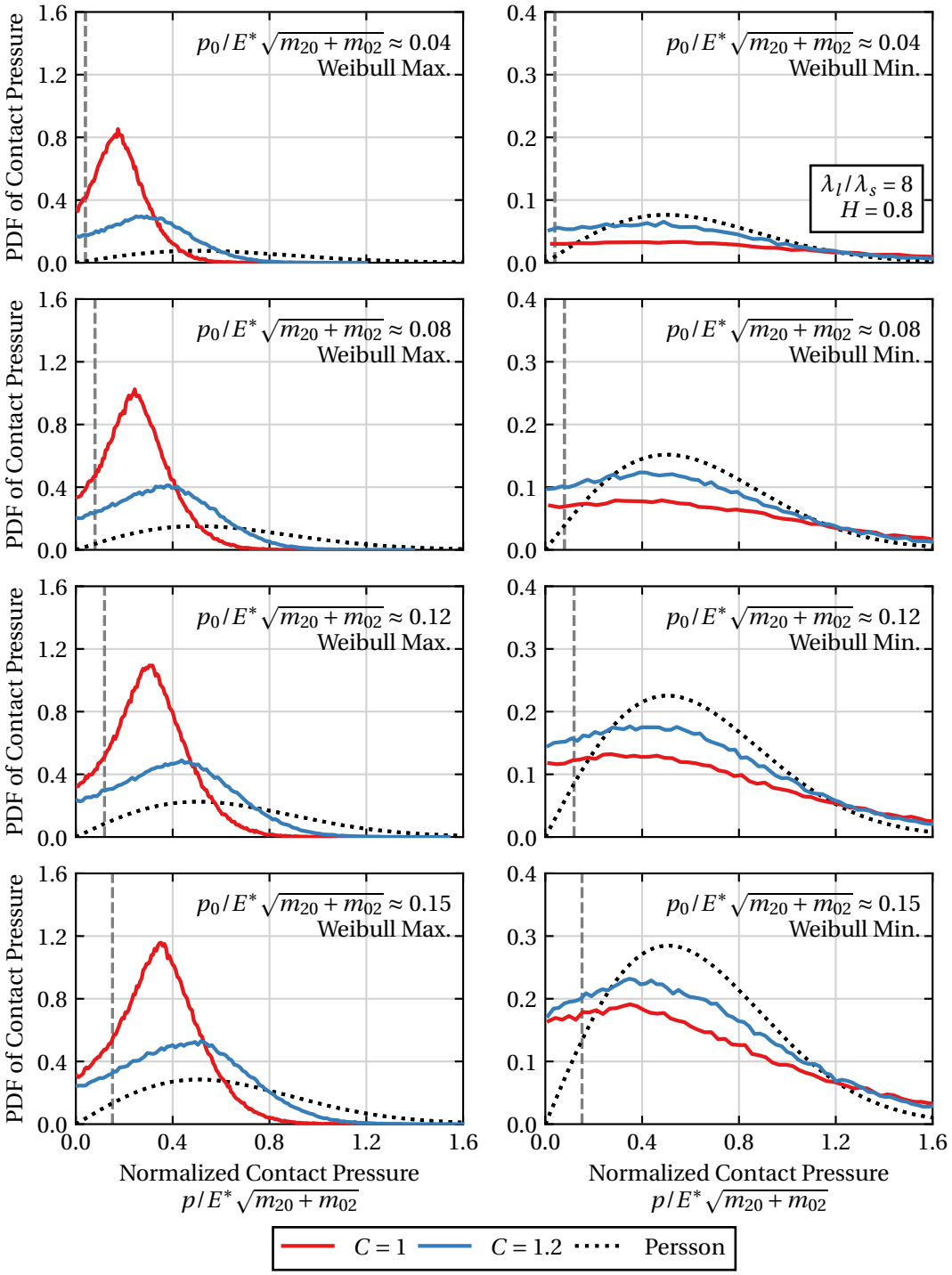


**Figure 5.37:** Comparison of the contact pressure distribution for different values of the shape parameter $C$, in both Weibull cases and over four different values of normalized external pressure $p_0/E^*\sqrt{m_{20}+m_{02}}$. The Gaussian result is presented through Persson's model solution and the value of the increment is presented as a vertical and grey dashed-line.

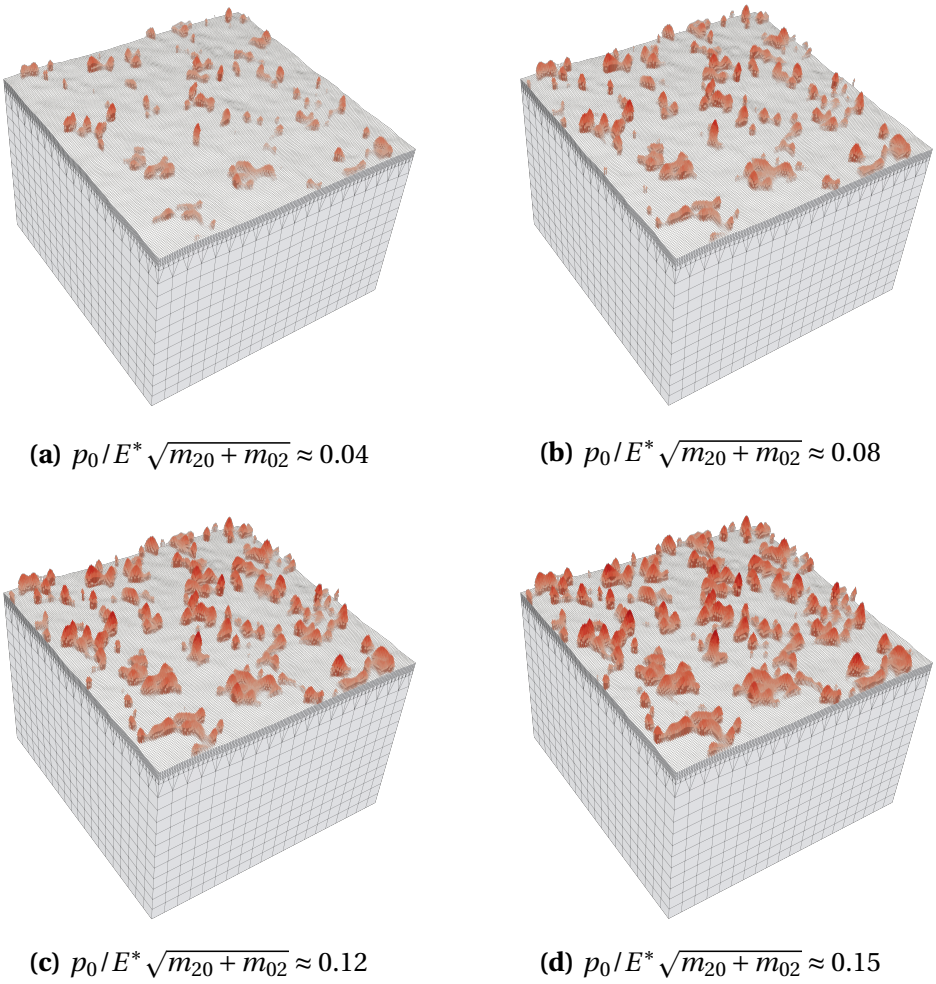


**(a)** $p_0/E^*\sqrt{m_{20}+m_{02}} \approx 0.04$ **(b)** $p_0/E^*\sqrt{m_{20}+m_{02}} \approx 0.08$

**(c)** $p_0/E^*\sqrt{m_{20}+m_{02}} \approx 0.12$ **(d)** $p_0/E^*\sqrt{m_{20}+m_{02}} \approx 0.15$

**Figure 5.38:** Visual representation of the distribution of the contact stresses for the Weibull Maximum case with $C = 2$.

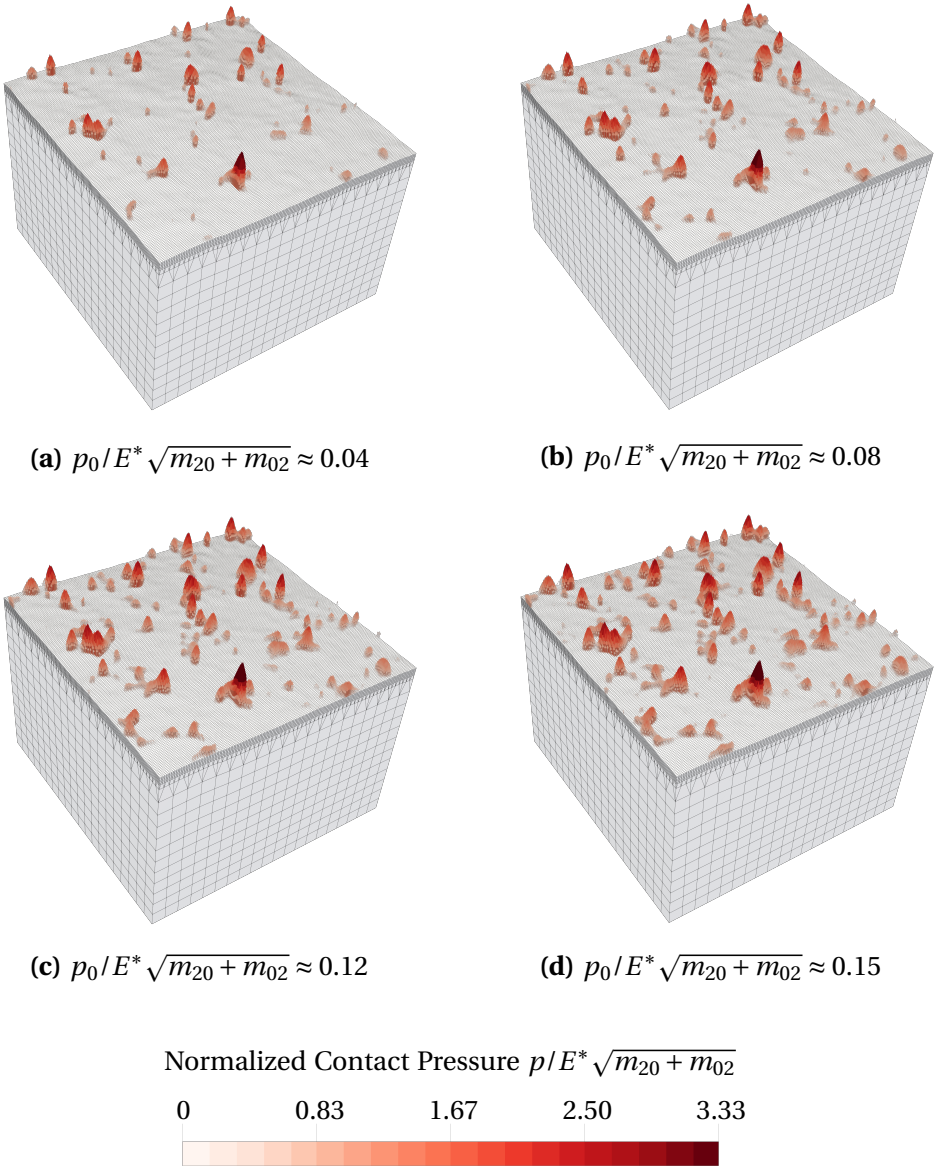


**Figure 5.39:** Visual representation of the distribution of the contact stresses for the Weibull Minimum case with $C = 2$.

## 5.5 Closing comments

This chapter started with a mesh convergence study on a non-Gaussian 2D RCE, in order to test the framework and to select the most appropriate mesh size value. The results obtained have shown that both area computation strategies verify convergence and that the rate of convergence is increased if an average area value is considered. The value of $\lambda_s/\Delta x = 8$ was chosen with a good compromise between representativeness and computational cost.

The second part of this chapter was dedicated to the 2D FEM study of non-Gaussian rough surfaces, where the parameters that describe the topographies were individually studied. One has seen that Weibull Maximum and Weibull Minimum topographies have very distinctive area values between each other and also when comparing to the Gaussian case. In the light contact conditions, Weibull Maximum is seen to have superior values while Weibull Minimum has a slow growth rate. However, with the increase of the external pressure, the Weibull minimum starts a steep increase in area, ultimately overtaking its counterpart. In this evolution, the shape parameter acts as a regulator approximating or moving away from the curves. For $C = 3.062$ very similar results to the Gaussian case are obtained. When comparing with Gaussian results these effects highlight various differences in shape and form of the area evolution curves at different regimes of external pressure. This sustains the importance of studying the contact of non-Gaussian rough surfaces since the Gaussian approximation might bring some unwanted errors into play. Furthermore, the spectral properties also provide some intricate results that are not consistent with Gaussian theories. For example, for Weibull Minimum topographies in light contact, for lower shape parameter values, the contact area increases with $\lambda_l/\lambda_s$ and $H$. This is the opposite result of the Gaussian case where higher $\alpha$ are expected to have lower values of the area. The analysis of contact pressure distributions was important to verify the consistency of the results. It was seen that while Weibull Maximum tends to have a mode value higher than the external pressure value, the opposite is verified in Weibull Minimum. The increase in area is often verified by an increase in the contact pressure values around the mode value. In addition, it is seen that Weibull Minimum have a greater tendency for having higher pressure values, a fact that is accentuated by lower $C$, higher $\lambda_l/\lambda_s$ and higher $H$. Some of the conclusions drawn in the 2D study were emphasized by the 3D FE application presented at the end of this chapter.

The numerical studies were performed using the Finite Element Method equipped with a dual mortar contact algorithm. This method is often considered the one of the most advanced and robust formulation to deal with contact problems (Popp, 2012). Also, it proves to be particularly good for solving contact problems with large deformations and so it is believed to be particularly interesting to solve rough contact of positively skewed rough surfaces (Weibull Minimum case), that contains steep summits that experience severe deformations in full contact conditions. Nonetheless, by using such a strategy the computational cost of the simulations gets incredible high, particularly for 3D contact problems, which constitutes a major drawback on this type of studies. For further investigations on the topic of elastic, non-adhesive and frictionless rough contact the hypothesis of using different numerical strategies should be addressed.

# Chapter 6

# Concluding remarks and future work

In this work, a contact homogenisation FEM approach to the elastic and frictionless contact of non-Gaussian rough surfaces was presented. Topographies modelled with Weibull distributions were extensively studied in terms of statistical features inspecting the effect of the topography's parameters. FE simulations were performed to characterize the micromechanical behaviour, focusing on the real contact area evolution and the contact pressure distribution. The main conclusions of this dissertation are presented in the following section, followed by an overview of interesting future works.

## 6.1 General conclusions

A first approach to non-Gaussian rough surfaces has focused on the comprehension of the statistics of this type of topographies. Taking advantage of the well known Gaussian case, a first overview of the statistic of Gaussian surfaces was done by looking at Nayak's theory (Nayak, 1971). From this work, the probability density of summits heights $p_{\text{sum}}(z^*)$, joint probability density function $p'_{\text{sum}}$ for summits with normalized height $z^*$ and equivalent mean curvature $t_1$ were acknowledged as relevant topography descriptors. Important results from this theory were also remarked, such as the dependency of only one parameter $\alpha$, the tendency of topographies with lower spectral content to have a higher concentration of higher height summits and the increasing trend on summits curvature with the height of summits. A numerical routine was built to numerically recover the statistics of sample topographies generated by using the algorithm proposed by Wu (2000b), available in the `LINKS-RC` framework. These numerical results obtained were validated by comparison with Nayak's analytical solutions.

The non-Gaussian topographies were assessed by means of the Weibull distribution due to its versatility to model several different types of topographies. Due to its formulation, it can be simply reduced to a one-parameter function which controls the shape of the probability function. This distribution can be assessed in two forms, one able to produce negatively skewed surfaces, Weibull Maximum, and the opposite case, Weibull Minimum. The range of skewness and kurtosis capable of being modelled with this distribution was depicted in Figure 3.14 where the validity of this function to model several practical non-Gaussian engineering surfaces were endorsed. A numeric study on the

statistics of non-Gaussian topographies was performed, modelling the heights distributions with the Weibull distribution, employed the numerical generation algorithm proposed by Pérez-Ràfols and Almqvist (2019) and the aforementioned geometry detection routine. The parameter range of this study was constrained by practical computational limitations. The non-Gaussian topography generator is more expensive when compared to the Gaussian method since it has to iterate multiple times over a normally distributed topography to obtain the final surface. Higher values of bandwidth $\lambda_l/\lambda_s$ lead to a rapid increase in the computation time.

The numerical results were assessed in a similar fashion to the Gaussian case, creating an interesting environment for comparing results. The impact of the height distribution, the shape parameter and the spectral properties ($\lambda_l/\lambda_s$, $H$ and $\alpha$) was extensively discussed. It was seen that the distribution of summits heights ($p_{\text{sum}}(z^*)$) tends to be dominated by two main factors: the tendency for summits to occur in higher heights and the shape of the heigh distribution. This results in Weibull Maximum topographies having impressive higher concentrations of higher height summits, much larger than the Gaussian case, while Weibull Minimum topographies tend to have more summits at lower heights, yet without the magnitude verified in its counterpart. The shape parameter $C$ acts as regulator of this effect going from extremely deviating topographies, like $C = 1$, to near the Gaussian case $C = 3.602$. For Weibull Maximum surfaces, it was shown that the curvature tends to decrease with the height (the opposite result of Gaussian topographies). On the other hand, Weibull Minimum topographies show summits with an average curvature growth trend with height, having considerable higher values of $\bar{\kappa}_m$ than the Gaussian case, for higher height summits. The impact of the spectral properties on the statistical properties was less clear, yet some important trends have been figured out. It was seen that Weibull Maximum topographies tend to follow the Gaussian relation, i.e., the tendency for lower $\alpha$ to have a higher concentration of higher height summits. In Weibull Minimum the results captured were different since the majority of the summits is located at lower heights and higher $\alpha$ tend to lead to higher concentrations of lower height summits. Relatively to the influence on the curvatures, the most relevant observations are concerned with the curvature values at higher heights. While in Weibull Maximum the lower the $\alpha$ the higher the $\bar{\kappa}_m/\sqrt{m_4}$ the opposite is verified for Weibull Minimum. To end this study an analysis of the density of summits $D_{\text{sum}}$ was performed, where one has seen that Weibull Maximum topographies tend to have a higher concentration of summits especially for lower $C$ values. Both spectral properties also play an important role, with $D_{\text{sum}}$ increasing with $\lambda_l/\lambda_s$ but decreasing with $H$. These simple yet hard to assimilate results have proved to be extremely important by giving a much deeper knowledge about this type of topographies, from which very few characteristics were known. Knowledge obtained in this study was later applied in the Chapter 5.

To conclude Chapter 3, a small study on the dependence of the non-Gaussian topography statistics on the Nayak's parameter was done. This study was motivated by observations on the previous study that highlighted that topography statistics might not be fully defined by the $\alpha$ value, and that both wavelength ratio $\lambda_l/\lambda_s$ and Hurst exponent $H$ might have independent influences. Despite the short bandwidth range of the study, some small differences were verified in both summits height distribution and expected

mean curvature. While in Weibull Maximum summits height distribution the differences were small and with a tendency to decrease for higher $\alpha$, Weibull Minimum have shown different concentrations of lower height summits that tend to increase with $\alpha$. These results suggest further work on this topic as it will be proposed in the next section.

The second part of this work was dedicated to the FE analysis of the non-Gaussian rough contact—Chapter 5. Taking advantage of the FE framework equipped with a contact discretization using a dual mortar approach, several numerical contact simulations were performed. A first initial 2D study was done in order to verify mesh convergence and to properly choose the mesh size, given by $\lambda_s/\Delta x$. Several mesh sizes were studied for both Weibull Maximum and Minimum cases and the mesh convergence was verified by both upper and lower bound area computation strategies. With these results it was also verified that by averaging both area values the convergence rate is rapidly increased and coarse meshes can be used, reducing the computational cost. A mesh size value of $\lambda_s/\Delta x = 8$ was defined as appropriate for the remaining simulations.

The second and larger study was performed for a total of 80 different cases in order the extensively explore the behaviour of non-Gaussian rough surfaces under contact. The simulations results were analysed in the real contact area evolution and the contact pressure distribution and, when relevant, compared to Gaussian solutions, like Persson's model. A systematic analysis of the parameters was done by isolating the effect in the study. The first discussion focussed on the general behaviour of the different types of Weibull surfaces and comparing with the Gaussian results. It was seen that the area is completely dominated by Weibull Maximum surfaces in light contact regions. The predominance of higher heights in this type of distribution makes the contact area to grow faster with external pressure. For increasing values of pressure, one verifies that the initial slow progression of Weibull Minimum rapidly vanishes and a steep increase is verified overtaking Weibull Maximum in contact area value. Both shape and magnitude of contact evolution of Weibull distributions differ significantly from the Gaussian, highlighting the pertinence of studying this type of topographies. The comparison between contact pressure distribution has shown that mode values of Weibull Maximum tend to be higher than the normalized external pressure while in Weibull Minimum tend to be smaller. The shape parameter has once again shown its regulatory character, as it controls the deviation from the Gaussian results—smaller $C$ larger deviations from the Gaussian case. It was seen that Weibull Maximum topographies for lower values of pressure are much more affected by the shape parameter, as it plays with the concentration of higher heights, therefore being crucial in light contact conditions in this case. It was also verified that higher pressure values are more likely to happen in Weibull Minimum topographies, especially for a lower value of $C$.

Regarding the spectral properties, some interesting new observations were found in this study. It was seen that in Weibull Maximum topographies the trends observed in Gaussian results cannot be blindly applied. While in Gaussian topographies, in light contact, lower values of $\alpha$ result in higher areas, it was seen that maximum values of area we obtained for both $\lambda_l/\lambda_s = 64$ and $H = 0.8$, i.e., for large values of $\alpha$. This observations is even more expressive when $C = 1$ and is kept up to full contact conditions. On the other hand, Weibull Minimum topographies show a more evidenced dependency on the spec-

tral properties when compared with its counterpart. In the initial pressure regime, the larger area fractions are associated with lower $\lambda_l/\lambda_s$ and $H$, yet with the increase in pressure topographies, the contact area for higher bandwidths rapidly grows. The statistical evidence of these results is not very clear however, it was postulated that the contributions of $D_{\text{sum}}$ and curvatures might play central role. To conclude the analysis of this set of 2D results, a simple fitting procedure was done in order to summarize the results. It was seen that the typical Gaussian linear behaviour in low-pressure regions normally associated with asperity-based models is not recovered in Weibull topographies. Instead, concave forms are typically found which has encouraged the use of a power-law fitting function (Equation (5.1)). The fitting procedure, applied in the light contact region, was successful, insofar as the computed parameters allow to capture the trends with high accuracy.

Finally, a last three-dimensional application of the non-Gaussian contact problem was performed, which constitutes the ultimate goal of this type of study. Due to computational limitations, only a small number of cases was tested, yet the results obtained highlight several of the conclusions drawn from the 2D study, validating the main approach considered in this work.

## 6.2 Future work

During this work, several aspects were appointed to future work and developments. Some conclusions required further clarifications and further investigations. Additionally, since the majority of the work on the rough contact of non-Gaussian surfaces constitutes original contributions, several new research purposes can be envisioned.

- **Extension of the statistical study on non-Gaussian topographies.** In Chapter 3 the numerical study on non-Gaussian was carried out for a limited range of spectral properties considering only two values of the wavelength ratio ($\lambda_l/\lambda_s \in [8,16]$) and two values of the Hurst exponent ($H \in [0.2,0.8]$). This combination of properties only has allowed reaching a Nayak's parameter $\alpha$ value of 11.89, which in this context may be regarded as a low value. For example, reference numerical studies like Yastrebov, Anciaux, *et al.* (2017b) have studied topographies with $\alpha$ larger than 200. As seen, the increase of the bandwidth severely increase the computational cost, yet it might be beneficial to extend the value of $\lambda_l/\lambda_s$ to clarify some issues that were not so self-evident. Additionally, the number of realizations considered might have to be augmented in order to obtain more representative statistical values. A study on the convergence of the statistics with the number of realizations would also be interesting in order to ease future numerical studies.
- **Testing different types of height distributions using the non-Gaussian topographies generator.** In the current work, the non-Gaussian self-affine rough surfaces were modelled using two versions of the Weibull probability distribution. This choice has relied on previous works on the topic that justified the use of this distribution for several engineering applications, such as McCool (1992), Yu and Polycarpou (2001, 2004a) and Pérez-Ràfols and Almqvist (2021). However, one of the advantages of the used non-Gaussian topography generator method (Pérez-Ràfols

and Almqvist, 2019) is that it allows obtaining topographies with any different probability distribution. One can then test different types of probability distributions that might suit specific engineering applications. For example, surfaces that arise from a multiprocess manufacturing process often exhibit bimodal height probability distribution (Pawlus, 2008).

- **Study the accuracy of the Nayak's parameter for characterizing the statistics of non-Gaussian rough surfaces.** It was advanced in this work that the statistics of non-Gaussian rough surfaces might not be completely dependent the Nayak's parameter, a quantity that for Gaussian topographies holds all the information of the spectral content. A small study on the impact of the Hurst exponent was done on Section 3.2.5 by comparing statistics of topographies with the same Nayak's parameter value but different combinations of both $\lambda_l/\lambda_s$ and $H$. An extension of this study can be done by focusing on the impact of $\lambda_l/\lambda_s$ rather than the Hurst exponent. Different shape parameters values might also be taken, but most importantly an additional effort should be employed on the number of realizations. The tenuous differences observed on the summits height distributions may require extra samples to clarify the behaviours and better understanding the physical phenomena. An extension of this study to the 2D or 3D simulation of RCE should also be done allowing to infer the capability of $\alpha$ to describe real contact area evolution on elastic frictionless contact.
- **Extend the study to 3D using a faster numerical method.** The current study of the impact of non-Gaussian height distribution on the elastic frictionless contact was carried out using mainly 2D FE simulations, with only some 3D applications. As mentioned during the work, for this type of problem there are some numerical methods, namely the BEM, that can analyse the contact in a 3D rough surface with a great reduction in computational cost. A well-established numerical method in rough contact is the FFT-BEM, which showcases exceptionally efficient computation times (Rey *et al.*, 2017). Additionally, a recent open-source package, named `Tamaas`, which incorporates the aforementioned method have been publicly released (Frérot, Anciaux, *et al.*, 2020), which can be incorporated in the current `LINKS-RC` framework to extend the current results to 3D.
- **Extension to the contact of two rough surfaces.** In this dissertation, only contact of an RCE with a flat rigid surface was considered. However, in many engineering applications, both surfaces in contact might be rough and with very distinctive features. Thus, studying the real contact area between two RCEs with the same or different characteristics would be an interesting contribution to this research topic. In addition, while it is known that Gaussian surfaces are reproducive under addition, meaning that the contact between two rough surfaces can be treated as the contact between an equivalent surface and rigid flat boundary, the same does not apply for the non-Gaussian. Some authors, like McCool (1992), have advanced that the contact between two Weibull rough surfaces can be approximated by an equivalent surface with the distribution parameters computed to match specific conditions. Therefore, the extension to the contact of two rough surfaces can also incorporate the evaluation and/or validation of this type of simplification.

- **Definition of a Representative Contact Element for analysing non-Gaussian rough surfaces.** In this work the 2D RCE parameters considered were the same as defined in Couto Carneiro *et al.* (2020) for a Gaussian case. The results obtained did not highlight particular problems with the RCE definition adopted however, the considered parameters should be validated with a proper study. These investigations can also be extended to the definition of a 3D RCE of a non-Gaussian surface.
- **Extension to other problems of interest within the context of non-Gaussian rough surfaces.** The study has focused only on the elastic frictionless contact, which is only one of the several topics that can be studied within the context of non-Gaussian rough surfaces. Further investigations on the topic can include features like elasto-plastic material models, rough surfaces with anisotropy or even the evolution of contact under cycling loading.
- **Validation with experimentation.** Although the FEM is a robust tool with a high degree of reliability and correlation with real applications, there are always some uncertainty associated with the numerical studies performed. Therefore, experimentation is vital to validate numerical works and to tune and enhance the frameworks developed. For instance, the contact area evaluation might be performed with many different strategies. If one could define which methodology is the best or improve one of the methods, by experimental evidence, more precise area evolution prediction could be obtained.

# Appendix A

# Numerical fit parameters for the contact area curves in the 2D FEM study

In Section 5.3.5 a numerical fitting process of the area evolutions curves was presented. A power-law function was fitted to the numerical results using the non-linear least squares method through the `SciPy` package. The computed parameters $a$ and $b$ as well as the coefficient of determination $R^2$ are presented below from Table A.1 to Table A.4. For the sake of clarity and concision, the results are grouped by the type of the height distribution and the Hurst exponent value.

**Table A.1:** Power law fitting parameters $a$ and $b$ and respective coefficient of determination $R^2$ for the Weibull Maximum case and $H = 0.2$.

| $\lambda_l/\lambda_s$ | $C$ | $a$ | $b$ | $R^2$ |
|---|---|---|---|---|
| 8 | 1 | 1.6586 | 0.6320 | 0.9991 |
| 8 | 1.2 | 1.5240 | 0.6287 | 0.9991 |
| 8 | 1.5 | 1.4271 | 0.6535 | 0.9995 |
| 8 | 2 | 1.4386 | 0.7122 | 0.9998 |
| 8 | 3.602 | 1.4304 | 0.7953 | 0.9999 |
| 16 | 1 | 1.6270 | 0.6055 | 0.9992 |
| 16 | 1.2 | 1.5337 | 0.6264 | 0.9995 |
| 16 | 1.5 | 1.4368 | 0.6543 | 0.9997 |
| 16 | 2 | 1.4312 | 0.7095 | 0.9999 |
| 16 | 3.602 | 1.4994 | 0.8169 | 0.9999 |
| 32 | 1 | 1.6322 | 0.5959 | 0.9994 |
| 32 | 1.2 | 1.5470 | 0.6236 | 0.9997 |
| 32 | 1.5 | 1.4395 | 0.6473 | 0.9996 |
| 32 | 2 | 1.4245 | 0.7057 | 0.9999 |
| 32 | 3.602 | 1.4948 | 0.8149 | 1.0000 |
| 64 | 1 | 1.6095 | 0.5846 | 0.9990 |
| 64 | 1.2 | 1.5699 | 0.6215 | 0.9995 |
| 64 | 1.5 | 1.4959 | 0.6629 | 0.9997 |
| 64 | 2 | 1.4520 | 0.7179 | 0.9999 |
| 64 | 3.602 | 1.5580 | 0.8395 | 0.9999 |

**Table A.2:** Power law fitting parameters $a$ and $b$ and respective coefficient of determination $R^2$ for the Weibull Maximum case and $H = 0.8$.

| $\lambda_l/\lambda_s$ | $C$ | $a$ | $b$ | $R^2$ |
|---|---|---|---|---|
| 8 | 1 | 1.8117 | 0.6327 | 0.9983 |
| 8 | 1.2 | 1.6705 | 0.6312 | 0.9986 |
| 8 | 1.5 | 1.5218 | 0.645 | 0.9994 |
| 8 | 2 | 1.4549 | 0.6964 | 0.9993 |
| 8 | 3.602 | 1.3933 | 0.8005 | 0.9998 |
| 16 | 1 | 1.8475 | 0.6167 | 0.9980 |
| 16 | 1.2 | 1.6990 | 0.6164 | 0.9983 |
| 16 | 1.5 | 1.5067 | 0.6357 | 0.9990 |
| 16 | 2 | 1.4331 | 0.6993 | 0.9994 |
| 16 | 3.602 | 1.3997 | 0.8175 | 0.9997 |
| 32 | 1 | 1.8602 | 0.5991 | 0.9970 |
| 32 | 1.2 | 1.6749 | 0.6151 | 0.9989 |
| 32 | 1.5 | 1.5647 | 0.6551 | 0.9991 |
| 32 | 2 | 1.4912 | 0.7216 | 0.9996 |
| 32 | 3.602 | 1.5412 | 0.8811 | 0.9999 |
| 64 | 1 | 1.9271 | 0.6063 | 0.9977 |
| 64 | 1.2 | 1.7943 | 0.6189 | 0.9985 |
| 64 | 1.5 | 1.6375 | 0.6653 | 0.9988 |
| 64 | 2 | 1.5515 | 0.7350 | 0.9994 |
| 64 | 3.602 | 1.5937 | 0.9067 | 0.9998 |

**Table A.3:** Power law fitting parameters $a$ and $b$ and respective coefficient of determination $R^2$ for the Weibull Minimum case and $H = 0.2$.

| $\lambda_l/\lambda_s$ | $C$ | $a$ | $b$ | $R^2$ |
|---|---|---|---|---|
| 8 | 1 | 1.7311 | 1.0090 | 0.9998 |
| 8 | 1.2 | 1.6068 | 0.9594 | 0.9999 |
| 8 | 1.5 | 1.4449 | 0.8970 | 0.9999 |
| 8 | 2 | 1.4343 | 0.8496 | 0.9998 |
| 8 | 3.602 | 1.5112 | 0.8102 | 0.9999 |
| 16 | 1 | 2.2369 | 1.1128 | 0.9996 |
| 16 | 1.2 | 1.8895 | 1.0309 | 0.9999 |
| 16 | 1.5 | 1.5843 | 0.9361 | 0.9999 |
| 16 | 2 | 1.5291 | 0.8889 | 0.9999 |
| 16 | 3.602 | 1.5555 | 0.8274 | 0.9999 |
| 32 | 1 | 3.5598 | 1.2806 | 0.9992 |
| 32 | 1.2 | 2.4694 | 1.1335 | 0.9998 |
| 32 | 1.5 | 1.8871 | 1.0086 | 0.9999 |
| 32 | 2 | 1.6695 | 0.9255 | 1.0000 |
| 32 | 3.602 | 1.5591 | 0.8290 | 0.9998 |
| 64 | 1 | 6.2468 | 1.4411 | 0.9994 |
| 64 | 1.2 | 3.4045 | 1.2330 | 0.9997 |
| 64 | 1.5 | 2.2283 | 1.0689 | 0.9999 |
| 64 | 2 | 1.826 | 0.9673 | 1.0000 |
| 64 | 3.602 | 1.6216 | 0.8537 | 0.9999 |

**Table A.4:** Power law fitting parameters $a$ and $b$ and respective coefficient of determination $R^2$ for the Weibull Minimum case and $H = 0.8$.

| $\lambda_l/\lambda_s$ | $C$ | $a$ | $b$ | $R^2$ |
|---|---|---|---|---|
| 8 | 1 | 1.8664 | 1.0631 | 0.9999 |
| 8 | 1.2 | 1.5590 | 0.9864 | 0.9998 |
| 8 | 1.5 | 1.4545 | 0.9267 | 0.9996 |
| 8 | 2 | 1.4312 | 0.8861 | 0.9998 |
| 8 | 3.602 | 1.4654 | 0.8136 | 0.9996 |
| 16 | 1 | 2.3519 | 1.1570 | 0.9998 |
| 16 | 1.2 | 1.9594 | 1.0890 | 0.9998 |
| 16 | 1.5 | 1.7382 | 1.0241 | 0.9999 |
| 16 | 2 | 1.5707 | 0.9508 | 0.9998 |
| 16 | 3.602 | 1.5347 | 0.8518 | 0.9996 |
| 32 | 1 | 3.2637 | 1.2914 | 0.9999 |
| 32 | 1.2 | 2.7671 | 1.2485 | 0.9999 |
| 32 | 1.5 | 2.0977 | 1.1307 | 0.9999 |
| 32 | 2 | 1.9160 | 1.0630 | 0.9999 |
| 32 | 3.602 | 1.6856 | 0.9151 | 0.9996 |
| 64 | 1 | 4.6348 | 1.3816 | 0.9999 |
| 64 | 1.2 | 3.2103 | 1.2597 | 0.9999 |
| 64 | 1.5 | 2.5045 | 1.1832 | 0.9999 |
| 64 | 2 | 2.0017 | 1.0738 | 0.9998 |
| 64 | 3.602 | 1.7309 | 0.9434 | 0.9997 |

*Page intentionally left blank*

# References

**Adler, R. J., Firmin, D., and Kendall, D. G. (1981)**. "A Non-Gaussian Model for Random Surfaces". In: *Philosophical Transactions of the Royal Society of London. Series A, Mathematical and Physical Sciences* 303 (1479), pp. 433–462.

**Aghababaei, R., Warner, D. H., and Molinari, J.-F. (2016)**. "Critical Length Scale Controls Adhesive Wear Mechanisms". In: *Nature Communications* 7 (1) (1), p. 11816.

**Anciaux, G. and Molinari, J. F. (2013)**. "A Molecular Dynamics and Finite Elements Study of Nanoscale Thermal Contact Conductance". In: *International Journal of Heat and Mass Transfer* 59, pp. 384–392.

**Archard, J. F. and Allibone, T. E. (1957)**. "Elastic Deformation and the Laws of Friction". In: *Proceedings of the Royal Society of London. Series A. Mathematical and Physical Sciences* 243 (1233), pp. 190–205.

**Ben-David, O., Cohen, G., and Fineberg, J. (2010)**. "The Dynamics of the Onset of Frictional Slip". In: *Science*.

**Bendat, J. S. and Piersol, A. G. (2010)**. *Random Data: Analysis and Measurement Procedures*. 4th ed. Wiley Series in Probability and Statistics. Hoboken, N.J: Wiley. 604 pp.

**Bhushan, B., ed. (1999)**. *Handbook of Micro/Nanotribology*. Ed. by B. Bhushan. 2nd ed. The Mechanics and Materials Science Series. Boca Raton: CRC Press. 859 pp.

**Bhushan, B. (2013)**. *Principles and Applications of Tribology*. 2nd edition. Wiley. 1006 pp.

**Bonet, J. and Wood, R. D. (2008)**. *Nonlinear Continuum Mechanics for Finite Element Analysis*. 2nd ed. Cambridge: Cambridge University Press.

**Bowden, F. P. and Tabor, D. (1951)**. "The Friction and Lubrication of Solids". In: *American Journal of Physics* 19 (7), pp. 428–429.

**Bush, A. W., Gibson, R. D., and Thomas, T. R. (1975)**. "The Elastic Contact of a Rough Surface". In: *Wear* 35 (1), pp. 87–111.

**Campañá, C., Müser, M. H., and Robbins, M. O. (2008)**. "Elastic Contact between Self-Affine Surfaces: Comparison of Numerical Stress and Contact Correlation Functions with Analytic Predictions". In: *Journal of Physics: Condensed Matter* 20 (35), p. 354013.

**Carbone, G. and Bottiglione, F. (2008)**. "Asperity Contact Theories: Do They Predict Linearity between Contact Area and Load?" In: *Journal of the Mechanics and Physics of Solids* 56 (8), pp. 2555–2572.

**Carvalho, R. P. (2018)**. "Finite Deformation Contact Modelling at Different Scales Based on Dual Mortar Methods". PhD Seminar. Faculdade de Engenharia da Universidade do Porto.

**Chang, L. and Jeng, Y.-R. (2013)**. "Effects of Negative Skewness of Surface Roughness on the Contact and Lubrication of Nominally Flat Metallic Surfaces". In: *Proceedings of the Institution of Mechanical Engineers, Part J: Journal of Engineering Tribology* 227 (6), pp. 559–569.

**Chang, W. R., Etsion, I., and Bogy, D. B. (1987)**. "An Elastic-Plastic Model for the Contact of Rough Surfaces". In: *Journal of Tribology* 109 (2), pp. 257–263.

**Chaves, E. W. (2013)**. *Notes on Continuum Mechanics*. Lecture Notes on Numerical Methods in Engineering and Sciences. Springer Netherlands.

**Ciavarella, M. and Afferrante, L. (2016)**. "Adhesion of Rigid Rough Contacts with Bounded Distribution of Heights". In: *Tribology International*. 42nd Leeds-Lyon Symposium on Tribology- Surfaces and Interfaces: Mysteries at Different Scales 100, pp. 18–23.

**Couto Carneiro, A. M. (2019)**. "Modeling and Analysis of Rough Contact by Computational Homogenization". M.Sc. Thesis. Faculdade de Engenharia da Universidade do Porto.

**Couto Carneiro, A. M., Pinto Carvalho, R., and Andrade Pires, F. M. (2020)**. "Representative Contact Element Size Determination for Micromechanical Contact Analysis of Self-Affine Topographies". In: *International Journal of Solids and Structures* 206, pp. 262–281.

**De Lorenzis, L. and Wriggers, P. (2013)**. "Computational Homogenization of Rubber Friction on Rough Rigid Surfaces". In: *Computational Materials Science* 77, pp. 264–280.

**Derjaguin, B. V., Muller, V. M., and Toporov, Y. P. (1975)**. "Effect of Contact Deformations on the Adhesion of Particles". In: *Journal of Colloid and Interface Science* 53 (2), pp. 314–326.

**Dieterich, J. H. and Kilgore, B. D. (1994)**. "Direct Observation of Frictional Contacts: New Insights for State-Dependent Properties". In: *Pure and Applied Geophysics PAGEOPH* 143 (1-3), pp. 283–302.

**Farah, P., Popp, A., and Wall, W. A. (2015)**. "Segment-Based vs. Element-Based Integration for Mortar Methods in Computational Contact Mechanics". In: *Computational Mechanics* 55 (1), pp. 209–228.

**Frérot, L., Anciaux, G., *et al.* (2020)**. "Tamaas: A Library for Elastic-Plastic Contact of Periodic Rough Surfaces". In: *Journal of Open Source Software* 5 (51), p. 2121.

**Frérot, L., Bonnet, M., *et al.* (2019)**. "A Fourier-Accelerated Volume Integral Method for Elastoplastic Contact". In: *Computer Methods in Applied Mechanics and Engineering* 351, pp. 951–976.

**Fuller, K. N. G. and Tabor, D. (1975)**. "The Effect of Surface Roughness on the Adhesion of Elastic Solids". In: *Proceedings of the Royal Society of London. A. Mathematical and Physical Sciences* 345 (1642), pp. 327–342.

**Greenwood, J. A. and Johnson, K. L. (1984)**. "A Unified Theory of Surface Roughness". In: *Proceedings of the Royal Society of London. A. Mathematical and Physical Sciences* 393 (1804), pp. 133–157.

**Greenwood, J. A., Williamson, J. B. P., and Bowden, F. P. (1966)**. "Contact of Nominally Flat Surfaces". In: *Proceedings of the Royal Society of London. Series A. Mathematical and Physical Sciences* 295 (1442), pp. 300–319.

**Greenwood, J. (2006)**. "A Simplified Elliptic Model of Rough Surface Contact". In: *Wear* 261, pp. 191–200.

**Hertz, H. (1882)**. "Ueber Die Berührung Fester Elastischer Körper". In: *Journal fur die Reine und Angewandte Mathematik*.

**Holmberg, K. and Erdemir, A. (2017)**. "Influence of Tribology on Global Energy Consumption, Costs and Emissions". In: *Friction* 5 (3), pp. 263–284.

**Holzapfel, G. A. (2000)**. *Nonlinear Solid Mechanics: A Continuum Approach for Engineering*. 1st edition. Chichester ; New York: Wiley. 455 pp.

**Hüeber, S. and Wohlmuth, B. I. (2005)**. "A Primal–Dual Active Set Strategy for Non-Linear Multibody Contact Problems". In: *Computer Methods in Applied Mechanics and Engineering* 194 (27), pp. 3147–3166.

**Hüeber, S. (2008)**. "Discretization Techniques and Efficient Algorithms for Contact Problems". PhD Thesis. Universität Stuttgart.

**Hyun, S. *et al.* (2004)**. "Finite-Element Analysis of Contact between Elastic Self-Affine Surfaces". In: *Physical Review. E, Statistical, Nonlinear, and Soft Matter Physics* 70 (2 Pt 2), p. 026117.

**Johnson, K. L. (1985)**. *Contact Mechanics*. Cambridge University Press. 456 pp.

**Johnson, K. L. *et al.* (1971)**. "Surface Energy and the Contact of Elastic Solids". In: *Proceedings of the Royal Society of London. A. Mathematical and Physical Sciences* 324 (1558), pp. 301–313.

**Johnson, N. L., Kotz, S., and Balakrishnan, N. (1994)**. *Continuous Univariate Distributions, Vol. 1*. 2nd edition. New York: Wiley-Interscience. 761 pp.

**Jost, P. (1966)**. *Lubrication (Tribology): A Report on the Present Position and Industry's Needs*. London: HM Stationery Office.

**Kikuchi, N. and Oden, J. T. (2001)**. *Contact Problems in Elasticity: A Study of Variational Inequalities and Finite Element Methods*. Nachdr. SIAM Studies in Applied Mathematics 8. Philadelphia: SIAM. 495 pp.

**Kim, T., Bhushan, B., and Cho, Y. (2006a)**. "The Contact Behavior of Elastic/Plastic Non-Gaussian Rough Surfaces". In: *Tribology Letters* 22 (1), p. 1.

**Kim, T., Bhushan, B., and Cho, Y. (2006b)**. "The Contact Behavior of Elastic/Plastic Non-Gaussian Rough Surfaces". In: *Tribology Letters* 22 (1), p. 1.

**Laursen, T. A. (2003)**. *Computational Contact and Impact Mechanics: Fundamentals of Modeling Interfacial Phenomena in Nonlinear Finite Element Analysis*. Berlin Heidelberg: Springer-Verlag.

**Longuet-Higgins, M. S. and Deacon, G. E. R. (1957a)**. "Statistical Properties of an Isotropic Random Surface". In: *Philosophical Transactions of the Royal Society of London. Series A, Mathematical and Physical Sciences* 250 (975), pp. 157–174.

**Longuet-Higgins, M. S. and Deacon, G. E. R. (1957b)**. "The Statistical Analysis of a Random, Moving Surface". In: *Philosophical Transactions of the Royal Society of London. Series A, Mathematical and Physical Sciences* 249 (966), pp. 321–387.

**Lopes, I. A. R. (2019)**. "Multi-Scale Modelling and Analysis of Multi-Phase Solids Using Second-Order Computational Homogenisation at Finite Strains with Parallel Computing". PhD Thesis. Faculdade de Engenharia da Universidade do Porto.

**Mainsah, E., Greenwood, j., and Chetwynd, D., eds. (2001)**. *Metrology and Properties of Engineering Surfaces*. Ed. by E. Mainsah, j. Greenwood, and D. Chetwynd. Springer US.

**Mandelbrot, B. B. (1967)**. "How Long Is the Coast of Britain? Statistical Self-Similarity and Fractional Dimension". In: *Science* 156 (3775), pp. 636–638.

**Mandelbrot, B. B. (1982)**. *The Fractal Geometry of Nature*. 2nd prt. edition. San Francisco: Times Books. 468 pp.

**Manesh, K. K., Ramamoorthy, B., and Singaperumal, M. (2010)**. "Numerical Generation of Anisotropic 3D Non-Gaussian Engineering Surfaces with Specified 3D Surface Roughness Parameters". In: *Wear* 268 (11), pp. 1371–1379.

**McCool, J. I. (1986)**. "Comparison of Models for the Contact of Rough Surfaces". In: *Wear* 107 (1), pp. 37–60.

**McCool, J. I. (1992)**. "Non-Gaussian Effects in Microcontact". In: *International Journal of Machine Tools and Manufacture*. Proceedings of the 5th International Conference on Metrology and Properties of Engineering Surfaces 32 (1), pp. 115–123.

**McCool, J. I. (2000)**. "Extending the Capability of the Greenwood Williamson Microcontact Model". In: *Journal of Tribology* 122 (3), pp. 496–502.

**Minet, C. *et al.* (2010)**. "Analysis and Modeling of the Topography of Mechanical Seal Faces". In: *Tribology Transactions* 53 (6), pp. 799–815.

**Nayak, P. R. (1971)**. "Random Process Model of Rough Surfaces". In: *Journal of Lubrication Technology* 93 (3), pp. 398–407.

**Nitsche, R. (2011)**. "A Multiscale Projection Method for Contact on Rough Surfaces". PhD Thesis. Hannover: Institut für Kontinuumsmechanik. 153 pp.

**Oden, P. I. *et al.* (1992)**. "AFM Imaging, Roughness Analysis and Contact Mechanics of Magnetic Tape and Head Surfaces". In: *Journal of Tribology* 114 (4), pp. 666–674.

**Panda, S. *et al.* (2016)**. "Spectral Approach on Multiscale Roughness Characterization of Nominally Rough Surfaces". In: *Journal of Tribology* 139 (031402).

**Pastewka, L. and Robbins, M. O. (2014)**. "Contact between Rough Surfaces and a Criterion for Macroscopic Adhesion". In: *Proceedings of the National Academy of Sciences* 111 (9), pp. 3298–3303.

**Pawlus, P. (2008)**. "Simulation of Stratified Surface Topographies". In: *Wear*. 10th International Conference on Metrology and Properties of Engineering Surfaces 264 (5), pp. 457–463.

**Pei, L. *et al.* (2005)**. "Finite Element Modeling of Elasto-Plastic Contact between Rough Surfaces". In: *Journal of the Mechanics and Physics of Solids* 53 (11), pp. 2385–2409.

**Pérez-Ràfols, F. and Almqvist, A. (2019)**. "Generating Randomly Rough Surfaces with given Height Probability Distribution and Power Spectrum". In: *Tribology International* 131, pp. 591–604.

**Pérez-Ràfols, F. and Almqvist, A. (2021)**. "On the Stiffness of Surfaces with Non-Gaussian Height Distribution". In: *Scientific Reports* 11 (1), p. 1863.

**Persson, B. N. J. (2001a)**. "Elastoplastic Contact between Randomly Rough Surfaces". In: *Physical Review Letters* 87 (11), p. 116101.

**Persson, B. N. J. (2001b)**. "Theory of Rubber Friction and Contact Mechanics". In: *The Journal of Chemical Physics* 115 (8), pp. 3840–3861.

**Persson, B. N. J. *et al.* (2004)**. "On the Nature of Surface Roughness with Application to Contact Mechanics, Sealing, Rubber Friction and Adhesion". In: *Journal of Physics: Condensed Matter* 17 (1), R1–R62.

**Popp, A. (2012)**. "Mortar Methods for Computational Contact Mechanics and General Interface Problems". PhD Thesis. Technische Universität München.

**Popp, A. *et al.* (2013)**. "Improved Robustness and Consistency of 3D Contact Algorithms Based on a Dual Mortar Approach". In: *Computer Methods in Applied Mechanics and Engineering* 264, pp. 67–80.

**Reis, F. J. P. (2014)**. "Multi-Scale Modelling and Analysis of Heterogeneous Solids at Finite Strains". PhD Thesis. Faculdade de Engenharia da Universidade do Porto.

**Rey, V., Anciaux, G., and Molinari, J.-F. (2017)**. "Normal Adhesive Contact on Rough Surfaces: Efficient Algorithm for FFT-Based BEM Resolution". In: *Computational Mechanics* 60 (1), pp. 69–81.

**Rigazzi, A. P. (2014)**. "The Effects of Roughness on the Area of Contact and on the Elastostatic Friction: FEM Simulation of Micro-Scale Rough Contact and Real World Applications". PhD Thesis. Università della Svizzera italiana.

**Rinne, H. (2008)**. *The Weibull Distribution: A Handbook*. 1st edition. Boca Raton: Chapman and Hall/CRC. 808 pp.

**Russ, J. C. (1994)**. *Fractal Surfaces*. Springer US.

**Sayles, R. S. and Thomas, T. R. (1978)**. "Surface Topography as a Nonstationary Random Process". In: *Nature* 271 (5644) (5644), pp. 431–434.

**Sayles, R. S. and Thomas, T. R. (1979)**. "Measurements of the Statistical Microgeometry of Engineering Surfaces". In: *Journal of Lubrication Technology* 101 (4), pp. 409–417.

**Sedlaček, M., Podgornik, B., and Vižintin, J. (2009)**. "Influence of Surface Preparation on Roughness Parameters, Friction and Wear". In: *Wear*. Tribology of Engineered Surfaces 266 (3), pp. 482–487.

**Sokolnikoff, I. S. (1964)**. *Tensor Analysis: Theory and Applications to Geometry and Mechanics of Continua*. Wiley. 380 pp.

**Spedding, T. A. *et al.* (1980)**. "The Pearson System of Distributions: Its Application to Non-Gaussian Surface Metrology and a Simple Wear Model". In: *Journal of Lubrication Technology* 102 (4), pp. 495–500.

**Stout, K. J., Davis, E. J., and Sullivan, P. J. (1990)**. *Atlas of Machined Surfaces*. Dordrecht: Springer Netherlands.

**Stout, K. (1980)**. "How Smooth Is Smooth? Surface Measurements and Their Relevance in Manufacturing". In: *Production engineer (London)* 59 (5).

**Stupkiewicz, S. (2007)**. *Micromechanics of Contact and Interphase Layers*. Lecture Notes in Applied and Computational Mechanics. Berlin Heidelberg: Springer-Verlag.

**Temizer, İ. and Wriggers, P. (2008)**. "A Multiscale Contact Homogenization Technique for the Modeling of Third Bodies in the Contact Interface". In: *Computer Methods in Applied Mechanics and Engineering* 198 (3), pp. 377–396.

**Thomas, T. R. and King, M. B. (1977)**. *Surface Topography in Engineering: A State of the Art Review and Bibliography*. British Hydromechanics Research Association, Fluid Engineering. 140 pp.

**Thomas, T. R. (1998)**. *Rough Surfaces*. World Scientific. 296 pp.

**Tomota, T., Kondoh, Y., and Ohmori, T. (2019)**. "Modeling Solid Contact between Smooth and Rough Surfaces with Non-Gaussian Distributions". In: *Tribology Transactions* 62 (4), pp. 580–591.

**Tzanakis, I. *et al.* (2012)**. "Future Perspectives on Sustainable Tribology". In: *Renewable and Sustainable Energy Reviews* 16 (6), pp. 4126–4140.

**Vakis, A. I. *et al.* (2018)**. "Modeling and Simulation in Tribology across Scales: An Overview". In: *Tribology International* 125, pp. 169–199.

**Vallet, C. *et al.* (2009)**. "Real versus Synthesized Fractal Surfaces: Contact Mechanics and Transport Properties". In: *Tribology International* 42 (2), pp. 250–259.

**Wang, W.-z. *et al.* (2006)**. "Effect of Surface Roughness Parameters on Mixed Lubrication Characteristics". In: *Tribology International* 39 (6), pp. 522–527.

**Whitehouse, D. J. (1982)**. "The Parameter Rash — Is There a Cure?" In: *Wear* 83 (1), pp. 75–78.

**Whitehouse, D. J. and Whitehouse, D. J. (2011)**. *Handbook of Surface and Nanometrology*. 2nd ed. Boca Raton: CRC Press. 975 pp.

**Whitehouse, D. J. (1994)**. *Handbook of Surface Metrology*. CRC Press. 1048 pp.

**Whitehouse, D. J. (2004)**. *Surfaces and Their Measurement*. Gulf Professional Publishing. 430 pp.

**Whitehouse, D. J., Archard, J. F., and Tabor, D. (1970)**. "The Properties of Random Surfaces of Significance in Their Contact". In: *Proceedings of the Royal Society of London. A. Mathematical and Physical Sciences* 316 (1524), pp. 97–121.

**Whitehouse, D. J., Phillips, M. J., and Tabor, D. (1978)**. "Discrete Properties of Random Surfaces". In: *Philosophical Transactions of the Royal Society of London. Series A, Mathematical and Physical Sciences* 290 (1369), pp. 267–298.

**Whitehouse, D. J., Phillips, M. J., and Tabor, D. (1982)**. "Two-Dimensional Properties of Random Surfaces". In: *Philosophical Transactions of the Royal Society of London. Series A, Mathematical and Physical Sciences* 305 (1490), pp. 441–468.

**Williamson, J. *et al.* (1969)**. "The Shape of Solid Surfaces". In: *Surface Mechanics, ASME, New York*, pp. 24–35.

**Wohlmuth, B. I. (2000)**. "A Mortar Finite Element Method Using Dual Spaces for the Lagrange Multiplier". In: *SIAM Journal on Numerical Analysis* 38 (3), pp. 989–1012.

**Wriggers, P. (2006)**. *Computational Contact Mechanics*. 2nd ed. Berlin Heidelberg: Springer-Verlag.

**Wriggers, P. (2008)**. *Nonlinear Finite Element Methods*. Berlin Heidelberg: Springer-Verlag.

**Wriggers, P. and Laursen, T. A., eds. (2010)**. *Computational Contact Mechanics*. Ed. by P. Wriggers and T. A. Laursen. Softcover reprint of hardcover 1st ed. 2007 edition. Wien: Springer. 255 pp.

**Wu, J.-J. (2000a)**. "Characterization of Fractal Surfaces". In: *Wear* 239 (1), pp. 36–47.

**Wu, J.-J. (2000b)**. "Simulation of Rough Surfaces with FFT". In: *Tribology International* 33 (1), pp. 47–58.

**Yang, C. and Persson, B. N. J. (2008)**. "Contact Mechanics: Contact Area and Interfacial Separation from Small Contact to Full Contact". In: *Journal of Physics: Condensed Matter* 20 (21), p. 215214.

**Yang, G. *et al.* (2014)**. "Numerical Simulation of 3D Rough Surfaces and Analysis of Interfacial Contact Characteristics". In: *CMES - Computer Modeling in Engineering and Sciences* 103, pp. 251–279.

**Yastrebov, V. A. (2013)**. *Numerical Methods in Contact Mechanics*. 1st edition. London : Hoboken, NJ: Wiley-ISTE. 416 pp.

**Yastrebov, V. A., Anciaux, G., and Molinari, J.-F. (2012)**. "Contact between Representative Rough Surfaces". In: *Physical Review E* 86 (3), p. 035601.

**Yastrebov, V. A., Anciaux, G., and Molinari, J.-F. (2015)**. "From Infinitesimal to Full Contact between Rough Surfaces: Evolution of the Contact Area". In: *International Journal of Solids and Structures* 52, pp. 83–102.

**Yastrebov, V. A., Anciaux, G., and Molinari, J.-F. (2017a)**. "On the Accurate Computation of the True Contact-Area in Mechanical Contact of Random Rough Surfaces". In: *Tribology International* 114, pp. 161–171.

**Yastrebov, V. A., Anciaux, G., and Molinari, J.-F. (2017b)**. "The Role of the Roughness Spectral Breadth in Elastic Contact of Rough Surfaces". In: *Journal of the Mechanics and Physics of Solids* 107, pp. 469–493.

**Yastrebov, V. A., Cailletaud, G., *et al.* (2015)**. "Three-Level Multi-Scale Modeling of Electrical Contacts Sensitivity Study and Experimental Validation". In: *2015 IEEE 61st Holm Conference on Electrical Contacts (Holm)*, pp. 414–422.

**Yu, N. and Polycarpou, A. A. (2001)**. "Contact of Rough Surfaces With Asymmetric Distribution of Asperity Heights". In: *Journal of Tribology* 124 (2), pp. 367–376.

**Yu, N. and Polycarpou, A. A. (2004a)**. "Combining and Contacting of Two Rough Surfaces with Asymmetric Distribution of Asperity Heights". In: *Journal of Tribology* 126 (2), pp. 225–232.

**Yu, N. and Polycarpou, A. A. (2004b)**. "Extracting Summit Roughness Parameters From Random Gaussian Surfaces Accounting for Asymmetry of the Summit Heights". In: *Journal of Tribology* 126 (4), pp. 761–766.

**Zhang, S., Wang, W., and Zhao, Z. (2014)**. "The Effect of Surface Roughness Characteristics on the Elastic–Plastic Contact Performance". In: *Tribology International* 79, pp. 59–73.

**Zienkiewicz, O. C., Taylor, R. L., and Zhu, J. Z. (2013)**. *The Finite Element Method: Its Basis and Fundamentals*. Seventh edition. Amsterdam: Elsevier, Butterworth-Heinemann. 714 pp.